The application of microwave radiation in materials chemistry

Flora Marcela Piña-Sandoval

Doctor of Philosophy

School of Chemistry

University of Edinburgh

2007

Abstract

Microwave radiation is becoming an increasingly widely accepted source of energy in heating chemical reactions, producing remarkable increases in reaction rate, and sometimes better yields and product distributions compared to when they are heated conventionally. When microwave heating is applied to solutions, the reason for the improvement can mostly be attributed to the faster, and more usually direct delivery of energy to the reagents, often leading to superheating. The application of microwaves to solid-state and materials synthesis and processing is much more poorly understood. Where rate enhancements have been seen, they are often for reasons analogous to those recognized in wet media -direct and rapid transfer of heat to specific parts of the reactive system, sometimes leading to small, hot regions of material with a relatively high microwave susceptibility (so-called 'hot spots'). There has been relatively little work to try to explore such effects. Here we present new microwave applicators or reactors that have been designed to be used in conjunction with X-ray and neutron diffractometers, and applied to a number of solid-state systems. In particular, we have developed tuned or tunable microwave cavities to be used in conjunction with an X-ray diffractometer working either in transmission mode with a capillary sample, or in reflection mode, with a flat plate. We have also developed further a microwave cavity that enables high-resolution neutron powder diffraction patterns to be taken, and tested it successfully on the High Resolution Powder Diffractometer (HRPD), at the ISIS Facility, UK. One application that was planned was the elucidation of synthetic steps in the microwave-assisted formation of the zeolite ZSM-5; we established a reproducible method for microwave-assisted synthesis that is appreciably faster than when it is heated conventionally, but found that progress would require the brightness of a synchrotron X-ray source. We also studied microwave-assisted processing of zeolites Na-Y and H-ZSM-5, accelerating the insertion of copper ions in the solid-state. Phase transitions in the ferroelectric materials $BaTiO_3$ and $KNbO_3$ were studied by *in situ* diffraction to determine whether microwave irradiation can influence the transition between phases of different dielectric susceptibility, and evidence was found for a lower transition temperature in the later case compared to that of conventional heating. *In situ* neutron diffraction measurements have provided the first direct evidence of differential heating under microwave irradiation of heterogeneous catalysts in the form of MoS_2 or Ni particles dispersed over a high surface area Al_2O_3 support. This employed high-resolution measurements of the cell parameters at a series of temperatures achieved both under conventional and microwave heating, using the former

to produce a calibration curve to establish a temperature scale, and the latter to determine the effective temperature of every crystalline phase under microwave heating. A differential temperature of the order of tens of Kelvin was found when the mean sample temperature was one or two hundred Kelvin above room temperature. Finally, we performed *in situ* X-ray diffraction on a sample of AgI held in a glass capillary to observe the transformation between the dense β phase, and the more open, fast-ion conducting α phase; this revealed a significant reduction in the transition temperature, possibly arising from a strong interaction between the microwave field and the defects or lattice modes implicated in the transition.

Acknowledgements

This project would have not met its objectives, had it not been for the ongoing support of many individuals to whom I am forever grateful. Particularly, I would like to express my debt of gratitude to my supervisor Proffesor Andrew Harrison, who has afforded me the privilege of working with him. His help and advice has been the guiding light of this project.

I am very grateful to the National Conseil for Science and Technology (CONACyT) in Mexico for their financial support through my studies.

Thank to Dr. Gavin Whittaker, who has imparted invaluable advice throughout the design stages and the use of the microwave equipment. Special thanks goes to David Paden and Stuart Main (mechanical workshop, school of chemistry), who kindly and patiently built and maintained the microwave applicators.

I must also thank Dr. Richard M. Ibberson (of the ISIS Facility at the Rutherford Appleton Laboratory) for all his help with the neutron diffraction experiments and Dr. Gary Bond for his contribution to my work on microwaves and catalysts.

I would like to take this opportunity to thank all those who have been in charge of several equipments at the University of Edinburgh for giving their time to help me with various techniques applied in my research. They are Mr. Geoff Angell (now retired, School of GeoScience) for his help with the X-ray diffraction analysis of the zeolites synthesis, Dr. Nicola Meller (Centre for Science at Extreme Conditions) for her help with the use of capillaries during X-ray diffraction, and Dr. Nicola Cayzer (School of GeoScience) for her help with the SEM analysis.

I must not forget my colleagues from Lab. 79, PhD students, post-docs and project students for their thoughtful feedbacks during my stay at the Chemistry department: Kenji, Marina, Keith, Graeme, Vin, Fiona, Phil, Mark, Goran, Adrian; particularly, Rachel Lees, Simon Clarke and Diego Gonzalez, with whom I worked closely at several stages of my project. Specially, many thanks goes to Gaetan Giriat for all his help during the final editing stages of this work.

I would like to thank all my friends for the gift of their friendship. Especially, Marco Antonio who has always been the person on whom I could rely. Thanks flaco!

I also would like to say a big thanks to Amin who has given me support through all the time we have known each other. Thank you darling.

Finally, I would like to dedicate this work to my family, the most important part of my life. It is a special dedication to my Mom and Dad who have had to endure my absence during the difficult times of my Mom's illness. My thanks and dedication also go to my brothers, sister, and all the little ones who have always been the pillars of support around me to ensure that I reach farther. I love you all.

Declaration

I declare that this thesis was composed by myself, that the work contained herein is my own except where explicitly stated otherwise in the text, and that this work has not been submitted for any other degree or professional qualification except as specified.

(*Flora Marcela Piña-Sandoval*)

TO MY PARENTS

Table of Contents

List of Figures

List of Tables

Chapter 1

Microwave radiation

1.1 Introduction

'Microwave radiation' is the term normally used to characterise the part of the electromagnetic spectrum with frequencies between 300 MHz and 300 GHz (wavelengths of about 1 m and 1 mm respectively), which lies between infrared and radio frequency radiation (figure 1.1).

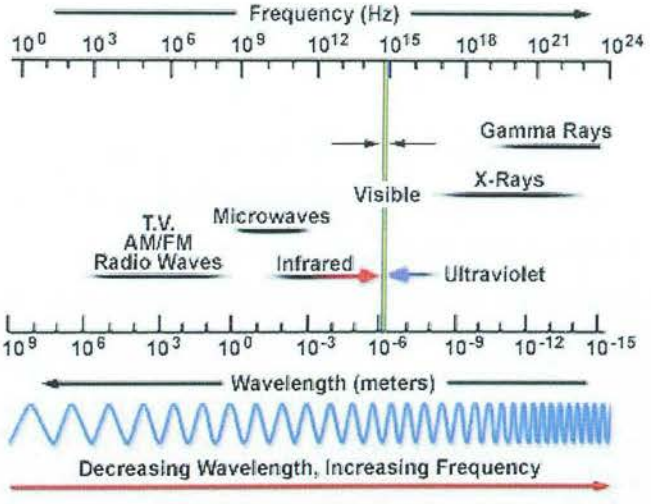

Figure 1.1: Electromagnetic spectrum showing the microwave region[1].

The first large-scale technological application of the microwave spectrum was for communications and information processing purposes. In order to permit an efficient use of the spectrum a list of frequency allocations and regulations on permitted radiations or conducted signals was produced. Only narrow frequency bands, centred at 900 MHz

and 2.45 GHz, are permitted for microwave heating purposes in order to avoid interference with telecommunication and RADAR (**ra**dio **d**etection **a**nd **r**anging) devices.

In general, the applications of microwave radiation fall into a few distinct categories[2]:

- The most common use of microwaves now is as a source of heat. Examples of this include domestic microwave ovens and industrial heating applications such as the production of radio-labelled drugs[3] among others. Frequency bands used for this purpose are 2.45 GHz and 900 MHz respectively.

- The second most important use is in RADAR equipment. Generation of a microwave beam, which is bounced off an object, and then detected, will give information about the object such as its position, something about its shape, and sometimes whether it is wet or dry. In that way, RADAR instruments can guide missiles, locate storms, and direct aircraft pilots along flight paths.

- Communication systems. In this case, the information is encoded into a microwave beam and sent from a transmitter to a receiver. Virtually all communication by satellites uses microwave beams in this way; as well as wireless communication systems, for example mobile telephones and wireless computer networks.

- Radiotelescopes. Radiotelescopes are microwave receivers used to study microwave emissions from stars, galaxies, and even the leftover microwave energy from the Big Bang. Sensitive receivers can be built to detect the naturally occurring microwave radiation that comes from any warm body, for example the human body.

Electromagnetic radiation propagates in space in the form of waves with two orthogonal components - an electric field (**E**, V m^{-1}) and a magnetic field (**B**, A m^{-1}) - which are also perpendicular to the axis of propagation (see figure 1.2). The mathematical description of the way these two fields interact was given by J. C. Maxwell in 1873[4]. However, the reproduction of this description is beyond the scope of this thesis.

Because the field components are transverse to the direction of travel (there is no field component in this direction) this kind of wave is called transverse electromagnetic

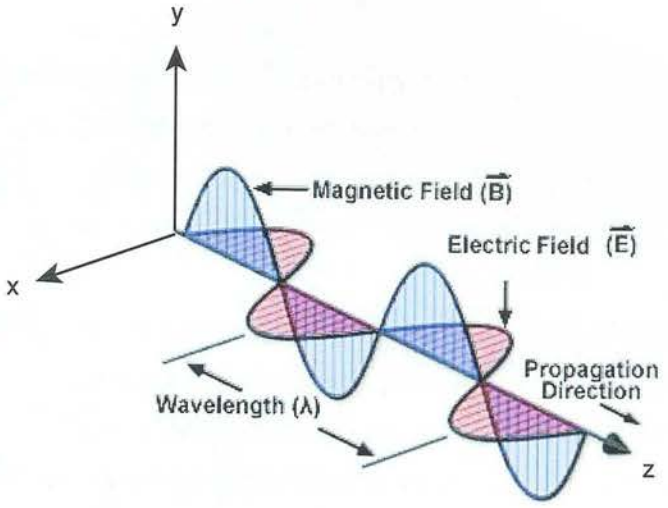

Figure 1.2: Illustration of plane-wave components[5].

(TEM). The field components E_y and B_x vary sinusoidally in time and in space and can be represented by[6]:

$$E_y = E_0 sin(\varpi t - \beta z) \tag{1.1}$$

$$B_x = \frac{E_0}{Z_0} sin(\varpi t - \beta z) \tag{1.2}$$

where:

E_0	is the amplitude factor (V)
ϖ	is the angular frequency (radians s^{-1})
$\beta = \frac{2\pi}{\lambda_0}$	is the propagation constant (radians m^{-1})
Z_0	is the characteristic impedance (Ω)
t	is time (s)
z	is the propagation direction (m).

For free space, Z_0 gives the ratio between the electric and magnetic fields. It is defined as:

$$Z_0 = \sqrt{\frac{\mu_0}{\varepsilon_0}} = 377\Omega \tag{1.3}$$

ε_0 being the permitivity, and μ_0 the permeability of free space. The permitivity relates to the mechanical forces existing between two electrostatic charges in vacuum. The permeability relates to current loops that are similarly spaced apart. The values for these two constants are: 8.854 x 10^{-12} F m^{-1} and 1.257 x 10^{-6} H m^{-1} respectively.

This thesis is primarily concerned with the study of the effect of microwave radiation on the structure, processing and reactivity of a number of solid-state materials. We will first introduce the nature of microwaves and microwave-materials interactions, before considering in greater detail the application of microwaves in materials synthesis and processes, and the challenges to be faced in studying the mechanism of such processes. Finally in this chapter, we will outline the aims of the thesis and its structure.

1.2 Dielectric properties of materials and microwave heating

The passage of microwave radiation through a medium may lead to electrical and magnetic polarisation, of which the former is generally the more important in delivering heat to that medium. The electrical polarisation arises from the displacement of charged particles in the medium from their equilibrium positions and may possess both permanent and induced components. The former is common in systems containing dipolar molecules while the latter may involve the polarisation of electrons of individual atoms, or in more extended states such as those in molecules or metallic bands, as well as the distribution of charge in an ionic medium. In all of these cases we quantify the response in terms of the *complex permittivity* (also known as the 'the complex relative permittivity'), ε^*.

This constant is a complex quantity, composed of two parameters; the real part or *real permittivity* (also known as the dielectric constant) (ε') and the imaginary part called the *dielectric loss* or *loss factor* (ε''). The dielectric constant is described mathematically as[7]:

$$\varepsilon^* = \varepsilon' + i\varepsilon'' \tag{1.4}$$

ε' describes the ability of the medium to be polarised by the electric field, while ε'' describes the efficiency with which the energy of the electromagnetic radiation can be converted into heat. Note that Z_0 in equation 1.3 is equal to $\sqrt{\frac{1}{\varepsilon^*}}$. These quantities commonly depend on the frequency of the microwave radiation in relation to the characteristic relaxation time, τ, of electrical polarisation in the medium. This may be illustrated by considering the time-dependent polarisation of a fluid containing dipolar molecules. If an electric field is applied, the medium may be polarised as the molecular dipoles align with the field, and when the field is switched off this polarisation will relax as the molecules collide and reorient themselves randomly at a rate $1/\tau$ [8]. The relaxation time for a spherical dipole using Stokes' theorem is given by:

$$\tau = 4\pi r^3 n_v / kT \tag{1.5}$$

where,
n_v is the viscosity of the medium,
r is the radius of the dipolar molecule,
k is Boltzmann's constant,
and T is the absolute temperature.

The relation between the dielectric properties of such a system (ε'', ε') and τ is given by the Debye equations.

$$\varepsilon' = \varepsilon_\infty + \frac{\varepsilon_s - \varepsilon_\infty}{(1+\varpi^2\tau^2)} \tag{1.6}$$

$$\varepsilon'' = \frac{(\varepsilon_s - \varepsilon_\infty)\varpi\tau}{(1+\varpi^2\tau^2)} \tag{1.7}$$

where, ε_∞ and ε_s are the high frequency and static dielectric constants and ϖ is the frequency, which together with τ characterise the rate of build up and decay of polarisation. When τ approaches the inverse-excitation frequency, the dipolar polarisation mechanism becomes significant.

In general terms, when the microwave frequency is very large compared to the rate of relaxation of electrical polarisation in the medium, both ε' and $\varepsilon''$are very small, while at relatively low microwave frequencies, the degree of polarisation may be large (i.e. ε' may be large), but the energy loss will be small (i.e. ε'' is small). Energy loss is

generally highest somewhere between these two extremes, as illustrated schematically in figure 1.3, which shows the frequency dependence of both ε' and ε''.

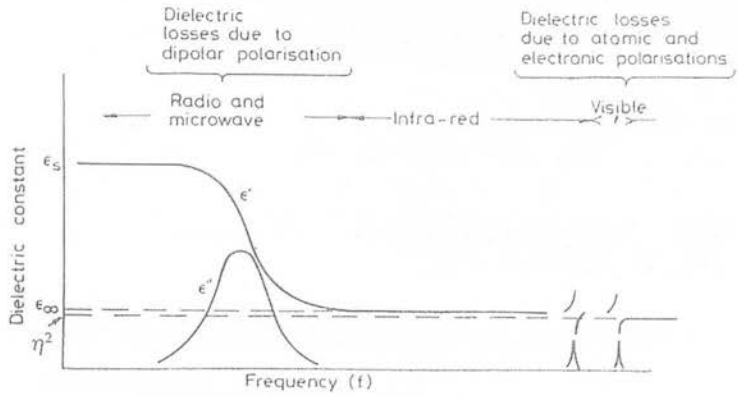

Figure 1.3: Schematic illustration of the real and imaginary components of the dielectric constant as a function of frequency for collection of dipolar molecules. In the figure is also shown the refractive index, $\eta^{2\,(9)}$.

The key parameter that is used to quantify the effectiveness of the microwave field in delivering heat to the medium is the tangent of the phase lag δ between the electric field component of the microwaves, and the polarisation of the medium. This is called the (dielectric) *loss tangent*; it may depend on the frequency of the microwave radiation and on temperature, and may be expressed as follows:

$$tan\delta = \frac{\varepsilon''}{\varepsilon'} \tag{1.8}$$

Although we have described the mechanism of microwave heating, and explored the dielectric response in terms most appropriate to molecular solids, where any charges are bound to molecules, there are other systems where the charged particles are free to move (for example electrons in metals, or ions in solution or in melts). In all these cases, ε' and ε'' are used to describe the dielectric response, and tan δ is used to quantify the efficiency of energy transfer. We now consider the nature of the dielectric response in a wider range of systems.

1.3 Dielectric polarisation

In the previous section we described the time-dependent electrical polarisation of molecular dipoles in a microwave field. In general, there are several contributions to the total polarisation (α_t) of a material in an electric field.

$$\alpha_t = \alpha_e + \alpha_a + \alpha_d + \alpha_i \tag{1.9}$$

where the different contributions to α_t are defined as follows.

- α_e the electronic polarisation, which arises from the realignment of electrons around specific nuclei.
- α_a the atomic polarisation, that results from the relative displacement of nuclei due to the unequal distribution of charge within the molecule.
- α_i the interfacial polarisation effect (Maxwell-Wagner) that occurs when there is a build-up of charges at interfaces.
- α_d the dipolar polarisation, that results from the orientation of permanent dipoles by the electric field.

The time scales for the electronic and atomic polarisation/depolarisation, α_e and α_a, are much faster than the microwave frequencies. As a result, neither of these contribute significantly to the dielectric heating effect. Additionally, in heterogeneous materials, the interfacial polarisation is insignificant at microwave frequencies. In contrast, the time scale for polarisation (α_d) associated with the permanent dipole moment in many molecular materials is comparable to microwave frequencies; therefore this is the most important mechanism contributing to microwave heating, illustrated schematically in figure 1.4. A good example of such a system - indeed the most common both in microwave chemistry and in domestic applications - is water. In the previous section it was stated that the transfer of energy from the microwave field to the water is most effective when the frequency of the radiation was comparable to $1/\tau$. At very low frequencies, τ is shorter than the cycle time of the electric field, and the dielectric polarisation keeps in phase with it. The field provides the energy necessary to make the molecules rotate into alignment with the electric polarisation. Some of the energy is transferred to the random motion of molecules in the fluid each time a dipole is knocked out of alignment and realigned. The transfer of energy in this case is very small so that the temperature hardly rises. If the electric field oscillates very rapidly, it

changes direction *faster* than the response time of the dipoles. Since the dipoles cannot then rotate, no energy is absorbed and the substance does not heat up.

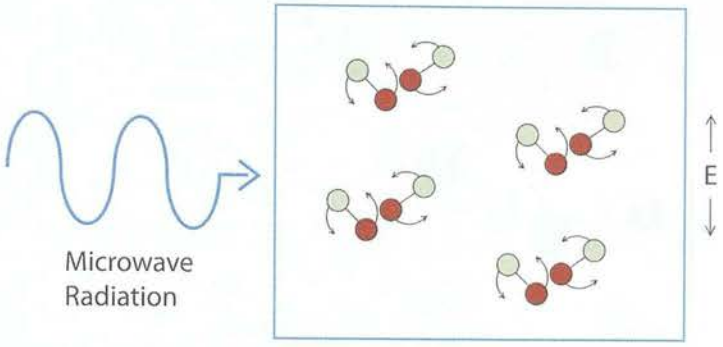

Figure 1.4: Polar molecules rotating under the influence of the electric field component of microwave radiation.

However, when the timescale of the electric field oscillation is comparable to the response time of the dipoles, they do rotate but there is also an inertia, arising in part from intermolecular forces that damps their response, and gives rise to the phase lag, δ. This leads to a displacement current that is 90° out of phase with the driving electric field, and the rate of heat transfer is proportional to this component of the current times the driving voltage supplied by the microwave field.

Microwave radiation may also polarise and heat materials that are not commonly regarded as molecular. Many ionic materials have a significant response to microwave radiation and that response is more commonly described in terms of periodic displacement of the constituent ions, that is in terms of the excitation of vibrations or phonons in the material. We describe such phenomena in more detail in section 1.7.

1.4 Conduction effects

One of the ways in which microwaves interact with the matter is through conduction mechanisms. For an electrical conductor, for instance, the charge carriers such as electrons or ions are moved through the material when placed in an electric field ($\mathbf{E}$), resulting in polarisation. The sample heats up due to the induced currents. The addition of dissolved salts in water, for example, markedly affects the dielectric properties as the ionic conduction increases and it becomes more significant than the dielectric dipolar

losses. The dielectric losses of solids with significant conductivity arise from these conduction terms[10] and may be strongly affected by temperature. A visualisation of this phenomenon can be seen in figure 1.5.

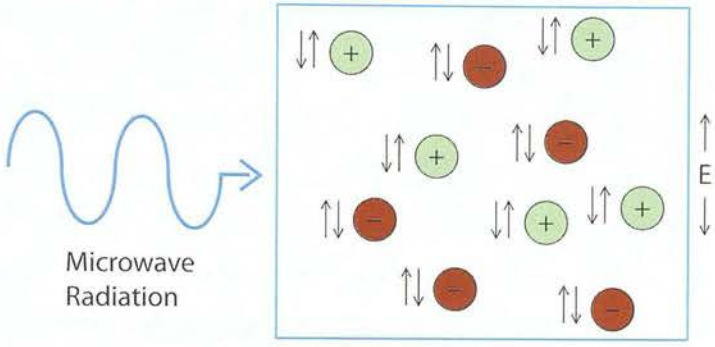

Figure 1.5: Charged particles moved under the influence of an electric field.

1.5 Interaction between microwaves and different states of matter

Microwave radiation was first used in research laboratories as a source of heat after scientists realised that microwaves not only heat water as in domestic applications but can also speed up chemical reactions[11], assist organic synthesis[12,13] and help the synthesis of solids[14,15,16,17,18].

As this *in situ* mode of energy conversion depends on the nature of the material being irradiated it is hoped that this allows some additional control of the properties of the material and may lead to reaction selectivity in some cases. In previous sections the different mechanisms of coupling between the radiation and the material were considered, and these, together with the influence of heat on the properties of the material play a central role in assessing the potential for microwave heating to be useful in synthesis and materials processing. It should be noted too that the interaction of microwave radiation with gases of dipolar molecules has quite a different nature, and we contrast such a response with that of many liquids and solids in the following sections.

1.5.1 Interaction with gases

Molecules with dipole moments are free to rotate in the gas phase and they may be excited by microwave radiation whose energy corresponds to that of transitions between quantised, rotational energy levels. This is the basis of microwave spectroscopy, and the dependence of the spectrum on the symmetry of the molecule and its moments of inertia make it a powerful tool in determining molecular structure[19]. The width of the resonance lines depends on non-ideal phenomena such as the Doppler effect and intermolecular collisions. The resonance frequencies of these spectra consist of various components that are products of the isotope shift and the hyperfine splitting in the gas. Isotope shifts tell us about atomic level properties and are due to the influence that atomic nuclei of different masses and charge distributions have on the electronic energy levels. The hyperfine splitting, on the other hand, is the splitting of energy levels as a result of the interaction between the magnetic moment of valence electrons and the magnetic field associated with the nuclear spin angular momentum.

Although there is clearly a transfer of energy from the radiation to the collection of molecules, and some of this energy will be converted into random motion (heat), the power levels involved are very low and this is not conventionally regarded as a method of heating the system. It should be noted, however, that microwaves may be used in quite a different fashion to transfer considerable quantities of heat to a gas: for relatively high fields it is possible to produce charged species in the gas - most commonly after the gas has been 'seeded' with charged species using a spark - and such particles may be strongly accelerated by the field, leading to high-energy collisions and inducing break-down of gas molecules to produce further gas species. The cascade of ionised species that follows creates a very hot gas known as a *plasma*. Microwave-induced plasmas (MIPs) may be used as a hot reaction medium in which synthesis may be performed, and MIP methods are being more widely used in materials synthesis and processing[20,21].

1.5.2 Interaction with liquids

Much of the early work on microwave-assisted chemical synthesis yielded significantly enhanced reaction rates, and sometimes increased yields, compared to when conventional heating was used. In many, if not most cases, this is now believed to arise from an increased tendency for *superheating* to occur with microwave radiation. Boiling

occurs when the free energy of formation of vapour becomes less than the free energy of condensation, which is related to the surface tension. Under conventional heating, heat is usually transferred into the reaction vessel from the outside, and the walls of the vessel are generally hotter than the interior; furthermore, there are generally imperfections, or adsorbed particulate matter at the walls, and these aid nucleation of vapour bubbles as they lower kinetic barriers. Boiling therefore usually occurs first at the walls of the container. However, during microwave heating, the walls are not heated directly and the energy is dissipated inside the bulk liquid. The temperature at the inner surface of the wall, due to outward heat transfer, is generally lower than that of the bulk liquid. There are generally fewer species at the interior of the vessel to aid bubble nucleation, so the temperature of the interior may rise significantly beyond that of the thermodynamic boiling point before bubbles form. The result is that the boiling point of solvents may be raised by 10% or more above their normal values, though this may be reduced by the introduction of nucleating species to the solvent. It should be noted too that the efficiency with which a liquid may be heated with microwaves depends on the dielectric constant (which may be further modified by the introduction of charged species), and on the temperature, which may have an influence on the viscosity, and hence the characteristic relaxation time for molecular re-orientation. Liquids of non-polar molecules will not be heated with microwaves, though the introduction of species such as metal particles may bring about coupling[10].

1.5.3 Interaction with solids

Materials may be classified for the purposes of applications according to their interaction with microwaves as follows[12].

- Microwave reflectors: bulk metals and alloys that are used to produce microwave guides.
- Microwave transmitters: materials transparent to microwave radiation that are mainly used to make containers for microwave applications. Among such materials are fused quartz, zircon, ceramic (without transition metals), many types of glasses, and polymeric materials such polytetrafluoroethylene (PTFE).
- Microwave absorbers: materials that absorb energy from microwave radiation and convert it to heat.

These bulk characteristics depend on the electronic properties of the material as follows[19].

Insulators. Most solid materials are classified as insulators because they offer a large resistance to the flow of electric current. They therefore do not couple to microwave radiation via the conduction mechanism, but if they have a high dielectric constant, they may be classified as microwave absorbers. If the dielectric constant is low, they may be used as microwave transmitters. Further consideration of the mechanisms of microwave heating in such systems is given in section 1.7.

Metals. Metals have a high specific electric conductivity (typically $\sigma \approx 10^7$ Sm^{-1}) and a high collision frequency ($\nu_{col} \approx 10^4$ Hz) of the charge carriers. Due to the fact that the frequency of an electromagnetic field in the microwave part of the spectrum is smaller than the collision frequency of metals, the energy that electrons take from the field is dissipated rapidly by interaction with the lattice.

In bulk and powdered metals, heating will depend heavily on conduction losses. Metal powder, which interacts strongly with microwaves, contrary to larger metal objects, do not produce sparks when they are irradiated due to their small dimensions and large surface areas. Such effects have been exploited in synthesis, for example to make metal chalcogenides[15,17] such as CrS, CrSe, Cr_2Te_3, as well as chlorides, oxochlorides, bromides and nitrides[16].

Semiconductors and ionic conductors. When temperature increases, the dielectric loss factor of semiconductors and ionic conductors increases as the number and/or mobility of conducting species increases; heating becomes more effective and the differential in temperature with respect to time (*dT/dt*) increases rapidly. The rapid increase in temperature under these circumstances is described as *thermal runaway*. This property has also been used in synthesis, for example to prepare a wide range of mixed metal oxides[18] such as $CuFe_2O_4$, $BaWO_4$, and KVO_3 by way of melt and quench approach, where the sample cools rapidly after the power is turned off.

1.6 Microwave radiation *versus* conventional heating

Heating is one of the most common processes in industry, yet there are still challenges in delivering heat in a controlled fashion, and also in minimising cost and environmental impact.

In practise, heat transfer may be achieved through any combination of three mechanisms: conduction (by means of atomic or molecular agitation within a material without any motion of the material as a whole); convection (by mass motion of a fluid such as air or water when the heated fluid is caused to move away from the source of heat, carrying energy with it); radiation (by the emission of electromagnetic waves which carry energy away from the emitting object). However, the heating process will also be affected by the physical properties of the object such as its specific heat, thermal conductivity and density. In other words, the thermal diffusivity of the material, which comprises the latter three properties, will determine the temperature rise inside the object as a function of time and depth from the surface, subject to the conditions in the exterior. The larger the object is, the longer the heating will take.

Microwave radiation is sometimes found to heat an object faster than conventional methods, and the distribution of heat in the object throughout the process may be quite different. First consider the heating rate. In conventional heating, this is limited by thermal conductivity and, for fluids, convection currents. In contrast, provided the microwaves can penetrate the medium and couple with it, the transfer of energy can be very rapid. It is also not necessary to heat the reaction vessel directly with microwaves, whereas most conventional methods convey externally-applied heat through the vessel walls.

For materials with a modest dielectric susceptibility, the radiation penetrates and heats fairly evenly throughout the medium, but cooling is fastest at the outside, so the interior may get hotter and heat transfers occurs from the centre of the material towards the outside[11].

If the material contains a second phase with a high dielectric susceptibility - for example for many heterogeneous catalysts comprising metal particles on a ceramic support - then the second phase may be heated directly and rapidly. The comparison

between the different ways of heating is illustrated in figure 1.6.

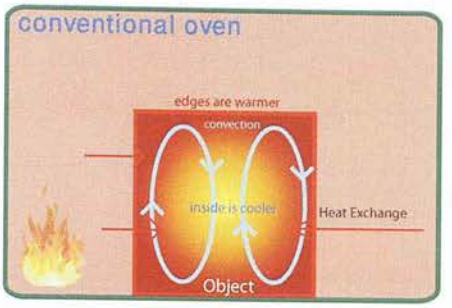

(a)

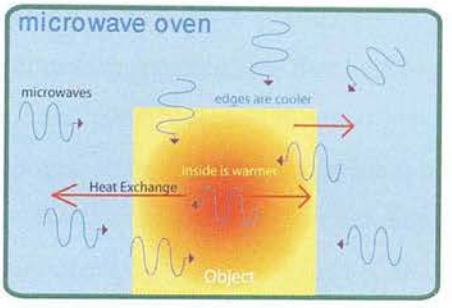

(b)

Figure 1.6: Illustration of differences between (a) conventional and (b) microwave heating.

Some advantages that microwave dielectric heating may offer over conventional methods are as follows[10,8].

- Indirect contact between the energy source and the reacting materials due to remote introduction of the microwave radiation to the chemical reactor.
- Selective heating of different materials can be induced because they may interact differently with microwave radiation. This means that it may be possible to arrange for only reactants to be directly heated.
- The coupling of microwave energy is very efficient for lossy materials leading to rapid temperature increases, and this may be important where kinetic control is desirable, or where there is a limited time to complete a reaction (for example in the synthesis of molecules for radiotherapy where the active isotope has a short half-life).

- Controlled superheating might lead to particularly fast reactions in liquid phases.
- The sample can be cooled rapidly by switching off the power, making possible flash heating experiments.
- The differences in temperature profiles in microwave heating may lead to differences in product distribution in chemical reactions.

1.7 Microwave-specific effects in chemical synthesis

The observation that microwave radiation may drastically reduce times for synthesis or processing through enhancements in rate, as well changes to products, has generated interest in discovering more about the mechanisms that lead to such effects. Where the reaction is performed in solution, and where accurate and precise measurement of the temperature is made, any changes compared to conventional heating may often be attributed to *superheating*. However, a variety of 'microwave specific effects' have also been postulated. In a sense superheating is a microwave specific effect because it may arise through the particular way in which heat is delivered to the system, so a distinction should be made between those effects that arise as a consequence of the way in which microwave radiation changes the temperature profile of the system, and those effects that are not a direct consequence of heat - sometimes called 'non-thermal' effects.

The study of any such effects depends crucially on good experimental technique - particularly in thermometry, and in developing methods to follow changes in structure and composition during irradiation. For example, the thermocouples that are often employed to measure temperature under conventional conditions may couple directly with a microwave field, distorting both the field and the temperature they are intended to measure. Alternative types of thermometer all have limitations, and we explore these in greater detail in section 1.9.

In general terms, theories about anomalies in heating with microwaves involve the following effects[22]:

1. lowered activation energies - particularly through the coupling of polar intermediates or transition states with the microwave field;

2. enhanced diffusion due to increased vibrational frequency of the ions caused by the electric field of the microwave radiation;

3. the excitation of a non-equilibrium phonon distribution in crystal lattices[23];

4. quasi-static polarisation of the lattice near point defects;

5. the ponderomotive action of the high frequency electric field on charged vacancies in the ionic crystal lattice[24].

We now explore some of these effects in greater detail, focusing on those that are particularly relevant for solids[25,26].

It has been suggested[26] that the activation energy for ionic motion of crystalline solids may be reduced during microwave heating as a consequence of the excitation of non-thermal phonon distributions by the microwave field. The suggestion is that radiation energy couples into low frequency elastic lattice oscillations, and generates a non-thermal phonon distribution that may enhance the ionic mobility and increases diffusion. Enhanced ionic motion has also been proposed in NaCl and AgCl[27]; it was shown that oscillatory defect fluxes, driven by the microwave field, are rectified near crystal surfaces and boundaries. Charge defects can then be driven away from or pulled towards a surface, producing a near-surface depletion or accumulation. The diffusive flow of the defects within the material might result in creep deformation and/or formation of a quasi-stationary distribution of electric potential. Enhanced mass transport in a microwave field was demonstrated in a particularly elegant experiment designed to disentangle thermal and non-thermal effects[28]. Here, a pressed disc-shaped pellet of $YbBa_2Cu_3O_{7-x}$ was placed inside a larger pressed pellet of $YBa_2Cu_3O_{7-x}$ then heated in a microwave cavity with a known polarisation relative to the interface between the two materials. After extended periods of irradiation, the interface between the two materials was studied with a scanning electron microscope which enabled the distribution of Y and Yb to be mapped, and it was revealed that the ionic diffusion was significantly enhanced along the direction of polarisation of the electric component of the field compared to the perpendicular direction.

It is often difficult to draw a line between 'thermal' and 'non-thermal' effects. Even if an accurate and precise means of thermometry was available, it would generally

provide a measure of temperature averaged over a region of the material. There is increasing evidence that the microwave heating of solids leads to 'hot-spots', some of which may extend over very short length scales. These in turn may lead to local rate enhancement when the material in question is part of a reactive system. In an experiment using powdered alumina, Stuerga[29] showed that differences in reaction yield between classic and microwave heating can be explained in terms of localised superheating. This localised rate enhancement is observed in organic synthesis and inorganic solids, and is due to the fact that these materials do not posses efficient mechanisms of redistributing heat. These local effects may arise in heterogeneous materials - for instance supported metal catalysts, as will be explored in Chapter 6 - or homogeneous granular materials in which strong field gradients may be established, and in which electrical discharges may occur across such gradients, leading to high local heating and even plasma discharge.

The point at which one distinguishes between such local effects, which could be regarded as a form of superheating - and hence a 'thermal' effect - and coupling with atomic defects, which also lead to a transfer of energy to a specific region of the solid, is not clear. There is also still work to be done on understanding better the mechanism of coupling of microwave radiation with solids in general[30,25]. The general features of the coupling are moderately well understood. First, the modes that are excited directly must have some dipolar change associated with them, that is they must be optical modes. However, the typical frequency scale for such modes is in the THz region, whereas microwaves are generally three orders of magnitude lower in frequency, and one would expect the coupling efficiency to be very low. For this to occur, that is, for the microwave energy to match a *difference* in phonon energy, the microwave absorption has to be seen as a multiphonon process. In principle the efficiency of such processes could be modelled and used to predict or rationalise the strength of coupling. However, there is a related property of the material that is also crucial in rationalising microwave effects in solids (which is less commonly studied). This property is the rate at which the energy deposited into particular phonons is redistributed. Intuitively one would expect the rate of such equilibration processes to take place at a similar rate to the vibrations in the solid, i.e. of the order of THz, so if a pulse of microwave energy were to be delivered to a material, one would expect an equilibrium distribution of phonons beyond timescales of the order of 1 ps. However, if a solid is subjected to continuous microwave irradiation, the continuous redistribution of such energy - which

relies on anharmonicity and the efficiency of coupling between phonon modes - could be in some cases insufficiently efficient to prevent a significant perturbation away from equilibrium.

1.8 Microwave transmission and applicators

In order to develop a better understanding of the various mechanisms of microwave heating, it is necessary to know the nature of the microwave field and temperature experienced by the sample. Commercial equipment does not cater for these needs very well, particularly at elevated temperatures. We therefore designed, built and applied custom apparatus for our work and in order to establish the principles on which the design was based, we describe here some of the fundamentals of microwave generation and transmission of microwave radiation in heating systems. We will also explain the importance of reliable temperature measurements in microwave heating systems. A more specialised description of some of the subject matter is beyond the scope of this thesis. However, there is an extensive literature on microwave transmission theory[6].

In general terms, for many, a 'microwave' system connotes a microwave oven such as the one used in kitchens for heating food. However, since the early 1980's[31], microwave heating systems can also be used in industrial and medical applications for several different processes[32,33,34,35,36] and the demands of such applications are often beyond what a domestic microwave oven can deliver.

Microwave heating systems have been designed and developed over the years based on their application and in a variety of arrangements. Commonly, microwave heating systems can be described as consisting of three major parts: a generator, a transmission line and/or an applicator, and a system for the control of temperature, pressure, and power, among others. This is illustrated in figure 1.7, where the scheme of a relatively simple microwave system such as a domestic microwave oven is shown.

In this system, a magnetron (a high-power source) generates microwave energy that is fed through a waveguide (the transmission line) to the oven cavity (the applicator, which is a rectangular multi-modal cavity made of metallic reflective walls). The power with which microwave is applied to the sample is controlled by the electronic

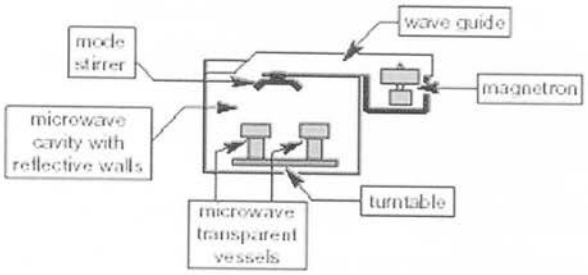

Figure 1.7: Schematic drawing of a domestic microwave oven - as applied to simple laboratory experiments[37].

control systems (not shown in the figure). In this particular example, a 'mode stirrer' (a metallic fan blade) and a rotating plate are used to ensure a more uniform heating of the sample as will be explained in the following sections.

1.8.1 Microwave generators

Microwaves can be generated in a variety of ways. Methods in use are classified according to the type of energy carrier involved such as electrons in a vacuum (vacuum tubes) or charge carriers in semiconductors (solid state devices). Solid-state devices use materials such as silicon or gallium arsenide. They also include several types of transistors and diodes. Vacuum tubes however, use devices that operate basically as 'electron guns' under controlled electric or magnetic fields. These include the klystron, the gyrotron, the travelling wave tube (TWT) and the magnetron[38].

1.8.1.1 Klystron

A klystron is a velocity modulated tube in which the velocity of the electrons is modulated using a transit-time effect. In a two-cavity klystron, when energised, a cathode emits electrons that are focused into a beam after passing by a 'control' grid set at a low positive voltage. The beam is then accelerated by a high positive DC potential that is applied with equal amplitude to two more grids - the 'accelerator' and the 'buncher' grids. The buncher grids are connected to a resonator cavity with a superimposed AC potential caused by the oscillations within the cavity. These oscillations in turn produce an oscillating electrostatic field between the buncher grids causing the direction of the field to change according to the frequency of the cavity. Here, the electrons of the beam, after passing through the grids, are accelerated and decelerated alternately.

The area after the buncher grids is called the *drift space*. In the drift space, the electrons will form bunches when the fast (accelerated) electrons overtake the slow ones (decelerated).

The 'catcher' grids in the second cavity have the function of absorbing energy from the electron beam. Thus, they are placed along the beam where the bunches are completely formed. To ensure maximum energy transfer to the catcher cavity, the location of these grids is determined according to the transit time of the bunches at the natural resonant frequency of the cavity. This is when the electrostatic field is of the correct polarity to slow down the electron bunches.

The two-cavity klystron is used as an amplifier with narrow bandwidth. When more amplification or output power is required, this can be achieved by placing more cavities in series in the same klystron. The power produced in the intermediate cavities is not removed. In fact, the induced current is used to generate extra velocity modulation as a cascade of amplifiers.

1.8.1.2 Travelling wave tubes

A travelling wave tube (TWT) is an electronic device used to produce high-power radio frequency signals. The operating frequencies range from 300 MHz to 50 GHz. This device is an elongated vacuum tube with a heated cathode (the electron gun) at one end. A solenoid coil wrapped around the tube creates a magnetic field that focuses the electrons into a beam. The beam is then sent through the middle of a wire helix to strike a collector placed at the end. The wire helix is used to stretch the length of the tube and also acts as a delay line, where a radio frequency signal travels at the same speed as the electron beam along the tube. In lower-power devices, the solenoid coil can be replaced by permanent magnets.

One of the two-directional couplers is fed with a low-powered radio signal. A two-directional coupler is either a waveguide or an electromagnetic coil. A low-powered radio signal is introduced near the emitter to induce a current in the helix. This induced current causes the electromagnetic field to interact with the electron beam, giving rise to bunching of the electrons (velocity modulation). Because of the beam current, the electromagnetic field induces more current back into the helix. This feedback effect leads to current build up which is amplified as it passes through.

A second directional coupler, positioned near the collector, receives an amplified version of the input signal from the far end of the helix. An attenuator prevents any reflected wave from travelling back to the cathode.

1.8.1.3 Gyrotron

A gyrotron is another travelling wave tube also known as a free electron MASER (Microwave Amplification by Stimulated Emission of Radiation). Here, an electron beam is sent at an angle into a cylindrical waveguide where a strong magnetic field forces an electron beam to travel into a cyclotron motion. Typical output powers for this type of tube range from 10's of KW to 1-2 MW with output frequencies from around 20 to 250 GHz. Unlike conventional vacuum tubes, at lower wavelengths (within millimetres), the power can be very high because its dimensions can be much larger than the wavelength. Also, the output is not dependent on material properties, as is the case with conventional MASERs.

1.8.1.4 The magnetron

The magnetron is also called the 'crossed-field' device. This is due to the fact that both magnetic and electric fields are employed in its operation. They are also produced perpendicular to each other so that they cross. In principle, a magnetron is a coaxial diode that is placed in a strong axial magnetic field to force the electrons into curved orbits.

In a cavity magnetron, the anode is divided into a number of segments connected by resonators allowing different modes of vibration. In order to create a mode in which the barriers between the cavities have alternating polarities, big and small cavity sizes are also alternated.

Electrons from a hot filament placed at the centre (the cathode) are bunched together in groups by an AC electric field that is created adopting a pattern in the form of wheel with 'spokes'. These spokes pass the opening of the cavities where a decelerating magnetic force deflects them so they tend to sweep around in circle (see figure 1.8). When this happens they 'pump' the natural resonant frequency of the cavities. The currents around the resonant cavities cause them to radiate electromagnetic energy at that resonant frequency. The applied magnetic field is constant and the central cathode

is heated to supply energetic electrons which would, in the absence of the magnetic field, tend to move radially outward to the ring anode which surrounds it.

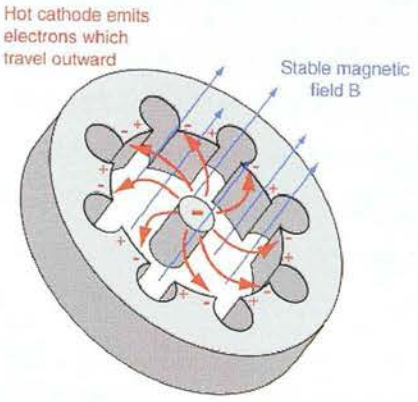

Figure 1.8: Schematic illustration of a magnetron[39].

Due to the extended interaction of the high-frequency electromagnetic field with the electron beam the conversion efficiency is much higher with magnetrons (60%) than with reflex klystrons (6%)[19]. Hence, magnetrons are preferably used in microwave heating devices, in particular in domestic ovens. In a microwave oven, for instance, a 1100 watt input will generally create about 700 watts of microwave energy, an efficiency of around 65%. This is far more efficient than the klystron, which typically operates around 30%. Modern solid state microwave sources typically operate around 25 to 30%, and are used primarily because they can generate a wide range of frequencies. Thus the magnetron remains in widespread use in roles where precise frequency control is not important.

1.8.2 Transmission lines

Thought microwave radiation is part of the electromagnetic spectrum, it can not be manipulated in the same manner as other types of radiation. Instead, microwave radiation is treated more as a wave, as opposite of a beam of photons, and therefore the components for transmitting microwaves are much like those used for electricity transmission. Open wires, coaxial cables and parallel plates have been used to transmit microwaves in the elementary TEM mode, as in free-space transmission. Waveguides have also been used which have the advantage that can be operated in different electromagnetic modes depending on their dimensions.

Although microwave radiation may be transmitted using open wires, for example along a pair of conductors, this is not very practical at microwave frequencies. On these transmission lines, the physical separation between the conductors, which is an important of the wavelength, becomes significant a distant point. This has as a consequence a deficient power transmission and radiation losses into space. Waveguides on the other hand, have the advantage of behaving as a transmission line at lower frequency in many important aspects while energy and power are transmitted more efficiently.
In the fellowing sections we describe some of these transmission lines and their characteristics.

1.8.2.1 Parallel-wire line, parallel plates and coaxial line

The essential feature of these transmission lines is that in the fundamental mode the energy propagates with the associated electric and magnetic fields transverse to the axis of the line, thus there is no axial component of both fields. As seen before, when the electric field and the magnetic field are transverse to the direction of propagation the wave is said to be propagating in a transverse electromagnetic mode (TEM). A TEM mode it is very desirable because it has no dispersion and no low frequency cutoff. The propagation velocity of the TEM wave is the same as for a plane wave in the dielectric medium. For example, consider the voltage generated between two straight parallel conductors carrying a direct or low frequency alternating current to a terminating resistor. Both the resulting electric- and magnetic-field patterns comprise only components lying in the transverse plane to the axis, as predicted in electrical theory, hence there will be not upper limit to the frequency for the TEM mode. As there is not an axial component of either the **E** or the **H** fields then the system is very similar to a plane wave: this is, the propagation velocity of the TEM wave is the same as for a plane wave in the dielectric medium[(2)].

The characteristic impedance (Z_0) of a TEM transmission line is $\sqrt{(L/C)}\ \Omega$, where L is the inductance and C is the capacitance per unit length of the line. The values for the three TEM configuration for a parallel plate, a coaxial line and parallel conductors are shown in table 1.1[(7)].
From these transmission lines, parallel-plate line is of importance as the basis of heating ovens with with conveyor bands, while the coaxial line is often used as the output section of magnetrons because is a conveniently flexible line for low power (<1 kW).

Table 1.1: Characteristics of TEM transmission lines for air dielectrics.

Line type	L / H m^{-1}	C / F m^{-1}	Z_0 / Ω
Parallel plate; spacing a, width b	$\frac{\mu_0 a}{b}$	$\frac{\varepsilon_0 b}{a}$	$\frac{a}{b}\sqrt{\frac{\mu_0'}{\varepsilon_0}}$
Coaxial line; inner diameter a, outer bore b	$\frac{\mu_0 log_e\left(\frac{b}{a}\right)}{2\pi}$	$\frac{2\pi\varepsilon_0}{log_e\left(\frac{b}{a}\right)}$	$\frac{1}{2\pi}\left\{\sqrt{\frac{\mu_0}{\varepsilon_0}}\right\} log_e\left(\frac{b}{a}\right)$
Parallel conductors; conductor radius r, spacing d	$\frac{\mu_0}{\pi} log_e\left(\frac{d}{r}\right)$	$\frac{\pi\varepsilon_0}{log_e\left(\frac{d}{r}\right)}$	$\frac{1}{\pi}\left(log_e\left(\frac{d}{r}\right)\right)\sqrt{\frac{\mu_0}{\varepsilon_0}}$

However, coaxial lines suffer from high attenuation which can lead to over-heating.

One disadvantage of parallel conductor lines are that they can not be used at microwave frequency because they are very long compared with the wavelength, and radiate heavily. However, they are widely used in radiofrequency applications at 27 MHz.

1.8.2.2 Waveguides

In almost every industrial and commercial microwave oven, waveguides have an essential role in transmitting power from the generator to the load. The heating chamber itself is often base too in waveguide technology. It is therefore important to understand the some of the characteristics of waveguide transmission. For a more detailed description please refer to the specialised literature[2,7].

1.8.2.2.1. Rectangular waveguide

From Maxwell's equations derived for rectangular co-ordinates (see figure 1.9) x, y, z to the **E** and **H** fields we have:

$$\frac{\partial^2 H_z}{\partial x^2} + \frac{\partial^2 H_z}{\partial y^2} + k^2 H_z = 0 \tag{1.10}$$

$$\frac{\partial^2 E_z}{\partial x^2} + \frac{\partial^2 E_z}{\partial y^2} + k^2 E_z = 0 \tag{1.11}$$

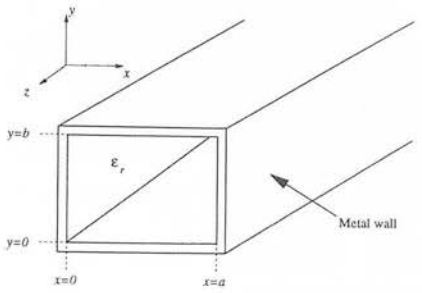

Figure 1.9: Rectangular waveguide coordinate system[2].

where:

$$k^2 = \varpi^2 \mu_0 \varepsilon_0 + \gamma^2 \tag{1.12}$$

and:

$$\gamma = \alpha + j\beta \tag{1.13}$$

where,

k is the wave number,

γ is the complex propagation constant,

α is the attenuation constant (nepers m^{-1}), and

β is the phase constant (radians m^{-1}).

The propagating waves based on equation 1.10 are designated **H** modes or **TE** (transverse -electric) modes as they have an axial component of the magnetic field but not an axial electric field ($E_z = 0$). Similarly, propagating waves based on equation 1.11 are designated **E** modes or **TM** modes (transverse-magnetic) where the axial magnetic field $H_z = 0$.

Also possible is the solution where both E_z and H_z are zero ($k = 0$) which are designated TEM modes. Figure 1.10 shows an schematic representation of some of these modes for a rectangular waveguide.

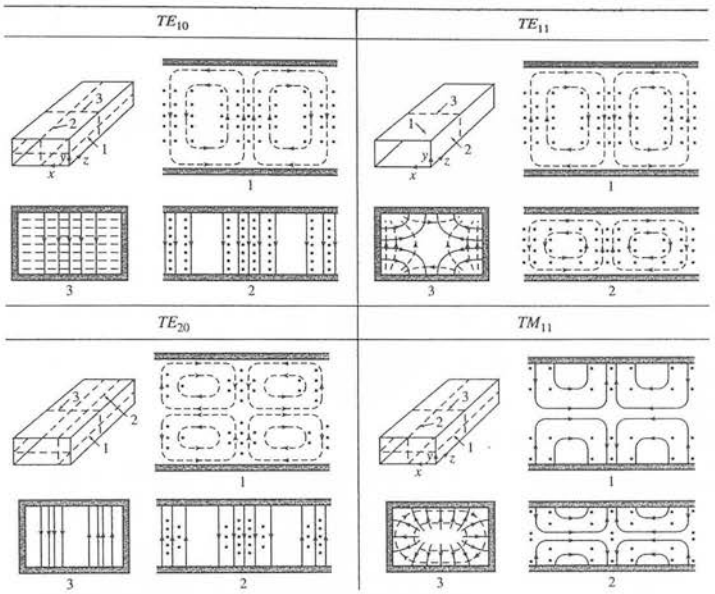

Figure 1.10: Field patterns of some fundamental modes in a rectangular waveguide[2].

1.8.2.2.2. Circular waveguide

We consider two cases of circular waveguides: a circular dielectric waveguide (or optical fibre) and a metallic circular pipe (see figure 1.11). The solution to Maxwell's equations for the propagation wave in this geometry is complicated by the fact that circular cylindrical co-ordinates are needed (r, θ, z).

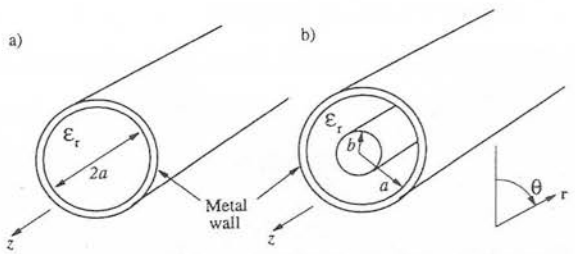

Figure 1.11: Schematic drawing of circular waveguides and coaxial cable.

The derivation of the field equations follows the pattern as for the rectangular waveguide, resulting in a pair of wave equations like equations 1.10 - 1.13 expressed in cylindrical coordinates whose solution can be expressed in Bessel functions and deriv-

atives.

A circular waveguide also supports both the **TE** and **TM** waves as is shown in figure 1.12.

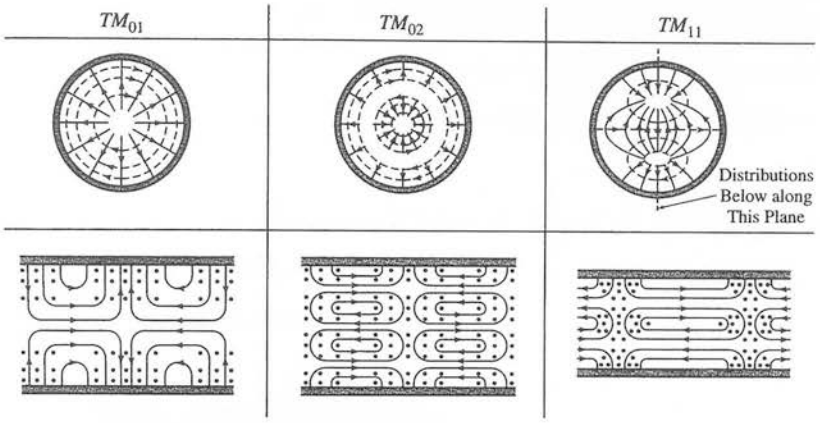

Figure 1.12: Field patterns for some fundamental modes in a circular waveguide[2].

As there is a family of modes for each type of wave, each with their own cut-off wavelength, a double subscript notation is used to designate the various modes. The first subscript being a measure of the circumferential variation in the field pattern. The second subscript being a measure of the radial variation of the field pattern.

1.8.3 Microwave applicators

Microwave applicators are devices designed to heat a sample by exposing it to a microwave field in a controlled environment. In order to achieve this, a controlled interaction between the sample and the microwave radiation has to occur under safe, reliable, repeatable and economical operating conditions.

The two general classes of microwave applicators are multimode and single cavities. Each of them will be described in the following sections.

1.8.3.1 Multimode applicators

The most commonly used form of multimode applicators is as multimode ovens. Multimode ovens are often used for processing bulk materials or arrays of discrete materi-

als with large dimensions. The simplest configuration for this type of applicator takes the form of a closed metal box that is excited at a frequency well above its fundamental cut-off frequency. In principle, a multimode oven supports a large number of resonant, high-order modes simultaneously (similar to waveguide type modes). In order to establish a reasonably uniform electric field throughout the cavity, as many as possible modes have to be excited. When this happens, more uniform heating is obtained even when the field perturbing effects of the sample being heated are also present.

Uniform heating can be achieved by means of metallic mode stirrers to ensure that all the possible modes are excited and by a rotating turntable for the sample which will enhance the uniformity of irradiation of the sample.

1.8.3.2 Single mode resonant applicators

A resonant cavity essentially consists of a metallic enclosure into which a microwave signal of correct EM field polarisation will suffer multiple reflections between preferred directions. The superposition of the incident and reflected waves will give rise to a standing wave pattern, well defined for simple structures. Knowledge of the configuration of the electromagnetic field will allow the correct placement of the sample at the position of maximum electric field for optimum transfer of the electromagnetic energy.

Single mode applicators are in general more compact and have much higher power densities (10^7kW m^{-3}) compared to multimode cavities, and because of this, operation must be within narrow frequency bands in order to maintain high coupling efficiencies. The large energy storage in such cavities can be transformed into heat via displacement and conduction currents through the dielectric material as soon as it is placed in the heating zone.

1.9 Temperature measurement during microwave heating

One of the most common problems encountered during microwave heating experiments comes from the fact that inhomogeneous heating may occur inside microwave ovens or cavities or even more significantly inside the sample itself as is illustrated

by table 1.2. This displays the temperature at which boiling is observed for various solvents during microwave irradiation, compared to the conventional boiling point.

Table 1.2: Comparison between the temperatures at which boiling is observed during the microwave heating of various solvents measured with a p-xylene thermometer, a fluoroptic sensor, and an IR pyrometer[34].

		Measured boiling temperature / K		
Solvent	b.p./ K	p-xylene thermometer	Fluoroptic sensor	IR pyrometer
H_2O	373	377	377	378
MeOH	338	351	357	357
2-PrOH	355	360	373	381
THF	339	352	354	376
CH_3CN	354	370	380	393

The difference between some of the boiling temperatures recorded in this table for different solvents - 4 to 30 K - is very significant and arises from the superheating effect described in section 1.5.2. In this case, it was noted that the fluoroptic sensor is not ideal because the temperature is just taken in one point, and the IR pyrometer gives the average measurement of a surface layer of liquid.

This example shows that an accurate temperature measurement during microwave irradiation is notoriously difficult. One reason for this difficulty is due to direct microwave heating of ordinary thermocouples and thermometers, which may often absorb much more of the energy than the system whose temperature they should measure.

In alcohol thermometers, for example, microwaves heat the alcohol directly and, when it is used within a liquid medium that is a poor microwave absorber, the thermometer will tend to give readings above the actual temperature. On the other hand, mercury thermometers may be subject to electrical discharges that not only reduce reliability, but can also be dangerous in the presence of flammable liquids. So, devices used to measure the temperature in microwave heating apparatus are expansion thermometers containing a non-polar liquid, fluoroptic sensors or IR pyrometers. Some of these devices and their applications are described in greater detail in following sections.

1.9.1 Xylene thermometer

Xylene could be a replacement fluid in the alcohol/mercury thermometer because is an 'inert' liquid, electrically non-conducting and it has a very low dielectric loss tangent. Despite these characteristics, the use of this thermometer is limited since it cannot be readily used as the basis of a control system for the magnetron. It was found out that measurements taken by this device were typically accurate to within 0.5 K[10].

1.9.2 Gas pressure thermometer

A gas pressure thermometer[40] consists of a capillary tube with a large bulb on one end and a pressure transducer (0-1 atm) at the opposite end. The gas used in this device is typically nitrogen, which is introduced in the capillary; this gas can be evacuated via a T-joint adjacent to the transducer. The transducer registers the analogue voltage output (translated as pressure values with a suitable calibration) when the pressure of the gas in the bulb increases due to increments in the temperature. With suitable amplification, this may provide the basis for control of the microwave power.

1.9.3 Infrared (IR) pyrometer

IR pyrometers[41] can measure the temperature of an object without the need for contact. This can be useful when the object to be measured is small, or it moves or is inaccessible, or where a fast response is required (such as in dynamic processes), or for processes at very high temperatures - 1200 K and above. A disadvantage of this technique is that it only probes the temperature of the surface, and this may be significantly different from that of the interior.

The technology involved in an IR radiation pyrometer is based on the principle that all objects that are hotter than their surroundings are net emitters of radiation at wavelengths in the IR region of the electromagnetic radiation spectrum(wavelengths of 0.4 to 0.75 μm). This radiation is intercepted and measured by the thermometer and returned as an output signal calibrated in different ranges. The typical temperature range, which allows measurements over distances from centimetres to kilometres, is between 223 K to 3273 K.

Different kinds of materials and gases have different emissivities, and will therefore

emit IR radiation at different intensities for a given temperature. The emissivity of a material or gas is a function of its molecular structure and surface characteristics. In the case of visible light, for example, the more highly polished some surfaces are, the more IR energy the surface will reflect. The surface characteristics of a material will therefore also influence its emissivity. In temperature measurement this is most significant in the case of infrared opaque materials which have an inherently low emissivity. Thus a highly polished piece of stainless steel will have a much higher emissivity than the same piece with a rough or machined surface. This is because the grooves created by the machining prevent as much of the IR energy from being reflected. In addition, a third factor affecting the apparent emissivity of a material or gas is the known sensor's spectral response (or wavelength sensitivity of the sensor). As stated earlier, only IR wavelengths between 0.7 and 20 μm are used for practical temperature measurement. Within this overall band, individual sensors may be used and operated in only a narrow part of the band, such as 0.78 to 1.06, or 4.8 to 5.2 microns, for better results.

1.9.4 Fluoroptic thermometry

The fluoroptic thermometer[42] can be a very useful system in microwave heating measurements due to the fact that the probe does not contain any metallic or high loss material. The probe is based around a fibre optic cable with a temperature-sensitive phosphor painted onto the tip. The phosphor, manganese-activated magnesium fluorogermanate, displays a deep red fluorescence on being activated with blue light (a filtered xenon flashgun for example) whose decay time is temperature dependent. The fluorescence produced in the phosphor is transmitted back to a sensor and correlated to the detect's internal calibration table and the temperature of the probe tip is displayed. A disadvantage of this equipment is that it is expensive and fragile and in its current commercial form is limited to temperatures below approximately 500 K.

1.9.5 Thermocouples

Thermocouples are sensors which consists of two dissimilar metals, joined together at one end, which produce a small unique voltage at a given temperature. This voltage is measured and interpreted by a thermocouple thermometer.

Thermocouples have been assigned alphabetic types, and have a color code. Two of the more popular types are J and K. A type J thermocouple uses a junction of iron and

constantin (constantin is an alloy of nickel and copper) and can be used over a range of 273 to 1023 K. A type K thermocouple uses a junction of nickel-chrome and nickel aluminium. This thermocouple has a useful range of 73 to 1523 K.

It was intimated earlier in this Chapter that the use of thermocouples in microwave radiation systems are not recommended due to the perturbations to the electric field that such devices produce. However, due to their high reliability and low cost, thermocouples have been incorporated in many microwave systems: for *in situ* measurements, the device can be grounded through contact with the oven or applicator wall, whilst thermocouples may also be used *ex situ*, inserting them into the sample shortly after irradiation. In the first case, 'thermocouple effects'[43] may still be seen such as distortion of the EM field, conduction of heat away from the sample, induction of thermal instabilities and microwave breakdown. In the second case, even a small delay in the measurement can be significant if the sample cools rapidly.

1.10 Aim of the thesis

The increasing use of microwave heating in solid-state and materials synthesis and processing has not been matched with progress in the study of how such processes proceed. Very frequently, the microwave oven is treated as a 'black box', with little knowledge of the way in which the radiation couples to the reactants or products, or even the temperature. This project aims to develop a particularly incisive tool: that of diffraction applied to microwave-driven processes *in situ*. The systems to which it is applied are some of those in which microwave irradiation has been shown to offer significant advantages: zeolite synthesis and processing, and the heating of solids with significant electrical conductivity; it is also applied to heterogeneous catalysts in the form of metal particles supported by a high-area ceramic, to investigate the possibility that there may be significant thermal gradients between the two.

The structure of the thesis is as follows: in Chapters 2 and 3 we establish the principles of diffraction, and of the design and construction of equipment to enable diffraction data to be taken with different types of diffractometer during microwave irradiation. In Chapter 4 we establish some of the conditions under which a particular zeolite may be synthesised with the aid of microwave radiation with a view to future *in situ* diffraction measurements and describe work to look at post-synthesis modification of zeolites, ac-

celerating the exchange of bound species with microwave heating. In Chapter 5 we present an account of the effect of microwave heating on phase transitions in ferroelectric materials, partly as a means of trialling the apparatus, and partly to determine whether such transition may be influenced by the microwave field. In Chapter 6 we demonstrate how high-resolution neutron powder diffraction may be used as a phase-specific thermometer, and then to use that method to determine separately the temperature of the active phase and its support in heterogeneous catalysis systems. Finally, in Chapter 7, we present work on the fast-ion conductor AgI, in which previous studies indicate that the transition between phases of quite different conductivity may be brought down in a microwave field. Chapter 8 presents conclusions and suggestions for future work.

Chapter 2

Diffraction studies of solid materials

2.1 Principles of diffraction in solids

The majority of solids are crystalline, and most commonly bulk samples are polycrystalline. The basis of understanding their properties - and modifying them to produce new materials - is to have a system for describing their structure. This chapter outlines the principles of diffraction in solids, as well as methods of determining structure, with an emphasis on techniques applied to polycrystalline samples. It also introduces methods of determining structure while a material is subjected to some external influence that may induce a change in structure. Such *in situ* methods, tailored for our particular problem of microwave-induced changes, will be explored further in later chapters. For a more detailed

The most powerful method of studying the structure of a crystalline material is through the diffraction of particles or waves whose wavelength is comparable to the separation between atoms in the material. We first establish the principles of this process, couched in terms appropriate for X-ray diffraction, which is the most common technique[44].

The electric field component of electromagnetic radiation interacts with charged particles - the electrons in a solid - producing spherical wavelets originating from each point scattering source. The outgoing, or diffracted beam is then the result of interference - constructive or destructive - between these wavelets. One way of visualising this process is to think of the components of the incident beam as a series of rays that impinge on the lattice with the same phase, and individually maintain this phase on scattering. If adjacent scattered rays are in phase with each other constructive interference takes

place and a diffracted beam is obtained in that direction.

However, if the rays are scattered with an arbitrary phase difference, some degree of destructive interference will occur, and for rays scattered such that there is exactly half a wavelength phase difference between neighbours, a complete destructive interference or cancellation occurs. Thus, in the two latter cases, maximum light intensity will fall off gradually to zero as the phase difference changes from complete constructive to destructive interference.

Two criteria must be satisfied in order that constructive interference occurs and therefore diffraction will be observed.

The first criterion is given by Bragg's law, which is illustrated in figure 2.1:

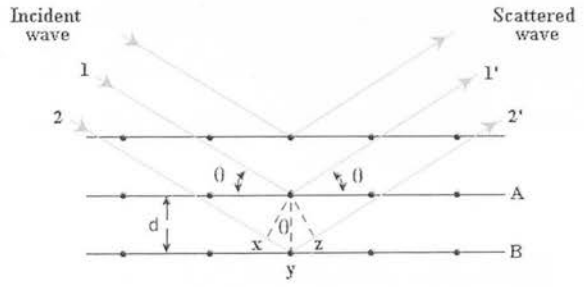

Figure 2.1: Schematic illustration of Bragg's law.

Bragg's law is based on regarding crystals as built up of layers or planes from which the X-ray beam is reflected as in a semitransparent mirror (see figure 2.1). Some incident X-rays are reflected off a plane with the angle of reflection equal to the angle of incidence, and some others are transmitted and subsequently reflected by succeeding planes.

When two X-ray beams (1 and 2 in figure 2.1) are reflected from adjacent planes within the crystal (A and B), for them to be in phase, the distance *xyz* for the beams 1' and 2' must equal a whole number of wavelengths. This means that beam 2 2' has to travel the extra distance *xyz* as compared with beam 1 1'. The relation between this distance *xyz*, the *d-spacing* and the Bragg angle (θ) is:

$$xy = yz = dsin\theta \tag{2.1}$$

and,

$$xyz = n\lambda \tag{2.2}$$

therefore,

$$n\lambda = 2dsin\theta \tag{2.3}$$

where λ is the wavelength of the X-ray, d is the spacing between planes of atoms in the solid, and θ is the angle of incidence. For a given set of planes, several solutions of Bragg's law are usually possible (n = 1, 2, 3, etc.) but normally n is established equal to 1 and the *d-spacing*, in the other cases, is halved by doubling up the number of planes in the set.

The second criterion is that the arrangement of atoms *within the unit cell* of the solid under examination allows constructive interference to occur for a particular set of planes with interplanar spacing d. This is quantified in terms of the *structure factor*, F(*hkl*), which is defined as the sum of the spherical waves that arise from the electrons of N atoms in a unit cell when excited by a plane-incoming wave. Then,

$$F(hkl) = \sum_{j=1}^{N} f_j \exp[2\pi i (hx_j + ky_j + lz_j] \tag{2.4}$$

where *hkl* are the Miller indices of the reflecting plane, x_j, y_j, z_j are the positions expressed as fractions of the appropriate cell dimensions, and f_j is the scattering factor of the jth atom in the unit cell. The exponential function gives the phase difference of the scattered waves with respect to a wave scattered at the origin of the unit cell. The structure factor represents the fact that the reflections *hkl* differ in amplitude and phase.

The allowed planes for constructive interference are those that satisfy the Bragg criterion, and for which F(*hkl*) is not zero. So, for example, in a face-centred cubic crystal structure (FCC) F(*hkl*) is not zero if the Miller indices h, k, and l of scattering planes are either all even or all odd, so allowed reflections are 111, 200, 220 and so forth. In contrast, for a body-centred cubic (BCC) structure the structure factor is finite when $h + k + l$ = an even integer so the allowed reflections have Miller indices 110, 200, 211, and so on. Thus, the systematic absence of diffraction from certain planes provides a

signature for identifying the atomic arrangement in the unit cell.

The scattering factor or atomic scattering factor (f_j in equation2.4) is defined as the ratio of the amplitude scattered by an atom at rest to that scattered by a single electron[46]. This factor is a function of the Bragg angle θ and decreases with $(sin\theta)/\lambda$.

Finally, it should be noted that the discussion so far has considered the array of atoms to be ideal - a perfectly occupied lattice of atoms at rest. In real materials, there may be imperfections in the lattice and there will also be some degree of motion of the atoms at any finite temperature. In principle, this could be incorporated into the way in which the sum in equation 2.4 is calculated, using an appropriate probability distribution function to describe small static displacements and the thermal motion of atoms. It is more common to factor these effects out and introduce an *anisotropic displacement parameter* (ADP) into the form factor as a pre-exponential term[47]. The ADP, $T_j(\mathbf{Q})$ for the jth atom is given by:

$$T_j(\mathbf{Q}) = \int p_j(\mathbf{u}) exp(2\pi \mathbf{Q} \cdot \mathbf{u}) d^3\mathbf{u} \tag{2.5}$$

where $\mathbf{Q}$ is the scattering vector, with magnitude $2sin(\theta)/\lambda$ and $\mathbf{u}$ is the displacement of the jth atom from its mean position. It is common to treat the thermal motion of the atoms using a Gaussian distribution, which is appropriate for a harmonic oscillation. When this is the only contribution to displacement from the mean position, this factor is sometimes called the temperature factor, and is also commonly referred to as the Debye-Waller factor. For isotropic, Gaussian displacement, it can be shown that equation 2.5 can be rewritten as:

$$T_j(\mathbf{Q}) = T_j(Q) = exp[-8\pi^2 \langle u_j^2 \rangle (sin^2\theta)/\lambda^2] \tag{2.6}$$

where $\langle u_j^2 \rangle$ denotes the mean square displacement of the jth atom from the ideal lattice position.

2.2 Diffraction from crystalline materials - practical issues

Different types of information may be obtained from diffraction experiments using either X-rays or neutrons[45]:

- *Ab initio* structure solution from single-crystal samples; for relatively simple crystalline materials, *ab initio* methods may also be applied to powders.

- Phase identification, primarily applied to powder samples and using the diffraction pattern in conjunction with standard data-bases to provide a 'finger-print' for such phases. Coexisting phases in the same sample can be identified, and relative quantities estimated, provided that each phase is crystalline and present at the level of 2-5 percent or more, depending on the instrument used and degree of crystallinity.

- Structure refinement of data taken from powders using profile refinement techniques, described in greater detail below. This requires a good starting model for the structure and is usually applied to materials that have minor modifications relative to an existing material.

- Chemical or physical transformations in crystalline phases may be followed by *in situ* diffraction.

- Information about state of division or texture may be derived from peak widths and intensities of powder patterns. From the intensities of the peaks associated with different crystallographic planes of the same phase the preferred orientation of the phase can be qualitatively estimated. From the full width at half maximum of a peak, the grain size (for a polycrystalline sample) or the particle size (for a powder sample) can be estimated from the Scherrer equation for particle size less than about 1000 Å[48,49].

Seen in the simplest fashion, a diffraction experiment consists of three components listed below (see figure 2.2):

a) The source of X-rays or neutrons, which can be monochromatic or of variable wavelength (λ).

b) The sample, which can be a single crystal or powder.

c) The detector, which is a radiation counter, photographic film, image plate or solid-state camera.

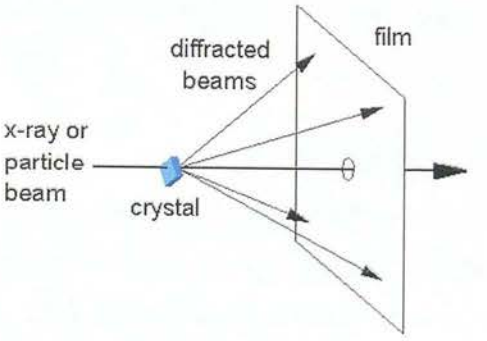

Figure 2.2: Simplified scheme of an X-ray diffraction experiment.

In this thesis we will only be considering diffraction using a monochromatic source incident on a polycrystalline or powder sample. The resulting diffraction pattern (diffracted beam intensity versus the scattering angle 2θ) was used for phase identification, structural refinement using the Rietveld technique (below), or the determination of cell parameters which in turn provide an estimate of sample temperature (see chapter 6).

2.2.1 X-ray diffraction

X-rays are electromagnetic radiation of wavelength approximately 1Å (10^{-10} m) lying between γ-rays and ultraviolet light in the electromagnetic spectrum. This kind of radiation is produced when high-energy charged particles collide with matter, for example electrons accelerated through potential differences of the order of kV. The electrons are slowed down by the collision and some of their lost energy is converted into electromagnetic radiation. The X-rays are usually produced in an evacuated tube. The cathode (held at a negative potential in the range -5 to -60 kV) is a tungsten filament, heated to emit electrons, and the anode is grounded at ground potential. The electrons, under this potential difference, are accelerated and hit the anode. Most of the energy heats the anode and it must therefore be cooled, generally by water; an alternative solution to avoid melting the anode is to rotate the anode.

Windows made of beryllium, or another element of low atomic number, permit the passage of the X-rays. For the absorption and shielding of the stray radiation lead is

generally used. A filter is commonly used to remove undesirable radiation and produce a monochromatic beam: for a Cu target, the key components to be removed are the Cu Kβ emission line and white radiation. The atomic number of the element in the filter will be generally one or two less than that of the target material. A foil sheet or a single crystal can be used as a filter.

X-ray detection was traditionally effected with photographic plates, but is now almost exclusively performed electronically with gas-ionising detectors, scintillators, image plates based on photostimulable charge-storage phosphors, and various forms of semiconductor devices such CCDs (charge coupled devices). One way of categorising detectors, is to divide them into those that are scanned in space to record X-ray photons as a function of position, and area detectors that are static, or moved between a small number of positions.

2.2.2 Neutron diffraction

Neutron diffraction, as an alternative method to X-ray diffraction, can also be used to determine the structure of solids. The difference between this two techniques is based on the fact that neutrons, having no charge and with a mass slightly higher that that of a proton do not interact directly with electrons (as X-rays does). Neutron hence are confined to direct nuclear effects (elastic and inelastic) and nuclear reactions (the absorption of a neutron by the nucleus and the emission of electromagnetic radiation or an energetic particle). As the nucleus of an atom is 10,000 times smaller than the electron cloud surrounding it, the possibility of neutrons interacting with a nucleus is very small. This allows neutrons to travel a long distance through matter before interacting.

For this reason, neutrons give information about atomic positions more directly. By contrast, in X-ray diffraction the location of the atoms is given indirectly at the centres of the electron cloud. Another characteristic is that with neutrons lighter atoms may be detected (which can be difficult using X-rays) because the scattering cross-section is not proportional to the atomic number.

Neutrons may be produced in a nuclear reactor, or as a consequence of bombardment of a heavy-element target with high-velocity ions, with de Broglie wavelengths of the

order of 1Å. In the work described in this thesis, we used neutrons produced exclusively by the second method, known as *spallation*, and we now outline the method of production and application of such neutrons as carried out at the ISIS Facility of the Rutherford-Appleton Laboratory, UK.

Negative hydrogen ions (H^-) formed by electrical discharge through a mixture of hydrogen gas and hot caesium vapour are accelerated to 775 keV and injected in to the linear accelerator (1 - see figure 2.3). In the drift tube linear accelerator, the hydrogen ions are accelerated to an energy of 70 MeV for injection into the synchrotron (2). On entering the synchrotron, the negatively charged hydrogen ions pass through a very thin 0.3 μm aluminium oxide foil that removes electrons from the ions, leaving only bare proton nucleus (3). Once the proton beam has been accelerated to 800 MeV in the synchrotron, it is deflected by 3 fast kicker magnets for transport to the neutron and muon targets. The injection and extraction process is repeated 50 times a second, and the current in the kicker magnets rises from 0 to 5000 Amps in a 100 nanoseconds (4). The extracted proton beam line passes over the synchrotron on its way to the neutron and muon targets (5). The proton beam makes approximately 10,000 revolutions of the synchrotron before being extracted. It is steered and focused by dipole and quadrupole magnets, and accelerated by alternating voltages applied across six double-gap cavities in the ring (6). A chain of magnets keeps the proton beam tightly focused as it passes through the intermediate graphite muon production target before hitting the neutron target inside the target station (7). Neutrons are created in the centre of the target station when the beam of high energy protons collides with the nuclei of tantalum ions within the target. The energised nucleus of each tantalum ion releases energy by evaporating nuclear particles, mainly neutrons, in all directions. Each proton produces approximately 15 neutrons (8).

The neutrons are used by a set of instruments distributed radially about the target, at the end of guide tubes. The energy energy of the neutrons produced at the target has a broad spectrum which may be modified to some degree so that it better matches the needs of the various spectrometers or diffractometers. This is effected primarily by means of a moderator which contains a material with which the neutrons thermalise to some extent through collisions. The neutrons then continue to each instrument, where they are scattered by the sample and then detected. This generally involves the interaction between the neutron and an element that can capture it, and undergo a nuclear

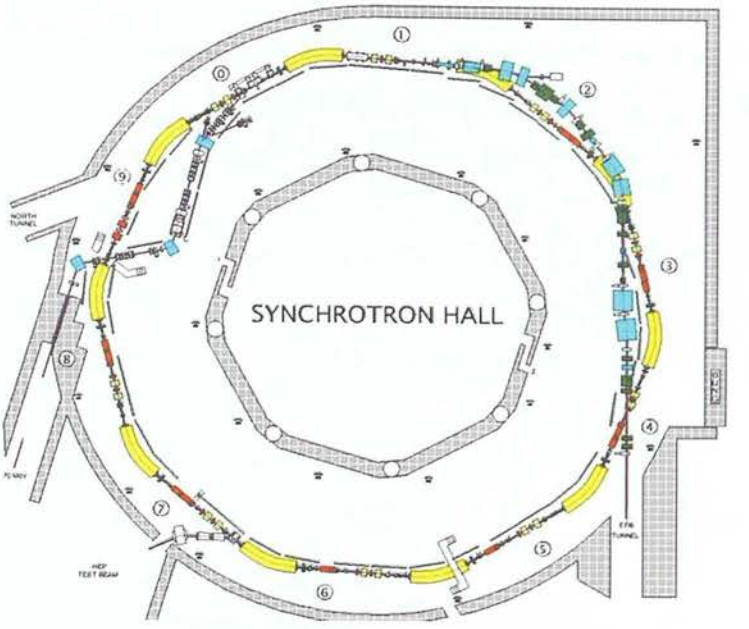

Figure 2.3: Scheme of a synchrotron configuration.

reaction to produce ionising radiation and charged particles: common elements for this role are ^{10}B and ^{3}He, and the radiation or charged particles may then be detected by a variety of techniques such as gas-ionisation as used in proportional counters, and scintillators coupled with a photomultiplier tube.

In this thesis we worked exclusively with the instrument HRPD, the High Resolution Powder Diffractometer at ISIS, which offers the highest resolution in *d-spacing* of any neutron powder diffractometer in the world. This is a consequence largely of the very long neutron flight-path, between the moderator and the sample, such that the uncertainty in measuring the neutron time-of-flight (TOF), which determines the uncertainty in the neutron wavelength, is very small compared to the TOF. TOF instruments offer a particular advantage with many types of *in situ* experiments because the variable incident wavelength means that reflections with a wide range of d-spacings may be collected at a detector of fixed geometry, and this in turn makes it easier to accommodate some of the constraints imposed by the sample environment. In the case of the HRPD, there are three detector banks, affording three broad bands of d-spacing, and further details of these are given in table 2.1 and are depicted with the rest of the instrument in figure 2.4.

Table 2.1: Detector bank details for the HRPD at the ISIS Facility.

	Backscattering	**90°**	**Low angle**
Detector specification	ZnS scintillator	ZnS scintillator	1/2" 10atm He^3 gas tubes
Fixed scattering angle	$160° < 2\theta < 176°$	$87° < 2\theta < 93°$	$28° < 2\theta < 32°$
Resolution($\Delta d/d$)	$\sim 4-5x10^{-4}$	$\sim 2x10^{-3}$	$\sim 2x10^{-2}$
d-spacing range (30-230 ms)	$\sim 0.6-4.6$ Å	$\sim 0.9-6.6$ Å	$\sim 2.2-16.5$ Å

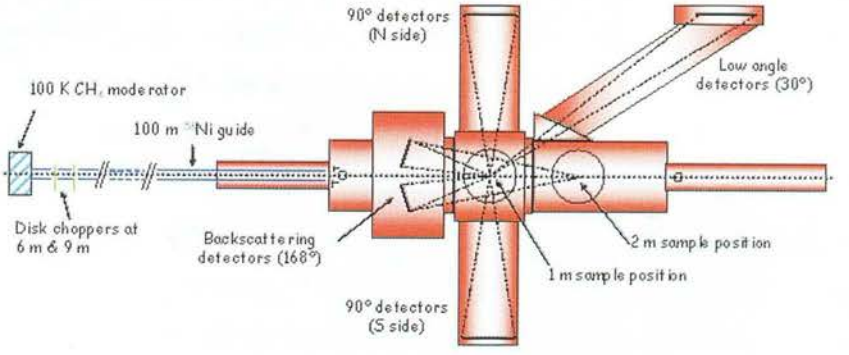

Figure 2.4: Configuration of the HRPD at ISIS Neutron Diffraction Facility[50] showing the configuration of the diffractometer and detectors.

2.2.3 Powder diffraction techniques

In finely powdered crystalline samples, the various lattice planes are randomly arranged in every possible orientation. For each set of planes, therefore, at least some crystals must be oriented relative to the incident beam at the Bragg angle (θ) and thus give rise to diffraction. Those diffracted beams can be detected with a static detector (photographic film, image plate or solid-state detector such as a CCD camera), or with a mobile detector.

In practise two general types of powder method may be used - measurement in *transmission* and measurement in *reflection* mode. In the former, a well-ground powder is loaded into a glass capillary tube that is centred in the incident beam. To reduce the effects of so-called 'texture' (a statistically preferred orientation) the sample is spun. For any set of lattice planes, the diffracted radiation forms the surface of a cone and

the only requirement is that the planes will be an at angle θ to the incident beam. The angle between diffracted and undiffracted beams will be 2θ and the angle of the cone 4θ. These cones of radiation are recorded for each set of planes on one of the various types of detector; where the detector is in the form of a strip of photographic film, the technique is known as the Debye-Scherrer method.

The most common type of *reflection* mode measurement uses what is called Bragg-Bretano geometry, in which the optics of the instrument are set up to bring the reflected beam into sharp focus at the detector. Reflections are generally measured one at a time by scanning the flat sample through the angle θ while the detector is rotated by the angle 2θ around the axis common to both circles. The distance from the X-ray source to the sample is equal to the distance from the sample to the entrance slit of the detector, and the focusing circle will be defined by three points: the source, the centre of the sample, and the entrance slit of the detector. The flat sample is positioned tangentially to the focusing circle and the focusing condition will be fulfilled for the points there. The divergence normal to the diffraction plane is improved by a set of parallel foils of strongly absorbing material at an equal distance from one to another. The fluorescence radiation produced in the sample by the primary beam can be removed by a monochromator inserted in the front of the detector.

2.2.4 Refinement of powder diffraction data

For a long time it was believed that only a small amount of information could be obtained from a powder pattern. There were two challenges or problems associated with analysing such data. First, the random orientation of crystallites in the beam means that information is lost with regard to the specific *hkl* reflection in a set of *hkl* reflections with the same d-spacing. Second, powder reflections may overlap with the consequence that is difficult to assign intensities to specific reflections. By the mid-sixties, it became apparent for some diffractionists that the invention of more powerful computers could help to obtain more information through analysis of the diffraction profile. It was recognised that in a step-scanned pattern, for example, there is some information associated with each intensity at each step in the pattern, even if there is no Bragg reflection intensity at such a point, or if it is partial and initially scrambled (as the sum of contributions from several Bragg reflections). Rietveld first solved this problem by means of computational analytical procedures, a technique now known as

the Rietveld method[51]. This method was first applied to data obtained on neutron diffractometers with cylindrical samples, due to the fact that the line-shape of the reflections is simple, but nowadays it is also widely used for powder X-ray diffraction in both transmission and reflection mode.

In this technique, the least-squares refinement is carried out with increasing numbers of variables until the best fit is obtained between the entire observed powder diffraction pattern and the entire calculated pattern based on a model for the crystal structure(s), the optical properties of the diffractometer and perhaps also the microstructure of the polycrystalline sample such as strain and particle size. It should be stressed that the Rietveld method is not a structure solution technique but rather a crystal structure refinement process. Because the refinement process is a non-linear least-squares process, the refinement must be started from a 'reasonably good' model of the crystal structure and the experiment. Of great importance in this method is the knowledge of structure because it allows the allocation of intensities to overlapping individual reflections.

2.2.5 Applying the Rietveld method

The first stage in a Rietveld refinement is to produce the diffraction pattern in a digitised form, generally as a set of values of detected intensity y_i, at each step i in scattering angle, 2θ, or some function of energy such as velocity (TOF - time-of-flight for neutron data) or wavelength (for X-ray data collected with an energy-dispersive detector and an incident beam of white X-radiation). In any case, the number of steps in the powder diffraction pattern will be usually of the order of thousands. The quantity minimised in the least-squares refinement will be the residual, S_y defined as follows:

$$S_y = \sum_i w_i (y_i - y_{ci})^2 \tag{2.7}$$

where:

$w_i = 1/y_i$,

y_i = observed (gross) intensity at the *ith* step,

y_{ci} = calculated intensity at the *ith* step.

A powder diffraction pattern of a crystalline material can be seen as a collection of individual reflection profiles, each of which has a peak height, a peak position, a breadth,

and an integrated area which is proportional to the Bragg intensity, I_K, where K stands for the Miller indices, *hkl*. Additionally, I_K is proportional to the square of the absolute value of the structure factor $| F(hkl) |^2$.

The calculated intensities, y_{ci}, are determined from the $| F(hkl) |^2$ values calculated from the structural model by summing the calculated contributions from neighbouring Bragg reflections (for example, within a specific range) plus the background.

$$y_{ci} = s\sum_K L_K \mid F(hkl) \mid^2 \varphi(2\theta_i - 2\theta_K)P_K A + y_{bi} \tag{2.8}$$

where:

s is the scale factor,

L_K contains the Lorentz, polarisation, and multiplicity factors,

φ is the reflection profile function,

P_K is the preferred orientation function,

A is an absorption factor, which differs with instrument geometry,

F_K is the structure factor for the Bragg reflection K,

y_{bi} is the background intensity at the *ith* step.

The least squares minimisation procedure then will lead to a set of normal equations that involve derivatives of all of the calculated intensities, y_{ci}, with respect to each adjustable parameter and the solution is obtained using the inversion of the normal matrix with elements M_{jk} given by,

$$M_{jk} = -\sum_i 2w_i \left[(y_i - y_{ci}) \frac{\partial^2 y_{ci}}{\partial x_j \partial x_k} - \left(\frac{\partial y_{ci}}{\partial x_j} \right) \left(\frac{\partial y_{ci}}{\partial x_k} \right) \right] \tag{2.9}$$

where the parameters x_j, x_k are the same set of adjustable parameters.

The solution then for an m by m matrix (where m is the number of parameters to be refined) where the residual function is not linear and the solution must be found with an iterative procedure in which the shifts,Δx_k, are defined as.

$$\Delta x_k = \sum {M_{jk}}^{-1} \frac{\partial S_y}{\partial x_k} \tag{2.10}$$

The calculated shifts are applied to the initial parameters to produce an improved model and the whole procedure is then repeated. Because the relationships between the adjustable parameters and the intensities are non-linear, the starting model must be close to the correct model or the non-linear least squares procedure will lead to a false minimum or even diverge. This can be avoided by using different least-squares algorithms at different stages of refinement or, using constraints.

The model parameters that may be refined then include not only atom positional, thermal, and site-occupancy parameters but also parameters for the background, lattice, instrumental geometrical-optical features, specimen aberrations specimen displacement and transparency), an amorphous component, and specimen reflections-profile-broadening agents such as crystallite size and micro strain. The usual parameters to be refined (simultaneously) in this method are listed below in table 2.2.

Table 2.2: Parameters that can be refined for structure refinement of powders. Note that the isotropic thermal parameter is equivalent to the form of ADP defined in equation 2.6 when there is no static disorder.

For each phase present	**Global parameters**
- Position coordinates x_j, y_j, z_j	- 2θ-Zero
- The isotropic thermal parameter, B_j	- Instrumental profile
- The site-occupancy multiplier, N_j	- Profile asymmetry
- The scale factor, s	- Background
- Specimen-profile breadth parameters	- Wavelength
- Lattice parameter	- Specimen displacement
- Overall temperature factor (thermal Parameter)	- Specimen transparency
- Individual anisotropic thermal parameters	- Absorption
- Preferred orientation	
- Crystallite size and microstrain (through profile parameters)	

Criteria for 'goodness of fit'. The particular 'best fit' obtained will depend on the adequacy of the model and on whether a global minimum, rather than a local ('false')

minimum is reached. Due to this, various criteria for the 'goodness of fit' are needed and some kind of indicators in each cycle of the procedure will help in order to judge if the refinement is proceeding satisfactorily and becoming sufficiently near to completion to be stopped. Some of these criteria (numerical or numerical and graphic) are:

- The R-values such as the 'R-Bragg' and the 'R-structure factor' that are based not only on the observed Bragg intensities but also on those deduced with the help of the model. Among them is the 'R-weighted pattern', R_{wp}, (equation 2.11) which from a mathematical point of view is the most meaningful because the numerator is the residual being minimised and can reflect the progress of the refinement.

$$R_{wp} = \left\{ \frac{\sum w_i (y_i(obs) - y_i(calc))^2}{\sum w_i (y_i(obs))^2} \right\}^{1/2} \tag{2.11}$$

- The 'goodness of fit', S, (equation 2.12) is another numerical criterion. A model may be considered to be quite satisfactory if the value of S is 1.3 or less. A large S may simply mean that the continuing statistical errors far outweigh the model errors either because of poor continuing statistics or because of a high background which, being slowly varying in angle, is easily modelled.

$$S = \left[\frac{S_y}{(N-P)} \right]^{1/2} = \frac{R_{wp}}{R_e} \tag{2.12}$$

$$R_e = \text{'R-expected'} = \left[\frac{(N-P)}{\sum w_i y_{oi}^2} \right]^{1/2} \tag{2.13}$$

- The Durbin-Watson statistic, 'd' (equation 2.14). The ideal value for 'd' is 2.00. Since the statistical errors in the intensity measurements at successive steps across a reflection profile do not depend on each other, there is no serial correlation in a statistical sense. If, on the contrary, the calculated and observed profile functions just do not match well, whether for reasons of shape or area, there will be strong serial correlation of the residuals and the 'd' value will be far from its ideal value.

$$\text{'d'} = \sum_{i=2}^{N}(\Delta y_i - \Delta y_{i-1})^2 \Big/ \Delta(\prod_{i=1}^{N} y_1)^2 \quad (2.14)$$

$$\Delta y_i = y_{oi} - y_{ci} \quad (2.15)$$

- Other criteria, both numerical and graphical, are also useful. One particularly useful device is a weighted difference plot, a graph of the fractional difference between observed and calculated intensity at each point divided by the standard deviation, σ_i(normally based only on counting statistics):

$$\Delta y_i(weighted) = \left[\frac{y_{oi} - y_{ci}}{y_{oi}}\right] \Big/ \sigma_i \quad (2.16)$$

  This way of presenting the data accentuates angular trends and emphasises misfits in low and high intensities.

In general, numerical criteria are needed to assess the fit quantitatively in detail, while graphical criteria readily reveal gross errors and omissions, and often also provide a reality check for a refinement that may look respectable in terms of numerical goodness of fit, but still omits key features of the diffraction pattern that cannot readily be attributed to impurities. At the end of the refinement process it is of course important also to check that the final structure makes sense both structurally and chemically - for example, to check that bond lengths are physically meaningful.

For this work, the General Structure Analysis System (GSAS)[52,53] suit of programs - one of a number of computer programs available - was used to refine powder diffraction data. One of the advantages of this programs is that data obtained from X-ray as well as from neutron diffractometers can be used. In the case of neutrons, refinement of magnetic structure can be also attained. GSAS is based on several different peak profile functions (which are incorporated in the program) designed for used with data from specific instrument types. The functions used for the several refinements in this thesis are described in Appendix A.

In GSAS the overall 'goodness of fit', or reduce χ^2, is defined by a minimisation function as:

$$\chi^2 = \frac{\sum_n w_n(I^n_{obs} - I_{calc}\, n)^2}{N_{obs} - N_{var} + N_{cons}} \quad (2.17)$$

where,

w	are the weights derived from an error propagation scheme,
n	is the number of data points,
I_{obs}, I_{calc}	are the observed and calculated intensities and,
N_{obs}, N_{var}, N_{cons}	are the number of observables, variables and constrains applied in the refinement.

Typical values expected for this parameter are of that of $\chi^2 \leq 5$ which, complemented by the 'R-values' and the graphical visualisation of the fitting will help to determine the best possible result.

2.3 *In situ* diffraction studies

The study of the chemical processes that occur during the synthesis of inorganic solids has been attracting increasing attention in the last 20 years with the appearance of more modern equipment (such as CCD cameras and energy-dispersive diffractometers and synchrotron radiation in crystallography), and the introduction or wider application of new techniques (such as solid-state nuclear magnetic resonance). The understanding of the mechanisms of formation or crystallisation of inorganic solids may allow scientists to design more effective materials for particular applications, with specific properties such as catalytic activity, microporosity, superconductivity, and other electronic or magnetic behaviour. Mechanistic data could include for example, a quantitative understanding at an atomic level of the chemical process leading to the formation of the solid. However, it is often difficult to obtain such information, because conditions required for the reactions frequently involve elevated temperatures or pressures in sealed, thick-walled reaction vessels, making it difficult to follow the process in real time.

X-ray diffraction is an appropriate technique for following the formation of a crystalline solid and, in some cases, obtaining qualitative information about the course of the reaction and the identification of the different species at each step. In addition, time resolved diffraction techniques can give quantitative kinetic information through the relation between the Bragg reflection and the amount of solid, and this information might be the first step to postulate reaction mechanisms.

Many studies have been done in zeolites and microporous materials using in situ X-ray diffraction techniques because the species involved are often crystalline and this has led to a better knowledge of the crystallisation processes in real time. Given the success of such studies, and the generic nature of such work in the context of the broader field of solid-state chemistry, we shall briefly review the field. Among X-ray diffraction studies, two methods were used - angular-dispersive synchrotron powder diffraction[54,55,56,57], and energy dispersive diffraction (EDXRD), also generally performed at a synchrotron source[58,59,60,61,62,63].

Among studies with angular-dispersive measurements, an example is provided by the work of Norby's group which has been focused on zeolite Na-LTA and metal aluminophosphates (MeAlPO, where Me = Co, Mg, Mn and Zn). These studies were carried out in a specially designed capillary cell[57] to follow the crystallisation process under hydrothermal conditions. The results relating to MeAlPO materials confirmed the strong relation between the kinds of amine template used and the composition and structure of the crystalline product and in at least one case - that of MnAlPO-5 - led to the proposal of a kinetic model for the crystallisation.

EDXRD techniques in combination with synchrotron radiation have allowed an increase in scope of the types of reactive system that can be studied because they permit larger, thicker reaction vessels to be used, or enable relatively fast data collection over a range of *d*-spacings. Such methods have been used, for example, to follow the crystallisation process for zeolites[60,61] in combination with *ex situ* techniques like scanning electron microscopy (SEM) to identify the different phases involved in the crystallisation, their sequence of formation or dissolution and their stability[62], as well as revealing the kinetics of some of these processes. In a typical experiment, the sample was loaded into a capillary (0.5-1 mm), mounted on a goniometer head and pressure (N_2 or He) was applied through a T-piece. Pressures up to 45atm and temperatures up to 533 K were obtained in this way. The sample was generally heated using a stream of hot air and a thermocouple placed 1 mm from the capillary gave the temperature. A small resistance heater placed under the capillary is another means to heat the solution. To avoid problems with thermal gradients, the X-ray beam was kept smaller than the hot zone (normally about 7 mm wide). To obtain the relation between the temperature in the interior of the capillary and the thermocouple, in one of the experiments a calibration curve was derived based on the thermal expansion for silver, measured in the

capillary. Quartz glass was used because it is relatively chemically inert even when it was known that strongly alkaline solutions or gels at high temperature and long exposition time weaken it or even can react with it.

Employing a synchrotron radiation source, which allows the penetration of significant quantities of dense materials by X-rays, a commercial hydrothermal autoclave may be used[54]. The steel wall in this autoclave (25 ml of capacity) was thinned to 0.3 mm to minimise absorption of the X-rays. The heat source employed is an aluminium heating block and, a magnetic stirrer is placed in the base of the cell. A temperature up to 523 K and autogenous pressure is normally reached with this apparatus. Rapid data collection with this method (less than 1 min) can be obtained and used for kinetic studies.

In the next chapter we will consider the particular requirements of *in situ* diffraction experiments during microwave irradiation and present a number of technical solutions.

Chapter 3

Equipment for *in situ* diffraction studies during microwave heating

3.1 Introduction

In Chapter 1 the possibility was established of 'non-thermal' or 'microwave-specific' effects as a way of explaining the enhancement of processes in solid state during microwave heating. In Chapter 2 it was also shown that an accurate determination of structural changes in solids when exposed to external influences could help to elucidate the mechanisms of interaction with such influences. In order to study and gain understanding on certain of the microwave specific processes, several microwave applicators were constructed or modified. This chapter describes the characteristics of each applicator and the way they were adapted to the different diffractometers used in this work.

In Chapter 2 we introduced the principal technique - *in situ* diffraction - that has been used to follow physical or chemical changes in the components or reactants involved in, for example, the synthesis of a material or the charge/discharge cycles in batteries[55,59,60,61,62]. Most of this work has been based at central facilities for synchrotron X-rays, which are very bright and may be used to study either very small samples or relatively rapid processes, or for neutrons, which have much lower fluxes, but are also highly penetrating, so they can access samples in dense containers such as many types of reaction vessel. However, approval of time to use such facilities is slow and their production is very costly. Fortunately, laboratory X-ray diffractometers with higher intensities are now becoming available allowing, in some cases, relatively rapid acquis-

ition of data of sufficient quality for structure determination. For powder diffraction, for instance, the information that can be obtained covers phase transformations, components in solid-state reactions or temperature variations through structural changes in the sample[64,63,65].

In the present chapter, a detailed description is made of the microwave applicators designed and built for the *in situ* diffraction studies of solids during microwave irradiation. A description of the modifications of these applicators and the final arrangements to adapt them for use with different diffractometers is also given.

3.2 Microwave heating equipment specifications

The design of a microwave applicator to be used in conjunction with X-ray or neutron diffraction must meet certain minimum conditions[66,67,68,69].

1. Allow the passage of X-rays or neutrons from the source to the detector(s) to enable good quality data collection with minimal background scattering. It has been observed that for neutron diffraction, where the beam is able to penetrate dense or thick materials, the incorporation of small holes (not bigger than the microwave wavelength) is permitted. For angular-dispersive laboratory X-ray diffraction, however, where data can be collected over a wide range of scattering angles, the incorporation of 'windows' into the cavity body is required. These windows have to be made of a material with good electrical conductivity and low attenuation of the X-ray beam.

2. Construction from a non-magnetic, conductive material allowing a controllable level of microwave radiation to be applied to the sample with no leakage of radiation. In some cases, fine tuning can also be achieved through movable short circuit termination or ceramic screws inserted into the cavity.

3. A reliable measurement and control of sample temperature. This is generally achieved through the use of fibre optic temperature probes, which are microwave transparent and which provide the input for the control of power and hence temperature *via* a PC and suitable software.

4. A sample holder that is inert and transparent to microwaves. Among the characteristics of the most commonly used materials (listed below) for microwave

sample containers are low thermal and electrical conductivity.

- PTFE (polytetrafluoroethylene)[70] also known as Teflon™.
- Macor™ a machinable glass ceramic composed of approximately 55% fluorophlogopite mica and 45% borosilicate glass[71].
- Shapal M™ a machinable ceramic based on a mixture of aluminium nitride and boron nitride (~13% content)[72].

In general terms a microwave set-up for *in situ* diffraction studies is composed of three parts: (1) a microwave generator, (2) a microwave applicator whose design depends on the diffractometer geometry and, (3) microwave power and temperature controls. Figure 3.1 illustrates the arrangement as designed for neutron diffraction experiments that were carried out at the ISIS Facility at the Rutherford Appleton Laboratory in the UK.

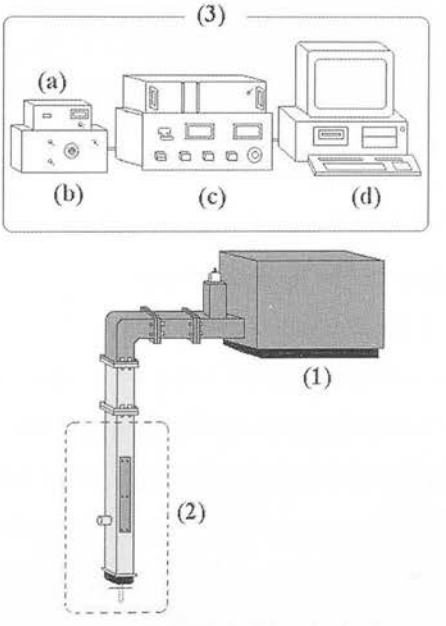

Figure 3.1: Schematic drawing of the arrangement for *in situ* X-ray/neutron diffraction studies during microwave radiation. The drawing shows the particular waveguide geometry for neutron experiments at the ISIS Facility. (1) Microwave generator, (2) microwave rectangular waveguide applicator and (3) power and temperature controls comprising (a) fibre optic temperature sensor box, (b) stepper motor, (c) microwave power supply and, (d) PC for power and temperature controls.

Microwave radiation at 2.45 GHz was generated in a commercial magnetron unit (ASTEX AX2110, 20 to 1000 W of power) and the temperature monitored during the process using a fibre-optic probe (Neoptix T1, Tmax. 523 K, resolution of 0.1 K) at all times in intimate contact with the sample. Microwave power was controlled using the PC.

The microwave radiation was directed to the sample through a rectangular waveguide of non-magnetic material (WR 284 Waveguide 10, H. Rollet waveguide). This was either extended to enclose the sample, or it fed a resonant microwave cavity with a different geometry. The two applicators were designed and adapted for three different diffractometers: X-ray diffraction in flat plate geometry on a Philips PW1730 diffractometer; time of flight (TOF) neutron diffraction on the High Resolution Neutron Diffractometer (HRPD) at the ISIS Facility, and X-ray diffraction from a sample in a capillary on a Bruker D8 diffractometer.

3.2.1 *In situ* rectangular waveguide applicator for X-ray or neutron diffraction.

The first applicator design to be used in the Philips PW1730 X-ray diffractometer was built from a rectangular brass waveguide with standard dimensions to operate in the fundamental TE_{10} mode. A standard flange was welded to the top while a stepper motor was fitted to the bottom. Two 2.5 x 10 cm windows were cut out of both sides of the waveguide to allow the passage of incident and scattered X-rays to the detector. The windows were covered with thin aluminium foil ($\sim$10 micron) as a more suitable alternative to beryllium which is prone to forming a highly toxic oxide. The attenuation of the X-ray beam from the use of aluminium foil was found to be acceptable. The configuration of this applicator is shown in figure 3.2.

For this arrangement, the microwave generator had to be located on the roof of the X-ray shielding hutch in which a hole was cut to allow the connection of the applicator to the microwave generator (figure 3.3(a)). Additional waveguide pieces and one 90° bend were joined together to increase the length of the the waveguide without disruption of the microwave currents. Any remaining holes in the shielding hutch were sealed again using lead sheet or tape for safety purposes. The microwave applicator was kept in position by means of a metallic stand fixed to the diffractometer box (see

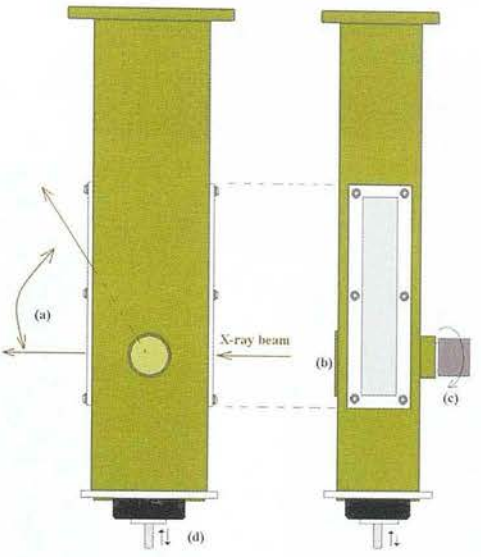

Figure 3.2: Schematic drawing of the rectangular waveguide applicator showing the X-rays passage and angle of the scattered radiation (left hand side of the drawing) and the lateral view showing the aluminium foil windows (right hand side). (a) X-rays scattered, (b) mobile lid covering a 2-cm aperture used in neutron experiments, (c) channel for spindle access to the microwave applicator, (d) stepper motor for fine tuning.

figures 3.3 (a) - (c)). A detailed drawing with all the dimensions can be found in figure B.2 in Appendix B.

The maximum scattered angle, 2θ, than can be attained with this set-up was 75°, the limit being set at the point at which the detector does not collide with the applicator.

The sample holder for this diffractometer is normally supported on a metallic spindle so that it can rotate about the same axis as the detector, and maintain a constant θ-2θ relation with the incident beam. For the microwave experiments this was extended using Macor™ and inserted into the microwave applicator through a 2 cm channel (approximately $\lambda/4$ in relation to the microwave wavelength) which permits the rotation of the spindle and the sample (left hand side of figure 3.2). The fibre optic temperature sensor was passed through a hole made in the ceramic spindle, placed directly into the sample, and held in place with Teflon™ tape, to avoid interference with the X-ray beam. A small flat plate sample holder made either of Macor™ or PTFE was fitted in place by sliding it into the spindle (figure 3.3(c)).

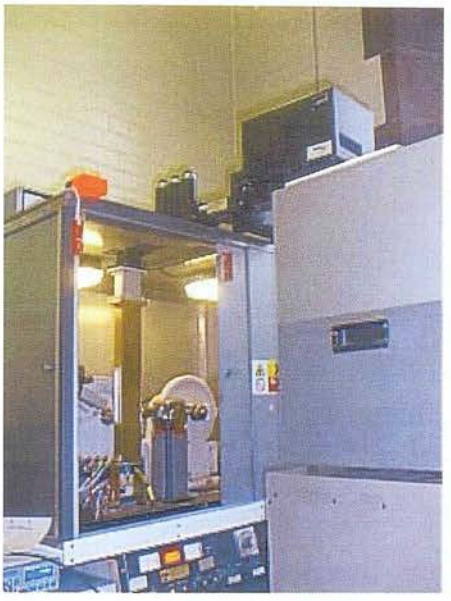

(a)

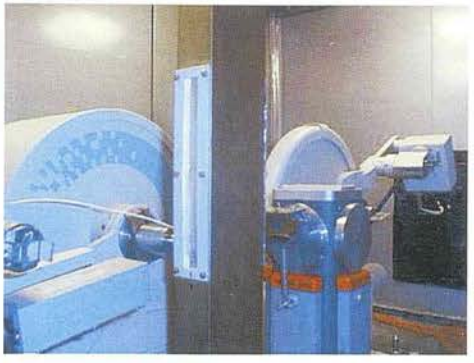

(b)

(c)

Figure 3.3: Final arrangement of the system for *in situ* microwave heating of solids. (a) Waveguide mounted inside the diffractometer box, (b) close-up of the waveguide, and (c) PTFE sample plate and fibre optic temperature probe.

A stepper motor was connected to the end of the waveguide, allowing the system to be tuned more finely through a sliding plate and hence improve the heating efficiency of the samples. Figure 3.4(A) shows a schematic view of the interior of the waveguide for this arrangement.

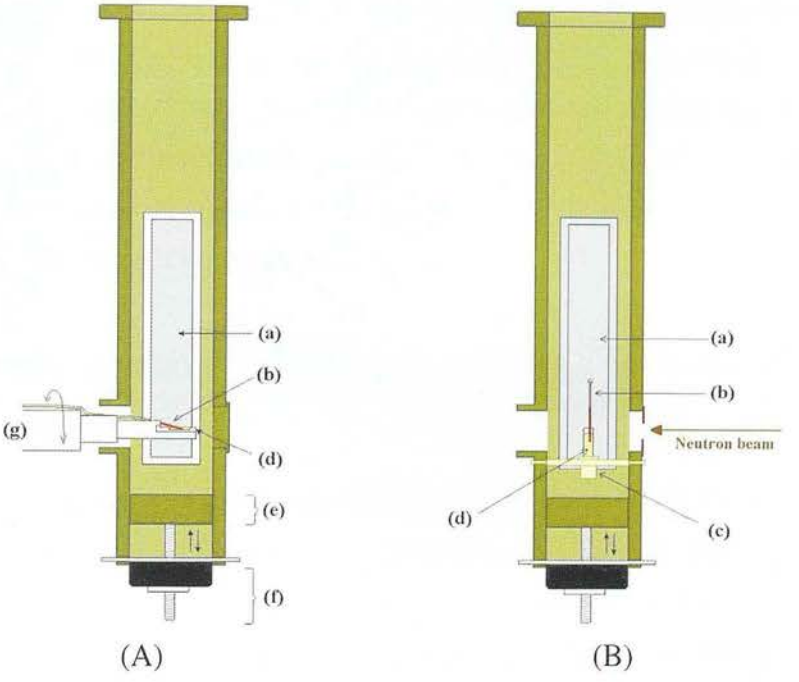

Figure 3.4: Schematic drawing of the inside of the rectangular waveguide and sample location for X-ray/neutron diffraction studies. (A) X-ray and (B) neutron diffraction set-up. (a) Aluminium foil window to allow the passage of X-rays, (b) fibre optic temperature sensor, (c) ceramic holder, (d) sample holders, (e) sliding short-circuit, (f) stepper motor, (g) metal-ceramic spindle used for X-ray diffraction.

The same applicator was modified to be used in neutron diffraction studies carried out on the HRPD at the ISIS Facility at the Rutherford Appleton Laboratories. The modifications, shown in figure 3.4(B) were made as the HRPD has a different configuration and bulkier samples can be analysed. In the first place, the two lateral windows through which the X-ray beam penetrates the cavity were covered with solid aluminium covers as they were not used for these experiments. The passage of neutrons through the waveguide was facilitated by 2 cm diameter holes for the incident beam and scattered beam. Neutron-absorbing gadolinium sheet was used to try to minimise scattering

from other components of the microwave heating system.

Initial experiments using a sample holder made of Shapal M™ failed due to the high proportion of BN in this material (> 13% content): the element B is a very strong neutron absorber, and its presence in the ceramic was not apparent until the problems with neutron transmission were encountered. A thin-walled piece of silica tube was then used as a sample holder, supported on the ceramic bottom part of the holder made of Shapal M™ and fixed in position onto the waveguide walls by means of ceramic screws. The fibre optic temperature sensor was inserted through a tiny hole in one of the lateral windows and directly placed in intimate contact with the sample. As Shapal M™ is microwave transparent the fine tuning of the microwave guide was also possible using the stepper motor attached to the waveguide.

3.2.2 *In situ* single mode resonant applicator for X-ray diffraction in capillaries.

The second applicator, a single mode resonant cavity (or resonant heater), was built from a 50 mm long x 86 mm internal diameter brass pipe-shaped piece to operate in the TM_{010} mode. Microwaves were fed by coupling a piece of brass rectangular waveguide through a 44 x 23 mm aperture located at the centre of the cavity body. The cavity was enclosed by welding one end while the other end can be fitted in place by means of two small screws in the cavity walls. This was done in order to gain access to the inside of the cavity for the mounting and alignment of the glass capillary which acts as the sample holder.

Two small outer channels (3 mm internal diameter x 5mm length) were cut at the centre of the plates through which the capillary containing the sample could be inserted into the cavity. For the passage of X-rays two 15 mm-wide windows were cut along the surface of the cavity at 10 mm distance from the welded end side of the cavity. The first window, used for the entrance of the X-rays, had a length of 30 mm while the second window had to be cut with a 110° arc to cover a wide range of scattering angle 2θ. Both windows were again covered with aluminium foil which in this case had to be 'glued' to the cavity walls using silver conductive paint. Four ceramic screws (alumina, M5 x 30 mm) were fitted to the end of the cavity (at an equal distance from the capillary centred entrance) as a means of fine-tuning the cavity. A schematic drawing

of this microwave applicator is shown in figures 3.5 (a) - (c). A detailed drawing showing all the measurements can also be found in figures B.2(a) and B.2(b) in Appendix B.

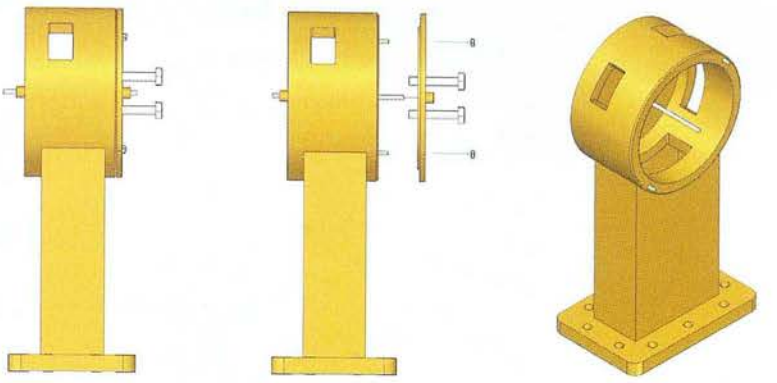

(a) (b) (c)

Figure 3.5: Schematic drawings of the microwave resonant cavity. (a) Lateral view showing one of the two windows for the entrance and exit of the X-ray beam, (b) removable lid to allow the alignment and setting up of the capillary and fibre optic temperature probe. The ceramic screws used for fine tuning are also shown here together with the small metallic screws and nuts to fix the plate and (c) shows a dimetric view of the inside of the cavity showing the capillary position and the aperture through which the microwaves are fed to the cavity.

The samples were placed inside a 1 mm glass capillary (glass No. 50, 80 mm length, Hampton Research) followed by the fibre optic temperature sensor whose tip is kept in close contact with the sample while the fibre optic cable is fixed to the capillary using Teflon™ tape. Glass capillaries were chosen among others such as PEEK (polyetheretherketone, 2 mm ID) and quartz capillaries (2 mm ID) as the most suitable option. PEEK is microwave transparent and will withstand continued use at temperatures up to 373 K. Early attempts using PEEK tubing as a sample holder showed that although scattered from the tubing was also observed -in addition to that of the sample- experiments that required to be carried out at higher temperatures were not possible. Quartz capillaries, on the other hand, can withstand higher temperatures but have a higher linear absorption coefficient, μ, than glass (75.8 compared to 71.0 cm^{-1} for Cu K radiation[73]). μ indicates the amount of radiation that is absorbed by the capillary during X-ray data collection.

Finally, the microwave resonant applicator was attached to the microwave generator by two 90° bends. For this arrangement, the microwave generator had to be placed inside the X-ray shielding box and a set of adjustable stands (one for the microwave generator and one for the microwave applicator) were used to align the equipment with the goniometer head (see figure 3.6).

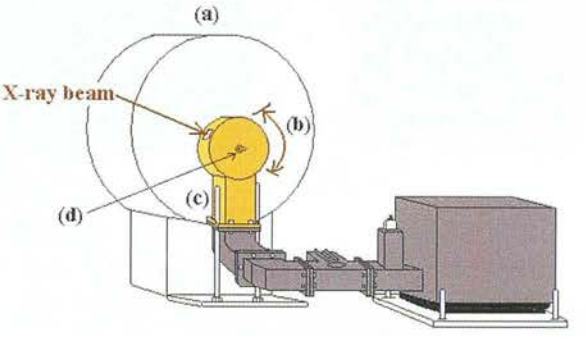

Figure 3.6: Schematic drawing of the arrangement for *in situ* X-ray diffraction studies during microwave radiation using capillary samples. (a) X-ray goniometer head (b) scattered X-ray radiation that can be detected in the position sensitive detector, (c) microwave resonant cavity and, (d) glass capillary.

Figures 3.7(a) - (d) show the final arrangement of the applicator mounted inside the diffractometer as well as the beam alignment (by means of using a fluorescent disc) once the microwave cavity is set in place.

The cavity can be tuned to resonance at a selected frequency by adjustment of the relative sizes of the cavity and dielectric (capillary with sample) as well as by the use of the ceramic screws[7]. The effect of the cavity diameter size was observed to be significant for this applicator, leading to negligible heating of certain samples. For example, AgI couples strongly with 2.45 GHz radiation, but when it was placed in cavity with a diameter of 96 mm, the resonant mode to which it was subjected dropped to 2.28 GHz, a frequency at which coupling was much less efficient. It was only when a second cavity, with an internal diameter of 86 mm was used that the resonant modes rose to 2.47 GHz, and heating could occur (see figure 3.8).

The measurements of the frequency of resonant modes in the cavity were performed

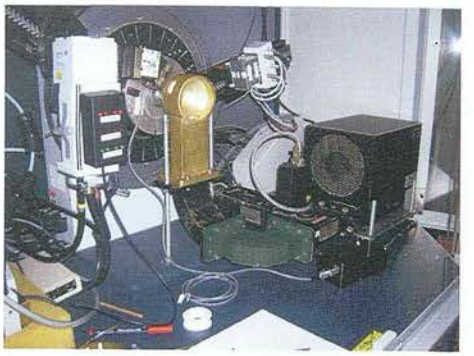

(a)

(b)

(c)

(d)

Figure 3.7: Final arrangement of the system for *in situ* microwave heating in capillaries. (a) Microwave resonant cavity mounted inside the diffractometer hutch, (b) X-ray beam alignment shown on a fluorescent disc, (c) close- up showing the position of the fibre optic probe in the capillary and, (d) final arrangement of the equipment, with the removable plate in place.

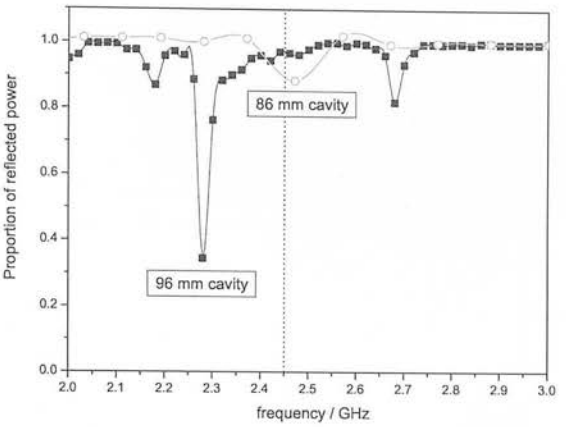

Figure 3.8: Proportion of reflected power in two microwave resonant heaters: 96 mm (■) and 86 mm(○) diameter respectively.

using a Hewlett Packard 8752A Vector Network Analyser (VNA), which determines the reflected microwave power as the frequency is swept (from 300 KHz - 3 HGz).

In a typical measurement, an AC current of voltage, V^+, is output from one of the ports of the VNA and conveyed along a coaxial cable to the microwave cavity using a coaxial to waveguide transition. The voltage, V^-, and the relative phase of the signal returned from the cavity are then measured at the same port (1-port measurement). In addition to the electrical length of the line, real coaxial cable is not perfect and will give rise to losses and reflections that must be removed from the measurement. To cancel out the effects of the electrical length and imperfection of the cable, a calibration procedure is used. The open-short-load (OSL) calibration method is one of the most widely used techniques. In this technique, two high reflection coefficient standards of widely separated reflection phase, an extremely low reflection matched termination are used. The three standard physical devices were connected to the end of the co-axial line in turn: a short, an open and a matched load. The VNA measures the responses of each of the three devices and automatically calibrates itself, moving the measurement plane to the end of the co-axial line.

This technique enabled us not only to determine the frequency characteristics of various cavities, but also follow how they changed as the a capillary empty or loaded with sample was introduced, and when the ceramic screws are inserted (figure 3.9(A)) for the 86 mm cylindrical cavity. The same figure also shows the response obtained when the capillary was loaded with samples of different dielectric properties (figure 3.9(B)).

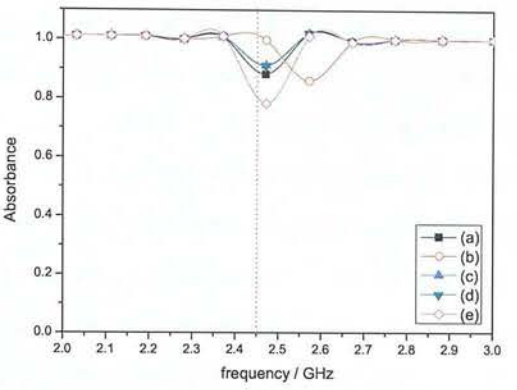

(A)

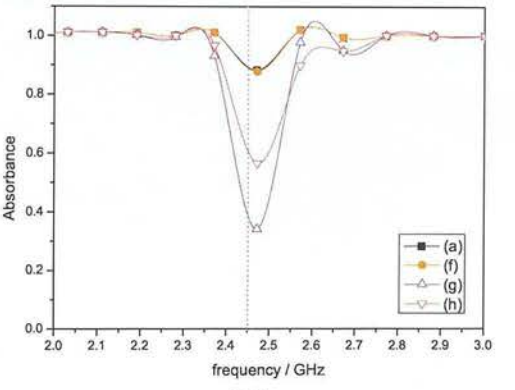

(B)

Figure 3.9: Response of absorbance on frequency for an 86 mm internal diameter microwave resonant heater showing the influence of (A) the tuning screws and capillary insertion and (B) several samples of different dielectric properties on the performance of the applicator. (a) Empty cavity with all four screws far into the cavity, (b) empty cavity with all four screws fully retracted, (c) with a 1 mm diameter glass capillary, (d) with a 2 mm quartz capillary, (e) with a 2 mm PEEK tubing , (f) with a glass capillary filled with AgI, (g) with a glass capillary filled with graphite powder and, (h) with a glass capillary filled with water. In (c)-(g), the ceramic tuning screws were screwed far into the cavity while (b) and (h) the screws were fully retracted.

3.3 Summary

This Chapter has presented new designs for microwave applicators that will enable a wider range of reactive systems, or physical properties to be studied by in situ diffraction. The basis for some of these designs was previously established in Edinburgh[69], but it was clear that there were limitations. First, for laboratory-based X-ray measurements, applicators were previously of fixed length, and optimised for flat-plate samples. We have presented modifications in which the cavity dimensions may be tuned continuously during an experiment by altering its effective dimensions with a moveable end-plate driven by a stepper motor. We have also presented an applicator with a cylindrical sample environment optimised for use with capillary samples mounted on a laboratory-based diffractometer. Finally we have described an applicator with rectangular cross-section for neutron diffraction studies on a time-of-flight instrument. We next go on to look at a variety of systems on which these applicators may be used.

Chapter 4

Microwave synthesis and processing of microporous materials

4.1 Introduction

In this chapter work is described whose aim was to assess the application of microwave heating in zeolite synthesis and processing. It is divided into two parts. First, work to establish some of the conditions under which a specific zeolite - ZSM-5 - may be prepared with the aid of microwave heating, and ultimately to perform such synthesis in a glass capillary to enable the various processes to be studied by *in situ* diffraction. Second, to explore the potential for microwaves to be used to facilitate ion-exchange processes, leading to post-synthetic modification of the material. We first review some of the features of the structure, composition and properties of zeolites, as well as more recent work to look at the potential for microwave radiation to improve certain steps of their synthesis.

Zeolites are minerals composed of three dimensional structural arrangements of $[SiO_4]^{4-}$ and $[AlO_4]^{5-}$ polyhedra (figure 4.1) linked through their corners to form a framework. Generally, zeolites are a well-defined class of crystalline aluminosilicates formed of silicon, aluminium and oxygen in their framework, and cations, water and/or other molecules inside the pores. These frameworks generally are very open and contain channels and cavities in which cations and water molecules are located. Many zeolites are naturally produced minerals, and are extensively mined throughout the world. Other zeolites (synthetic zeolites) are produced commercially for specific purposes. In some cases, natural zeolites can be produced synthetically, but some synthetic zeolites do

not have natural counterparts, being made only in the laboratory.

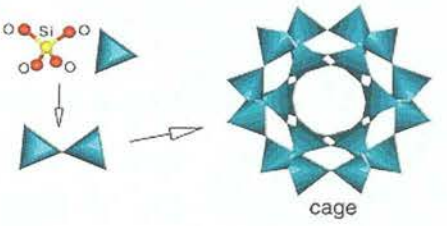

Figure 4.1: Representation of a $[SiO_4]^{4-}$ tetrahedral structure.

The cations in the pores of a zeolite often have a high degree of mobility, so that ion exchange may be easy and the water molecules may also be readily lost and regained, giving them the well-known property as desiccants. The name zeolite comes from the Greek word 'zeo', which means 'to boil' and 'lithos', that means 'stone': 'boiling stone'. Another important property of zeolites arises from the regular array of apertures which, depending on the size, permits the passage of some molecules but not the passage of others into the porous structure depending on the effective molecular dimensions. That is why these materials are sometimes also called molecular sieves. The pores or voids in such materials typically range between 5 and 20 Å.

A general formula for zeolites can be established starting from pure silica, which consists of SiO_4 tetrahedra sharing all the vertices. The replacement of some of the SiO_4 tetrahedra by AlO_4 tetrahedra occurs, maintaining the charge balance by the simultaneous incorporation of cations into the structure. In other words, '$MAlO_2$' or $M_{0.5}AlO_2$ replace 'SiO_2', where M is a mono cation (such as Na^+ or K^+) or a divalent cation (such as Ca^{2+} or Ba^{2+}). The cations introduced alongside the aluminate tetrahedra are frequently hydrated leading to a general formula for zeolite of three components: cavity cations, absorbate (water) and framework[74].

$$\{[M^{n+}]_{x/n}\,[\,mH_2O\,]\}\,\{\,[\,AlO_2\,]_x\,[\,SiO_2\,]_{1-x}\}$$

In this general formula, the first group $\{[M^{n+}]_{x/n}[\,mH_2O\,]\}$ describes the species present in the cavities, and the second group $\{[\,AlO_2\,]_x\,[\,SiO_2\,]_{1-x}\}$ describes the tetrahedral species forming the framework in the zeolite. The net negative charge of the

aluminosilicate framework is neutralised by the exchangeable M cations, of valence n, and m molecules of water in the unit cell occupying the void space, that can be greater than 50% of the volume.

Nowadays, the use of zeolites is worth billions of pounds per annum, leading to a considerable interest in the synthesis of new zeolites and microporous materials for different applications. The application of zeolites may depend on whether the zeolite is natural or synthetic[75]. The uses for natural zeolites include animal litter and bedding, water treatment, horticultural applications, additives in animal feed, uses as heavy metal cleaning, odour control and moisture control. These kinds of zeolites were used, for example, during the cleaning up of radioactive material at the Chernobyl nuclear plant. Among the major uses of the synthetic zeolites, which are generally tailored to have specific pore sizes or chemical activity, are as detergent components, absorbents and, the major economic driver, as catalysts. In this last application, zeolites are mainly used for catalytic petroleum cracking with a few applications in fuel-related and petrochemical hydrocarbon reactions.

In order to have a clear idea of the way zeolites work, some of these applications are detailed below.

- Gas separation. The ability of zeolites to act as molecular sieves depends on the pore or channel sizes which vary according to zeolite type - typically from 2.5 to 4.3 Å diameter. This facilitates the adsorption of gases such as ammonia, hydrogen sulphide, carbon dioxide, formaldehyde, and others. This potential use has been exploited in industry for selective removal of gases from composite gaseous mixtures.

- Water adsorption/desorption. The natural affinity for water and their capacity to absorb or desorb it without damaging the crystal structure makes zeolites appropriate substances to be used as desiccants, controlling moisture levels, and producing low humidity. This same property, added to a high heat of adsorption, gives natural zeolites the capacity to efficiently store heat energy for later use at low cost compared with energy systems that not utilise zeolites as heat storage media.

- Ion exchange. The loosely bound nature of extra-framework metal ions (such as those in zeolite NaA) means that they are often readily exchanged for other types

of metal when in aqueous solutions. This is exploited in a major way in water softening, where alkali metals such Na^+ or K^+ prefer to exchange out to the zeolite, being replaced by the 'hard' Ca^{2+} and Mg^{2+} ions from the water. Many commercial washing powders thus contain substantial amounts of zeolite. Commercial waste water containing heavy metals and nuclear effluents containing radioactive isotopes can also be cleaned up using such zeolites.

- Catalysis. Another important use of zeolites is as catalysts for chemical reactions which may take place within the internal cavities. One of the important classes of reactions is that catalysed by hydrogen-exchanged zeolites, whose framework-bound protons give rise to very high acidity. This property is widely used in organic reactions that include crude oil cracking, isomerisation and fuel synthesis. When other metals are introduced into the framework, zeolites are also used as oxidation or reduction catalysts, for example Ti-ZSM-5 in the production of caprolactam, and copper zeolites in NO_x decomposition. An important and very interesting property in this area is so-called shape selectivity where the shape and size of a particular pore system exerts a steric influence on the reaction, controlling the access of reactants and products. Increasingly, attention has focused on fine-tuning the properties of zeolite catalysts in order to carry out very specific syntheses of high-value chemicals, for example in pharmaceuticals and cosmetics industries.

4.2 Synthesis and processing

The traditional way of synthesising crystalline zeolites is from aqueous alkaline gels containing sources of silica, alumina and cations. This process can take weeks to form the final product and reactions generally need to be done under pressure and temperatures between 353 and 474 K. A mineralised medium containing acid and fluoride ions, which will give an acidic pH (pH$\leq$5), has been used as an alternative route after important advantages were discovered[76]. Larger crystals can be formed because nucleation rates are reduced and, for zeotype synthesis, the structural incorporation of the heteroatoms (such B, Al, Ga and Ti) from where the precursor will be precipitated, is benefited by an acid or neutral pH.

During the synthesis, the use of different templates (commonly organic cations, partic-

ularly quaternary ammonium salts) lead to a range of products with many characteristics and interesting effects such as high-alumina zeolites or tailored zeolites with certain specifications. Modification of zeolites can also be made after synthesis through exchange of framework species, for example dealumination procedures to change the Si/Al ratio or the introduction of different atoms to the framework such as B, Ga, Fe and Ti, among others[77].

Hydrothermal synthesis. Hydrothermal synthesis has been used in the preparation of many important solids, including microporous crystals, superionic conductors, chemical sensors, electronically conducting solids, complex oxide ceramics and fluorides, magnetic materials, and luminescence phosphors[78]. Condensed materials as nanometer particles, gels, thin films, equilibrium defect solids, specific helical and chiral structures and particularly stacking materials have also been prepared by this method[79]. Reaction is generally carried out above ambient temperature and pressure in sealed heated containers. The understanding of its mechanism becomes important in the directed synthesis of new materials with specific characteristics. Basically, the mechanism in hydrothermal synthesis is based on a liquid nucleation model[80].

- A small aggregation of precursors, which leads to unstable germ or embryos nuclei.
- The growth of some of these germs until they are stable nuclei.
- The deposition of more material on such nuclei to form larger crystals.

Zeolite crystallisation is generally started in an inhomogeneous gel, created from sources of silica and aluminium combined with water, under high pH conditions generated by significant OH^- ion concentrations. The control of the SiO_2:Al_2O_3 ratio in the gel will lead to the final framework composition of the product. Normally, with the exception of zeolite A, all the aluminium available is incorporated in the final zeolite[76].

An important issue in zeolite synthesis is the presence of impurities in the sources of materials. Such impurities could remain insoluble during crystallisation, producing undesired species that can act as nucleation centres, and may lead to the formation of a different silicate or metallosilicate species in solution, or may cause insoluble species to precipitate[81]. As a consequence the sources of aluminium, silicon and cations are

carefully selected, and the most common that have been used are[82]:

Sources of aluminium. Sodium aluminate is the most common substance used to provide aluminium during zeolite synthesis but other alternatives can be $Al(OH)_3$, freshly prepared Al_2O_3 or AlO(OH). Some syntheses could include also aluminium alkoxides, aluminium salts (like aluminium sulphate), and natural aluminium sources from glasses, sediments, feldspars and related minerals. Aluminium rich industrial wastes have also been employed in zeoglite synthesis. Zeolite production from aluminium sources is enhanced by the presence of the $[Al(OH)_4]^-$ moiety.

Source of silicon. The most widely used sources of silicon are soluble silicates and their hydrates such as sodium metasilicate pentahydrate, silica sols (30% by weight SiO_2), made from high surface area ('fumed') silica such as Cab-o-Sil, and commercial products such as Syntox. Less frequently used are silica gels and glasses (including volcanic glass), silicon esters, clays (kaolinite), volcanic tuffs (loose pyroclastic material), sand and quartz.

Sources of cations. As high pH favours zeolite crystallisation, alkali metals and alkaline earth hydroxides are the preferred cation sources in most cases for industrial zeolite production. Other oxides and some salts have been used in this role too and, of course, the soluble silicates and aluminates are themselves cation sources. Tetramethylammonium (TMA) salts may be employed too. Many syntheses involving organic cations have been developed and they are particularly useful in the synthesis of high-silica zeolites (for example ZSM-5), phases of silica with zeolitic properties (for example silicalite) and some zeotypes (for example $AlPO_4$).

Use of templates. The templates used in zeolite synthesis are commonly cationic species added to synthesis media in order to aid or guide in the polymerisation / organisation of the anionic building blocks that form the final framework[81]. The study of templates in the synthesis of zeolites started after it was observed that they were not just acting as charge balancing cations but also had a role in directing the synthesis of a particular molecular sieve structure. At the same time, after observing the correlation between size and shape of the template and the size and shape of the cavity formed in the zeolite the conclusion was that the templates build the molecular sieve structure around themselves by directing the condensing oxide tetrahedra into a particular geo-

metry. Two examples illustrate this. The synthesis of sodalite, using TMA cations, and the synthesis of high silica ZSM-5 using tetrapropylammonium cations. In the first case, the Me_4N^+ cations are located at the centre of the sodalite cages in the final product, proving that the zeolite must have formed around the cations because they are so big that they cannot enter or leave. In the second case, the cation is located at the intersection of the two intersecting channel systems with the four long alkyl chains lying along the four individual channels[77].

It was suggested[76] that the organic guest molecules could act in three distinct ways.

- *Space filling species.* The role of the organic template is to exclude the water from the voids in the framework by means of a decreasingly unfavourable energetic interaction between the solvent water and the growing molecular sieve. In this case, the nature of the template is not really important.

- *Structure directing agents.* The process in which a unique template leads to the formation of a unique structure that reflects the geometrical or electronic structure of the template. That means that the structure cannot be synthesised by another template. In this process, there is a very high correlation between the size of the organic molecule and the size and shape of the framework pore produced.

- *True templates.* This process is very rare and the best example is the synthesis of ZSM-18 using the triquaternary amine ($C_{18}H_{30}N_3^{3+}$). It is suggested that, during the synthesis and in the lowest energy conformation the template is held in a cage in the zeolite framework that has the same three-fold symmetry as the organic template and then, the organic molecule is not allowed to rotate in this cage. In this case, the shape of the template plays an important role in the localisation of the TO_4 groups around it and with that the structure of the final product.

Post-synthetic modification of zeolites. Once prepared, zeolites may be modified by ion-exchange to produce derivatives that may have quite different chemical character, for instance with regard to their behaviour in catalysis. Such ion-exchange is usually carried out in solution[83,84] although solid-state processes have become more common since the 1970's[85] because they are often easier. In the case of ion exchange in solution, for example, the method has to take into account many factors for obtaining a high dispersion of the salt into the channels of the zeolite. Among those factors are[86]:

type of zeolite (structure and pore size), nature of the ion to be exchanged (concentration, ion size, and whether or not the salt is hydrated), temperature of the process, and solvent (mainly water is used). In comparison, higher yields and high dispersions into the channels can often be obtained through solid-state methods in a single-step process.

For solid state ion exchange a dry powder of the zeolite and salts or oxides containing the cation to be exchanged are mixed together and then heated. The most favourable cases will lead to a very high degree of exchange in a single step allowing also certain metals to be exchanged in narrow pore zeolites. Equation 4.1 shows a representation of the processes that take place during solid state ion exchange in a zeolite[85].

$$pM_1^{n_1+}(Z^-)_{n_1} + qM_2^{n_2+}(A^{m-})_{n_2/m} \Longleftrightarrow xM_2^{n_2+}(Z^-)_{n_2} + (p-[n_1/n_2]x)M_1^{n_1+}(Z^-)_{n_1} + (n_1/n_2)xM_1^{n_1+}(A^{m-})_{n_1/m} + (q-x)M_2^{n_2+}(A^{m-})_{n_2/m} \quad (4.1)$$

where:

M_1 is the outgoing cation present in the zeolite,
M_2 is the ingoing cation to be exchanged,
n_1, n_2 are the valencies of M_1 and M_2 respectively,
A is the anion of the M_2-containing compound (salt or oxide),
m the valency of A,
Z^- is the monovalent fragment of the zeolite framework,
p, q, x are stoichiometric coefficients.

In both solid-state and solution ion exchange the exchange process leads to an equilibrium, but in the case of the solid-state process, conditions can be chosen so that the equilibrium is shifted to obtain an exchange of effectively 100%. This is generally brought about by the continuous removal of one of the components of the exchange product. This is represented in equation 4.2 for a mixture of a zeolite in its hydrogen form H-Z (M_1 = H and $n_1 = 1$) and $CaCl_2$ (M_2 = Ca, $n_2 = 2$, A = Cl and $m = 1$). Additionally the solid state reaction may be conducted with the salt being present in sub-stoichiometric ($q < p/2$), stoichiometric ($q = p/2$) or excess ($q > p/2$) quantities, allowing a desired degree of exchange to be achieved.

$$p\text{H-Z} + q\text{CaCl}_2 \longrightarrow x\text{Ca-Z}_2 + (p-2x)\text{H-Z} + 2x\text{HCl}\uparrow + (q-x)\text{CaCl}_2 \quad (4.2)$$

4.3 Synthesis facilitated by microwave irradiation

As in many areas of chemistry, the potential for microwave radiation to improve synthesis has been explored in recent years. The initial application of microwave heating in zeolite chemistry was to dry zeolites or remove ethanol from silicates. In this kind of work, studies[87] have focused on the microwave heating of zeolites to determine the amount of energy that those materials absorb. Samples of 'dry' and 'wet' commercial zeolites were heated by microwave radiation, confirming that the water in the 'wet' samples absorbs the microwave radiation and can be evaporated. Other conclusions were that commercial acid zeolites such as zeolite A, Y, US-Y, among others, do not absorb microwave energy strongly at 2.4 GHz but sodium and potassium zeolites absorb enough to be melted. Preparation of silica gels by conventional hydrothermal and microwave hydrothermal processes showed that remarkable reductions in processing time could be achieved; in some cases from 48 hours to 2 hours[88].

Another application of microwave radiation in zeolite synthesis is in the preparation of solids with strong basic properties for use as catalysts[89]. MgO dispersed in zeolite KL was radiated for a period of 10 to 40 min in a microwave oven (2.4 GHz). The results showed that MgO can be directly and more effectively dispersed in zeolite KL by microwave radiation producing strong basic sites and high activity in cis-2-butene. In another example, for the production of coloured plastics, it was shown that coumarine and azo dyes were monomolecularly encapsulated in $AlPO_4$-5 using microwave-assisted crystallisation[90]. Two stages of heating were used in this study changing from 1 kW to 0.25 kW and completing the crystallisation between 15 and 45 min. Microwave assisted crystallisation allowed the inclusion of the chromophores without decomposition.

The first synthesis of zeolite using microwave heating was of the zeolites Na-A and ZSM-5[91]. The synthesis was performed in an industrial oven and showed that zeolite Na-A was produced, crystallising in 12 min at 373 K instead of 2 hours in a steam box. ZSM-5 was heated with microwaves at 373 K for 100 min and found to have the same degree of crystallinity as a sample that had been heated conventionally for 6 hours. These are but two of many cases in which microwave processing has been shown to offer remarkable improvements in processing time for products of comparable quality. There has also been considerable work to try to determine just why microwaves

may bring about such changes[92]. What is apparent is that there is a strong need to develop methods to look at such processes *in situ*, revealing intermediate phases and the kinetics that govern their formation or consumption. Here we report preliminary work to determine the range of conditions under which a particular synthetic target - ZSM-5 - can be produced reproducibly with microwave irradiation. We also explored some aspects of a recently-reported problem concerning the observation that tetra-alkylammonium ions may break down during microwave irradiation at temperatures comparable to those at which synthesis is performed[93].

4.3.1 Aluminosilicate ZSM-5

The framework of ZSM-5 contains a configuration of linked tetrahedral units formed by eight five-membered rings (called pensil groups). These units, joined through edges, form chains and the connected chains, form sheets that lead to the three-dimensional structures (figure 4.2(a)). Another characteristic of this zeolite is the existence of two intersecting pore systems, zigzag channels with a near-circular cross section and straight channels of elliptical shape (figure 4.2(b)). All the intersections in this material are the same sizes and give the material its special adsorption characteristics and catalytic properties. The low aluminium content results in a low presence of cations. This material is hydrophobic and consequently its water content is low.

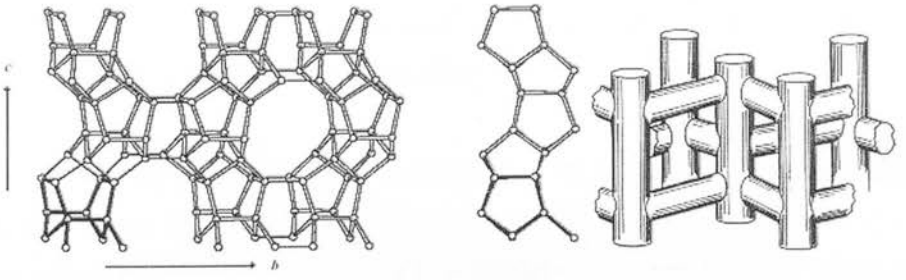

(a) (b)

Figure 4.2: Schematic representation structure and porous channel[94] system for ZSM-5. (a) Three dimensional structure and (b) intersecting pore system channels.

Zeolite ZSM-5 possesses useful catalytic properties and high thermal stability. Among the many applications of this material is the conversion of methanol to petrol, dewaxing

of distillates and the interconversion of aromatic compounds[95]. The catalytic properties of this and related materials are strongly dependent on the structure so in order to improve such properties it is important to have a good understanding of structure-property relations[96].

ZSM-5 is traditionally synthesised using the organic template tetrapropylammonium ion (TPA^+) to produce high silica zeolites via hydrothermal synthesis[81]. The crystallisation process takes of the order of 40 hours at a temperature of 453 K, yielding a final product with a crystal size of 6 μm. Tetrapropylammonium bromide (TPA-Br) has been used to produce a ZSM-5 catalyst for the isomerization of 1-butene to isobutene. This study was based on the hypothesis that the degree of crystallinity affects the catalytic behaviour of this zeolite. The synthesis was carried out again under hydrothermal conditions at 423 K for 72 hours. A zeolite with 86% crystallinity was obtained using this template[97]. In a study to explain the hydrophobic character of the structure-directing role of different templates (tetra-, ethanoltri- and diethanoldipropylammonium cations) used to prepare Si-ZSM-5, the so-called silicalite-1, the synthesis of this material took from 1 week for TPA and ethanoltripropylammonium to 2 weeks for diethanoldi- propylammonium[98]. In the case of zeolites with Si/Al ratios between 20 and 40, ethylamine was used to find the relation between the pH and the role of the small amines in the synthesis; the crystallization time was 65 hours at 433 K[99]. In a variation of this synthesis to study the nature of acid sites (Brönsted-Lewis sites) in ZSM-5, the zeolite was obtained after an overnight digestion stage followed by a 23 hours reaction to obtain the zeolite[100].

A study made by Lowe and Nee revealed that, in absence of organic molecules no formation of the ZSM-5 was possible[101]. The study was made with a system with composition $yK_2O : xAl_2O_3 : 60SiO_2 : 3000H_2O$ (where $5 < y < 20$ and $0 < x < 2$) at 423 K. The conclusion was that crystalline zeolite ZSM-5 could only can be prepared (for the conditions of this experiment) in the presence of 'impurities' such as ZSM-5 seeds or TPABr. However, some studies made on this area showed that the synthesis of ZSM-5 without an organic template is possible over a narrow range of Na^+ and aluminium concentration[77].

The sodium form of this zeolite (NaZSM-5)[102], the acidic form (HZSM-5)[103] and forms containing transition metals - Co (Ni)-ZSM-5[104] and Cu-ZSM 5[105] - have

been also prepared by ion-exchange methods. In some cases, solid-state processes with temperatures of 673 K permit the ion exchange in a few hours. In other cases, the stirred solutions were kept for 24 hours and then the solid was calcined for a further 24 hours to obtain the final product.

4.4 Microwave-driven solid-state ion exchange in zeolites

As with the synthesis of zeolites, microwave radiation has been proposed and tested as a means of accelerated ion-exchange both in solution and in the solid state[92,106,107,108]. However, experimental work is generally poorly documented, and carried out in domestic microwave ovens with poor or no determination of temperature. Here we explore one such system, that of the loading of copper ions into ZSM-5 by heating it with copper chloride dihydrate, $CuCl_2\ H_2O$; previous work[107] was based on monitoring the uptake of the copper salt through the loss of its characteristic X-ray diffraction pattern after microwave irradiation, and was taken to indicate a very efficient process in the microwave field. It should be noted too that the copper-loaded ZSM-5 also has highly desirable catalytic properties.

4.5 Experimental procedure and results

4.5.1 Establishing protocols for synthesis of ZSM-5 with conventional heating

The synthesis of zeolites is well known to be very sensitive to a wide range of factors, and it is also recognised that it is sometimes difficult to achieve reproducible products between different research groups so we first established protocols and an understanding of the relationship between samples prepared with conventional heating before attempting to look at the influence of microwave radiation on the synthesis.

ZSM-5 was synthesised using a concentrated gel with the following composition[109]:

$$((TPA)_2O)_{1.7}(Na_2O)_{6.7}(Al_2O_3)_{1.1}(SiO_2)_{46.2}(H_2O)_{1,675}$$

where TPA are the TPA^+ ions added as TPA-Br.

Two solutions containing the reactants were prepared as follows:

Solution A: Silica fumed (Aerosil, Degussa/Aldrich, 99.8%) + NaOH (Fisher Sci.) + H_2O /TPA-Br (Aldrich, 98.9%) + H_2O

Solution B: $NaAlO_2$ (Riedel-de Haën) + H_2O

Solution A was stirred for 30 min at 313 K after which solution B was added and maintained with stirring at the same temperature for one more hour[93]. The pH of the final gel was adjusted to 11 with sulphuric acid. The hydrogel thus formed was then loaded into a stainless steel digestion bomb with a PTFE (polytetrafluoroethylene) liner and heated at 423 K for 3 days[109]. The final product was isolated by filtration and washed several times with deionized water and dried in air at 393 K for 3 hours. In one case, after drying, the powder obtained was calcined at 773 K for 3 hours to compare it with commercial HZSM-5 zeolite (Laporte Laboratories). Samples were characterised using X-ray diffraction and scanning electron microscopy (SEM).

Figure 4.3 shows the diffraction patterns for the samples that were synthesised. It can be observed that well crystallised material was obtained with this method when compared with the commercial sample. Several factors such as the source of materials, pH and water content can influence the final product. The morphology of the crystals will depend on factors such as the aging time, the nature and concentration of the template, as well as the nature of the alkali cations. This was observed when batches of the same gel were allowed to age for several days (0, 7 and 14 days) before being loaded in the digestion bomb to be heated. The results were as might have been anticipated: the samples with the greatest aging time were more crystalline than those prepared with fresh gel (0 days) or less aging time (figure 4.3). No change in structure was detected when the sample was calcined to remove the TPA^+ used as template in this synthesis.

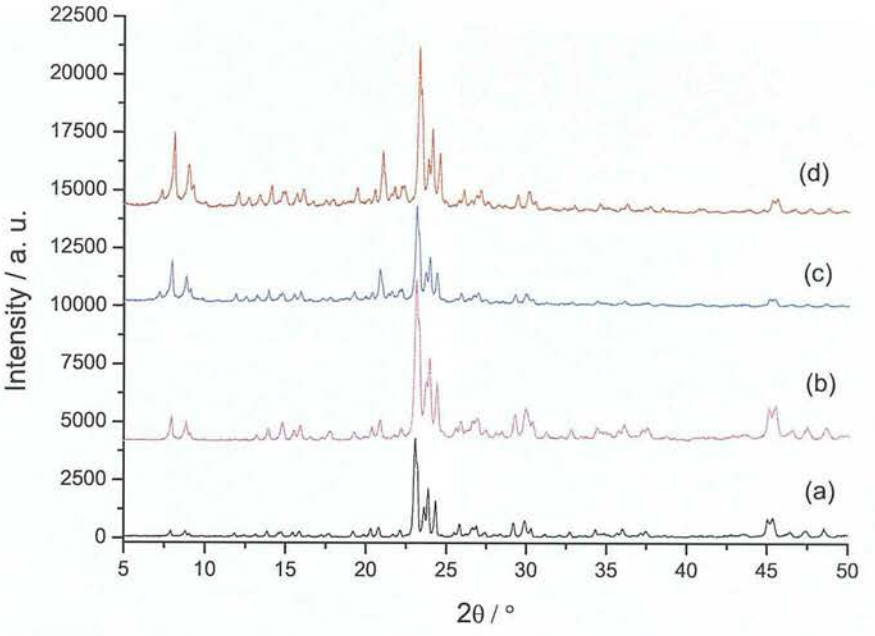

Figure 4.3: X-ray diffraction patterns of ZSM-5 samples produced under conventional heating. (a) commercial HZSM-5, (b) sample calcined for 5 h at 773 K from a fresh gel, (c) sample prepared with a 7 days aged gel -as synthesised-, (d) sample prepared with a 10 days aged gel -as synthesised.

Figure 4.4 shows the SEM micrographs obtained for the same samples using the same labelling as in figure 4.3 to distinguish between the conditions of synthesis, and also displaying, from left to right, pictures taken at increasing magnification. This reveals the changing structure of each sample at different length-scales, from the form of agglomerates to the shape of individual particles. In all the samples, spherical agglomerates were obtained which is in accordance with what is generally observed for this kind of material[109].

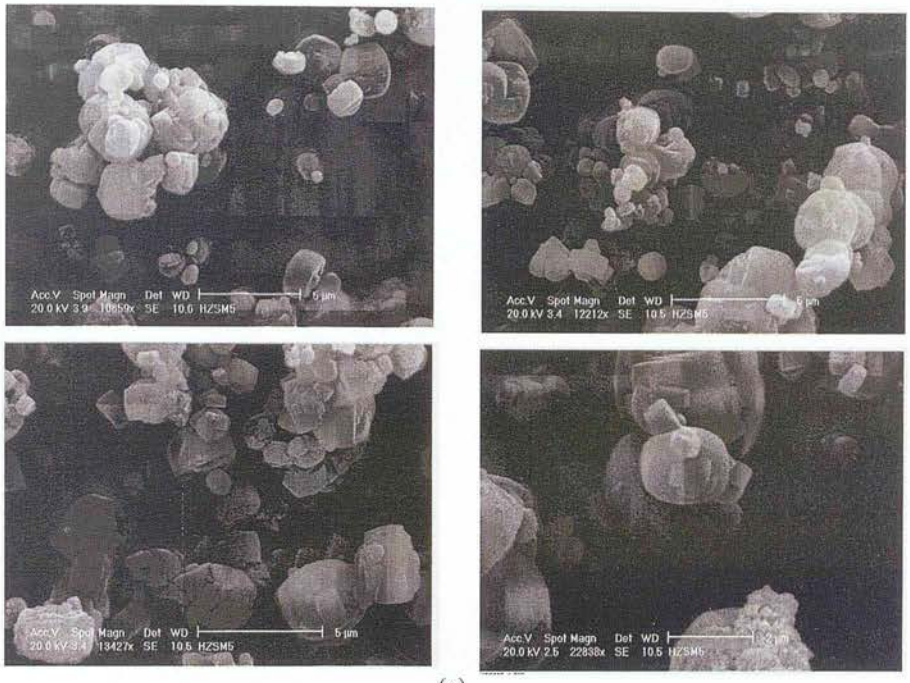

(a)

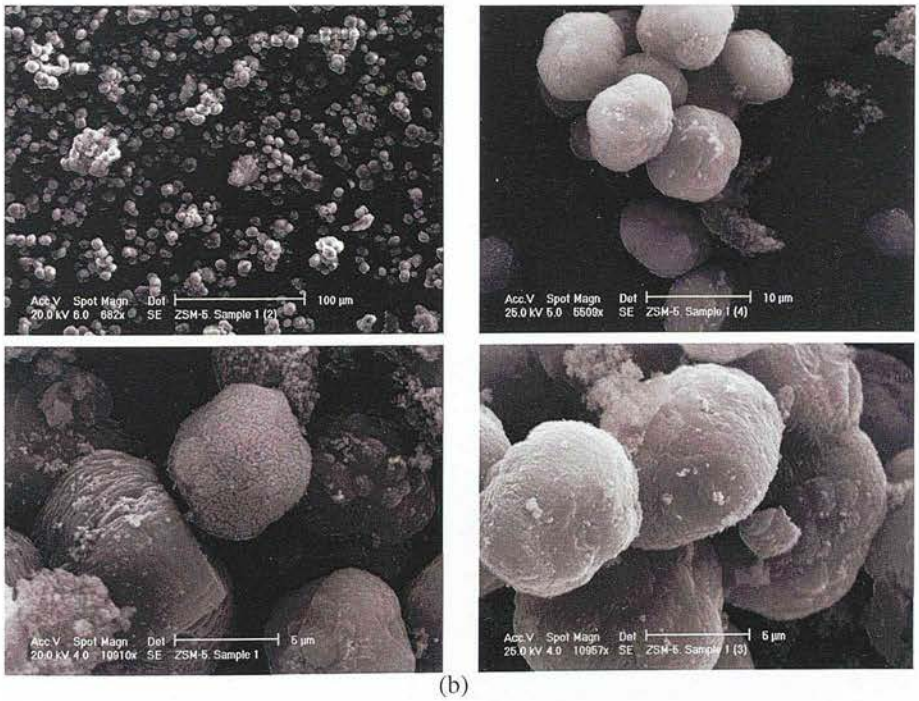

(b)

Figure 4.4: Micrographs of ZSM-5 samples produced under conventional heating. (a) commercial HZSM-5, (b) sample calcined for 5 h at 773 K from a fresh gel. For each sample, micrographs are shown at increasing magnification.

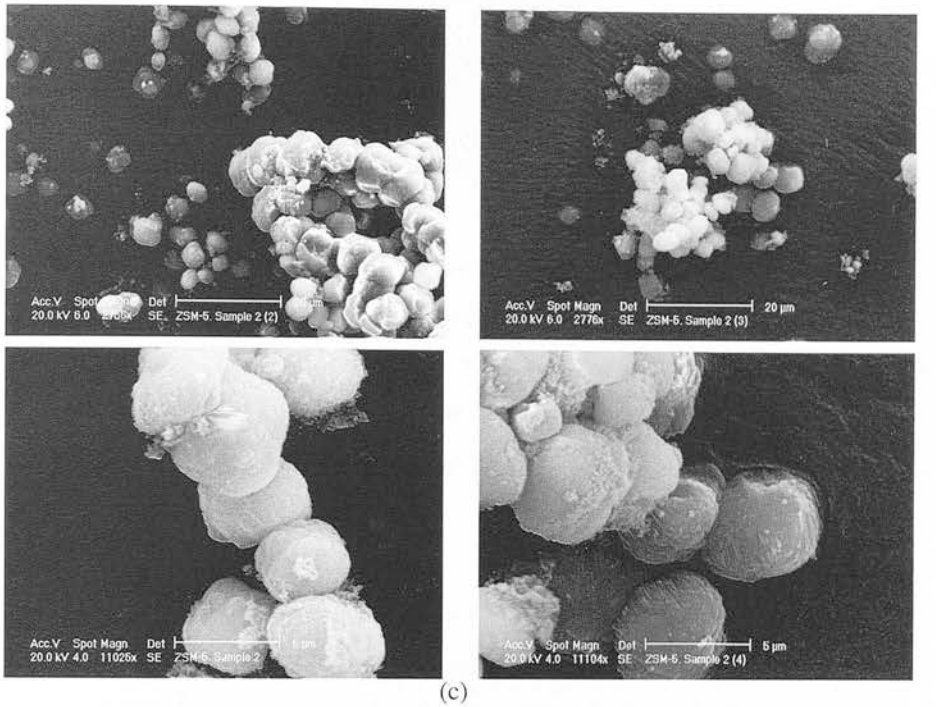

(c)

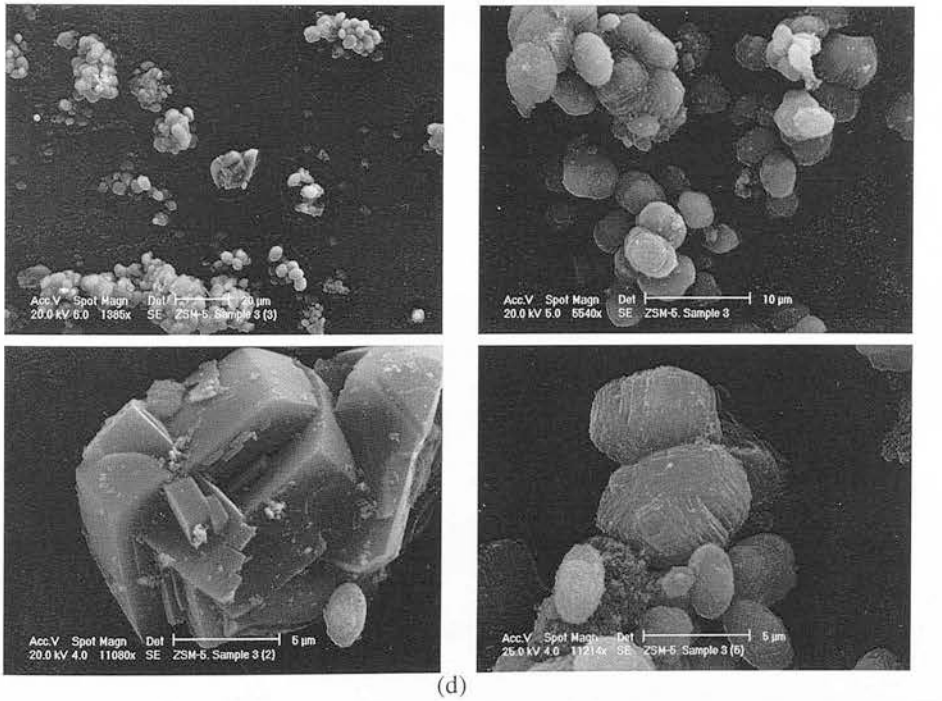

(d)

Figure 4.4: (Cont). Micrographs of ZSM-5 samples produced under conventional heating. (c) sample prepared with a 7 days aged gel -as synthesised-, (d) sample prepared with a 10 days aged gel -as synthesised-. For each sample, micrographs are shown at increasing magnification.

4.5.2 Synthesis of ZSM-5 with microwave heating

The gel used for the microwave-heated experiments was prepared in the same way as for conventional heating. In order to compare the influence of variables such as temperature or time of crystallization, the same gel was used when possible.

Two kinds of single-mode cavity microwave devices were used for the syntheses - the CEM Explorer PLS™ and the CEM Discover™ System. In both cases, the system consists of a circular single-mode cavity with a circular homogeneous field pattern. The sample is loaded in a sealed glass test tube and placed in the centre of the cavity where it may be continuously irradiated with microwaves through several slots in the cavity wall. The temperature is measured through an infrared temperature sensor positioned below the test tube and a pressure transducer needle is inserted in the lid of the test tube. In some cases, reactions can be quenched by means of compressed gas while maximum power is applied (the so-called Max Power feature). Compressed gas is forced into the reaction cavity and as the gas expands, it cools the atmosphere inside the cavity. When this feature is used, the real temperature in the sample is not known as the temperatures inside the tube and outside are different. Figure 4.5(a), 4.5(b) and 4.5(c) show both types of apparatus used and a schematic diagram of the single mode cavity inside them.

(a) (b) (c)

Figure 4.5: CEM microwave devices. (a) Explorer PLS™ equipped with an automated reaction handling module with a multiple sample deck, (b) Discover™ for individual samples, and (c) schematic drawing of the single-mode cavity, viewed from above.

The first attempts to synthesis ZSM-5 under microwave irradiation aimed to establish

the temperature and time required for zeolite crystallisation. In all cases, the product obtained after the samples were exposed to microwave radiation were filtered, washed several times with deionised water and dried at 393 K for 3h.

In the first attempt to synthesise ZSM-5 using microwave radiation, a sample of fresh gel was heated to 423 K for 2h using 70 W of power, as a means of comparison with what was obtained in conventional heating. The X-ray diffraction pattern of this sample (figure 4.6(b)) showed that under these conditions just amorphous material was obtained, and only when the gel is first allowed to age for several days (7 and 14 days) is the formation of small amounts of ZSM-5 seen (figure 4.6 (c) and (e)).

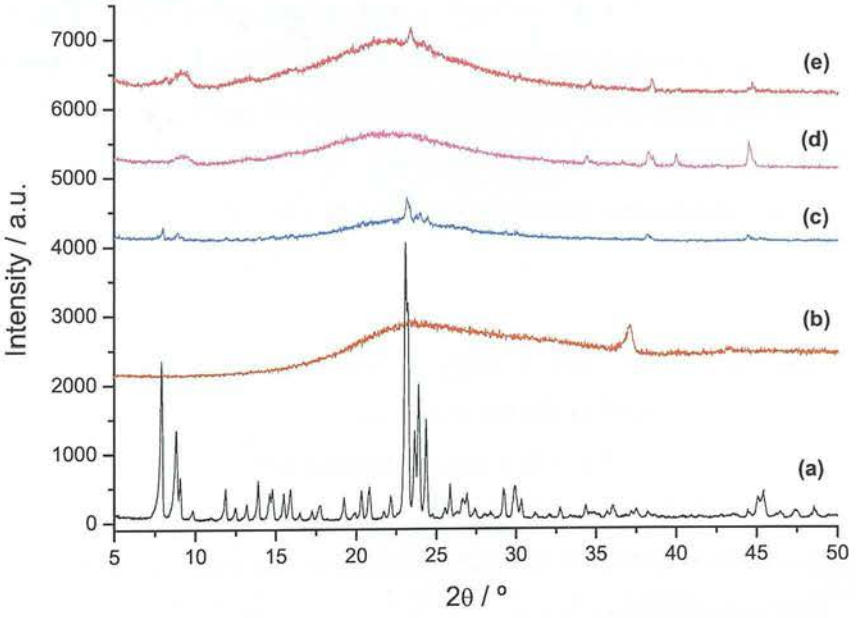

Figure 4.6: ZSM-5 synthesised under microwave heating at different conditions. (a) commercial HZSM-5, (b) sample prepared with fresh gel, heated at 423 K for 2 h, (c) sample prepared with a 7 days aged gel and heated at 423 K for 3 h, (d) sample prepared with a 7 days aged gel and heated at 433 K for 1 min plus 30 min at 413 K, (e) sample prepared with a 14 aged gel heated at 423 K for 3 h.

It has been reported[93] that ZSM-5 is obtained under microwave irradiation using a

temperature profile such that the sample is heated at high temperature (433 K for 1 min) in a short period of time then changed to the reaction temperature (413 K for 30 min) where it was claimed that the crystallization process takes place. A sample using 7 days aged gel was synthesised using these conditions but no crystalline material was obtained either (see figure 4.6(d)). A possible explanation is that the temperature observed was not the actual temperature in the sample but possibly sufficiently different to the set, control temperature. The IR thermometer which takes the control readings is placed near the bottom of the test tube, and does not necessarily reflect the mean, bulk temperature well. To investigate whether this particular synthesis failed because of such variations in the temperature, three samples of a 14 days aged gel were heated with microwave radiation under the following conditions: one sample was heated at 423 K for 3 h, a second sample was heated at 443 K for 3 h and, a the third sample was heated using the Max Power feature in the oven for 3 h with a set temperature of 443 K. The X-ray diffraction patterns of these samples are shown in figure 4.7 where it can be observed that ZSM-5 was successfully crystallised at 443 K for 3 h with or without the Max Power feature switched on, but as observed before the sample at 423 K was not crystalline, implying that this last synthesis actually ran cooler than the synthesis reported in the literature at 413 K[93].

The analysis of the samples with SEM (figures 4.8(a) - 4.8(b)) revealed that cube-shaped and sphere-shape agglomerates, characteristic of ZSM-5 zeolite were obtained but no crystals were seen in the sample prepared at 423 K (figure 4.8(c)) despite previous work in the literature[93]. Even for the sample prepared at 443 K with the Max Power feature applied, some amorphous material was still observed in the micrographs.

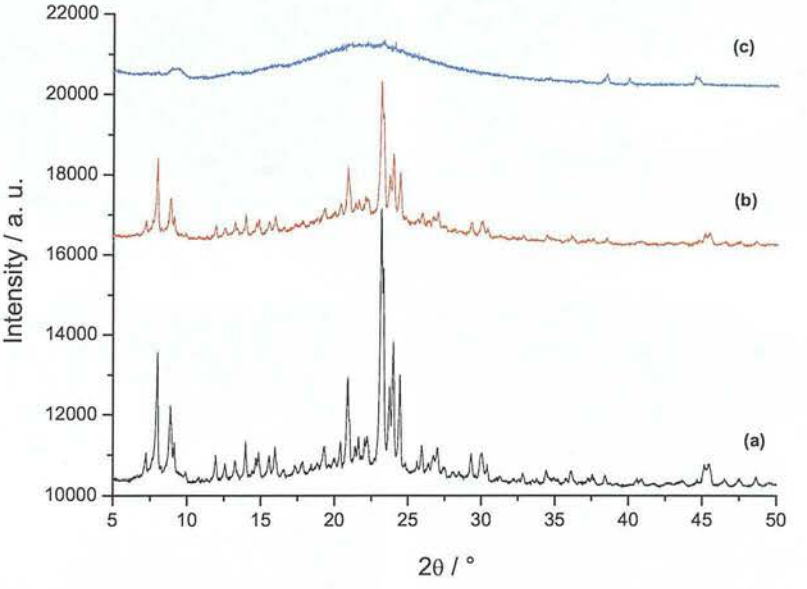

Figure 4.7: X-ray diffraction patterns for samples synthesised under microwave heating for 3 h. (a) 443 K, (b) 443 K with the Max Power feature enabled, and (c) 423 K.

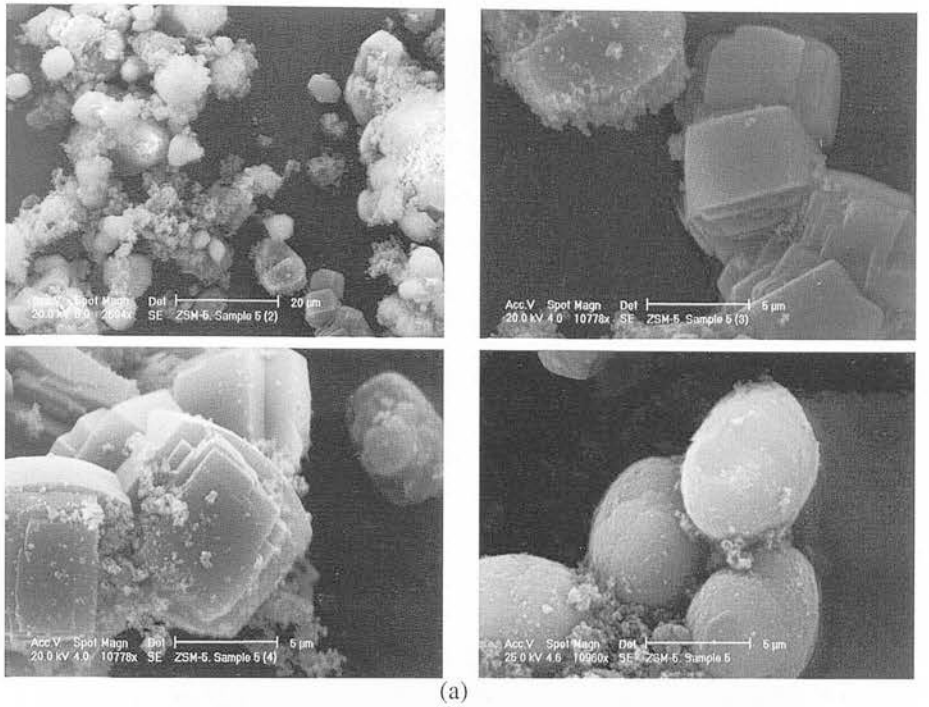

(a)

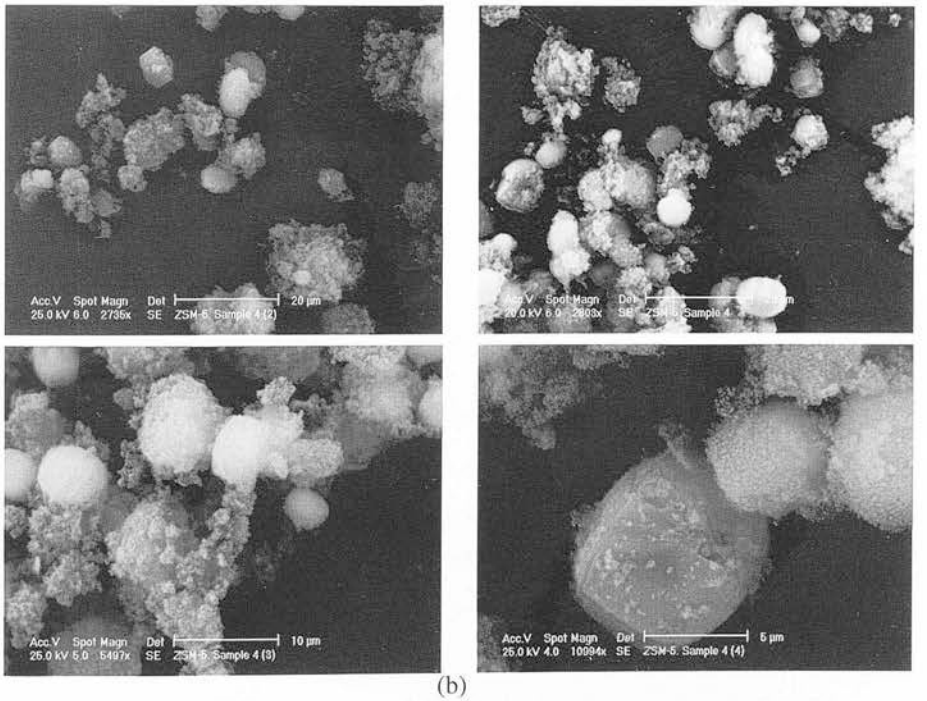

(b)

Figure 4.8: Micrographs of ZSM-5 prepared from a 14 days aged gel using microwave radiation. (a) Sample synthesised at 443 K for 3 h, (b) sample synthesised using the Max Power feature for 3 h. For each sample, micrographs are shown at increasing magnification.

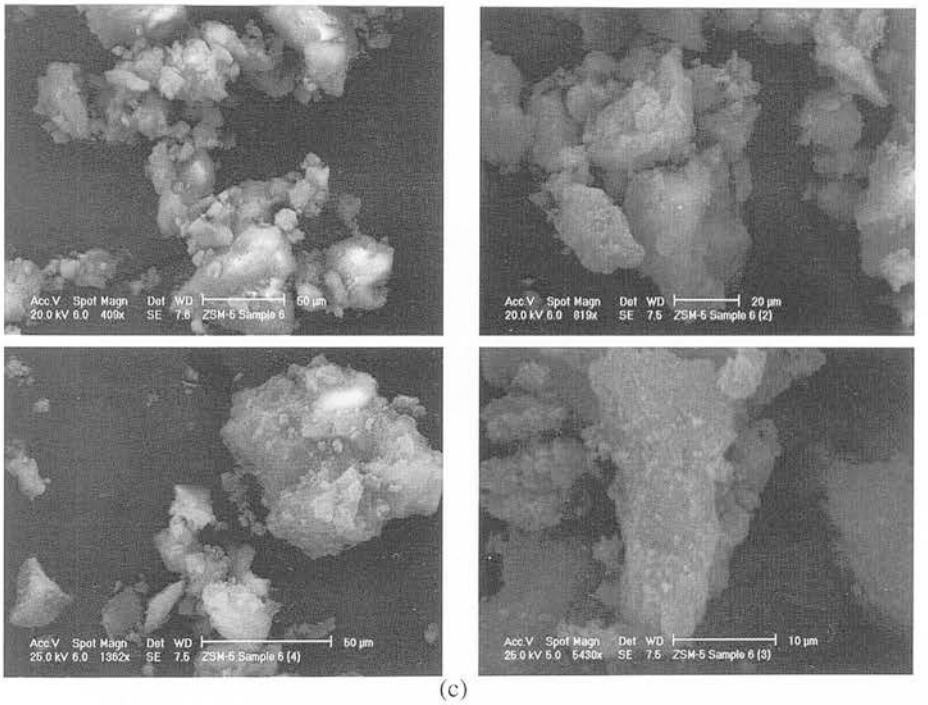

(c)

Figure 4.8: (Cont). Micrographs of ZSM-5 prepared from a 14 days aged gel using microwave radiation. (c) sample synthesised at 423 K for 3 h. For each sample, micrographs are shown at increasing magnification.

Having established that crystalline ZSM-5 could be synthesised under microwave irradiation at 443 K, a new series of samples was prepared at this temperature at different reaction times in order to understand how this factor affects the final product. Four samples from the same aged gel were used to study synthesis with the following reaction times: 20 min, 30 min, 2 and 3 hours. The X-ray diffraction patterns showed that reaction time can be reduced from 3 to 2 hours while retaining high crystallinity (figure 4.9) and this can also be observed in the electron micrographs taken for this sample (figure 4.10(c)). In the other cases, samples prepared with 20 or 30 minutes of irradiation showed no or little crystallinity (figures 4.10(a) and 4.10(b)). Pictures showing the now characteristic spherical agglomerates for the sample prepared at 3 hours are shown in figure 4.10(d).

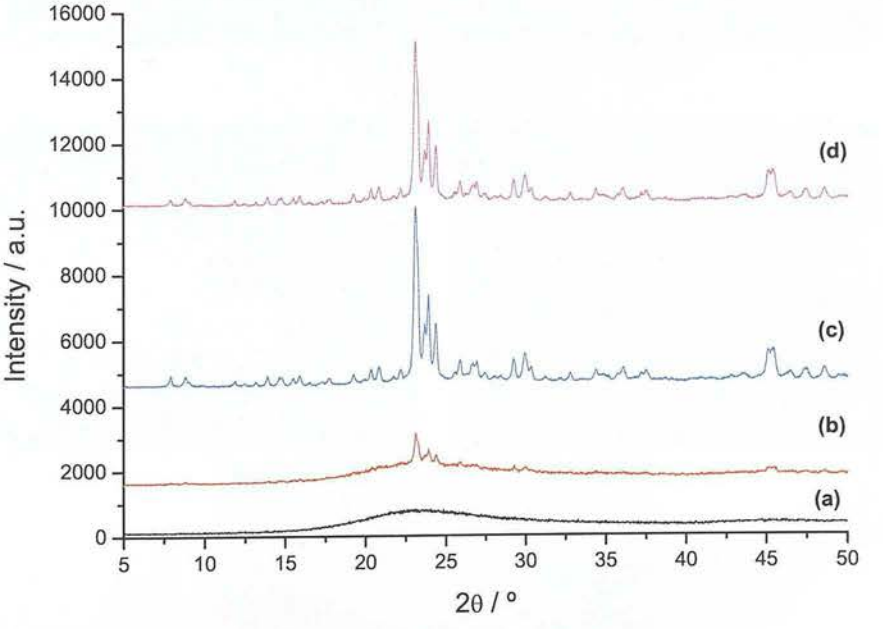

Figure 4.9: X-ray diffraction patterns for ZSM-5 under microwave radiation at different reaction times. (a) 20 min, (b) 30 min, (c) 2 h, and (d) 3 h.

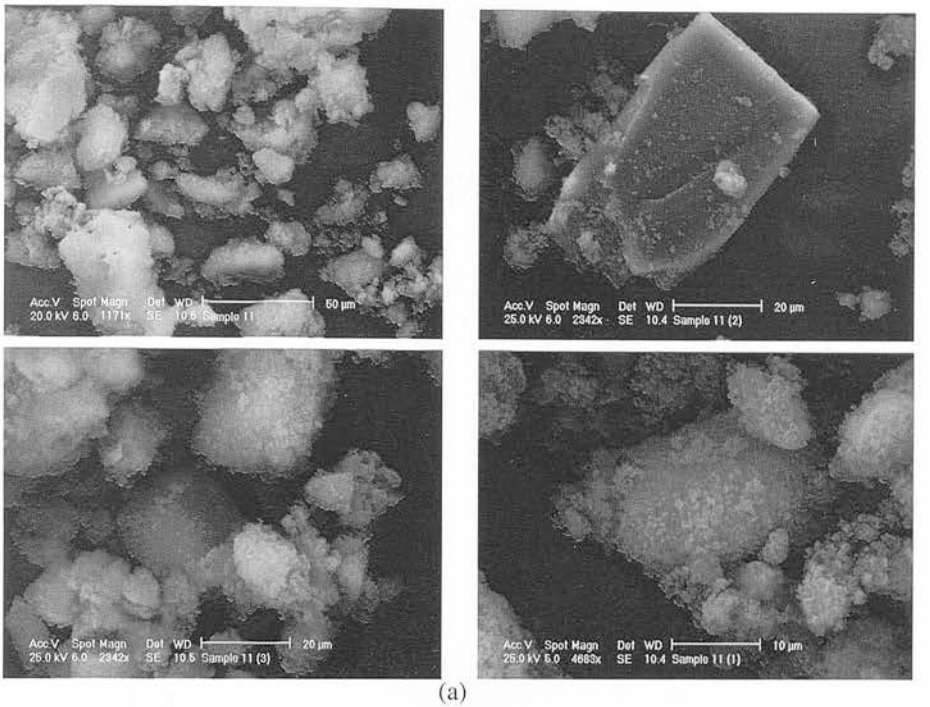

(a)

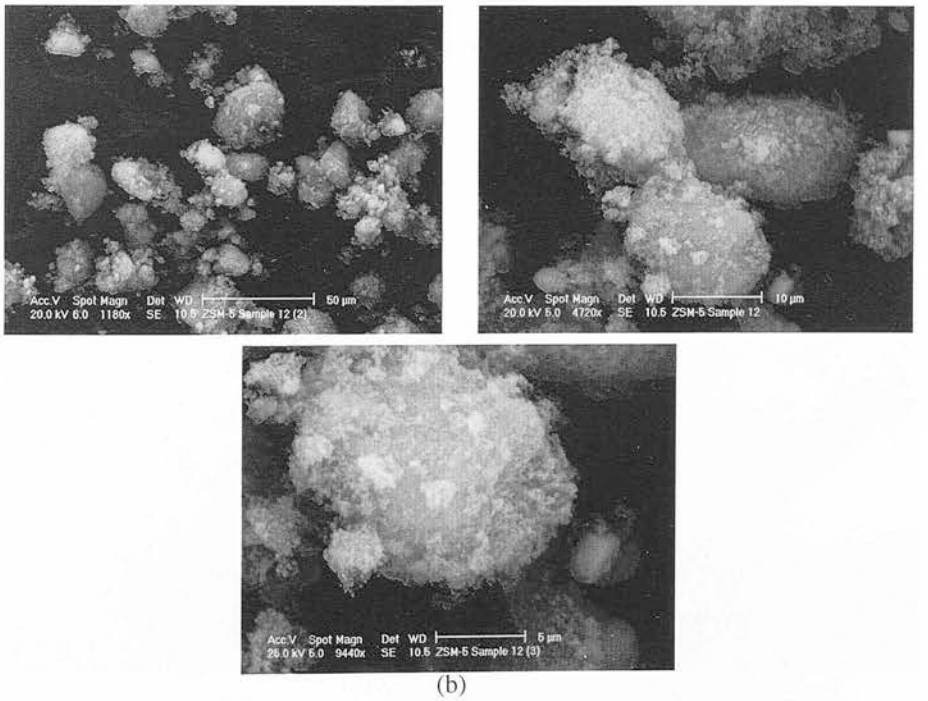

(b)

Figure 4.10: Micrographs of ZSM-5 prepared at 443 K from a 14 days aged gel using different lengths of microwave irradiation time. (a) Sample synthesised in 20 min, (b) sample synthesised in 30 min. For each sample, micrographs are shown at increasing magnification.

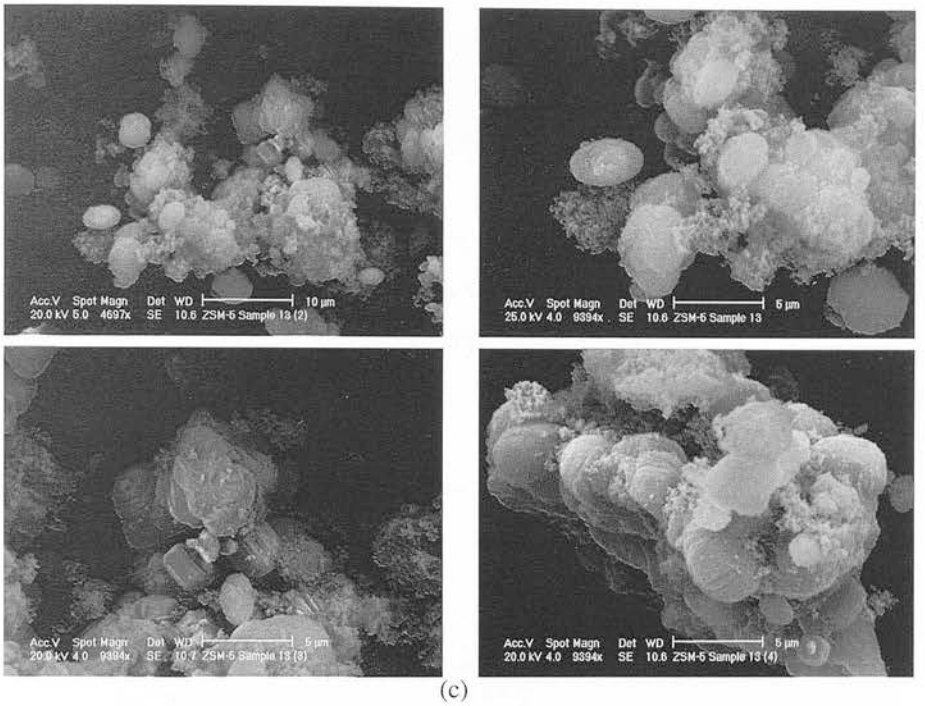

(c)

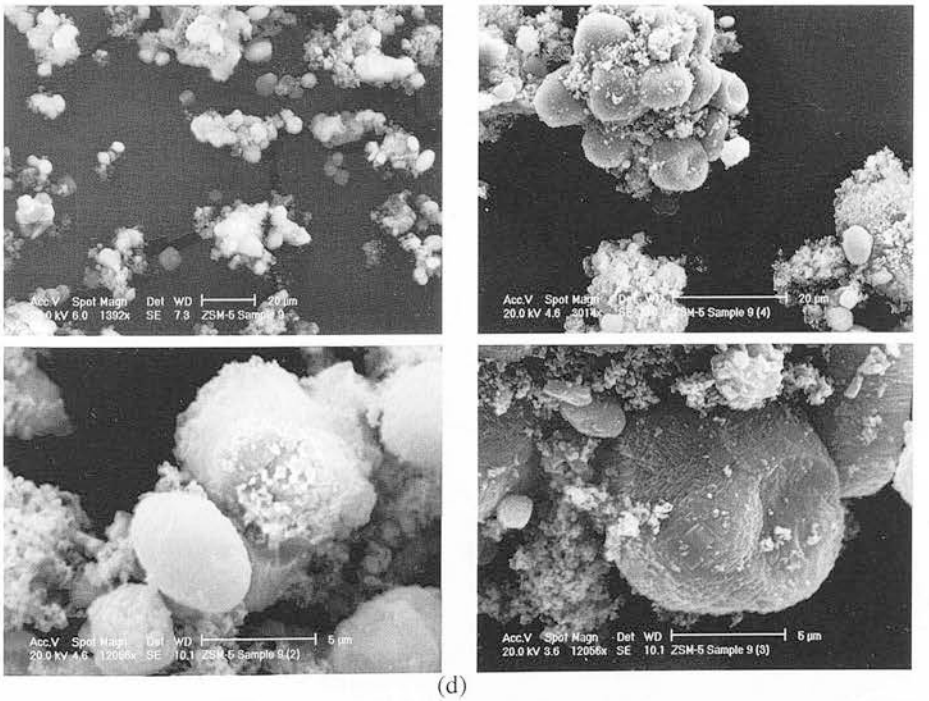

(d)

Figure 4.10: (Cont). Micrographs of ZSM-5 prepared at 443 K from a 3 days aged gel using different lengths of microwave irradiation time. (c) sample synthesised in 2h and (d) sample synthesised in 3h. For each sample, micrographs are shown at increasing magnification.

It has been claimed that the template can degrade during microwave radiation[93], so we also explored this idea by heating several samples of the same gel at different temperatures for 3 hours, from 423 K up to a maximum temperature of 458 K where no crystallization was expected to occur due to the degradation of the template.

Surprisingly, highly crystalline ZSM-5 was produced at 458 K as illustrated in the X-ray diffraction patterns (figure 4.11) and in the electron micrographs (figure 4.12) with well defined cube-shaped agglomerated crystals characteristic of this form of ZSM-5. No appreciable amorphous material was observed for this sample. The sample prepared at 443 K with this gel again gave highly crystalline ZSM-5, as observed before. The micrographs for samples prepared at 423 and 433 K, where it was observed that the crystallization process was not complete, are presented in the figures 4.13(a) and 4.13(b) respectively. In both cases, mainly amorphous material was observed.

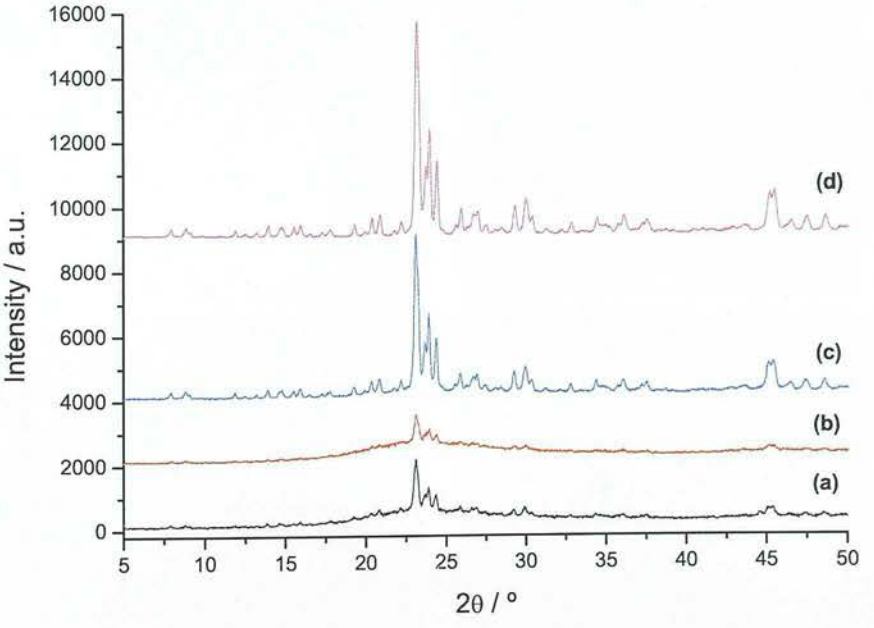

Figure 4.11: X-ray diffraction patterns for ZSM-5 synthesised under microwave radiation at different reaction temperatures. (a) 423 K, (b) 433 K, (c) 443 K, and (d) 458 K.

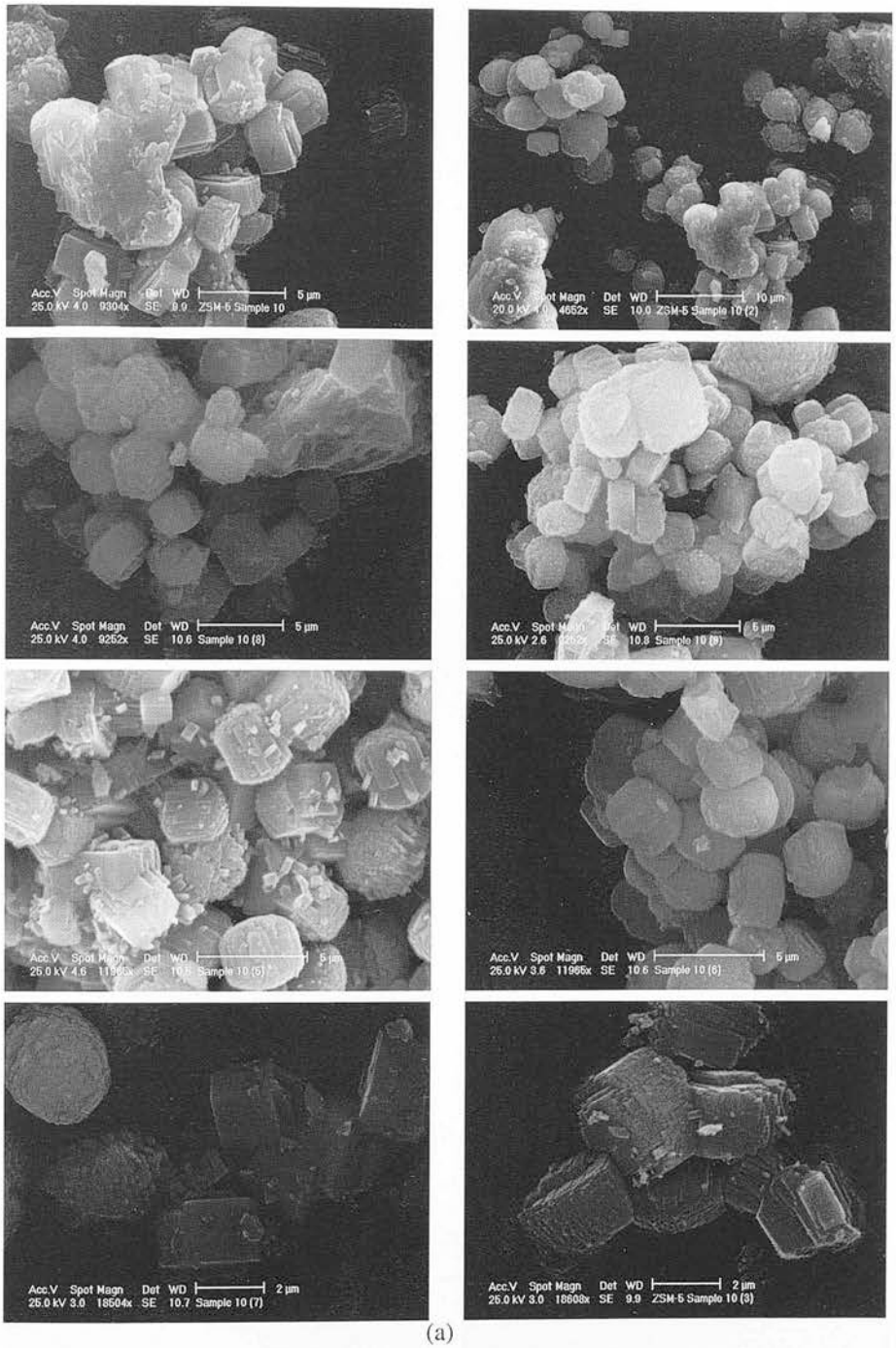

(a)

Figure 4.12: Micrographs of ZSM-5 prepared with a 14 days aged gel using microwave radiation for 3 h and different reaction temperatures. (a) Sample synthesised at 458 K. For each sample, micrographs are shown at increasing magnification.

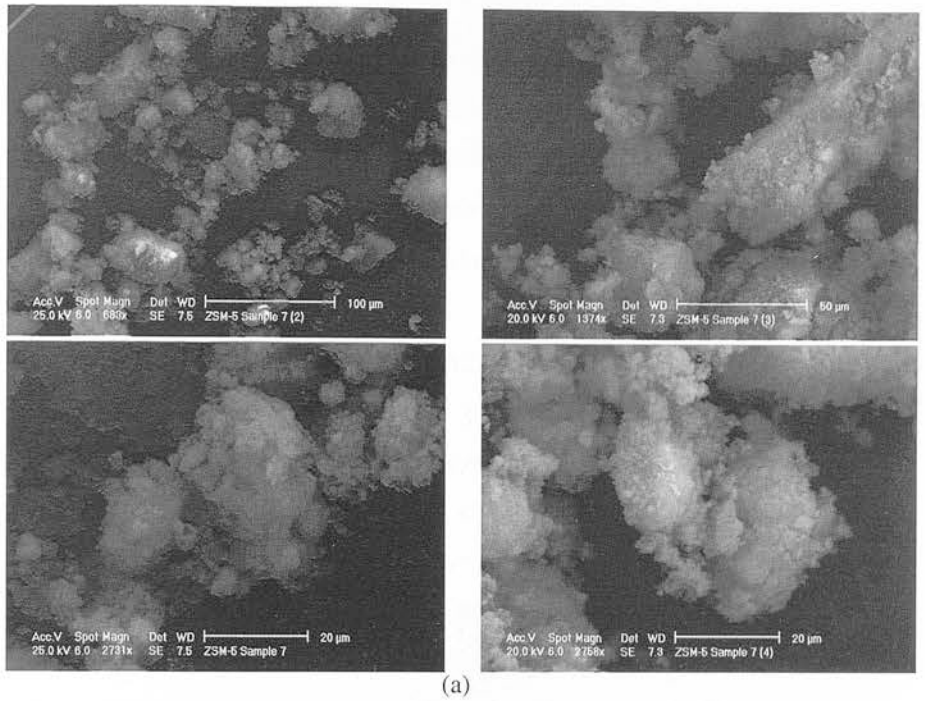

(a)

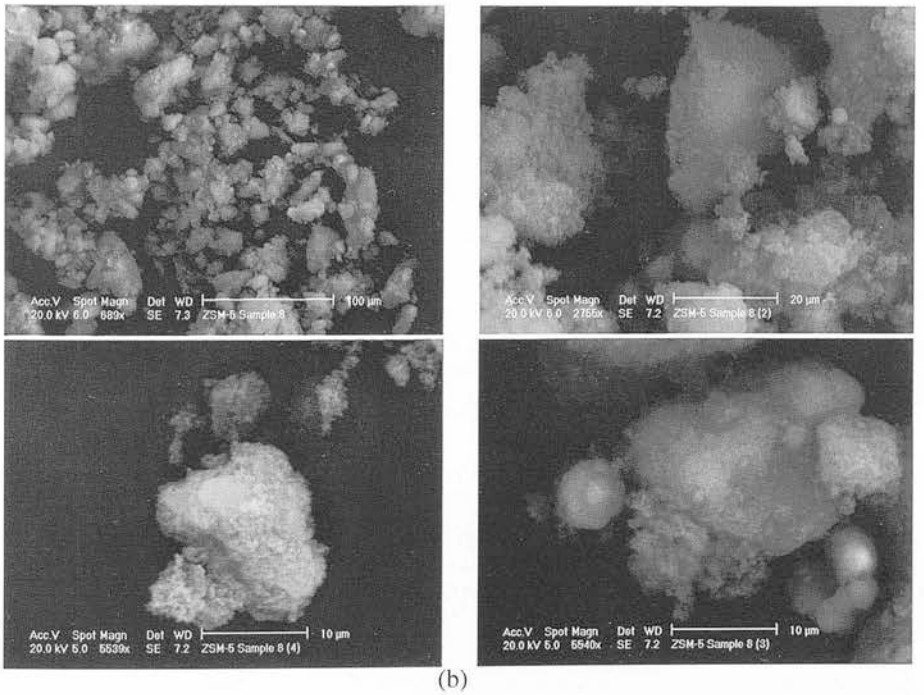

(b)

Figure 4.13: Micrographs of ZSM-5 samples synthesised using a 3 days aged gel and heated to (a) 423 and (b) 433 K for 3h with microwave radiation. For each sample, micrographs are shown at increasing magnification.

A new sample was prepared from a new gel and a new silica source (fumed silica, Aldrich, 200 m^2g^{-1}) and the same results were found for the higher temperature (458 K) and time (3h) which confirms that no template degradation takes place at this temperature assuming that the temperature observed represents the 'real' temperature in the sample. The reproducibility of the synthesis of ZSM-5 was also probed. As observed in the X-ray diffraction patterns shown in figure 4.14 and the micrographs in figure 4.15 the two samples produced similar crystalline materials.

Our attempts to synthesis ZSM-5 reproducibly and along similar lines to those reported in the literature met with mixed results. In general, we found that we needed a slightly higher temperature to achieve a similar degree of crystallinity, and this, together with a lack of evidence for template degradation at higher set temperatures suggests that the set temperatures for the instruments we used were lower than at least some of those reported in the literature. This underlines not only the sensitivity of this class of synthesis towards relatively small changes in reaction conditions, but also the challenges in reliable measurement of temperature during microwave synthesis.

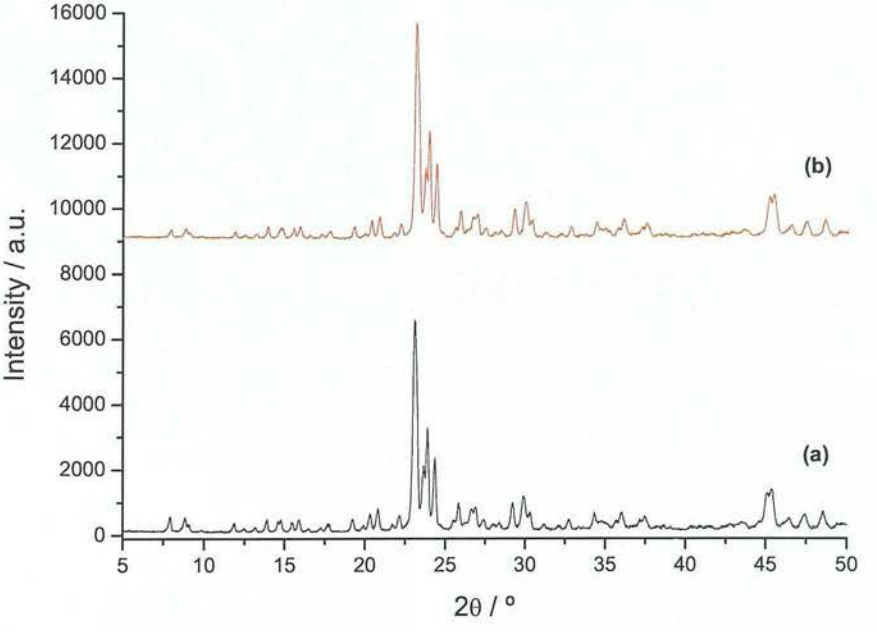

Figure 4.14: X-ray diffraction patterns showing reproducibility of samples of ZSM-5 prepared under the same conditions: 459 K for 3 hr with microwave irradiation. (a) Gel prepared using Aerosil and (b) gel prepared using fumed silica, Aldrich.

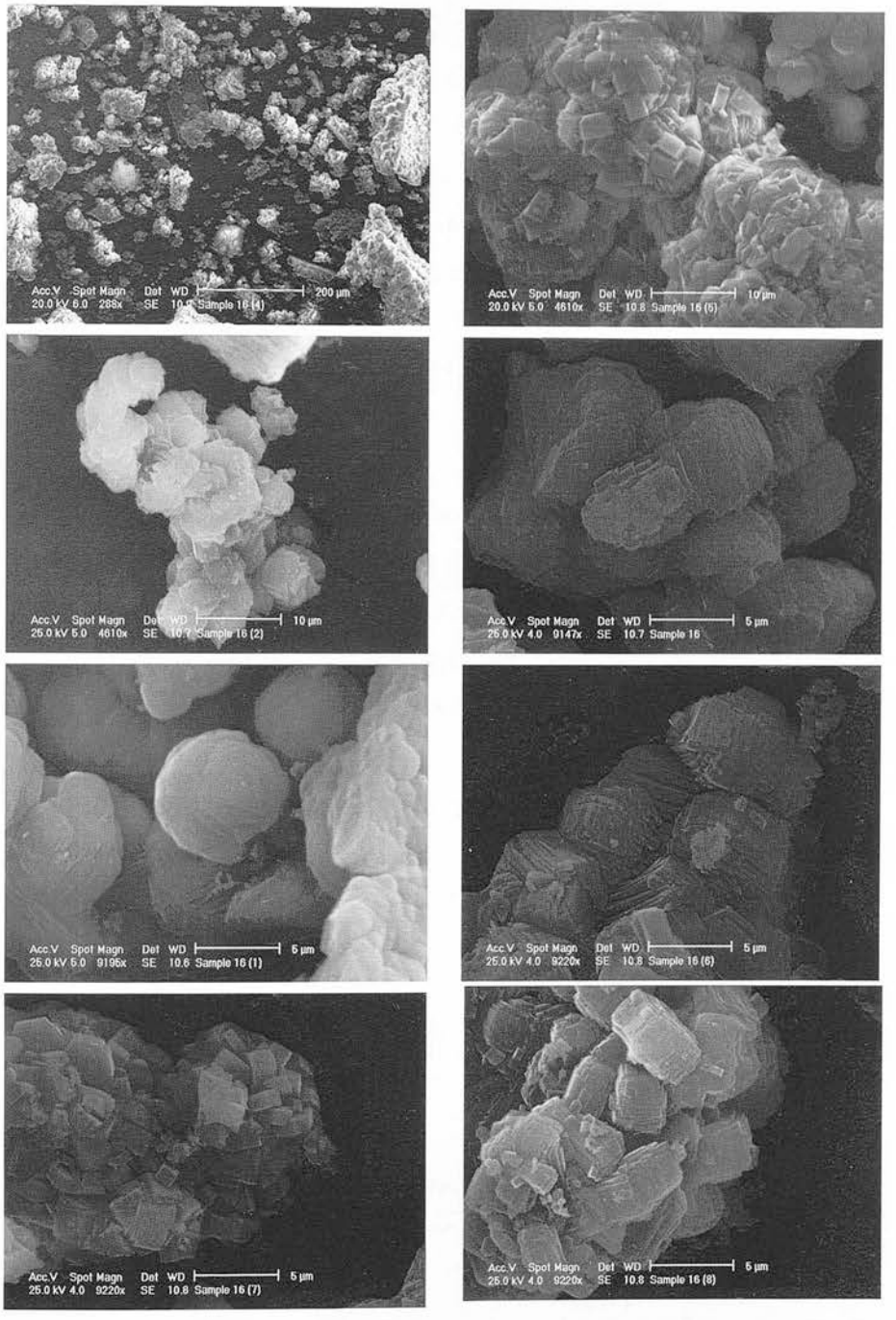

Figure 4.15: Micrographs of ZSM-5 synthesised from a a new silica source using microwave radiation at 458 K for 3h. For each sample, micrographs are shown at increasing magnification.

4.5.3 Solid-state ion-exchange under microwave irradiation

Previous work on microwave-driven insertion of copper ions from $CuCl_2\ 2H_2O$ into ZSM-5 used X-ray diffraction to monitor the $CuCl_2\ 2H_2O$ remaining after processing[107]. However, we suspected that the copper salt could heat and decompose in the microwave field on its own, and that the less hydrated product might not diffract as well or at all. This could account for some of the loss of the copper salt attributed in some of the work in the literature to insertion into the host. To explore this possibility further, more measurements were taken with greater care to observe the heated products, and control the extent to which they might be dehydrated. The preparation of the samples for this particular part of the project and the diffraction measurements were performed by a project student, Rachel Lees, using apparatus developed by F. M. Pina-Sandoval.

$CuCl_2\ 2H_2O$ (Sigma, 99.0%) was first heated on its own to 373 and 403 K using microwave radiation and a powder X-ray diffraction pattern taken (figure 4.16). The sample was then left overnight (14 hrs) in air and the diffraction pattern taken again. This indicates that the hydrated salt is dehydrated to produce a crystalline product, and this is largely converted back to the original hydrate on exposure to air. The most intense peaks of the hydrate, at 16.7° and 33.2°, were reduced in intensity by 50% and 90% respectively after this cycle of treatment.

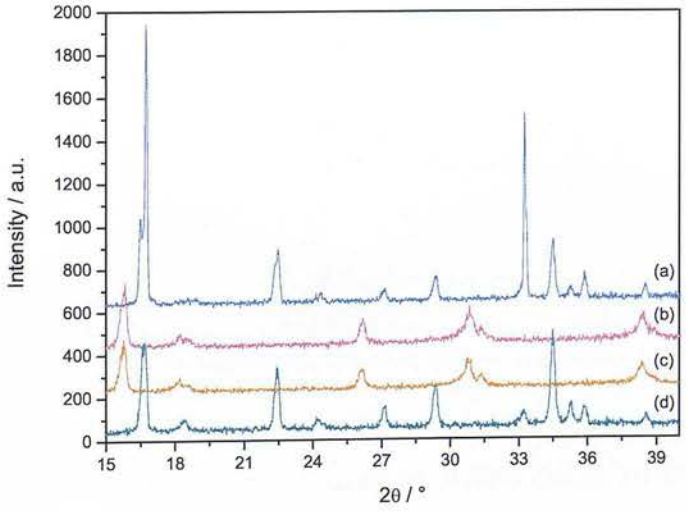

Figure 4.16: X-ray diffraction patterns of $CuCl_2\ 2H_2O$ salt. (a) before irradiation, (b) after microwave heating to 373 K, (c) after microwave heating to 403 K and (d) after overnight rehydration.

Samples of ZSM-5 (Laporte Inorganics) and $CuCl_2\ 2H_2O$ (at loadings of 10, 32 and 50%) were then mixed mechanically, with a mortar and pestle for around 20 min, and their structure investigated using the microwave rectangular applicator shown in figure 3.3 in Chapter 3. The samples were heated to 403 K at 250 W for 1 hour with XRD patterns taken before, during and 12 hours after, microwave heating to allow some degree of rehydration of the copper salt during exposure to the atmosphere.

For loadings of 10 and 32% of $CuCl_2\ 2H_2O$, there were no $CuCl_2\ 2H_2O$ peaks observed in the XRD pattern after both microwave heating and rehydration, suggesting that the salt had been thoroughly dispersed across the surface of ZSM-5 and within its channels (see figures C.1 and C.2 in Appendix C). There are also no changes in the peaks relating to ZSM-5 showing that microwave heating does not effect the crystallinity with heating at 250 W for 1 hour.

For 50% $CuCl_2\ 2H_2O$ loading, there is no trace of $CuCl_2\ 2H_2O$ in the diffraction pattern immediately after exposure to the microwave radiation, but some of it is recovered after overnight exposure to air; a comparison of the intensity of characteristice peaks suggests that the remaining intensity is of the order of 30% of the original (figure 4.17). The difference between this and the amount used in the initial mixture corresponds to the maximum loading of $CuCl_2\ 2H_2O$, which can be dispersed by microwave heating as determined by Xiao *et al*[107]

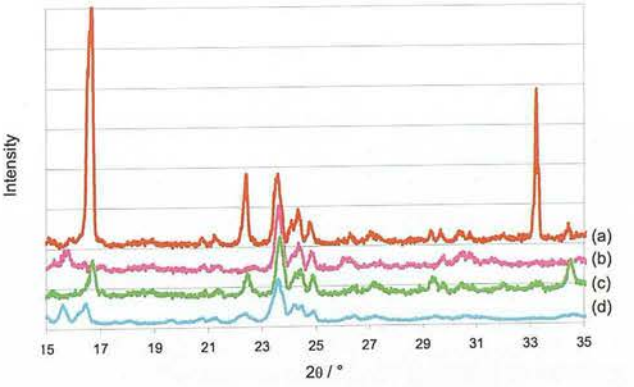

Figure 4.17: *In situ* X-ray diffraction patterns of 50% $CuCl_2\ 2H_2O$-ZSM-5 before and after microwave heating. (a) before processing, (b) after microwave irradiation to 403 K, (c) after further exposure to air overnight, (d) after heating conventionally at 473 K for 1 hour.

The change in the X-ray diffraction pattern of $CuCl_2$ when heated undermines the reliability of using XRD as a method to determine the degree of $CuCl_2$ $2H_2O$ dispersion in ZSM-5 and other zeolites. Therefore, alternative methods were tested to probe the degree of copper uptake in this last set of experiments with the ZSM-5 host. X-ray photoelectron spectroscopy (an MXRI electrostatic electron gun with Al Kα X-rays) failed to detect any signal that could be attributed to copper. However, the measurement of the magnetic susceptibility using a SQUID Magnetometer (Quantum Design, MPMS2), did show a significant magnetic response and in the absence of any other candidate with a paramagnetic response, this was attributed to Cu^{2+}. It is assumed that the response per Cu^{2+} ion is approximately 1.73 Bohr magnetons, which provides a good approximation for Cu^{2+} ions in many magnetic materials[110], then we can estimate the concentration of Cu^{2+} in the ZSM-5. Prior to measurement, samples were washed thoroughly in deionised water to try to remove any copper salt that might have adhered to the surface. Figure 4.18 shows the concentration of copper moles per unit mass of zeolite with microwave heating up to 1 hour (data recorded is shown in table C.1 in Appendix C).

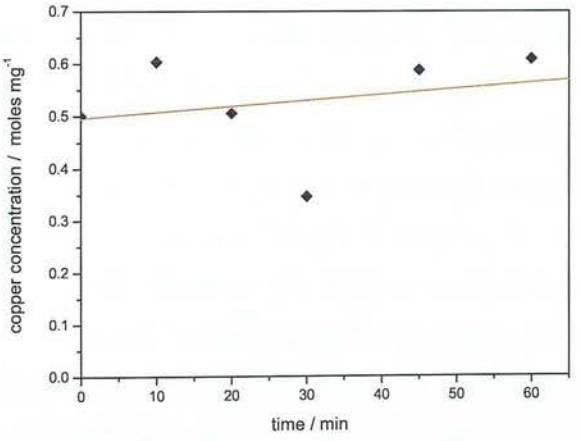

Figure 4.18: Concentration of Cu^{2+} ions in ZSM-5 after microwave heating from SQUID magnetometry measurements.

There is very little increase in the degree of copper loading as heating time is increased. It is possible that the copper migration may not have occurred fully throughout the sample with the majority of copper situated on the surface or within the channels close to the surface of the zeolite, which would therefore have been removed through the washing process. This could be a result of the external pores being blocked, or pore migration of the copper ions in solid state in 1 hour.

4.6 Conclusion

We have established a set of conditions under which ZSM-5 may be grown efficiently and reproducibly under microwave irradiation, in some cases offering significant advantages over conventional methods. Microwave irradiation for 3 hours at 458 K yielded a product comprising only cube-shaped crystals with a crystallinity comparable to that of a commercial sample prepared with conventional heating, as for samples reported in the literature for microwave irradiation[93,111,112,92]. However, there is an important difference, and that is that the temperatures we found necessary to achieve a particular yield or degree of crystallinity were significantly higher than other workers report for microwave synthesis, and this could reflect an error in the way in which the temperature of the bulk sample is determined in the commercial apparatus we used. Such a difference is also consistent with our failure to find any evidence for template degradation at 458 K, at variance with reports in the literature[93].

The next stage in such work would be to study the progress of the various stages of this reaction by *in situ* diffraction to reveal crystalline intermediates and study the kinetics for their formation or destruction. We have not explored the technical solution to this in any detail, but anticipate that it will be beyond the scope of current angular-dispersive laboratory-based diffractometers; instead, it is likely that the problem would require the brightness of a synchrotron source, or perhaps a laboratory-based energy-dispersive diffractometer. In either case, though would also have to be given to a suitable material or materials for containment at the elevated temperatures and pressures involved, and also to determination of the temperature *in situ*. This last parameter may be determined with a flouroptic probe, particularly if a method could be found to seal it into the capillary robustly and reversibly, perhaps using similar technology to that used in high-pressure liquid chromatography.

We have also performed an initial exploration of insertion of copper ions from $CuCl_2$ $2H_2O$ into ZSM-5 under microwave heating and looked critically at the application of powder X-ray diffraction to track this process through a reduction of the diffraction pattern of the copper salt. A problem was identified in this method, arising from the fact that microwave irradiation can dehydrate the salt, and it is only after samples have been allowed to rehydrate that a good comparison should be made with starting material to assess uptake. An alternative method of analysis was identified in the form

of SQUID magnetometry on well-washed samples. This provides a measure of the amount of paramagnetism in the sample, and as this can be reliably related to the concentration of Cl^{2+} ions, it provides a good measure of uptake of the salt.

Chapter 5

Phase transitions in ferroelectric materials during microwave radiation

5.1 Introduction

There are indications that microwave heating can influence the structure or microstructure of materials with significant dielectric susceptibility. Preliminary powder neutron diffraction measurements on $BaTiO_3$ indicate that during microwave heating, its cell parameters are anomalously high, while its ADPs are anomalously low compared to a conventionally heated sample when using a fluoroptic probe to monitor the average temperature[69]. Either observation taken separately might indicate a systematic error with the method of measuring temperature, but are difficult to explain in terms of equilibrium, thermodynamic properties when taken together. There was also some indication that a characteristic phase transition, from a tetragonal ferroelectric phase, to a cubic paraelectric phase, took place at a slightly lower temperature than is usual. Similar measurements on $KNbO_3$ indicate that under microwave irradiation, a significant fraction of the sample appears hotter than the average - again taken with a fluoroptic probe - based on the observation that some of sample adopts the structure of a relatively high temperature phase[113].

In order to explore both systems further, and also to test the performance of the *in situ* diffraction-microwave equipment, we proposed to conduct measurements both on an in-house powder X-ray diffractometer, a Philips PW1730 X-ray diffractometer, and on HRPD at the ISIS Facility at the Rutherford Appleton Laboratories. In both cases the microwave rectangular waveguide system described in Chapter 3 was used with

the modifications described therein to adapt to the different geometries of the two instruments. The X-ray measurements were of lower resolution, but had the advantage of ready access to the instrument, while we measured only $KNbO_3$ on the HRPD because of limited access. First we outline the phenomenon of ferroelectricity because both the high dielectric response of $BaTiO_3$ and $KNbO_3$ is related to their behaviour as ferroelectric materials over a range of temperatures.

5.1.1 Ferroelectrics

Ferroelectricity is a physical phenomenon in which a spontaneous electric dipole moment can be reoriented from one crystallographic direction to another by an applied electric field. Such reorientation processes will involve two or more domain states within the crystal or within the individual grains in a ceramic. At high temperatures such materials have no spontaneous electric polarisation and are said to be *paraelectric*. On cooling through the phase transition to the ferroelectric state, the symmetry is lowered and polar domain patterns are observed[114]. In the critical region and below there is commonly a complex interplay between the electrical, mechanical and thermal properties of the material, sometimes with a history dependence arising from strains that develop during heating and cooling cycles. The main uses of these kind of materials are as ceramic capacitors and piezoelectric transducers for sonar systems.

Ferroelectric materials often have a perovskite structure, with general formula ABO_3, where A is a monovalent or divalent metal and B is a tetra or pentavalent metal. Their structure can be regarded either as a cube with the A atoms at the corners, the B atoms at the centre and the O atoms at the face centres or, as a cubic array of BO_6 octahedra linked by shared oxygens with the A atoms occupying the spaces between. These compounds readily undergo structural transitions which involve non-polar phonons (associated with the tilting of the oxygen octahedra) as well as ferroelectric and antiferroelectric transitions[115]. In the cubic phase, small displacements of the cations towards the anions also lead to polarisation.

The ferroelectric behaviour it is thought to arise from either of the following:

- Displacive motion near the phase transition which is characterised by zone-centre vibrational modes or 'soft modes'[116].

- An order-disorder transition described by the 'eight-site' model in which the cubic phase experiences random distortions along eight cube diagonals [111], leading to various lower-symmetry phases; the tetragonal phase consist of displacements along four cube diagonals giving an average structure with a polarisation along [100]; the orthorhombic phase has two 'sites' occupied and a polarisation along [110]; the rhombohedral phase involves order along [111][117].

The materials used in this work, $BaTiO_3$ and $KNbO_3$, undergo four crystal structure changes, from cubic → tetragonal → orthorhombic → rhombohedral as they are cooled down. For $BaTiO_3$ the phase transition studied was the tetragonal to cubic transition which occurs at around 393 K[118] while for $KNbO_3$ the orthorhombic to tetragonal phase transition was studied, and this occurs near 498 K[119,120,121].

5.2 Experimental procedure and results

5.2.1 *In situ* X-ray diffraction: $BaTiO_3$

A small sample of barium titanate ($BaTiO_3$, Alfa Aesar, 99.99%) was loaded in the ceramic sample holder (Macor™) and mounted on the ceramic spindle. The fibre optic sensor was then attached to the spindle through a small hole, fixed to the spindle with Teflon™ tape and the tip placed in close contact with the sample. The rectangular microwave applicator was then put in place and attached to the microwave generator as shown in figure 3.4(a) in Chapter 3. The sample was then heated up to 423 K - beyond the phase transition to the cubic phase - and kept at this temperature for six hours. During this time a diffraction pattern was taken at low scan speed (8 steps/sec) to assure good quality of data for structure refinement. A diffraction pattern of the sample before heating (at approximately 295 K) was also taken for comparison. Figure 5.1 shows the diffraction patterns of the sample before and during microwave irradiation.

The two patterns collected were analysed by Rietveld refinement method using the General Structure Analysis System (GSAS) suite of programs[52]. The graphs generated from this process showing the quality of the refinement are shown in figures 5.2 (a) and (b). The data used for the starting model in the refinement was obtained from the Cambridge Structure Database (CDS)[122] for $BaTiO_3$ in its tetragonal and cubic forms. A relatively good fit ($\chi^2 \sim 2.794$ and 2.020 respectively) was obtained for both refinements. With the exception of a peak around 22°, which is thought to be due to

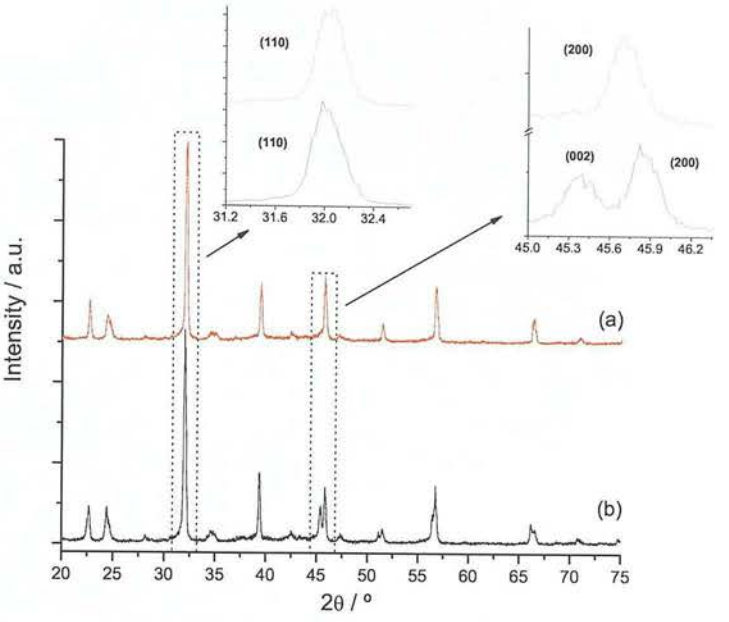

Figure 5.1: X-ray diffraction pattern of $BaTiO_3$ (a) before and (b) after microwave irradiation at 423 K for six hours. The insets show reflections for the cubic phase (in red) and reflections for the tetragonal phase (in black).

an impurity in the sample, it was concluded that the structures obtained were those for $BaTiO_3$ in its tetragonal and cubic phases respectively.

Once it was established that the material was receiving enough energy to undergo the phase transition, a series of experiments were carried out in the same fashion (each for 6 hours) from 295 to 423 K. Figure 5.3 shows the diffraction patterns obtained from these experiments. These indicate that the phase transition starts at 383 K (10 K lower than is reported in the literature[115]) where it was observed that the diffraction pattern differs from the one at room temperature (which is due to the tetragonal phase only). This was more clearly seen in the region from 43 to 48° (2θ) where one of the two reflections for the tetragonal phase decreased in intensity while the second reflection was slightly shifted to lower angles.

Despite the high quality of the data, Rietveld refinement for those diffraction patterns could not be carried out successfully for the two phases simultaneously. These is thought to be due to the high correlation between several parameters during the refinement, compounded by the fact that many reflections from both phases overlap. This difficulty is particularly acute when one phase is only present in a small proportion.

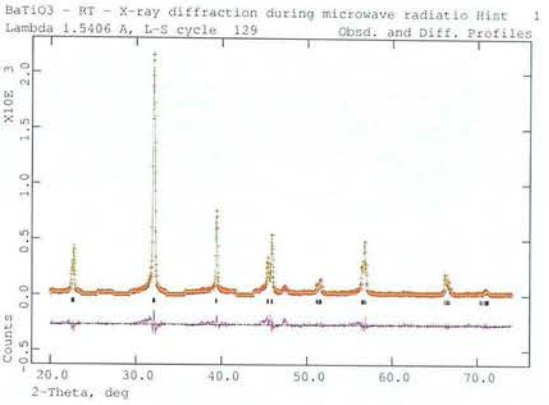

(a)

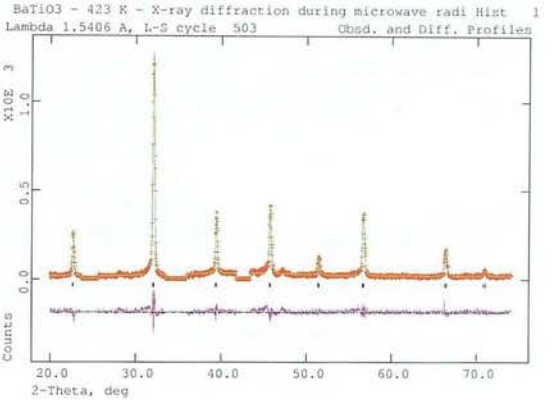

(b)

Figure 5.2: Rietveld refinement graphs for $BaTiO_3$. (a) tetragonal and (b) cubic phase. The small red + represent the observed pattern, the green continuous line represents the calculated pattern and the difference between the calculated and the observed pattern is shown in the bottom graph (in magenta). The tick marks show the reflections for the tetragonal and cubic phases respectively.

So, the cubic phase reflections are 'shadowed' by those of the tetragonal phase before the phase transition happens. The refinements, when only one phase was used yielded very good fits in all cases (χ^2 from 2.020 to 3.773) and very small differences between observed and calculated patterns (see figures D.1 and D.1 in Appendix D). The cell parameters obtained from the refinement are shown in figure 5.4 where the phase transition is clearly observed to have been completed at ~393 K.

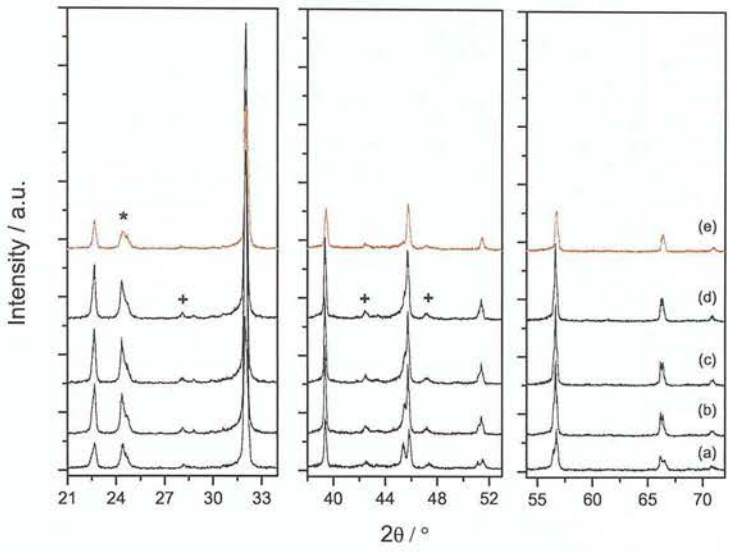

Figure 5.3: X-ray diffraction pattern of $BaTiO_3$ heated with microwave radiation at different temperatures. (a) 295 K, (b) 383 K, (c) 388 K, (d) 393 K and, 423 K. The symbols show the reflections other than the ones from $BaTiO_3$; (*) unkown impurities and (+) PTFE from sample holder.

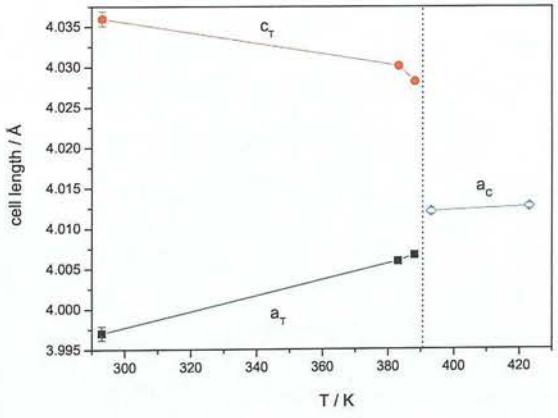

Figure 5.4: Cell parameters for $BaTiO_3$ determined by Rietveld refinement of X-ray data under microwave irradiation. a_T, c_T and a_C represent the cell parameters for the tetragonal (T) or cubic (C) phase. The dotted line marks the temperature at which the phase transition is reported for conventional heating.

From the above results, and as a way to corroborate that the phase transition occurred with microwaves at a lower temperature, a new set of experiments with microwave radiation were carried out with data taken only in the region from 43 to 48° (2θ). These measurements also served the purpose of determining whether a reliable and fast analysis of samples could be performed by scanning over a small angular range, perhaps with better counting statistics. Two sets of experiments were carried out for this purpose, using a fresh sample each time. In the first experiment, the sample was heated up at different temperatures from 295 to 413 K and held at each temperature while the diffraction pattern was taken. In the second experiment, the set of temperatures was chosen to be close to and below the conventional phase transition so the sample was heated from 378 K to 391 K.

As the Rietveld refinement method is used only for whole-pattern analysis, for this part of the analysis we choose to use a general curve-fitting program (OriginPro, v7.5) to treat these two reflections, and determine basic features such as height (related to relative amount of a particular phase), breadth (which may provide information about properties of the material such as strain and domain size) and position (which may indicate some cell parameter). The peaks were fitted to a set of Lorentzian curves, one for each Bragg peak, (details on this can be found on Appendix D) as this was found to yield a better fit. Although the diffraction peaks for a perfect sample are best approximated by a Gaussian curve in the scattering angle, Lorentzian broadening occurs as a consequence of strain and small domain size, both of which could be significant in this case. This analysis also enabled us to detect the co-existence of tetragonal and cubic phases (overlapped reflections) in this region quickly and simply. In this case, reflections (002) and (200) for the tetragonal phase and (200) for the cubic phase. The results of this procedure are shown in figures 5.5 and 5.6.

These data indicate that the phase transition has started at a temperature below the conventionally accepted value of 393 K is already well underway by 388 K and at 391 K (figure 5.6(g)) there is only a very small portion of the peak for the tetragonal phase present.

In figure 5.5 it can be seen that at 403 K and 413 K only one peak is observed, attributed to just the cubic phase. The parameters obtained for the different curves fitted to each reflection on all patterns can be found in tables D.2 and D.1 in Appendix D.

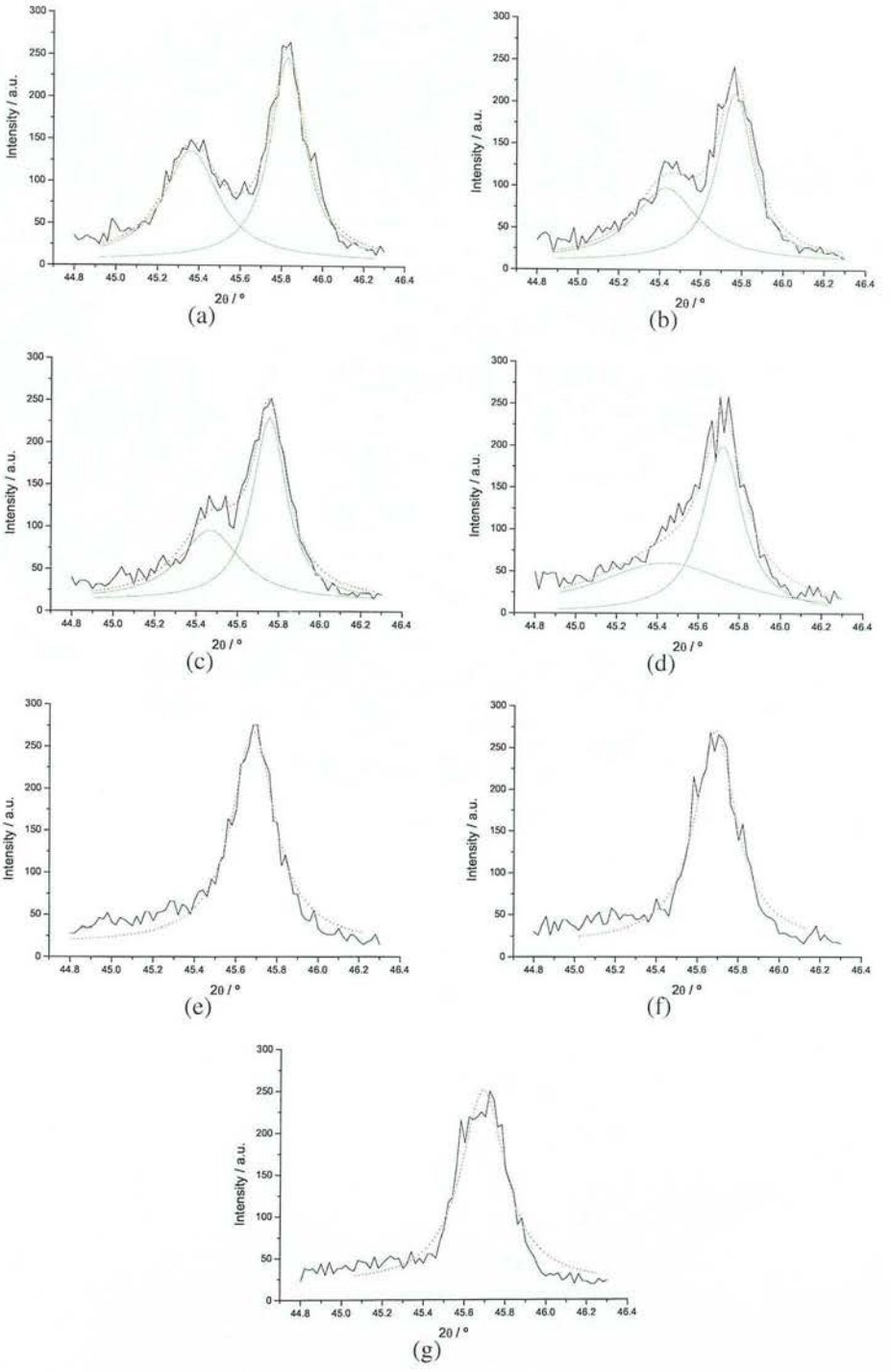

Figure 5.5: Results of fitting Lorentzian curves to reflections for the tetragonal and cubic phases of $BaTiO_3$ -in the region from 43° to 48° in 2θ- for microwave heated samples. (a) 295 K (b) 373 K, (c) 383 K, (d) 393 K, (e) 403 K, (f) 413 K and, (g) 433 K. The fitted curve for the contribution of each reflection -in the case of the tetragonal phase- is represented as a continuous green line while the fitted curve for both these reflections and the cubic phase reflection is shown as a dotted red line. Peak parameters can be found in Table D.2 in Appendix D.

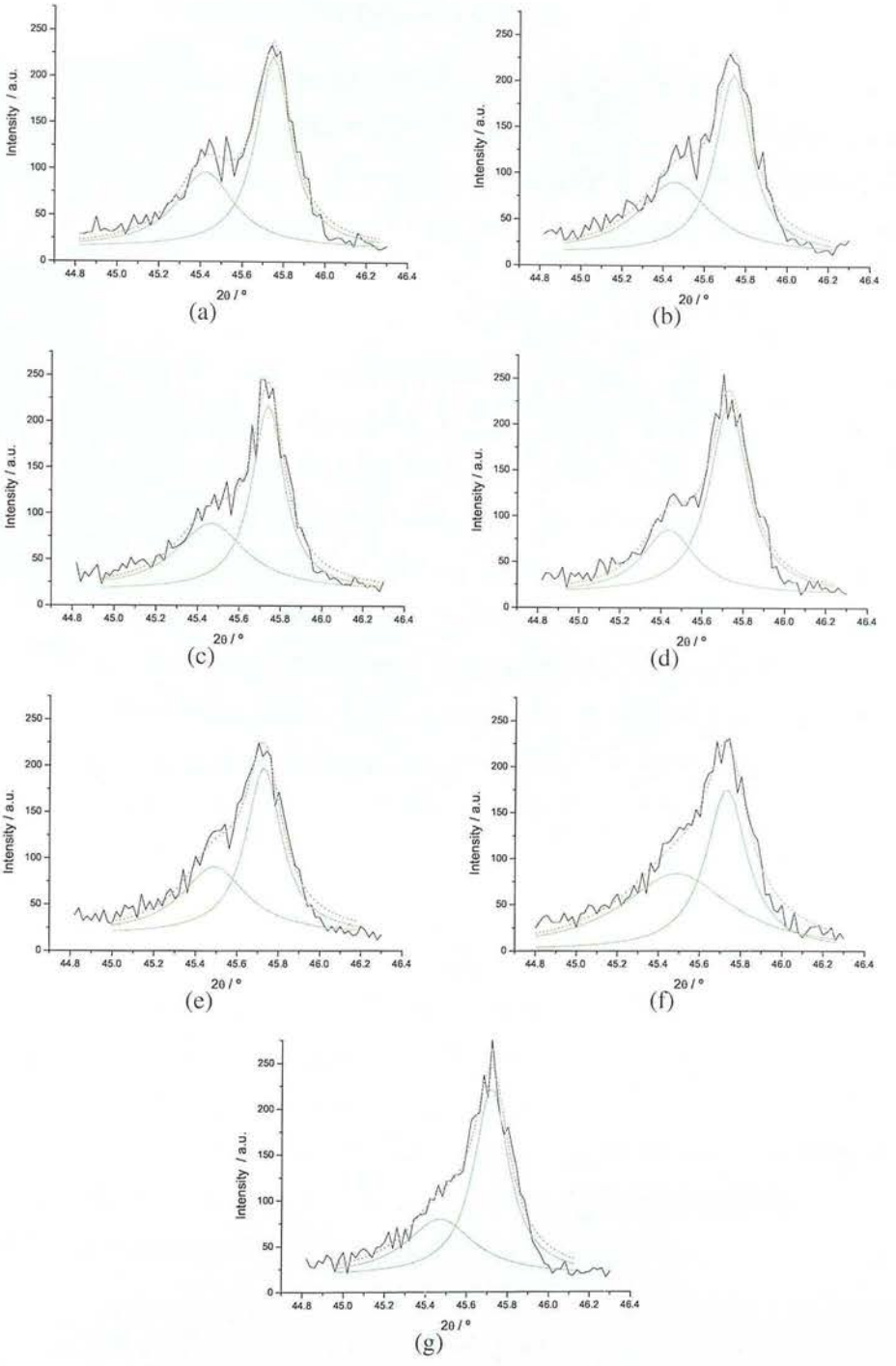

Figure 5.6: Results of fitting Lorentzian curves to reflections for the tetragonal and cubic phases of $BaTiO_3$ -in the region from 43° to 48° in 2θ- for microwave heated samples. (a) 378 K , (b) 381 K, (c) 383 K, (d) 385 K, (e) 387 K, (f) 388 K and, (g) 391 K. The fitted curve for the contribution of each reflection -from the tetragonal phase- is represented as a continuous green line and the fitted curve for both reflections as a dotted red line. Peak parameters can be found in Table D.1 in Appendix D.

5.2.2 *In situ* neutron diffraction: $KNbO_3$

Neutron diffraction experiments were performed on $KNbO_3$ with *in situ* microwave irradiation on the HRPD at the ISIS Facility at the Rutherford-Appleton Laboratory. The arrangement and description of the microwave-neutron diffraction set-up has already been given in some detail in Chapter 3. Here, only a short description of the experimental procedure is given.

The sample of $KNbO_3$ (Alfa Aesar, 99.999%) was loaded in a thin-walled piece of silica tube supported on a microwave-transparent ceramic holder and the temperature was monitored using a fibre-optic probe immersed in the sample. The passage of neutrons through the waveguide was by two two-centimetre diameter holes for the incident and scattered beam (refer to figure 3.4(B) in Chapter 3). Only data obtained from the 90° detector bank was used which in our case represented the data of better quality for structure refinement purposes. TOF neutron patterns were recorded *in situ*, between 32 and 120 msec. For a fixed temperature several scans at approximately six minute intervals were taken to explore the temperature stability when microwave radiation was applied. Sets of data taken in this way were measured for different temperatures from 343 K up to 516 K.

For comparison, *in situ* experiments with conventional heating were also carried out in a standard vacuum furnace with a vanadium element and heat shields. The furnace temperatures were controlled and monitored using two chromel/alumel thermocouples (type K) located at the top and bottom of a cylindrical vanadium canister. The powder neutron diffraction patterns were recorded at longer scan times (one hour each) at each temperature from 343 K up to 603 K. The series of diffraction patterns obtained for both methods of heating are shown in figure 5.7 and figure 5.8.

The different powder diffraction patterns thus obtained were indexed according to the expected phase for each temperature using the CDS database and analysed by Rietveld refinement using GSAS. When samples are mounted in the HRPD, the stick that positions them in the beam has been carefully engineered to ensure that it sits centrally in the flight path, as well as at a very precise position with respect to the neutron TOF from the target and moderator; different sticks may be used in conjunction with different cryostats, furnaces, or for ambient conditions, all with a well-defined TOF

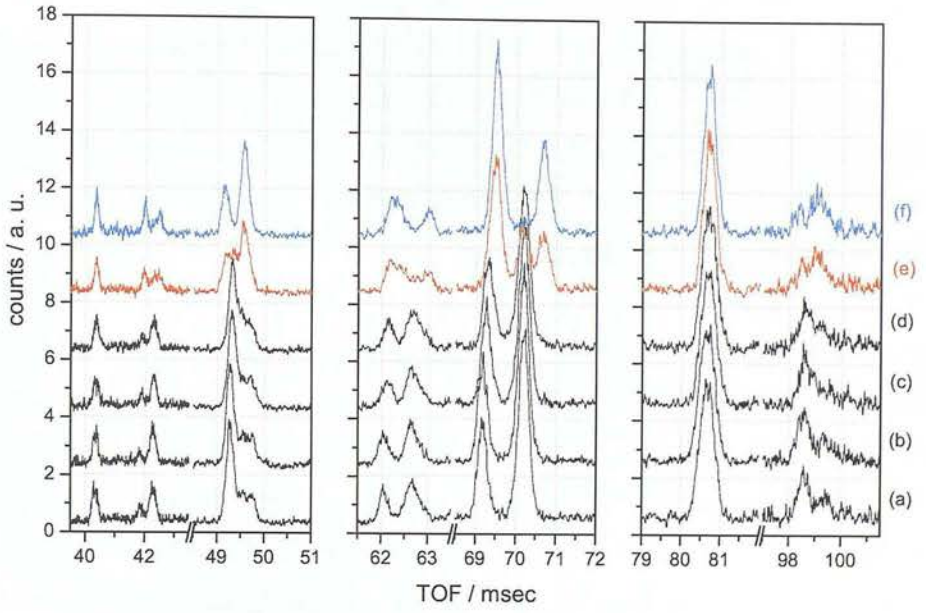

Figure 5.7: Selected regions of the neutron diffraction patterns of $KNbO_3$ during microwave heating taken at (a) 343 K, (b) 393 K, (c) 431 K, (d) 461 K, (e) 493 K and, (f) 516 K.

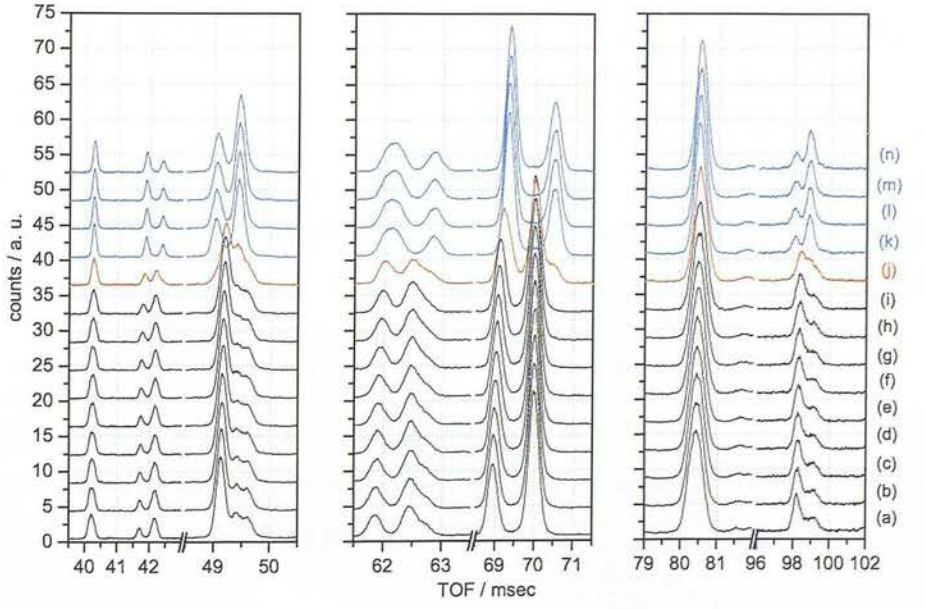

Figure 5.8: Selected regions of the neutron diffraction patterns of $KNbO_3$ during conventional heating taken at (a) 343 K, (b) 363 K, (c) 383 K, (d) 403 K, (e) 423 K, (f) 443 K, (g) 463 K, (h) 483 K, (i) 503 K, (j) 523 K, (k) 543 K, (l) 563 K, (m) 583 K and, (n) 603 K.

parameter to be used in the refinement of data. In the current experiments, the sample was not fixed in the beam with the same precision, partly because of constraints imposed by the optics of the waveguide and the way it was connected to the generator. Consequently, there were concerns about possible sample misalignment so the following procedure was followed for the refinement of data of the microwave heated samples to enable some degree of correction to be made, if necessary. Cell parameters obtained after refinement of the conventionally heated samples at 343 K (the lowest measured temperature for both heated systems) were used as fixed values for the refinement of the structure of the microwave-heated samples while the instrument parameter DIFC (which relates TOF to *d-spacing*, and is directly influenced by changes in position along the neutron flight-path) was allowed to vary, and refined to find a new, optimum value. This new value of DIFC was then used as a fixed value for all other refinements of the microwave-heated samples. Several scans for each temperature were refined simultaneously.

In this sample, it was observed that the transformation for the microwave heated sample took place between 461 and 493 K, 30 K lower (at around 493 K) than that observed for the conventionally heated sample (523 K). As the resolution of the HRPD is higher than that of conventional, laboratory X-ray diffractometer it was possible, in this experiment, to carry out a simultaneous refinement for the two phases. This revealed that the transformation occurred not in a single step but with the two phases coexisting at different proportions until the transformation was completed. One reason for this is that the microwave-heated sample could contain 'hot-spots', on either a micro- or macroscopic scale. The results for the proportions present of each phase for the conventional and microwave heated samples are shown in figure 5.9.

The cell parameters obtained from the structure refinements for each temperature are shown in figures 5.10(a) and 5.10(b). The whole set of results as well as all the graphs produce for each set of neutron patterns can be found in Appendix D.

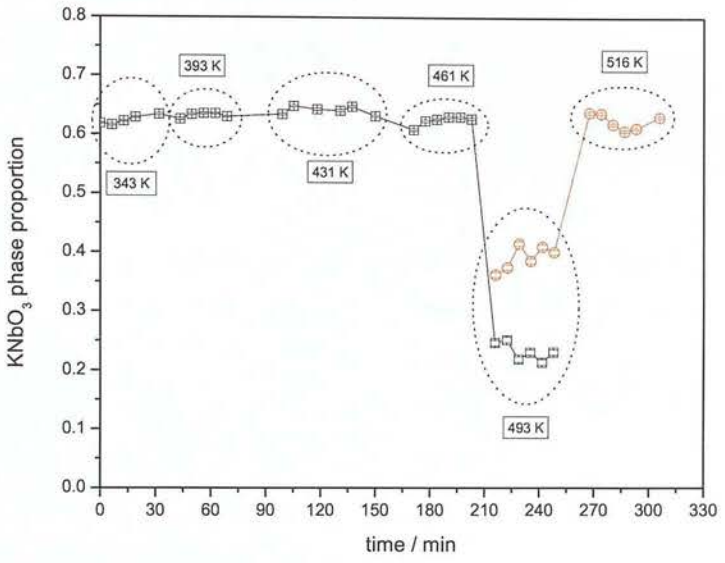

(a)

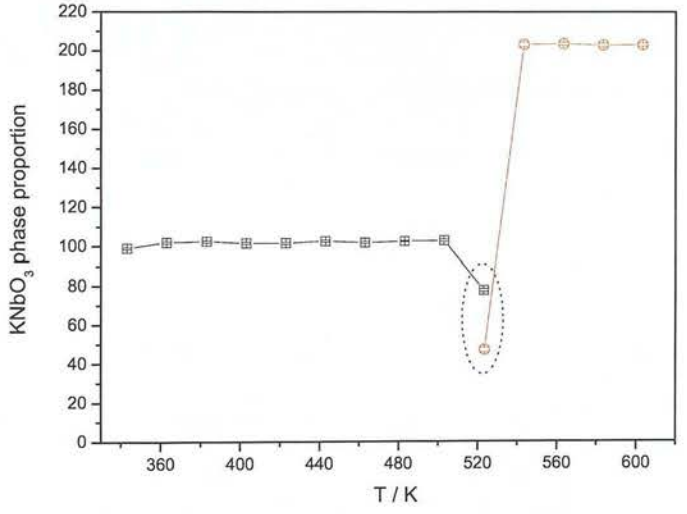

(b)

Figure 5.9: Orthorhombic (□) and tetragonal (○) phases fractions in $KNbO_3$ determined by Rietveld refinement for neutron diffraction data for (a) microwave heating and (b) conventional heating. The graph for microwave heating shows the several proportions obtained for the refinement of each individual neutron pattern taken at each temperature. The dotted circles are only used to indicate the set of scans for each temperature and the temperatures are stated in the small boxes for (a). Fractions may be inacurate because the contributions from the brass reflections which would give a systematic error.

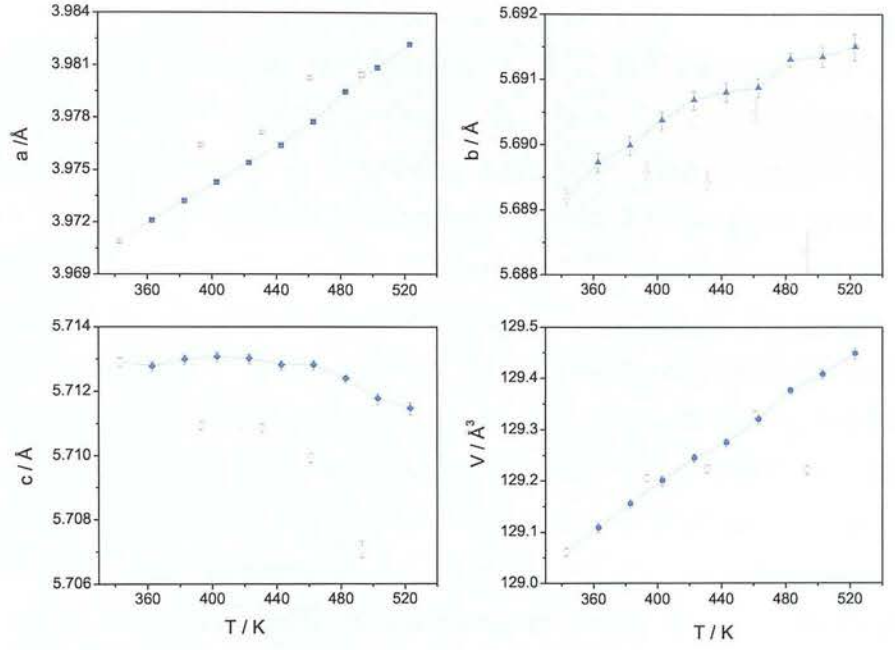

(a)

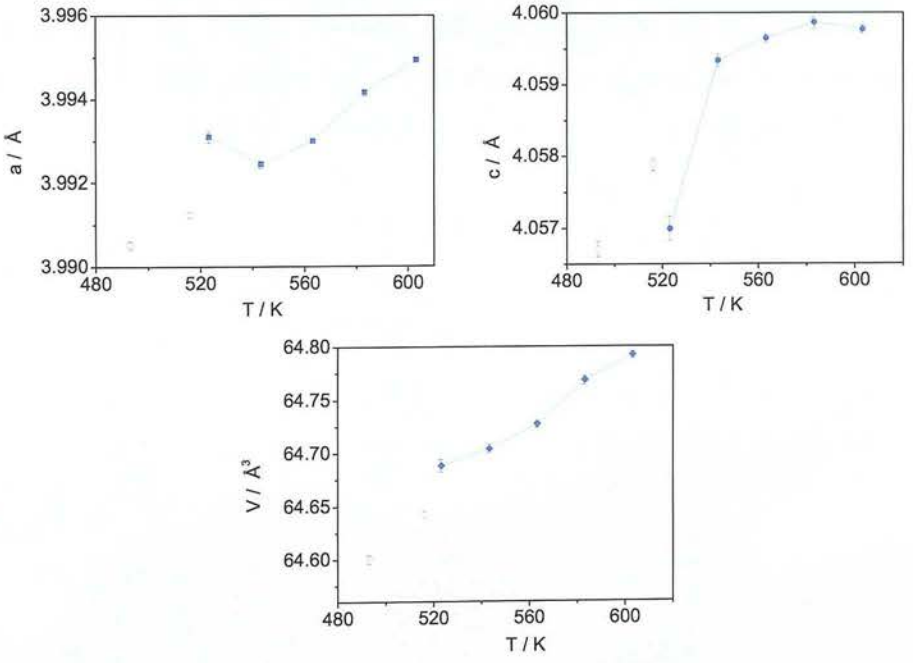

(b)

Figure 5.10: Cell parameters and cell volume for $KNbO_3$ determined by Rietveld refinement data with conventional (■, ▲, ♦, ●) and microwave heating (□, △, ◇, ○). (a) shows data for the orthorhombic phase and, (b) for the tetragonal phase respactively.

5.3 Conclusion

The X-ray powder diffraction measurements on $BaTiO_3$ clearly demonstrate that *in situ* data of sufficient quality for Rietveld refinement may be taken on a laboratory instrument using a conventional sealed-tube instrument. There is no clear indication that the transition temperature (T_c) between the cubic and tetragonal phases of this material are lowered significantly in the microwave field, though there is evidence that there is a distribution of temperature within the sample near T_c that is sufficient to produce a distribution of the two phases. The neutron powder diffraction measurements on $KNbO_3$ suggest that there might be a more significant reduction in transition temperature - in this case between the tetragonal and orthorhombic phases - but again there is some evidence for a distribution of temperature in the sample at either a micro- or macroscopic scale. To clarify what is happening in both materials requires further measurements, taken in closer steps in temperature near T_c with the higher resolution instrument to enable successful resolution of any coexisting phases. Such work should also be complemented by theoretical work to explore which lattice modes are most likely to couple to the microwave field, and how any of the energy that is put into the system in this manner is redistributed and manifested in structure deformation. This might then inform a more detailed study of more subtle structural parameters such as anisotropic ADPs[23].

Chapter 6

Selective heating in microwave irradiated supported-metal catalysts

6.1 Introduction

It was demonstrated in Chapter 5 that one of the most incisive techniques to monitor structural changes in most materials is diffraction of either X-rays or neutrons. These techniques may also provide real-time information about reaction intermediates which may then lead to mechanisms of processes[69]. Following the experience with the $KNbO_3$ system, where the phase transition between polymorphs was followed by *in situ* neutron diffraction, it was thought that this technique could be used to study changes in the lattice parameter with temperature for a material when irradiated with microwaves. This would effectively produce a phase-specific probe of temperature, once the expansivity of each phase had been determined over an appropriate range of temperature with conventional heating. This approach does of course assume that the mechanism of thermal expansion is not also perturbed by the microwave field, and there have been suggestions that it might[23]; we discuss such effects below and maintain that to a good approximation and unless the material being studied has very unusual properties, thermal expansion does provide a good indication of temperature. Further, in the systems to which we chose to apply the method - the response to microwave radiation of the supported catalysts MoS_2/α-Al_2O_3 and Ni(10%) /Al_2O_3, the key issue is whether there can be an anomalous temperature differential between the catalyst and the support, compared to the conventionally-heated case, and the determination of absolute temperature is not the central issue. In this Chapter we describe high-resolution neutron powder diffraction measurements to study this problem.

6.2 Thermal expansion

The thermal expansion of a crystal is the result of the changing balance between an increase in elastic energy and a reduction in the frequencies of various phonons, and is not necessarily a simple function of temperature[123]. However, over relatively small temperature ranges, linear expressions may be used to parameterize such dependencies quite effectively[124] so that, for example, the volume, $V(T)$, may be related to the temperature T with the following expression:

$$V(T) = V_0 + V_1.T + V_2.T^2 \tag{6.1}$$

Likewise, the length $L(T)$ may be related to temperature through the expression:

$$L(T) = L_0 + L_1.T + L_2.T^2 \tag{6.2}$$

A more approximate approach involves truncating such expressions at the linear term, which is perhaps the most common treatment of bulk expansivity data. The coefficient of thermal expansion (CTE) is defined as the fractional increase in length per unit rise in temperature. If it is specified at a precise temperature it is called the true coefficient of thermal expansion and it is related to the slope of the tangent to the length-temperature curve. When specified over a temperature range, it is called the mean coefficient of thermal expansion and it is determined by the slope of the chord between two points on this curve. There are two commonly used terms to define the expansivity. One is α (K^{-1}), the coefficient of linear expansion, defined by:

$$\alpha = \frac{\Delta L / L_0}{\Delta T} \tag{6.3}$$

where:

ΔL is the change in length (m),

L_0 is the length at T_0 (m),

L is the length at temperature T,

ΔT is the change in temperature $T - T_0$ (K).

The other is the coefficient of volume expansion, β (K^{-1}), defined in an analogous fashion to α. If the solid is isotropic - as is the case for cubic polycrystalline or amorphous solids - there is a simple relation between the coefficient of thermal expansion and the coefficient of volume expansion:

$$\beta = 3\alpha \tag{6.4}$$

It should also be appreciated that thermal expansion is strongly influenced by the degree of anharmonicity in the vibrational spectrum[123]. For a harmonic oscillator, the potential energy associated with the interatomic forces has a quadratic form, centred on the mean atomic separation, r_0. As the temperature is raised and the occupancy of higher vibrational states increases, there is no change in r_0. It is only when the force-field deviates from a form which is symmetric about r_0 - for example when anharmonic effects are significant - that r_0 may change upon heating, usually increasing as temperature is increased.

6.3 Microwave irradiation in heterogeneous catalytic systems

For microwave dielectric heating of catalytic systems, claims have been made that reaction rates may be enhanced and selectivity changed for a specific product[126,127,29] as a consequence of changes in the temperature gradients between the different components in the reaction. Such temperature gradients may be the result of 'hot-spots' on the catalyst bed[128,129] or selective heating of active sites[130]. However, there is relatively little sound evidence for such effects. In one case[131], the formation of hot-spots was postulated on the basis of the observation of the formation of traces of α-alumina in a sample whose support contained initially only γ-alumina, while the average temperature, measured with an optical fibre thermometer, remained well below the temperature at which the γ-α transition normally occurs. However, there have also been claims[132] that such temperature gradients are not significantly higher. In this case, the temperature measurements were made by inserting a thermocouple into the reaction zone after the microwave radiation was switched off and a temperature decay curve recorded and extrapolated back in time to obtain a reaction temperature at the moment the power was switched off. In all cases, it is clear that one of the most challenging aspects of the study of microwave-driven processes is an accurate and precise determination of the temperature of a material during microwave heating. Additionally, if a method that reveals chemical and structural changes *in situ* (while the process is taking place) is used, this could be a feasible way of detecting these temperature gradients in supported-metal catalysts and other solid-state processes.

Catalysts in which the active phase is dispersed on support materials are commonly prepared with relatively low loadings of active phase with the highest possible dispersion so as to optimize the surface area of the active material. Supported nickel catalysts provide an exception among working catalysts. They tend to use higher loadings of metal, typically between 10 and 40 atom percent and as a result have larger metal crystallites which lend themselves to study *via* diffraction techniques. They are used industrially for hydrogenation processes and for the production of synthesis gas *via* the steam reforming of methane. The nickel is generally supported on high surface area γ-Al_2O_3; consequently the support material is poorly crystalline so diffraction may provide only a very coarse measure of the temperature of that phase. Information about differential heating then comes from a comparison between the particle temperature determined through the expansivity, and the mean sample temperature, determined by conventional thermometry. It would be better to study a system in which both the support and the supported phase were highly crystalline. Therefore, we also studied the effect of microwave radiation on the structure of MoS_2 supported on crystalline α-Al_2O_3 - this also being an example of a system for which anomalous heating by microwaves has been reported[128,129].

6.4 Experimental Procedure

6.4.1 Catalyst preparation

A 10% wt nickel on alumina catalyst was prepared using a co-precipitation technique. Solutions of nickel nitrate (1.0 M, Aldrich) and aluminium nitrate (1.0 M, Aldrich) were mixed in appropiate ratios at 333 K prior to the addition of an excess of ammonium carbonate (1.0 M, Aldrich). The ammonium carbonate was added in a dropwise manner over a period of 90 minutes with continuous stirring. The result of this was the precipitation of the nickel and aluminium carbonates/hydroxycarbonates. The solution was then cooled before vacuum filtration. The filtrate was washed with deionised water and dried at 363 K. The oxidic catalyst precursor was obtained after heating the sample in air at 823 K for a period of 16 hours to remove carbonates/hydroxycarbonates. The catalyst in its active state was produced by reduction in a flow of 10% hydrogen in argon at 873 K for further 16 hours. The catalyst was cooled to ambient temperature before slowly increasing the concentration of air passing over the catalyst. This

procedure was undertaken in order to passivate the surface of the nickel metal without inducing deep oxidation of the nickel crystallites.

The MoS_2/α-Al_2O_3 catalyst was prepared from a mechanical mixture of 30% wt of molybdenum disulfide (Aldrich, 99%; < 2 micron) and 70% wt of α-alumina (corundum, Aldrich, 99%; -100 mesh). Both chemicals were throughly ground using a pestle and mortar for approximately 20 min.

6.4.2 *In situ* neutron diffraction studies

The experiments were carried out on the HRPD at the ISIS Facility at the Rutherford-Appleton Laboratory. The microwave heating apparatus, designed to be used mainly for *in situ* X-ray diffraction experiments (see Chapter 3) was modified accordingly for the purposes of this experiments. The experimental set up is described next.

The samples were loaded in a thin-walled piece of silica tube supported on a microwave-transparent ceramic holder (Shapal^{TM}). Temperature was monitored using a fibre-optic probe (Neoptix T1, Tmax. 523 K, resolution of 0.1 K) in intimate contact with the sample. The passage of neutrons through the waveguide was facilitated by two-centimetre diameter holes for the incident beam detectors for neutrons scattered (see figure 3.4(B)); of these, data taken on the 90° detector bank were of the highest resolution. Neutron-absorbing gadolinium sheet was used to try to minimise scattering from other components of the microwave heating system. TOF patterns were recorded *in situ*, between 32 and 120 msec, and for a fixed temperature several scans at approx. six-minute intervals were taken to explore the temperature stability when microwave radiation was applied. A series of temperatures from 291 K up to 518 K were explored in the same way for the two different samples.

For comparison, *in situ* experiments with conventional heating were also carried out in a standard vacuum furnace with a vanadium element and heat shields. The furnace temperatures were controlled and monitored using two chromel/alumel thermocouples (type K) located at the top and bottom of a cylindrical sample vanadium canister. The powder neutron diffraction patterns were recorded at longer scan times (one hour) from 291 K to up to 518 K for the nickel catalyst and up to 1073 K for the MoS_2/α-Al_2O_3 catalyst.

The different powder diffraction patterns obtained were indexed accordingly as hexagonal MoS_2, α-Al_2O_3 and cubic metallic nickel. All data collected were analysed by Rietveld refinement method using the General Structure Analysis System (GSAS) suite of programs[52]. In order to minimise any sample misalignment problems, the following procedure was followed for the refinement of data of the microwave heated samples. Cell parameters obtained after refinement of the conventionally heated samples at 291 K were used as fixed values for the refinement of the structure of the microwave heated samples while the instrument parameter DIFC (related geometry of the instrument) was allowed to be refined. The new DIFC value obtained was then used as a fixed value for the following refinements of the microwave heated samples (where several scans for one temperature were refined simultaneously) allowing the cell parameters to be refined freely.

6.5 Results

6.5.1 Nickel-supported catalyst

The neutron diffraction patterns of the two series of scans for conventional and microwave heated samples are shown in figures 6.1(A) and (B). For the microwave heated samples, and for illustrative purposes only, one scan is shown for each temperature. The extra features observed in the microwave heated samples were assigned to the reflections from the brass waveguide. No significant changes were detected between scans taken at each temperature (refer to figure E.2 in the Appendix E); hence, the refinement procedure was simultaneously applied to each member of the set of all scans taken at each temperature (each taken for approximately 6 minutes). Note that no distinct peaks that could be assigned to the support phase could be seen.

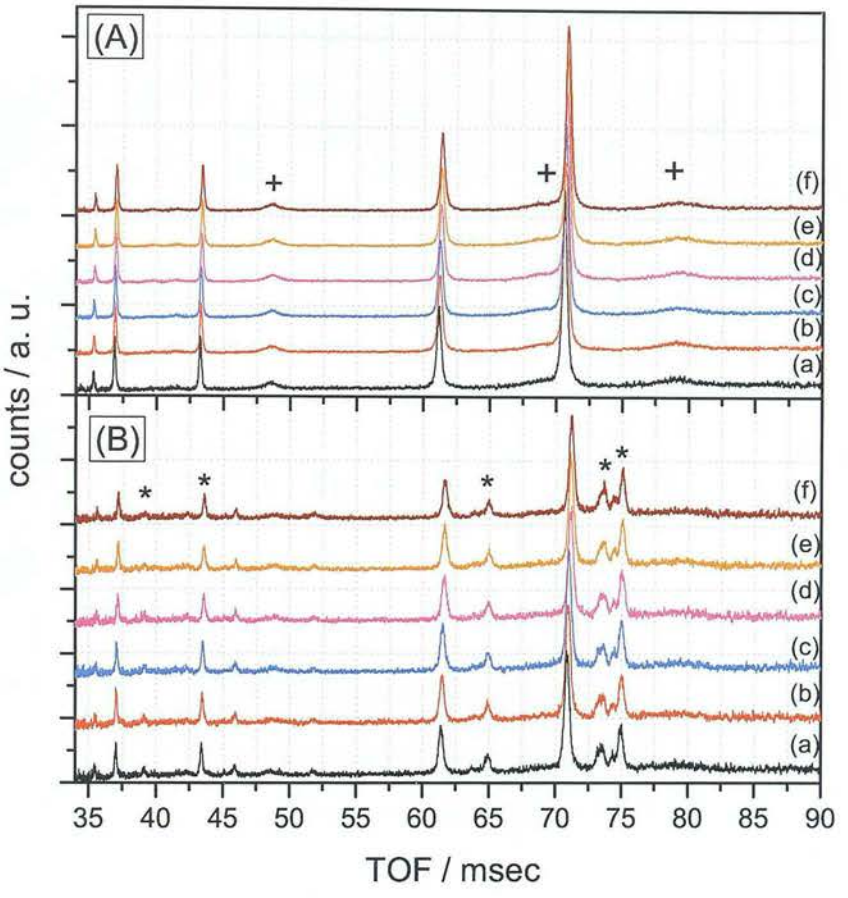

Figure 6.1: Ni(10%) /Al_2O_3 heated (A) conventionally and (B) with microwaves at (a) 291 K, (b) 323 K, (c) 373 K, (d) 423 K, (e) 473 K and (f) 516 K. Crosses (+) indicate the response of amorphous alumina and asterisks (*) the contribution from the microwave waveguide.

The results for the refinement of data taken for the supported nickel catalyst are shown in figure 6.2(a) and (b) for the two samples heated at 423 K using both methods. The additional features observed in the microwave heated sample (around 45-46, 63-64 and 73-74 msec) were due to scattering from the brass microwave waveguide and were indexed as two single brass peaks (CuZn, 35:65). These reflections were also included as two additional phases during the refinement due to the overlapping with the sample reflections. This procedure led to a more satisfactory refinement of the different data sets. The observed pattern (shown as red scattered crosses) and the calculated pattern (solid line overlapping the scattered crosses) were in agreement. The difference curves (shown in magenta) between the observed and the calculated patterns are shown at the bottom of each graph.

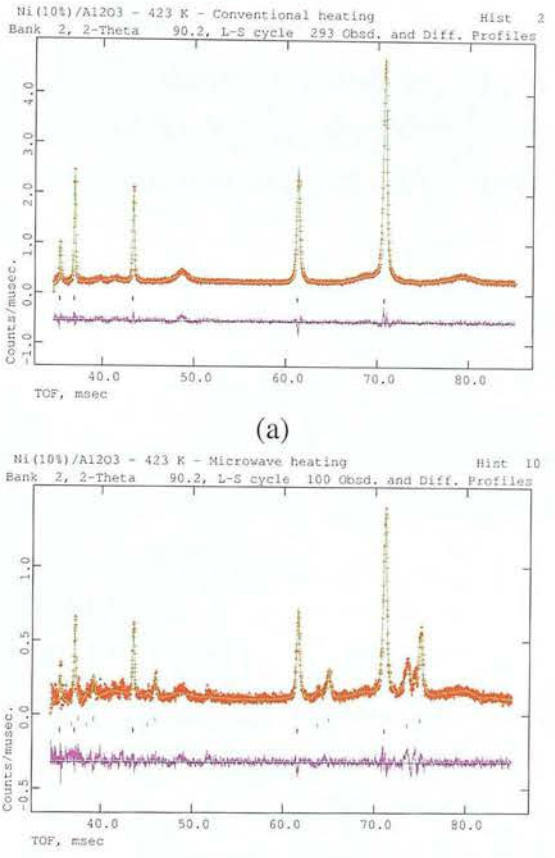

Figure 6.2: Rietveld refinement for Ni(10%) /Al_2O_3 at 423K with (a) conventional heating and (b) microwave heating. The small + represent the observed pattern, the green continuous line represents the calculated pattern and the difference between the calculated and the observed pattern is shown by the bottom line in magenta. The tick marks indicate the different phases used in the refinement - the upper two sets for the brass of the microwave waveguide, and the lower set for the nickel.

The graphs obtained for each pattern after refinement, as well as the graphs for the conventionally heated samples, can be seen in Appendix E together with all the cell parameters and profile parameters obtained from this analysis.

The cell parameters and cell volume (figures 6.3 (a) and (b)) for nickel metallic particles were obtained from this analysis for both the conventionally and microwave-heated cases. These values could be fitted to equations 6.1 and 6.2 as appropriate, with significant weighting of the co-efficient of the term in temperature squared[124], and values for the various co-efficients in these equations, together with the thermal expansion

coefficients (TEC) are reproduced in table 6.1. The values for the volume expansion under conventional heating were then used to produce a calibration curve with which to determine the temperature of the nickel fraction of the sample under microwave irradiation. If we specify this temperature as T^*, we can determine its value as a solution of the following equation:

$$(V_0 - V_{T^*}) + T^* V_1 + (T^*)^2 V_2 = 0 \tag{6.5}$$

Table 6.1: Results of fitting lattice parameters or volume to equations 6.1 and 6.2 for the thermal expansion of nickel particles. The coefficients x_n (n = 0,1,2), refer to length or volume, as appropriate.

Parameter	TEC $*10^5$ / K^{-1}	x_0 (Error)	x_1 (Error)	x_2 (Error)
$a_{Ni-CONV}$	0.58	3.51330	$2.0436*10^{-5}$	$3.7815*10^{-8}$
		(0.00201)	(1.0281^{-5})	($1.2731*10^{-8}$)
$V_{Ni-CONV}$	1.73	43.36570	$7.5154*10^{-4}$	$1.4261*10^{-6}$
		(0.07640)	($3.9116*10^{-4}$)	($4.8434*10^{-7}$)
a_{Ni-MW}	1.70	3.50457	$5.9546*10^{-5}$	
		(0.00153)	($3.7538*10^{-6}$)	
V_{Ni-MW}	5.18	43.03646	0.0022	
		(0.05724)	($1.4041*10^{-4}$)	

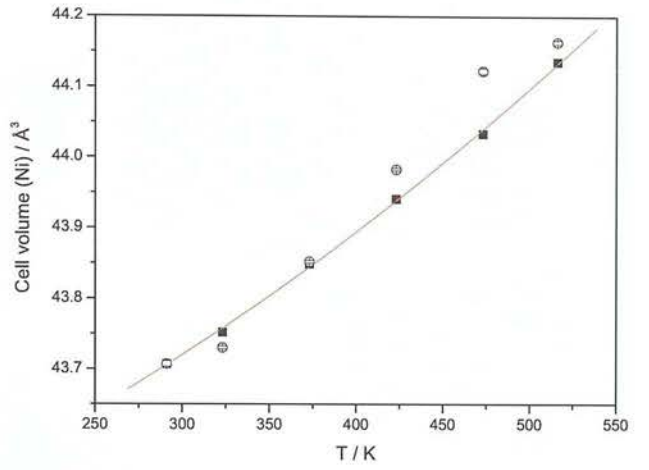

(a)

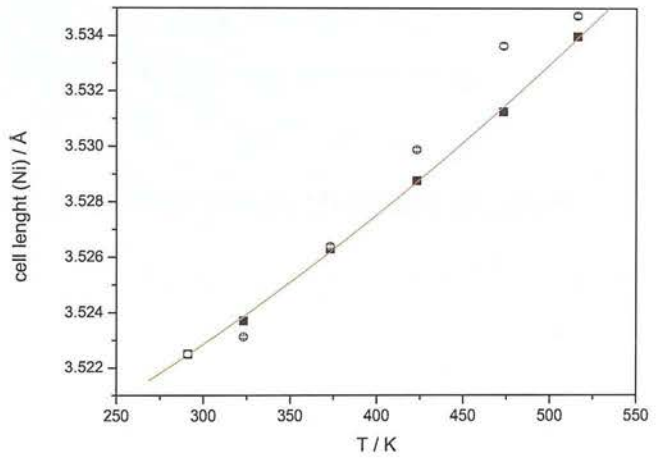

(b)

Figure 6.3: Thermal expansion for a Ni(10%)/ Al_2O_3 catalyst heated conventionally (■) and with microwave radiation (○). (a) Volume expansion and (b) linear expansion. The solid line represents the least-squares fit to the data for the conventionally heated sample to a quadratic in temperature.

Results of this analysis are plotted in figure 6.4 which shows that the nickel particles in the microwave heated samples appear to be 'hotter' than when heated conventionally. In contrast to the MoS_2-supported catalyst the nickel-supported catalyst was supported on non-crystalline alumina so only nickel crystallites could diffract to produce sharp peaks.

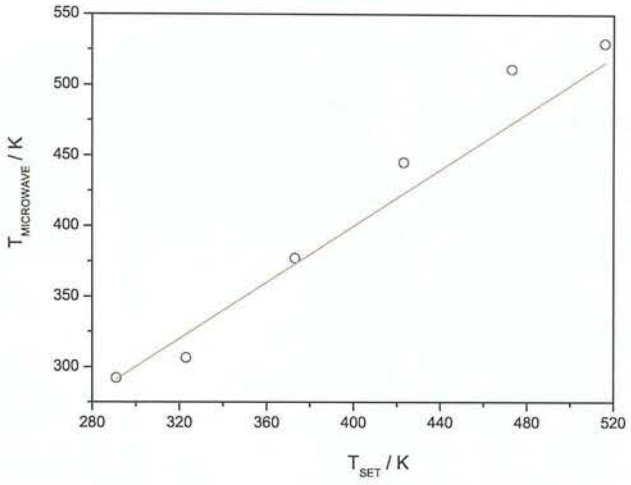

Figure 6.4: Temperature of nickel particles (○) on Al_2O_3 during microwave irradiation determined through measurement of the cell volume and plotted against the set temperature (dotted line) during the experiments.

6.5.2 Supported molybdenum disulfide catalyst

As in the previous experiments, the features observed in the microwave heated experiment that could not be assigned to the sample were indexed as two single brass peaks and included in the refinement procedure. The diffraction patterns of these samples are shown in figures 6.5(A) and (B) where, in the case of microwave irradiation, only one scan per temperature is shown for illustrative purposes. The complete set of scans for all temperatures, each taken for approximately 6 minutes (as before) can be found in figure E.11 in Appendix E.

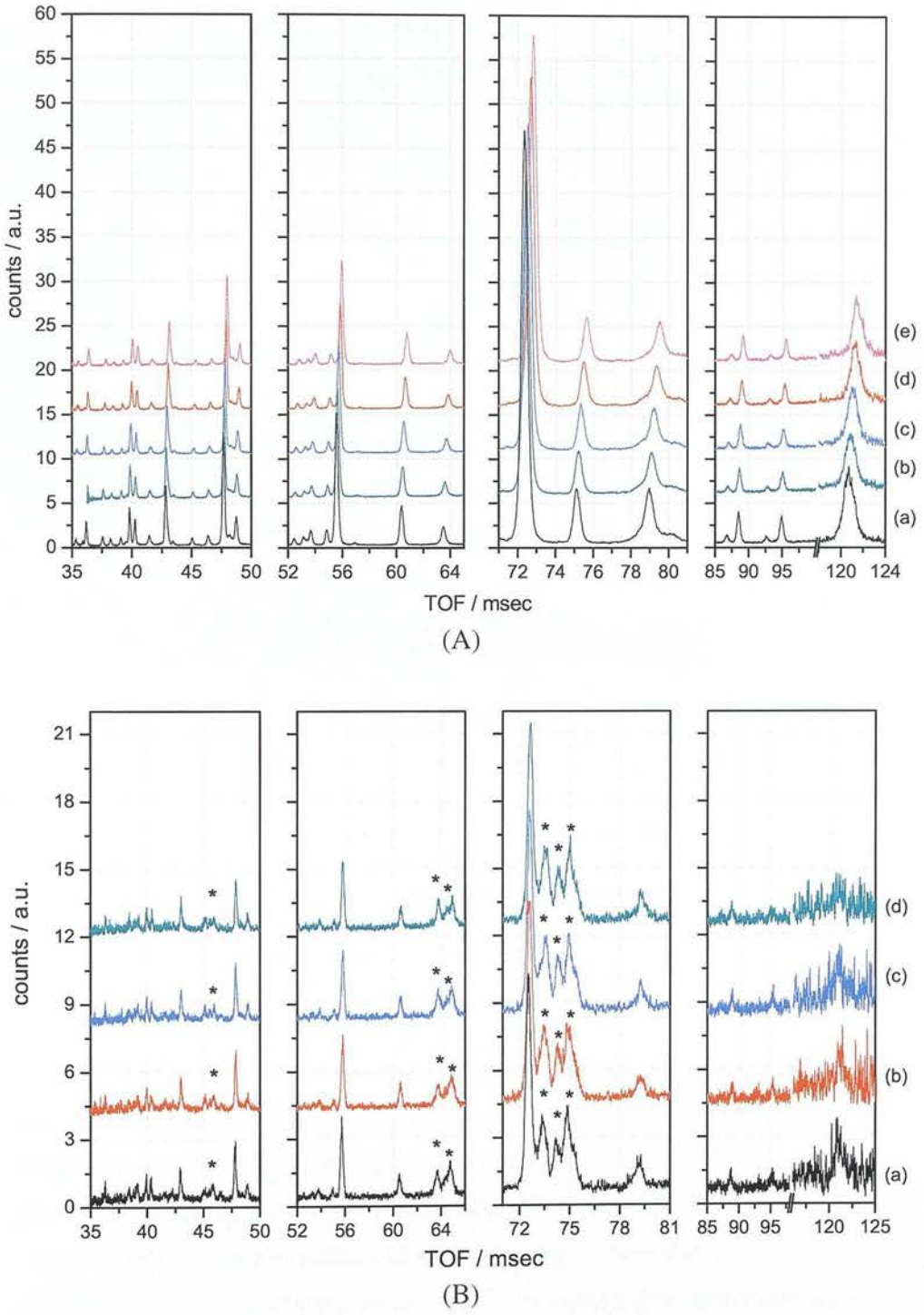

Figure 6.5: Powder neutron diffraction patterns for the MoS_2/α-Al_2O_3 catalyst. (A) conventionally heated samples at (a) 291 K, (b) 473 K, (c) 673 K, (d) 873 K, and (e) 1073 K; (B) microwave heated samples at (a) 291 K, (b) 353 K, (c) 413 K, and (d) 743 K. Asterisks (*) indicate reflections from the microwave applicator.

Figure 6.6 shows a sample result of the Rietveld refinement of data for the samples of supported-MoS_2 catalyst heated at 473 K conventionally and with microwaves. All the graphs showing the results of profile refinement of all this set of neutron diffraction patterns are shown in Appendix E.

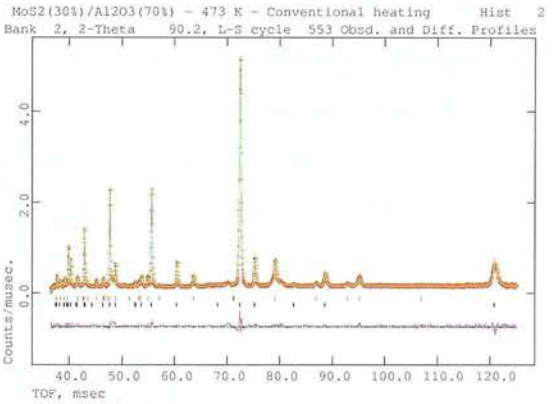

(a)

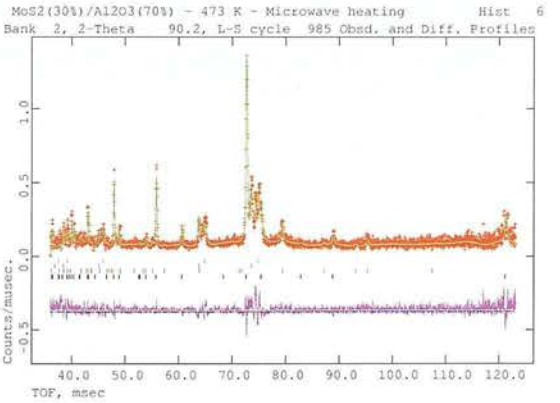

(b)

Figure 6.6: Rietveld refinement for MoS_2/α-Al_2O_3 catalyst heated at 473 K with (a) conventional heating and (b) microwave heating. The small + represent the observed pattern, the red and green continuous lines represent the calculated pattern and background respectively, and the difference between the calculated and the observed pattern is shown by the bottom line in blue. The tick marks indicate the different phases used in the refinement - the upper two sets for the brass of the microwave waveguide, and the lower sets for MoS_2 and α-Al_2O_3.

Refined values of cell parameters are shown in figures 6.7 and 6.8 from 291 K to 473 K for the two components in the catalyst: the MoS_2 particles and the α-Al_2O_3 support.

A table with all the results from the refinement can be found in the Appendix E. As with the data for the supported nickel catalyst, the conventionally-heated sample was used to produce a calibration curve, and then effective temperatures T^* of the MoS_2 were determined using equation 6.5. The change in volume of catalyst and support for both heating regimes are displayed in figure 6.7. The thermal expansion coefficients (from 291 to 473 K) for the two components of this catalyst are listed in table 6.2. The complete set of data for cell parameters *a* and *c* are also given in in figures E.9(A) and (B) in Appendix E. Note that, the expansion of the MoS_2 is significantly anisotropic, reflecting the structural anisotropy of this material: expansion is proportionally greater in the *c* direction than in the *a* direction (figure 6.8(a)).

Table 6.2: Results of fitting lattice parameters or volume to equations 6.1 and 6.2 for the thermal expansion of MoS_2 and α-Al_2O_3. The coefficients x_n (n = 0,1,2), refer to length or volume, as appropriate. (†) The thermal expansion co-efficient (TEC) was obtained by fitting only data from 291 K to 473 K.

Parameter	TEC$*10^5$ / K^{-1}	x_0	(Error)	x_1*10^5	(Error$*10^5$)
a_{MoS_2-CONV}	$0.66^\dagger$	3.15159		2.06923	
c_{MoS_2-CONV}	$1.05^\dagger$	12.24624		12.85990	
V_{MoS_2-CONV}	$2.38^\dagger$	105.33690		251	
a_{MoS_2-MW}	0.65	3.15195	(0.00131)	2.06159	(0.33619)
c_{MoS_2-MW}	2.14	12.20801	(0.02031)	26.08970	(5.22828)
V_{MoS_2-MW}	3.47	105.03056	(0.17589)	364	(45.27850)
$a_{Al_2O_3-CONV}$	$0.50^\dagger$	4.74669		2.38242	
$c_{Al_2O_3-CONV}$	$0.67^\dagger$	12.95549		8.62033	
$V_{Al_2O_3-CONV}$	$1.87^\dagger$	252.78954		472	
$a_{Al_2O_3-MW}$	0.78	4.74440	(0.00164)	3.71094	(0.421674)
$c_{Al_2O_3-MW}$	0.69	12.95442	(0.00175)	8.99003	(0.451701)
$V_{Al_2O_3-MW}$	2.27	252.52264	(0.20324)	574	(52.3214)

The results confirm that both the catalyst particles and the support were heated effectively with microwaves, and indeed both appear hotter than the mean sample temperature measured with the fluoroptic probe. This points to some systematic error in the measurements, but the differential between the catalyst particles and the cooler support

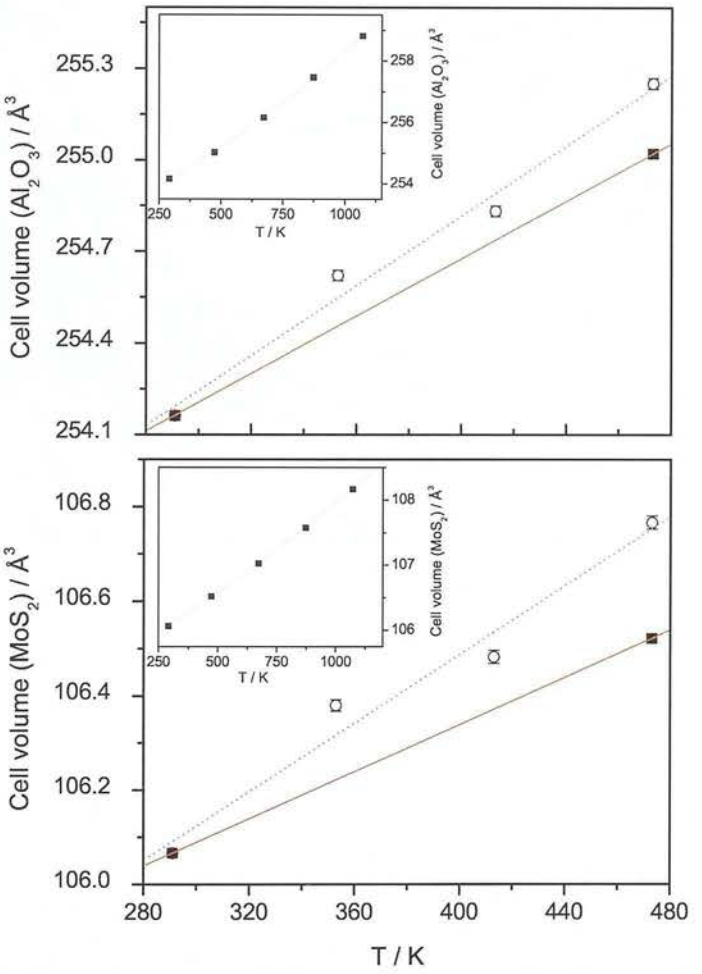

Figure 6.7: Change in cell volume for a MoS_2/Al_2O_3 catalyst heated conventionally (■) and with microwaves (○). The solid line represents fits to equations 6.1 and 6.2 as appropriate, while the dotted line is only a guide for the eye.

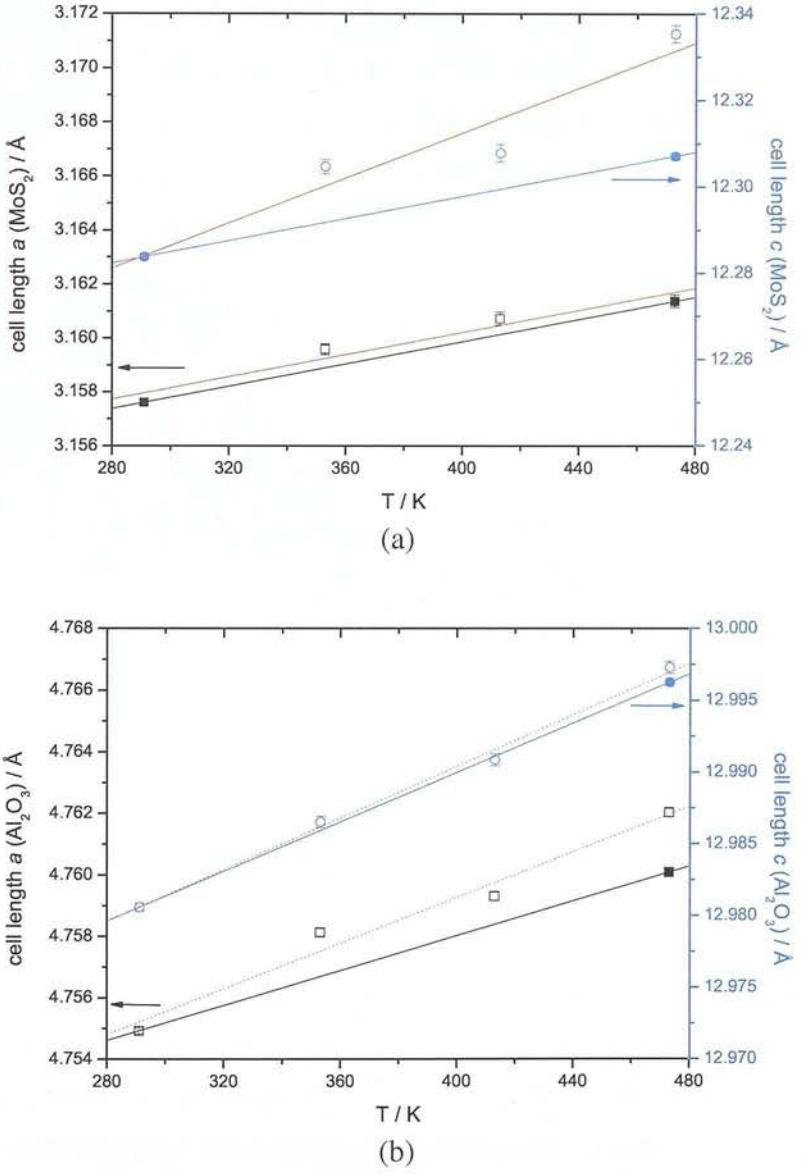

Figure 6.8: Change in cell parameter for a MoS_2/α-Al_2O_3 catalyst heated with conventional (■, ●) and microwave heating (□, ○). Cell lengths *a* and *c* for: (a) MoS_2 and (b) α-Al_2O_3 phases. Solid lines are only a guide for the eye.

implies the former are indeed hotter than the support.

As before, based on the coefficients determined for the cell volume of the conventionally heated (see table E.4 in Appendix E) sample, a 'true' temperature for the microwave heated samples was calculated as one of the solutions of equation 6.5. Results are plotted as in figure 6.9, comparing the set temperature and 'microwave' temperature for the two component in the catalysts. The difference in temperature between the two components is also plotted in the lower part of the graph as a dotted line.

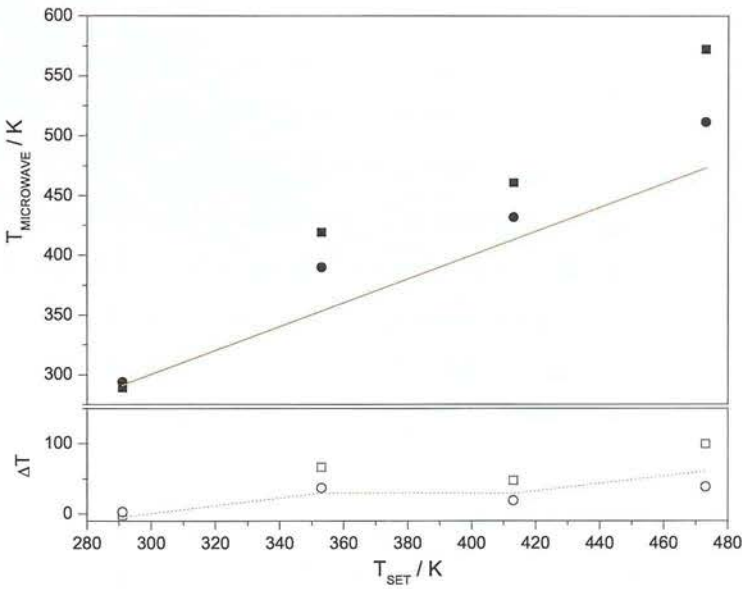

Figure 6.9: Temperature of MoS_2 (■) and α-Al_2O_3 (●) particles during microwave irradiation determined through measurement of the cell volume and plotted against the set temperature (solid line) during the experiments. The bottom plot shows the temperature of (□) MoS_2 and (○) α-Al_2O_3 relative to the average bulk temperature with the dotted line providing a guide to the eye.

We noted above that the thermal expansion is strongly influenced by the degree of anharmonicity in the vibrational spectrum[123] and it is conceivable that this in turn does couple to a microwave field[23]. Indeed, it has been argued that the measurement of the cell expansion may not be used to provide a reliable measure of temperature, and that it is better to use the anisotropic thermal displacement parameters (ADPs) which con-

tain a contribution from the mean thermal motion of the constituent atoms. However, it has also been argued that the perturbation of phonon densities of states from equilibrium (Boltzmann) values in a microwave field is generally very small[25]. Therefore, we have taken the cells' thermal expansion as a reasonable basis for estimates of the temperature (a further pragmatic point is that our data do not have a sufficient range of d-spacing to determine ADPs with sufficient precision for such analysis to be useful in this context). Another important factor to consider in heterogeneous systems is the feasibility of sustaining significant temperature differences over a small length-scale. It can be shown[133] that metal particles in the nm - micron range can heat up extremely quickly - at rates of the order of 1 - 1000 K s^{-1}- in microwave fields of comparable strength to those we employed (of the order of 10^6 V m^{-1}). Of course, these particles will rapidly transfer this heat to their surroundings - the support - and it is difficult to justify significant temperature differences between the two phases given the short length-scales involved and the high thermal gradients this implies. However, this argument is based on a system at equilibrium. It is conceivable that this is not the case for our system; the control circuit leads to fluctuations in the delivery of microwave power (study of the log that recorded the power applied as a function of time indicated this to be of the order of 2-3 Hz) so it is possible that for a fraction of the time the particles are subject to very high heating rate and that their temperature - and hence cell volume - is significantly higher for a fraction of the time.

6.6 Conclusions

In situ neutron diffraction measurements have provided the first direct evidence of a differential heating under microwave irradiation of highly-conducting particles, dispersed over a high surface area support. This may be significant in the study of the influence of microwave radiation in efficient activation of heterogeneous catalysts. However, these results come with a number of caveats. First, the basis of our measurements is the assumption that cell parameters or volume may provide a measure of temperature for materials under both conventional and microwave heating, and this is not necessarily rigorous for microwave heating because the mechanism of transfer of heat may differ. This is clearly an effect that needs to be studied in greater detail, possibly at first through theory and modelling of the strength of microwave-phonon and phonon-phonon coupling. Second, it has been argued that thermal gradients of some tens of Kelvin maintained over particles of a micron diameter or possibly much less,

are unfeasibly large to be compatible with likely heat flows in this type of system; a counter to this criticism is the observation that the temporal fluctuations in power levels applied to the supported catalysts may give significant power surges to the particles, producing short spikes in temperature that are not directly apparent in the mean temperature that the thermometer returns. One interesting follow-up experiment would be to imposes various time structures on the power controller's output.

Chapter 7

Fast-ion conductors

7.1 Introduction

One of the problems encountered while studying solids under microwave heating is accurate control of the applied power for samples whose microwave susceptibility changes significantly with temperature. This is the case when the sample approaches a transition between phases of quite different dielectric properties, and it has been suggested that this can lead to a change in the observed temperature of the phase transition in a microwave field[66,134].

The first rectangular waveguide applicators designed for *in situ* diffraction were not able to control the power at the sample very precisely[69,113]. In many cases, where the microwave susceptibility is modest and its response as a function of temperature relatively flat, this does not pose a problem. However, for materials in which the susceptibility rises very quickly on warming, rapid and sensitive feedback is essential to prevent thermal runaway. Ironically, some of the systems where 'microwave effects' are most likely to be most significant, fall into this category - for example materials that pass through a transition between two phases of quite different dielectric constant.

Perhaps the archetypal material for studies of 'microwave effect' in the solid state, and certainly the one that has attracted the most attention, is AgI[66,134]. This Chapter describes work that used the new applicator design to apply microwave power carefully to AgI samples, in conjunction with a more intense X-ray source, together with X-ray optics and detector of higher resolution than previously used, with the sample held in a glass capillary. The possible applications of this new microwave applicator for *in situ*

X-ray diffraction studies could then be extended -in the future - to not only solid state studies but to small scale reactions during microwave irradiation.

AgI is a model fast-ion conductor which is not actually used commercially as a conducting medium, but rather provides a model to gain a better understanding of other highly-conducting ionic materials. As a consequence it has been studied extensively to determine the mechanism of the conductivity, and its dependence on structure, temperature and defects.

At room temperature AgI has a relatively dense hexagonal structure, with modest ionic conductivity. However, upon warming through 461 K[135] it undergoes a structural phase transition from β-AgI to the cubic α- AgI phase, which has a much more open structure, and a much higher ionic conductivity associated with the more mobile, highly polarisable silver ions. There have been extensive studies of the nature of this transition and the charge transport mechanism in the more conducting state, pointing to the role of Frenkel disorder and anharmonic thermal vibrations in β-AgI through the transition[136,137]. Previous measurements of this material under microwave irradiation, using *in situ* X-ray diffraction and heat capacity data[66,134], indicate that the β to α transition may be lowered significantly by the microwave field. The X-ray measurements indicated a reduction in the transition temperature by tens of Kelvin, depending on the precise conditions; however, those measurements suffered from crude power control, and it is possible that the sample underwent significant excursions to higher temperature throughout the heating ramp, and this may have lead to anomalously high temperatures relative to the mean recorded temperature. The thermodynamic measurements were performed at lower power levels and more careful temperature control and reported a reduction of the transition temperature by about 2.5 K. In addition, we performed neutron powder diffraction measurements at the ISIS Facility of the Rutherford-Appleton Laboratory: limited access time only permitted us to perform these measurements under conventional heating, but at least this provides complementary diffraction data for the same sample, undergoing the β to α transition, and points out problems in refining data for the low temperature phase in both cases.

7.2 Experimental procedure

Samples of AgI (Aldrich, 99%) were loaded into a 1-mm external diameter glass capillary (80 mm length, glass No.50, Hampton Research). The mass of both atoms in silver iodide is relatively high, so relatively small amounts of the sample were used to avoid significant X-ray absorption. Around 2.5 - 3 cm of the capillary length was partially loaded with the much less absorbing material α-Al_2O_3 (corundum, Aldrich, 99% 100 mesh), after which a small amount of β-AgI was loaded. The fibre optic sensor was then attached to the capillary so that its tip was in close contact with the sample and it was fixed in place using Teflon™ tape. The capillary was mounted on the goniometer head and then the microwave cavity applicator was attached using two metallic stands to maintain the aligment of the cavity with the instrument and the X-ray beam at all times. Details of the configuration of the microwave cavity set-up for these experiments can be found in Chapter 3.

Microwave heating was applied to the samples to take them to different temperatures and the temperature was then kept constant while the diffraction pattern was taken. The rotation mechanism of the goniometer head suffered a mechanical problem during the experiments so no rotation of the samples was possible for these measurements. Errors arising from this problem might be manifested for samples in general in Rietveld refinement as anomalous values for parameters such as a preferred orientation; however, for a finely ground powder sample, particularly in the cubic phase, this was not anticipated as likely to produce major problems.

Initial experiments revealed a very strong reflection at approximately 45° which was attributed to scattering from the microwave cavity. In the case of the experiments carried out with AgI scans were run over the range $21° < 2\theta < 44.5°$, which covered key characteristic reflections of α and β. A scan speed of $0.004125° \text{ sec}^{-1}$ was used, which gave data of sufficient quality for structure refinement. The evolution of peaks in the selected 2θ region was followed for the AgI samples on heating and indexed using the CDS[122] data base as described in other chapters.

Neutron powder diffraction measurements with conventional heating were performed on the same sample on the HRPD at the ISIS Facility of the Rutherford-Appleton Laboratory using the same equipment described earlier in Chapter 5.

7.3 Results

7.3.1 Preliminary results for X-ray diffraction during microwave heating

The first experiments were performed on a sample of β-AgI heated with microwave radiation at a rate of 5 K min^{-1} -and an initial set point power of 250 W- to test whether the microwave cavity set-up delivered power to the sample with good control. The results are shown in figure 7.1 where it can be observed that once the set temperature was reached, the power levels dropped and the sample is kept at a constant temperature (figure 7.1(B)).

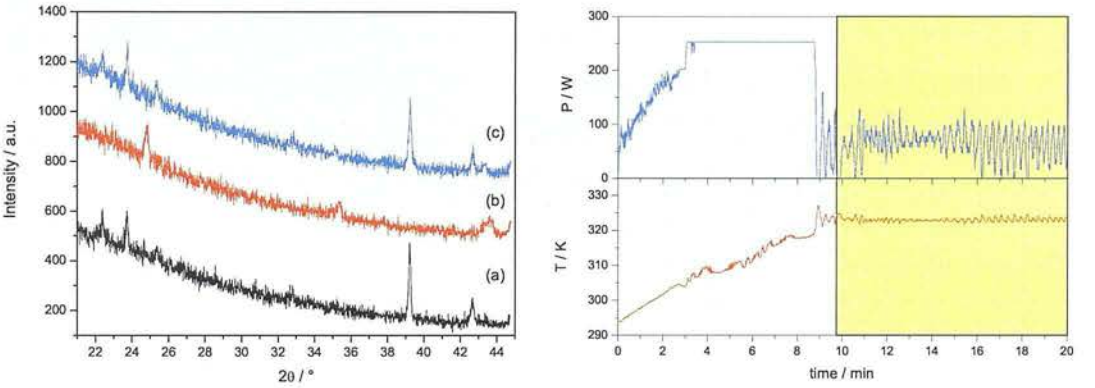

(A) (B)

Figure 7.1: Diffraction patterns (A) and temperature and power versus time graph (B) for β-AgI heated with microwave radiation at a rate of 5 K min^{-1} with a maximum achievable power of 250 W. (a) Sample at 293 K, before heating , (b) sample at 323 K and, (c) sample at 303 K, after heating. The lower part of (B) displays the temperature of the sample during the heating ramp, while the upper part shows the corresponding power level. The shaded part of this figure indicates the temperature and power levels during the time when the diffraction pattern was taken.

Next a second set of experiments using a fresh sample was carried out under the same conditions (5 K min^{-1}) but the maximum achievable power was set at a lower level (200 W) and the cavity tuned accordingly. Patterns were then recorded during heating from 298 to 426 K, then back down again, both under microwave irradiation. The sequence of diffraction patterns, together with the corresponding temperatures and mi-

crowave power levels, are shown in figure 7.2. A thermocouple (type K) was attached to the outside wall of the cavity giving us an indication of any heat losses (see figure 7.2(B)).

These measurements show that the temperature at which the β to α transition starts is at around 345 K (figure 7.2(A-c)) where the reflections of the α phase are clearly observed. The transition seems to be complete at around 413 K (figure 7.2(A-f)) - almost 10 K below that reported for conventionally heated samples. Unfortunately the quality of the data for these experiments - compromised partly by reflections from the applicator, and also by the relatively modest detected intensity - did not allow us to perform structure refinement with acceptable precision. The extra features observed in the diffraction pattern around the region $30^\circ < 2\theta < 38^\circ$ were seen to be due to scattering from the Teflon of the fluoroptic sensor tip as can be seen in figure 7.3. The fact that the reflections from the Teflon in the fibre optic sensor were detected also gives an indication of the position of the sensor with respect to sample, and gives us some confidence in the accuracy of the temperature measurements.

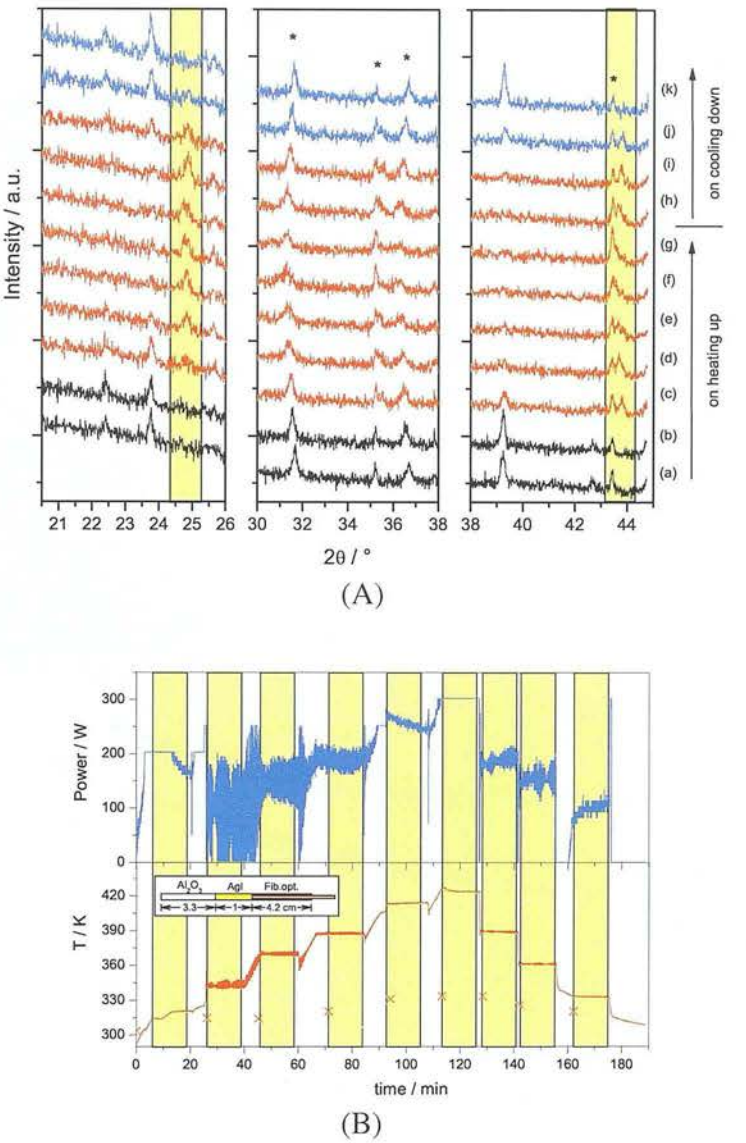

Figure 7.2: (A) Diffraction patterns and (B) temperature and power versus time for AgI on heating up to (a) 298 K, (b) 313-320 K, (c) 345 K, (d) 371 K, (e) 387 K, (f) 413 K and, (g) 426 K and then cooling down to (h) 389 K, (i) 361 K, (j) 333 K and, (k) 242 K with microwave radiation. The asterisks (*) denote the reflections for PTFE in the fibre optic temperature probe, and the shadowed areas the α-AgI reflections. In part (B) the lower section displays the temperature of the sample during the heating ramp, while the upper part shows the corresponding power level. The shaded part of this figure indicates the temperature and power levels during the time when the diffraction pattern was taken. The inset to (B) shows the arrangement for the sample in the capillary. The temperature measured at single point outside the cavity wall is shown as red scattered red crosses.

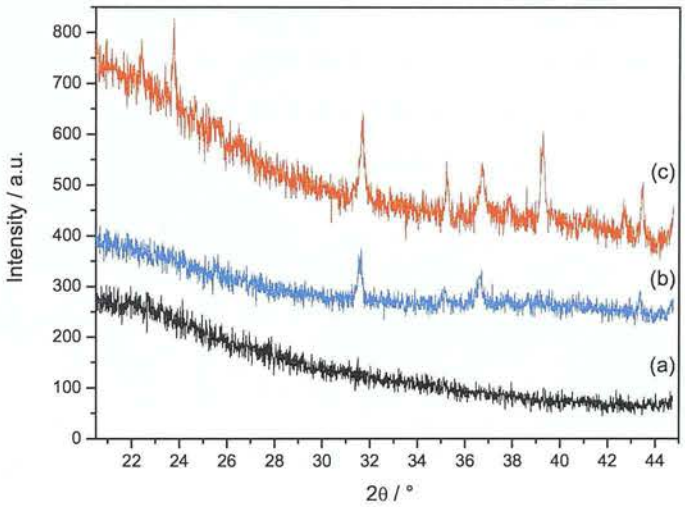

Figure 7.3: Diffraction pattern for (a) empty glass capillary, (b) fibre optic inside glass capillary and, (d) glass capillary filled with the β-AgI and fibre optic temperature sensor. This indicates clearly the presence of reflections from PTFE from the fibre optic temperature probe in patterns for β-AgI used in our microwave experiments.

7.3.2 X-ray diffraction during microwave heating

A second set of experiments was carried out on AgI to explore more carefully the transition, and the observation of co-existing phases near the phase transition. The simplest rationalisation of the observation of co-existing phases is that the sample temperature is not homogeneous, and in order to reduce the possibility of local heating or overheating by the microwave radiation, the experiment was carried out yet more slowly, at lower power levels. The sample was heated in two stages (over two days) at a rate of 2 K min^{-1} from 297 K to 380 K. The initial power level was set to be 100 W and tuning was applied accordingly. During the break between the two heating stages, the sample cooled down to room temperature, but on continuing the measurements for stage 2, it was warmed back up again to the next point in the sequence at the same rate of 2 K min^{-1}. The graphs of power and temperature versus time for this experiments are shown in figure 7.4. The results of these experiments are shown in figure 7.5.

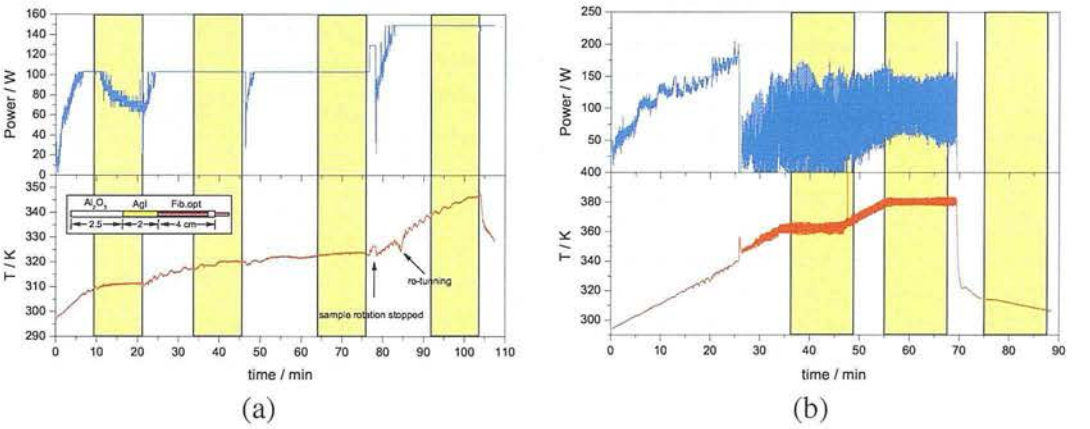

Figure 7.4: Power and temperature vs time for a sample of AgI heated with microwave radiation. Two days experiment. (a) Sample heated from 297 K to 346 K at 2 K/min and, (b) same sample as (a) the next day heated at the same rate from 293 K to 380 K. Shadowed areas represent the times were the diffraction patterns where taken. The inset in (a) shows the sample arrangement inside the capillary for this experiment.

The results showed again a reduction in temperature for the complete transformation of the β to the α phase in AgI at around 363 K which is compatible with the previous results. In this case there is no temperature at which peaks from the two phases can be seen to co-exist (figure 7.5 (d')).

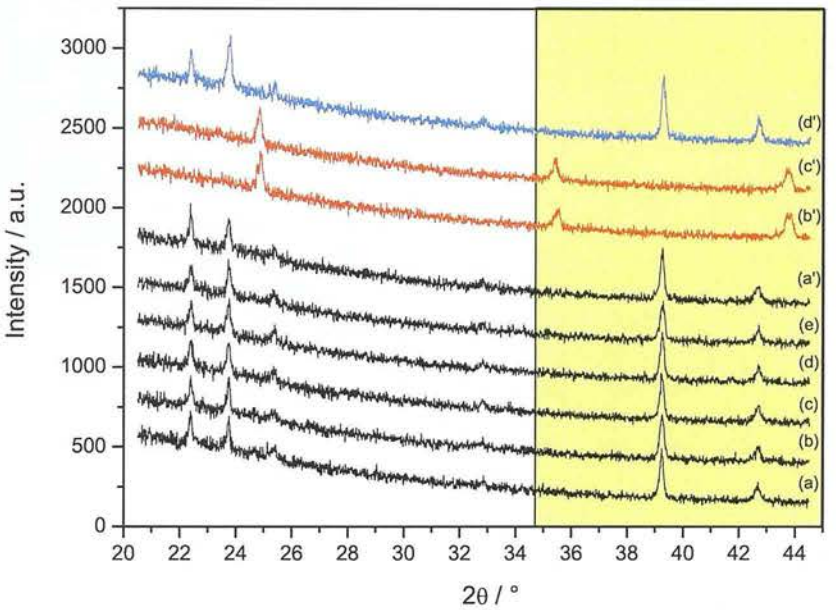

Figure 7.5: Diffraction pattern of AgI during heating in two stages (heating rate: 2 K min^{-1}) with microwave radiation. First heating stage (a) 297 K, (b) 309 K, (c) 319 K, (d) 323 K, (e) 346 K; and, second heating stage (second day): (a') 293 K, (b') 363 K (c') 380 K and (d') after microwave radiation: 310 K. The sample was also heated at 2 K min^{-1} between runs (e) and (a'). The shadowed area shows the reflections used for the Gaussian fit shown in 7.9.

7.3.3 Neutron diffraction during conventional heating

Powder neutron diffraction patterns were recorded with conventional heating from 363 K to up to 443 K, and the results are shown in figure 7.6. It was observed that the transition starts at a temperature between 418 and 423 K (figure 7.6(d) and (e)).

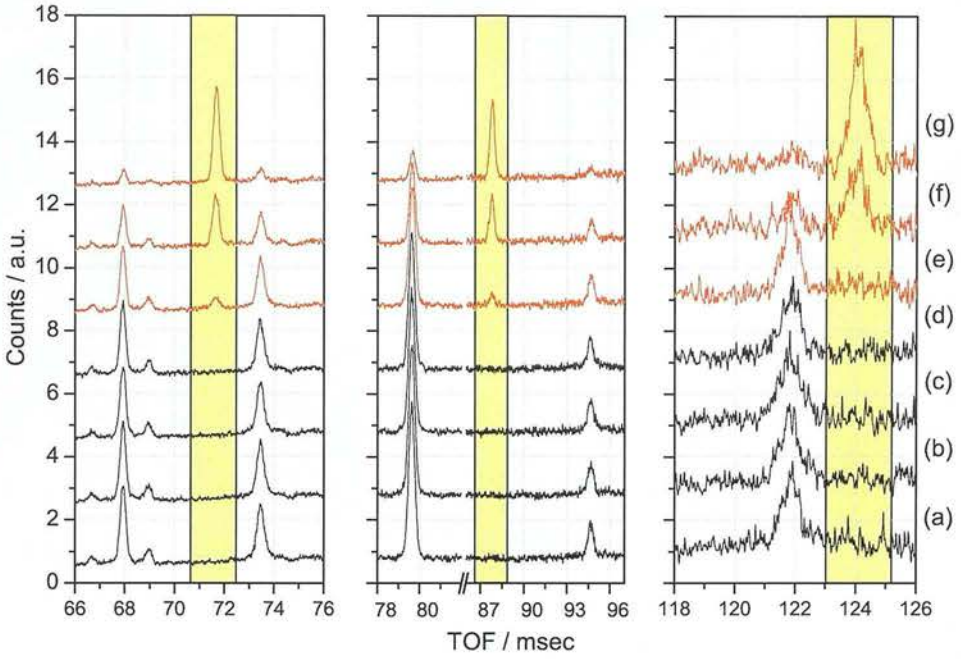

Figure 7.6: Neutron diffraction patterns of AgI during conventional heating. (a) 363 K, (b) 383 K, (c) 403 K, (d) 418 K, (e) 423 K, (f) 433 K (g) 443 K. The shadowed area shows the (200) and (211) reflections for α-AgI.

The diffraction patterns from both ways of heating were used for structure refinement analysis and the results are presented in the next section.

7.3.4 Rietveld refinement for AgI diffraction data

The Rietveld refinement graphs obtained for both conventional and microwave heating in both high- and low-temperature phases are shown in figure 7.7(a) - (d). This indicates poor fits for the samples where only the low temperature phase is present - figure 7.7(a) and (c)- and almost no difference between the observed and the calculated patterns for the high-temperature phase (as seen in the difference curve at the bottom of each graph) -figure 7.7(b) and (d)-. This is reflected in the shape of the curve for cumulative χ^2 shown in all graphs, giving an idea of the quality of the refinement.

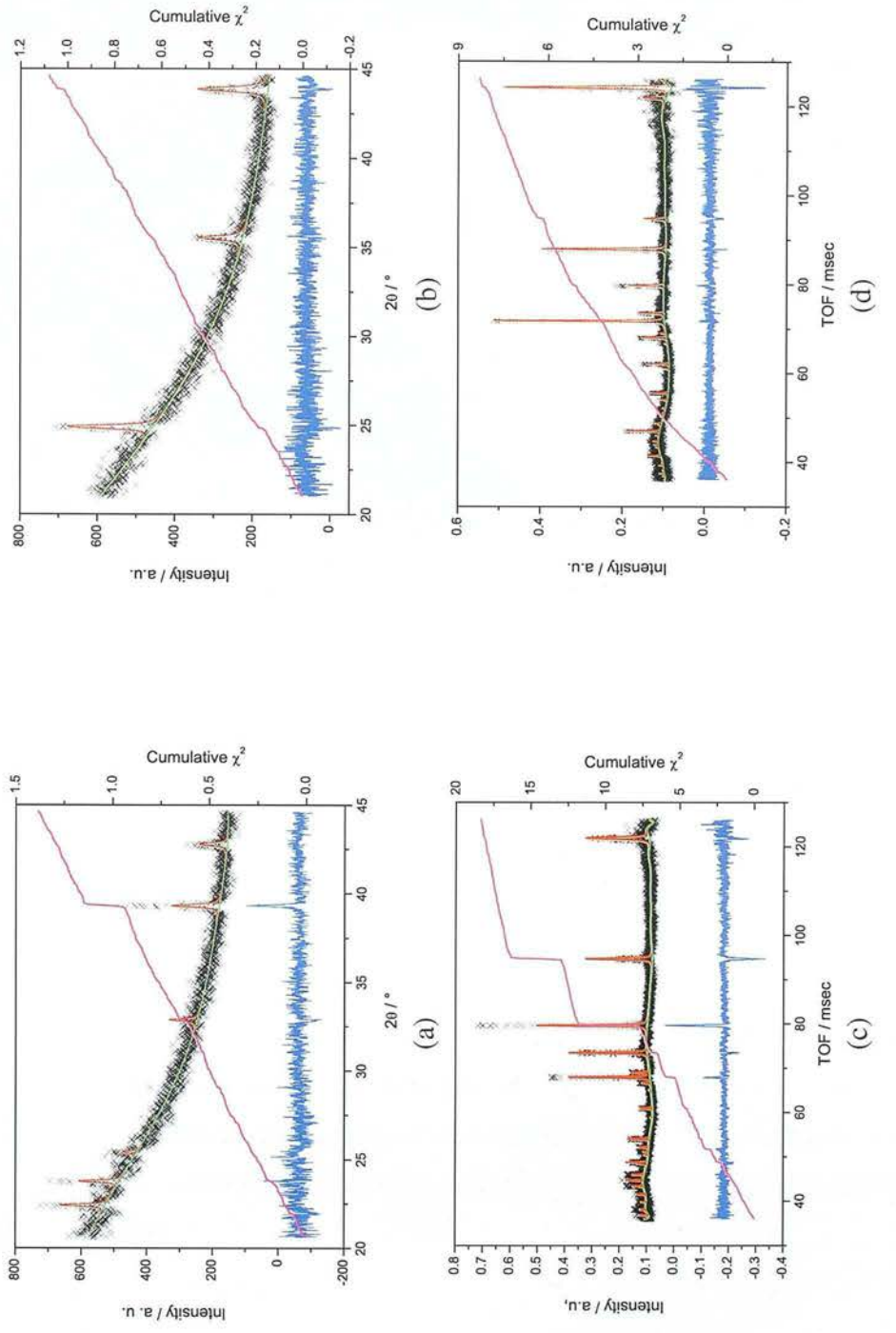

Figure 7.7: Rietveld refinement graphs for β- and α-AgI for *in situ* X-ray diffraction during microwave heating and neutron diffraction during conventional heating. X-ray diffraction with microwave heating at (a) 297 K and (b) 363 K, and neutron diffraction with conventional heating at (c) 363 K and (d) 443 K. The small crosses represent the observed pattern, the red and green continuous lines represent the calculated pattern and background respectively, the difference between the calculated and the observed pattern is shown as the bottom line in blue, while the cumulative χ^2 is shown in magenta.

The cell parameters determined by Rietveld refinement for AgI from these patterns are plotted in figure 7.8. The results from the Rietveld refinement can be found in figures F.1 - F.2 in Appendix F.

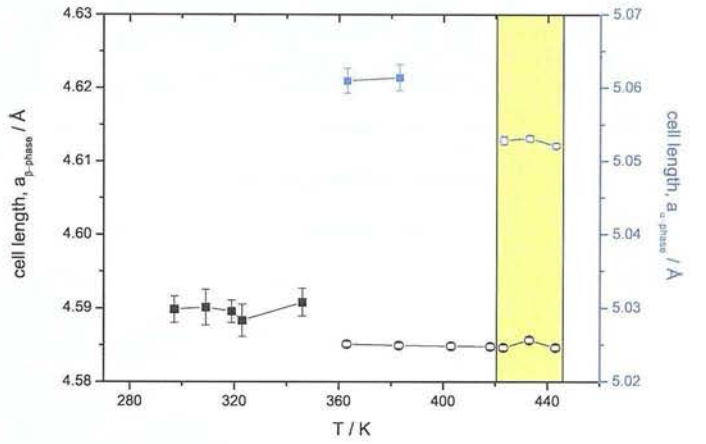

(A)

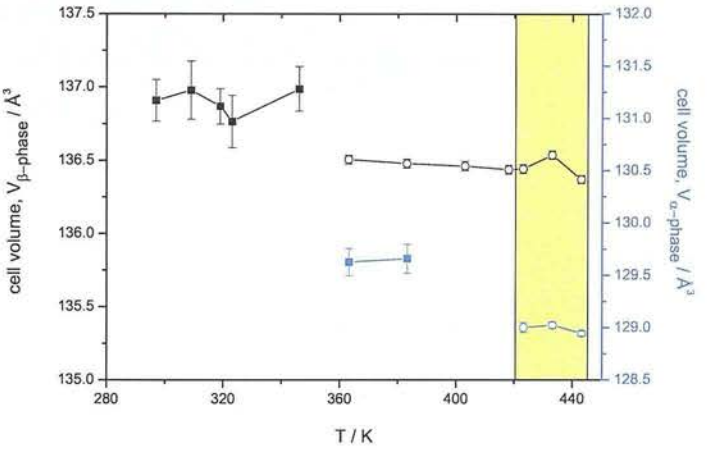

(B)

Figure 7.8: Cell length (A) and volume (B) for AgI determined by Rietveld refinement with X-ray diffraction during microwave heating (■, ○) and neutron diffraction during conventional heating (■, ○). The shadowed area marks the temperature range where both phases are present during conventional heating.

7.3.5 Gaussian fit for AgI diffraction data

A different approach was taken then to analysing this results. As it was seen in Chapter 5 the analysis of peak individual reflections can lead to useful information such as relative amount of a particular phase (extract from the peak height); information about properties of the material such as strain and domain size (breadth); and may indicate some cell parameter (peak position). For this reason, for this part of the analysis we choose to use a general curve-fitting program (OriginPro, v7.5) to treat two reflections for both β- and α-AgI phases and both heating methods. In this case, the best fit was obtained for a Gaussian curve which is described as a bell-shape curve like the normal probability distribution function.

$$y = y_0 + \frac{A}{w\sqrt{\pi/2}} \exp \frac{-2(x - x_0)^2}{w^2} \tag{7.1}$$

where

y_0 is the baseline offset,

A is the total area under the curve from the baseline,

x_0 is the centre of the peak,

w is 2σ, approximately 0.849 the width of the peak at half height.

The graphs and the fitting parameters for these experiments for various reflections can be found in figures F.3 - F.6 and table F.1 - F.4 in Appendix F.

The results for peak position, width, area and height determined in this way are shown in figures 7.9 and 7.10.

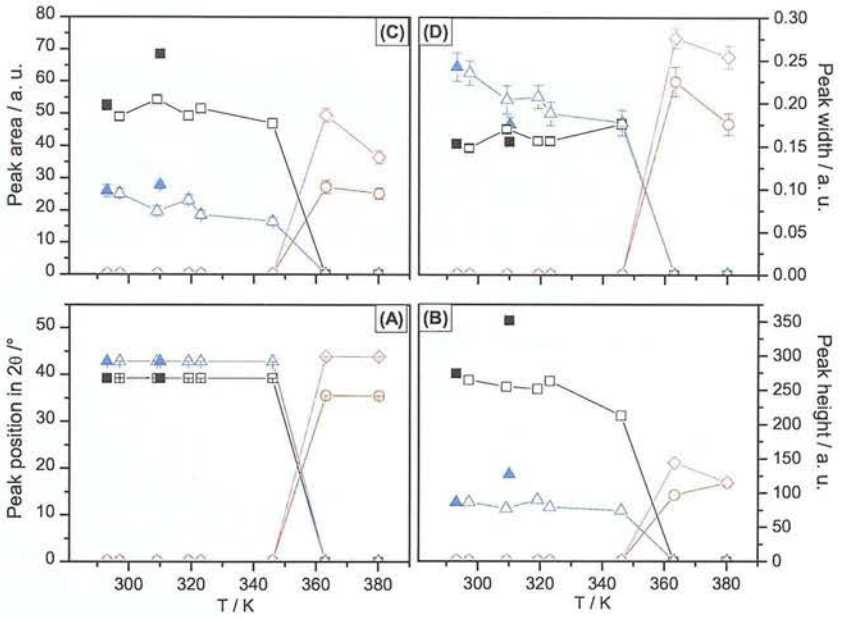

Figure 7.9: Results of Gaussian fit for (A) peak position, (B) height, (C) area and (d) width for a sample of AgI heated with microwave radiation. Symbols represent: β-AgI reflections (110) □, (103) △ and, α-AgI reflections: (200) ◇ and (211) ○.

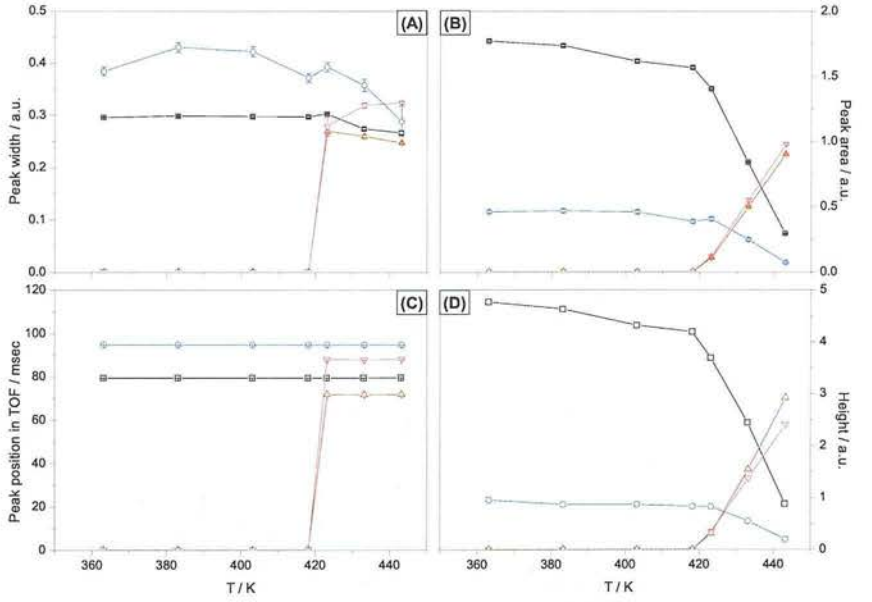

Figure 7.10: Results of Gaussian fit for (A) peak position, (B) height, (C) width and, (D) area for neutron diffraction patterns on AgI heated with conventional heating. Symbols represent: β-AgI reflections (110) □, (102) ○ and, α-AgI reflections: (211) △ and (200) ▽.

7.4 Conclusion

Our *in situ* experiment demonstrated the ability of the new apparatus to hold the sample temperature steady for a sample with a very non-linear response to microwave radiation. This enabled us to confirm a striking depression of the temperature for the β to α transition in AgI in such a field. Future measurements are required to determine more detailed structural features in both phases. This might provide information about anomalous cation distributions, both static and dynamic: both factors are believed to play a role in this particular structural transition, and it is conceivable that both may be influenced by the presence of the microwave field. Complementary theoretical work is also desirable to explore the possible mechanisms of photon-phonon and phonon-phonon interactions in this system.

Chapter 8

Conclusions and future work

The principal outcomes of this work, with some suggestion for further work, are as follows.

- We have designed, built and tested new microwave applicators that will enable studies of structural and chemical transformations to be performed during microwave irradiation. Applicators with rectangular cross-section have been developed for use in conjunction with both X-ray and neutron powder diffractometers, and both improve on previous designs[69,113]. A stepper motor enables the cavity length to be controlled, providing a greater degree of control over microwave power. Although the rectangular cross-section is less ideal with respect to correcting for the background than is a circular cross-section in neutron scattering, this is a relatively easy correction to make well, and the resulting microwave optics are more straightforward and provide better control. An applicator has been built for capillary samples and shown to provide excellent control of power and hence temperature, even for samples with sharply rising dielectric susceptibility as a function of temperature. One key further development that would desirable for all of these applicators is the provision of complementary, conventional methods of heating - for example through a hot gas stream - enabling better comparison to be made between the two heating methods, and also offering the possibility of hybrid heating. The capillary applicator is suitable for mounting at a synchrotron X-ray source, enabling faster, higher-resolution measurements to be made. Further, this apparatus may also be adapted to look at reactive systems, for example hydrothermal reactions, as indicated in the next section.

- We have established a set of conditions under which the zeolite ZSM-5 may be grown efficiently under microwave irradiation, in some cases offering significant advantages over conventional methods. The aim of this work is ultimately to explore why microwave heating drives this type of synthesis faster than conventional heating, using *in situ* diffraction and this is clearly still at an early stage. We made a preliminary trial (not reported in Chapter 4) of the feasibility of performing such measurements on a sealed-tube, laboratory-based X-ray diffractometer, and found that the detected flux was too low for practical kinetic work indeed it was a considerable challenge to see any signal from a crystalline sample suspended in water and held in a glass or PEEK capillary. A synchrotron X-ray source is clearly required to progress. Further, to perform meaningful kinetic measurements, we should also determine the temperature of the sample. One way of doing this would be to seal a fluoroptic probe into the reaction vessel for example using technology similar to that used to make seals with high-pressure liquid chromatography tubing.

- We looked at one example of post-synthetic processing of a zeolite by microwave-driven solid-state ion exchange with $CuCl_2\ 2H_2O$ and showed that some earlier work using X-ray diffraction to assess the degree of uptake was probably flawed through the loss of some of the signal from the $CuCl_2\ 2H_2O$ through dehydration in the microwave field. This is one example of many processes in zeolites that could be studied by *in situ* diffraction, again ideally at a synchrotron X-ray source using the capillary heating stage. It would also be interesting to explore the possibility of microwave-assisted template removal: in principle, microwave radiation could be directed at template molecules that possess a dipole, and perhaps absorbed preferentially in relation to the host lattice (clearly, this will depend on the presence of other potentially absorbing molecules such as water); this could then lead to enhanced diffusion or break-up of such molecules under gentler conditions than are common for conventional calcining, and perhaps preserving structures that might otherwise collapse under more robust treatment. Such work is not restricted to zeolites and there is a wide range of porous or layered materials for which microwave radiation may provide a better means of driving insertion/deinsertion processes.

- We have performed *in situ* diffraction measurements on phase transitions under microwave irradiation in the ferroelectric materials $BaTiO_3$ and $KNbO_3$ and

demonstrated that such measurements are feasible with a sealed-tube, laboratory-based X-ray diffractometer. We also found some evidence for a lowering of the transition temperature in $KNbO_3$ and an indication that the temperature is inhomogeneous across the sample. In both cases a more careful study is needed of more subtle structural features, such as peak shape and ADPs, which provide information about strain and perhaps anomalous static and dynamic distortions of the structure. Complementary theoretical work could play a valuable role here in elucidating just which phonons the microwaves couple to, and just how the energy imparted to the lattice in this fashion is redistributed. This would help to answer the question of whether microwave fields of the strengths used in synthesis can affect the phonons significantly in relation to the density of states expected at the same temperature with conventional heating.

- We have provided the first direct indication that support-metal catalysts and related materials - can be appreciably hotter than an insulating support during microwave irradiation. This work has been submitted for publication (Nature Materials (submitted, 2006)) The question of how this is possible in view of the nature of heat flow across thermal gradients was raised, and it was suggested that this could arise from fluctuations in the power of the microwave radiation. One next step in such work would therefore be to aim to deliver microwave power with a range of temporal behaviour, as well as to study and wider range of systems to try to reproduce the effects we saw.

- We have provided the first well-controlled measurement of the change in structure of AgI across the β-α transition as a function of temperature during microwave irradiation. This confirmed previous reports that the transition temperature may be significantly reduced relative to that for conventional heating, and raises the question of the mechanism of such a process. The next stage in this work should be a combined theoretical and experimental one. The β-α transition is known to be influenced by the presence of Frenkel defects involving the highly-polarised silver ions, and these may well couple strongly to the microwave field. Theory might elucidate the nature, strength and consequences of any coupling, while with X-ray or neutron scattering experiments on single crystals could be used to probe static and dynamic changes in structure, including that of the defects in the material.

Appendix A

Mathematical functions for GSAS

The following are the profile functions for constant wavelength X-ray diffraction and Time of flight (TOF) neutron diffraction used for Rietveld refinement in the GSAS[52] (General Structure Analysis System) suit of programs.

The contribution of a the intensity of a Bragg peak to a particular profile intensity will depend on: the structure factor and the amount of that particular phase; the peak shape and the width in relation to its position, the extinction factor, the absorption and, some geometric factors.

The profile coefficients from the Rietveld refinement with GSAS can give information about the microtexture of the sample as detailed below.

A.1 X-ray diffraction functions

The profile function used for constant wavelength (CW) measurements employs a multi-term Simpson's rule integration of the pseudo-Voigt, $F(\Delta T)$

$$H(\Delta T) = \sum_{i=1}^{n} g_i F(\Delta T') \tag{A.1}$$

where the pseudo-Voigt is

$$F(\Delta T') = \eta L(\Delta T', \Gamma) + (1-\eta) G(\Delta T', \Gamma) \tag{A.2}$$

The variance of the peak shape, σ^2, varies with 2θ as

$$\sigma^2 = U\tan^2\theta + V\tan\theta + W + \frac{P}{\cos^2\theta} \tag{A.3}$$

where U, V, W are the Cagliotti, Pauletti and Ricci coefficients and P is the Scherrer coefficient for Gaussian broadening and the Lorentzian coefficient, γ, varies as

$$\gamma = \frac{X + X_s\cos\phi}{\cos\Theta} + (Y + Y_e\cos\phi)\tan\Theta \tag{A.4}$$

from which the first term is the Lorentzian Scherrer broadening which includes an anisotropy coefficient, X_e, and the second term describes the strain broadening and also includes an anisotropy coefficient.

This function gives a better fit to asymmetric profiles and shows less correlation with the lattice parameters.

A.2 Neutron diffraction functions

The relationship between the $d-spacing$ for a particular powder line and its TOF, T_{ph} is:

$$T_{ph} = DIFC\,d_p + DIFA\,d_p^2 + ZERO \tag{A.5}$$

where $DIFC$, $DIFA$ and $ZERO$ are characteristic of a given counter bank on a TOF (μsec) diffractometer. $DIFC$ (μsec/Å) may be calculated from:

$$DIFC = 252.816 * 2\sin\theta\left(L_1 + \sqrt{L_2^2 + \frac{L_3^2}{16}}\right) \tag{A.6}$$

where:

θ is the Bragg angle,

L_1 is the primary flight path (m),

L_2 is the sample to detector centre distance (m),

L_3 is the height of the detector (m).

The profile function used for the TOF neutron refinement experiments was the Ikeda-Carpenter function convoluted with a pseudo-Voigt to give the full peak shape function:

$$H(\Delta T) = \int P(\Delta T - t) I_K(t) dt \tag{A.7}$$

The pseudo-Voigt is defined as a linear combination of a Lorentzian

$$P(t) = \eta L(t,\Gamma) + (1-\eta) G(t,\Gamma) \tag{A.8}$$

the Gaussian part being

$$G'(\Delta T) = \int G(\Delta T - t) I_K(t) dt \tag{A.9}$$

and the Lorentzian part

$$L'(\Delta T) = \int L(\Delta T - t) I_K(d) dt \tag{A.10}$$

The profile coefficients are defined by

$$\alpha = \frac{1}{\alpha_o + \alpha_1 \lambda} \tag{A.11}$$

$$\beta = 1/\beta_o \tag{A.12}$$

$$R = \exp\left(\frac{-81.799}{\kappa\lambda^2}\right) \tag{A.13}$$

$$\sigma^2 = \sigma_o^2 + \sigma_1^2 d^2 + \sigma_2^2 d^4 \tag{A.14}$$

$$\gamma = \gamma_o + \gamma_1 d + \gamma_2 d^2 + (\gamma_{1e} d + \gamma_{2e} d^2)\cos\phi \tag{A.15}$$

with the strain effecting the second term (γ_1). Assuming the instrumental contribution to be Gaussian (which means no correction for the instrumental contribution is needed)

the isotropic strain, S, can be defined as:

$$S = \frac{1}{C}\gamma_1 * 100\% \tag{A.16}$$

while the corresponding Lorentzian particle size broadening appears in the third term (γ_2) so the particle size, p will be given by:

$$p = \frac{CK}{\gamma_2} \tag{A.17}$$

Appendix B

Equipment design diagrams

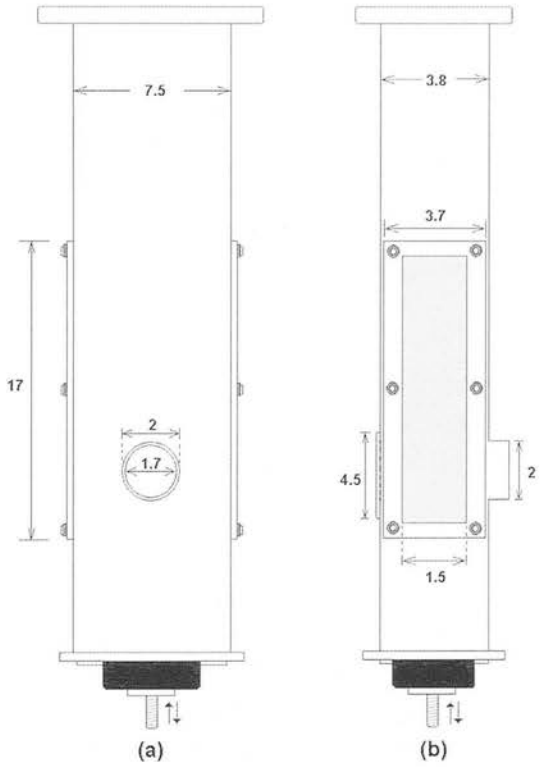

Figure B.1: Microwave rectangular waveguide dimensions for *in situ* X-ray/neutron diffraction studies. (a) Front view and, (b) lateral view. Refer to figure 3.4 in Chapter 3 for a more detailed description of this microwave applicator. Measurements are in centimetres.

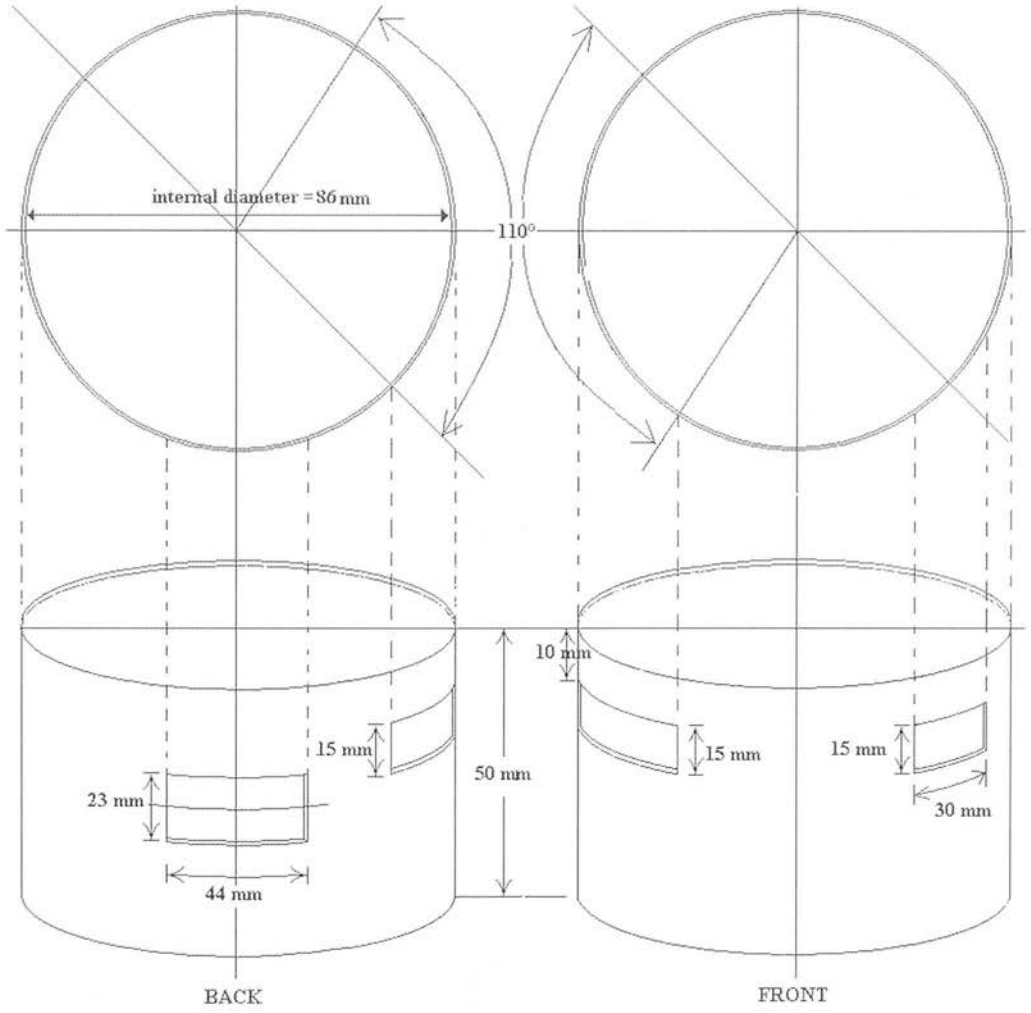

(a)

Figure B.2: Microwave resonant cavity for *in situ* X-ray diffraction studies on sample in capillaries giving dimensions of (a) body of cavity.

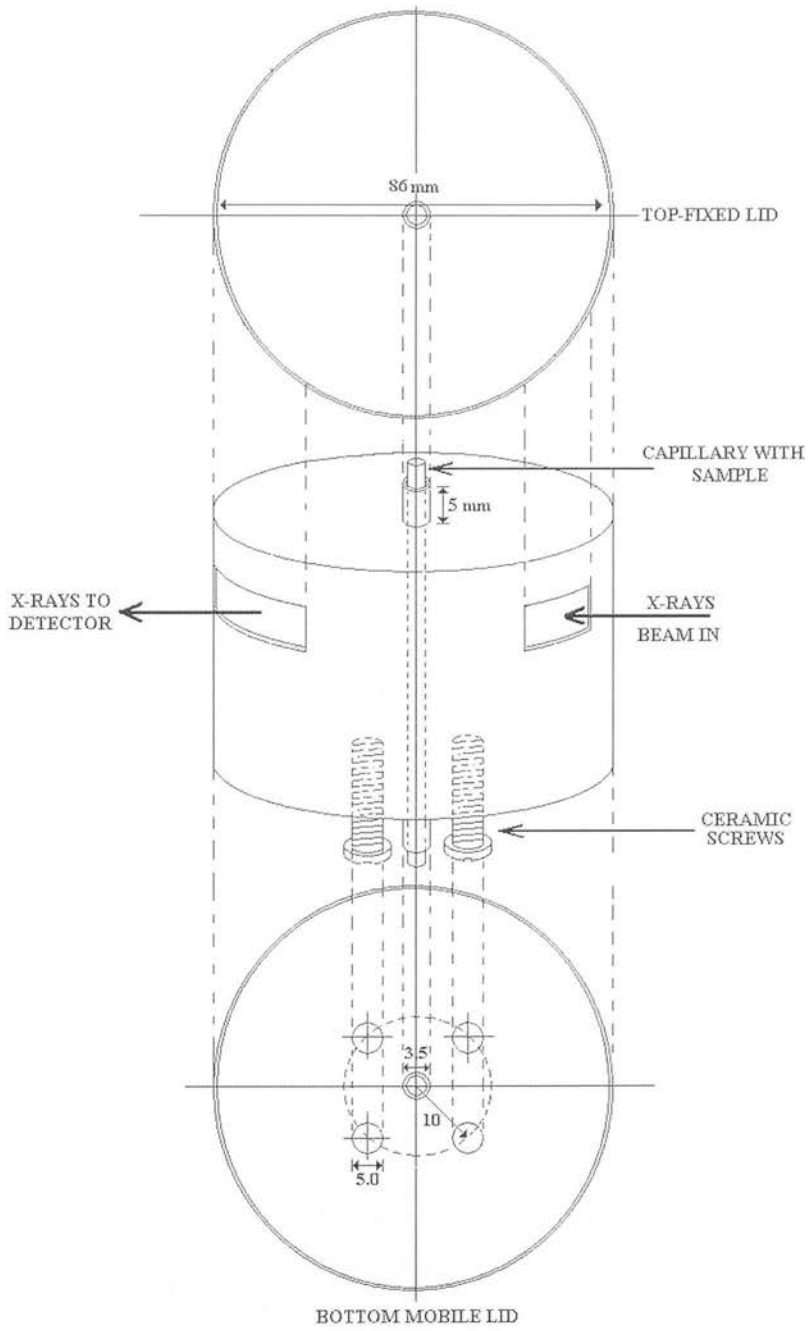

(b)

Figure B.2: (Cont). Microwave resonant cavity diagrams for *in situ* X-ray diffraction studies on sample in capillaries giving dimensions of (b) bottom and top of cavity.

Appendix C

Microwave synthesis and modification of zeolites

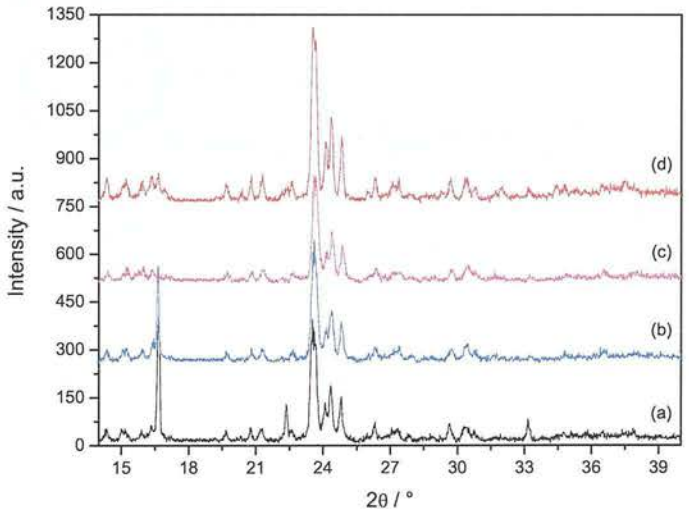

Figure C.1: *In situ* X-ray diffraction patterns of 10% $CuCl_2$ $2H_2O$-ZSM-5 before and after microwave heating. (a) before processing, (b) after microwave irradiation from 323 to 393 K, (c) after microwave radiation from 393 to 403 K, and (d) after further exposure to air overnight.

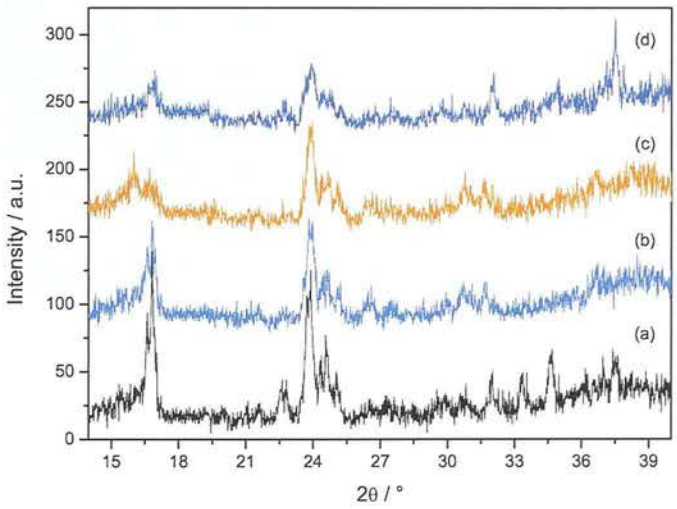

Figure C.2: *In situ* X-ray diffraction patterns of 32% $CuCl_2$ $2H_2O$-ZSM-5 before and after microwave heating. (a) before processing, (b) after microwave irradiation from 323 to 413 K, (c) after microwave radiation to 413 K, and (d) after further exposure to air overnight.

The number of moles of Cu^{2+} within a sample are determined by placing the long moment value, m, determined by the SQUID (Superconducting Quantum Interference Device) magnetron into equation C.1 and the magnetic susceptibility, χ_m, (equation C.2) of Cu^{2+} at 300 K.

$$\chi_m = \frac{m}{Hn} \tag{C.1}$$

$$\chi_m = \frac{3}{8T} \tag{C.2}$$

where,

χ_m is the molar magnetic susceptibility (in electromagnetic units, EMU mol^{-1}),

m is the magnetization of the sample (EMU),

H is the applied electric field (Gauss) and,

n is the number of moles of magnetic ions within the sample.

Results are shown in table C.1 for a sample treated with microwave radiation at different irradiation times.

Table C.1: Raw SQUID data for microwave heated solid state $CuCl_2$ $2H_2$ absorption in ZSM-5.

Time / min	Sample mass / g	Long moment x 10^5 / EMU	Moles x 10^5	Cu conc. / moles g^{-1}
0	0.0503	3.15	2.52	0.5004
10	0.0538	4.06	3.25	0.6037
20	0.0384	2.43	1.94	0.5056
30	0.0380	1.65	1.32	0.3465
45	0.0490	3.60	2.88	0.5878
60	0.0412	3.14	2.51	0.6088

Appendix D

Rietvel refinement results for $BaTiO_3$ and $KNbO_3$

D.1 $BaTiO_3$

D.1.1 Rietveld refinement of X-ray diffraction patterns

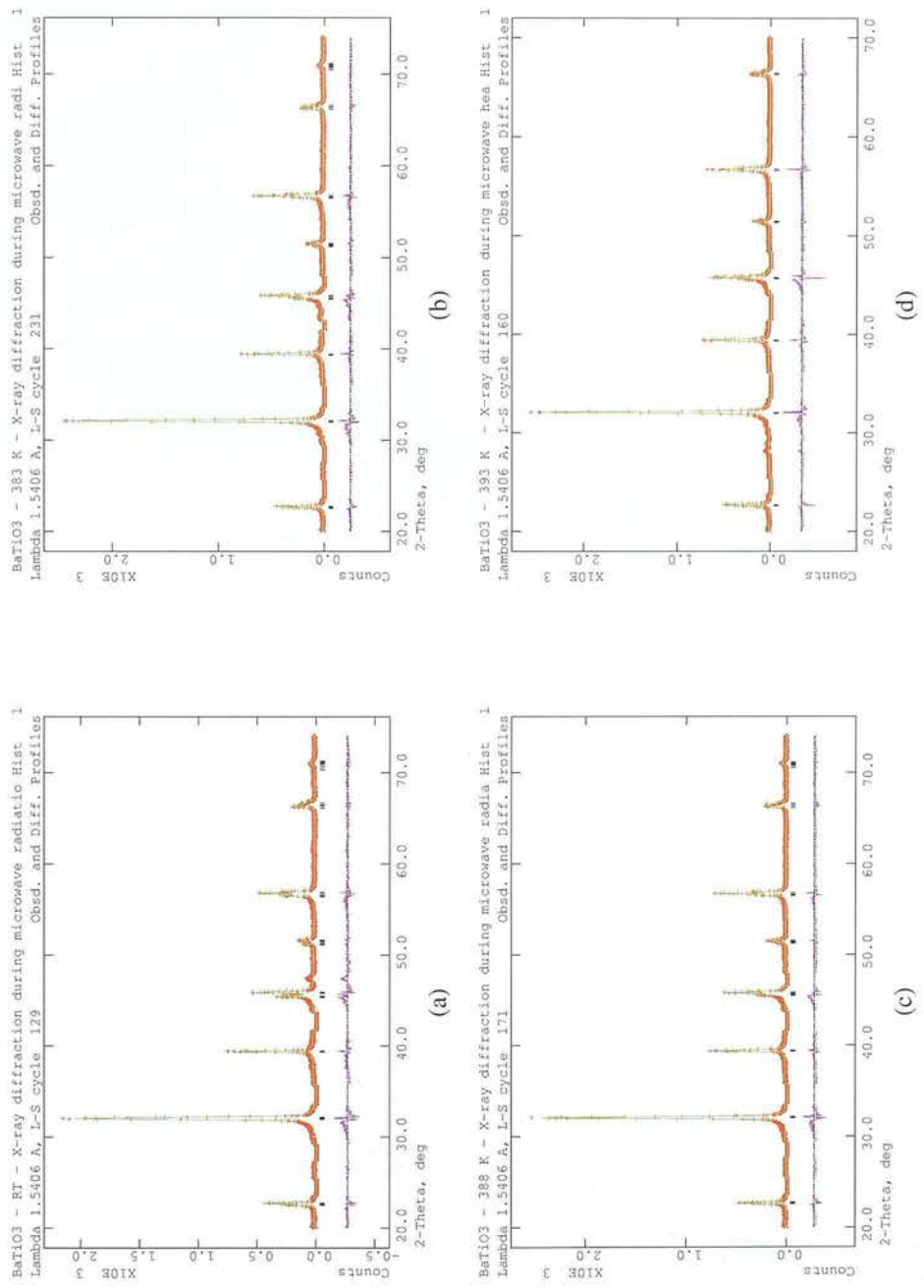

Figure D.1: Rietveld refinement graphs for $BaTiO_3$ for X-ray diffraction during microwave heating. (a) 295 K, (b) 383 K, (c) 388 K and, (d) 393 K. The small red + represent the observed pattern, the green continuous line represents the calculated pattern and the difference between the calculated and the observed pattern is shown in the bottom graph (in magenta). The tick marks show the reflections for the tetragonal phase.

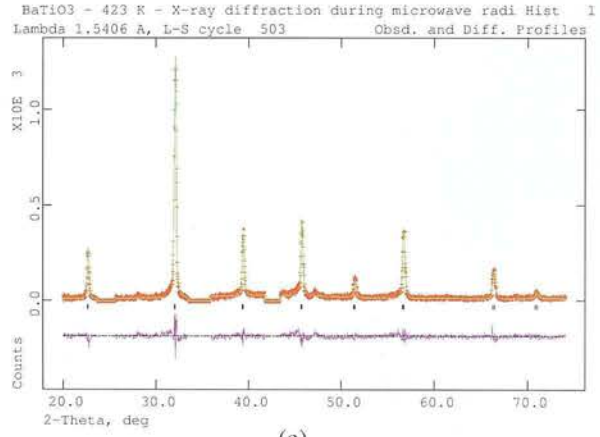

(e)

Figure D.1: (Cont). Retailed refinement graphs for $BaTiO_3$ for X-ray diffraction during microwave heating. (e) 423 K. The small red + represent the observed pattern, the green continuous line represents the calculated pattern and the difference between the calculated and the observed pattern is shown in the bottom graph (in magenta). The tick marks show the reflections for the tetragonal phase.

D.1.2 Lorentzian fitting of X-ray diffraction peaks on the region from 43 to 48° in 2θ

The Lorentzian model use describes a bell-shape curve like the normal probability distribution function with the form;

$$y = y_0 + \frac{2A}{\pi}\frac{w}{4(x-x_0)^2+w^2} \tag{D.1}$$

where:

y_0 is the baseline offset,

A is the total area under the curve from the baseline,

x_0 is the centre of the peak,

w is the full width of the peak at half height.

Table D.1 and table D.1 shows the results obtained after fitting - using the Lorentzian function describe above (equation D.1)- two $BaTiO_3$ diffraction peaks in the region from 43 to 48° in 2θ. The diffraction peaks fitted are those shown in figure 5.5 and figure 5.6 found in Chapter 5, section 5.2.1.

Table D.1: Lorentz fit parameters obtained for $BaTiO_3$ peaks in the region 43 to 48° in 2θ in figure 5.5 (Chapter 5). Parameters are defined from equation D.1.

Temperature / K	χ^2	y_0	xc_1	w_1	A_1	xc_2	w_2	A_2
293	122.07	5.47	45.36(0.01)	0.32(0.02)	65.37(5.16)	45.82	0.20(0.01)	76.73(3.33)
373	151.11	9.53(3.91)	45.28(0.01)	0.38(0.05)	53.09(8.04)	45.75	0.20(0.01)	65.89(4.55)
383	126.15	11.57(3.61)	45.46(0.01)	0.36(0.05)	47.36(7.99)	45.75	0.19(0.01)	68.20(4.65)
393	187.83	0	45.43(0.07)	0.83(0.05)	78.72(17.17)	45.71	0.23(0.02)	73.87(11.57)
403	226.13	15	45.65	0.25	100.51(2.71)			
413	273.99	16	45.48	0.24	97.34			

Table D.2: Lorentz fit parameters obtained for $BaTiO_3$ peaks in the region 43 to 48° in 2θ in figure 5.6 (Chapter 5). Parameters are defined from equation D.1.

Temperature / K	χ^2	y_0	xc_1	w_1	A_1	xc_2	w_2	A_2
378	118.03	14	45.43(4.34)	0.33(0.036)	43.43(4.34)	45.74(74)	0.20(0.01)	65.89(3.50)
381	152.05	13	45.45(0.02)	0.41(0.05)	51.19(8.39)	45.73	0.20(0.01)	63.68(6.44)
383	139.22	16	45.46(0.02)	0.407(0.05)	46.39(7.48)	45.73	0.18(0.01)	59.23(5.58)
385	160.80	15	45.43(0.01)	0.31(0.05)	34.45(5.92)	45.72	0.22(0.01)	72.88(5.14)
387	153.47	17	45.48(0.02)	0.37(0.06)	43.50(10.22)	45.72	0.20(0.02)	59.21(8.33)
388	138.06	0.59(11.7)	45.48(0.08)	0.64(0.21)	83.48	45.72	0.24(0.04)	67.03(22.12)
391	197.58	18	45.46(0.04)	0.40(0.08)	38.79(11.52)	45.71	0.20(0.02)	66.66(9.15)

D.2 $KNbO_3$

D.2.1 Rietveld refinement of Neutron diffraction patterns

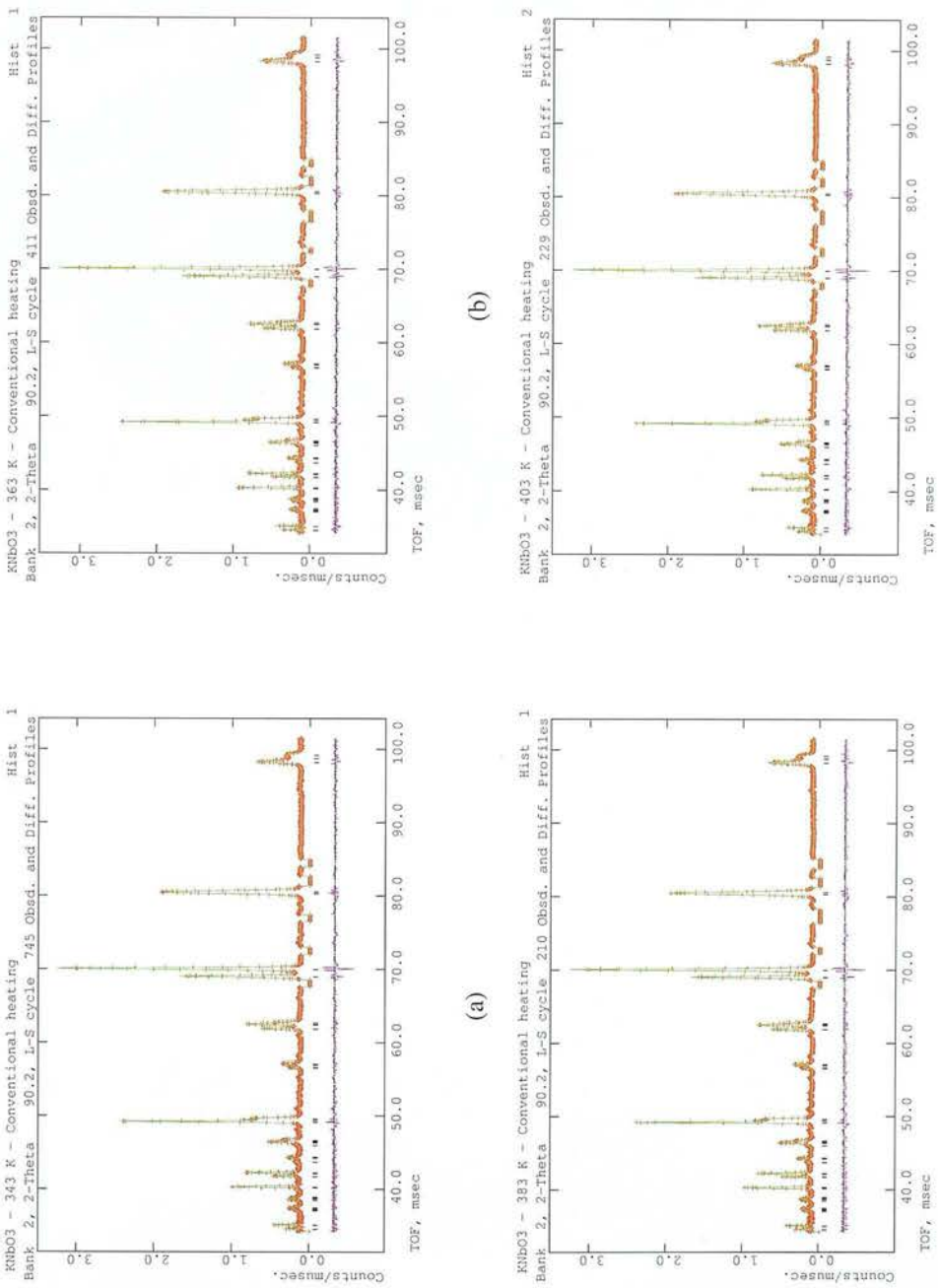

Figure D.2: Rietveld refinement graphs for $KNbO_3$ for neutron diffraction data during conventional heating. (a) 343 K, (b) 363 K, (c) 383 K and, (d) 403 K. The small red + represent the observed pattern, the green continuous line represents the calculated pattern and the difference between the calculated and the observed pattern is shown in the bottom graph (in magenta). The tick marks show the reflections for the orthorhombic phase.

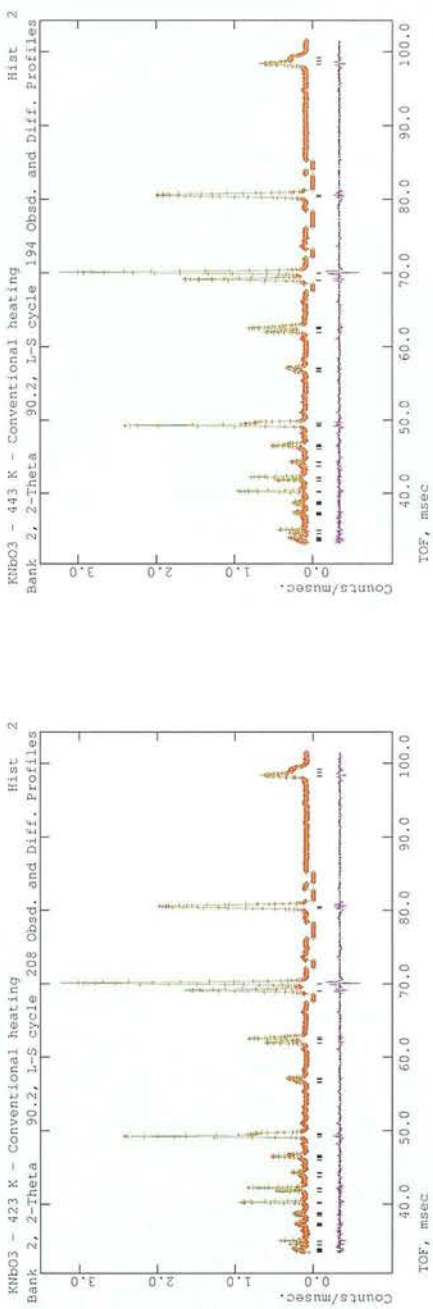

(e)

(g)

(f)

(h)

Figure D.2: (Cont). Rietveld refinement graphs for neutron diffraction data for $KNbO_3$ during conventional heating. (e) 423 K, (f) 443 K, (g) 463 K and, (h) 483 K. The small red + represent the observed pattern, the green continuous line represents the calculated pattern and the difference between the calculated and the observed pattern is shown in the bottom graph (in magenta). The tick marks show the reflections for the orthorhombic phase.

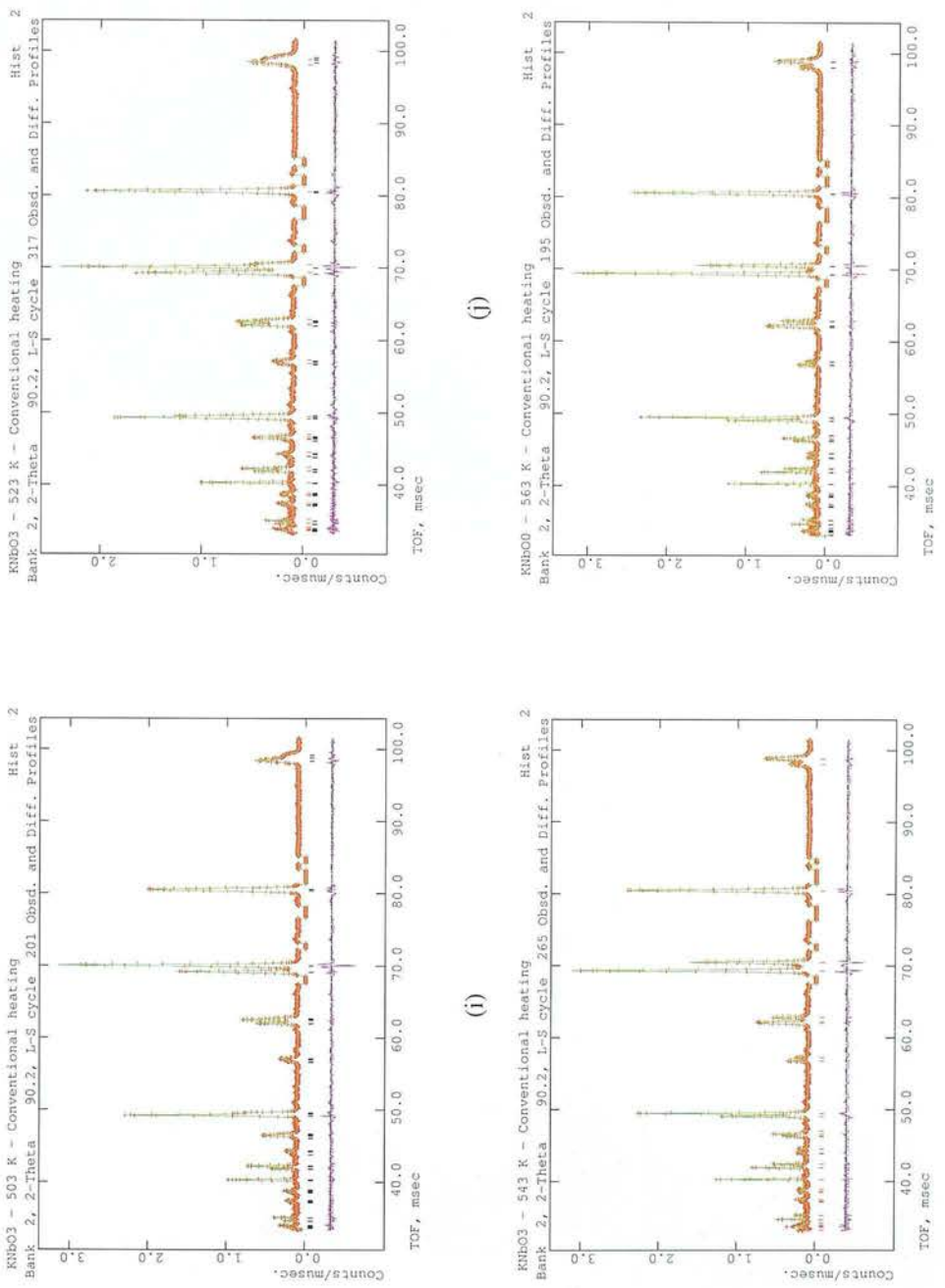

Figure D.2: (Cont). Rietveld refinement graphs for neutron diffraction data for $KNbO_3$ with conventional heating. (i) 503 K, (j) 523 K, (k) 543 K and, (l) 563 K. The small red + represent the observed pattern, the green continuous line represents the calculated pattern and the difference between the calculated and the observed pattern is shown in the bottom graph (in magenta). The tick marks show the reflections for the orthorhombic (black) and tetragonal (red) phases respectively.

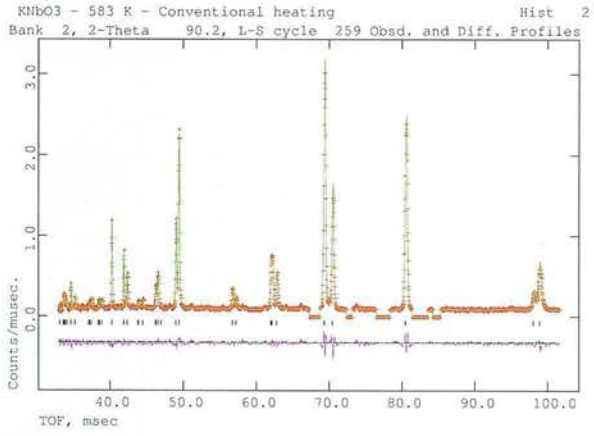

(m)

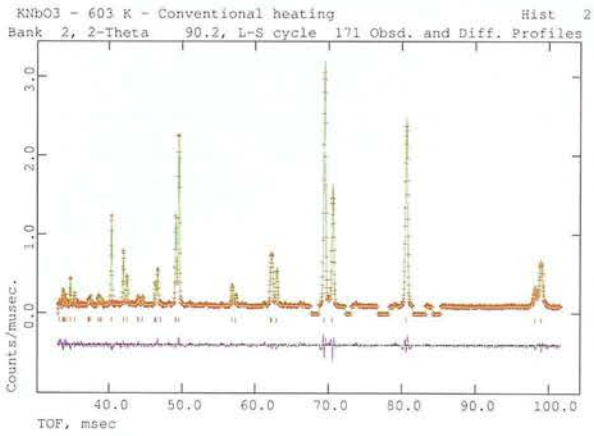

(n)

Figure D.2: (Cont). Rietveld refinement graphs for neutron diffraction data for $KNbO_3$ during conventional heating. (m) 583 K and, (n) 603 K. The small red + represent the observed pattern, the green continuous line represents the calculated pattern and the difference between the calculated and the observed pattern is shown in the bottom graph (in magenta). The tick marks show the reflections for the tetragonal phase.

Table D.3: Cell parameters for orthorhombic and tetragonal phases in $KNbO_3$ under conventional heating determined by Rietveld refinement of neutron diffraction data.

	Orthorhombic phase				Tetragonal phase		
Temperature / K	a / Å	b / Å	c / Å	V / Å^3	a / Å	c / Å	V / Å^3
343	3.970884(90)	5.689189(134)	5.712901(136)	129.061(8)			
363	3.972078(97)	5.689721(142)	5.712757(147)	129.108(9)			
383	3.973188(98)	5.689981(143)	5.712977(148)	129.155(9)			
403	3.974255(97)	5.690370(140)	5.713048(147)	129.200(9)			
423	3.975396(96)	5.690681(143)	5.712998(146)	129.244(8)			
443	3.976380(94)	5.690800(141)	5.712797(144)	129.274(8)			
463	3.977740(98)	5.690875(145)	5.712803(151)	129.32(9)			
483	3.979461(70)	5.691305(105)	5.712375(108)	129.376(6)			
503	3.980849(100)	5.691346(152)	5.711753(157)	129.408(9)			
523	3.982179(124)	5.691497(201)	5.711454(186)	129.448(10)	3.993089(134)	3.994931(171)	64.688(6)
543					3.992428(82)	4.05933(89)	64.704(4)
563					3.992996(54)	4.05965(59)	64.727(3)
583					3.994143(76)	4.05986(83)	64.768(4)
603					3.994931(53)	4.05977(58)	64.792(3)

Table D.3: (Cont). Atom parameters for the orthorhombic phase of $KNbO_3$ under conventional heating determined by Rietveld refinement of neutron diffraction data.

Orthorhombic phase	Temperature / K									
Atom parameters	343	363	383	403	423	443	463	483	503	523
K {0, 0, 0}										
$100*U_{11}$ / Å^2	0.633(163)	1.120(171)	0.686(169)	1.000(174)	0.924(0.173)	0.558(165)	0.953(175)	1.067(126)	0.685(175)	0.560(301)
$100*U_{22}$ / Å^2	0.520(241)	0.639(265)	1.093(275)	0.423(254)	1.180(269)	0.972(269)	0.972(261)	0.726(262)	0.711(262)	1.812(313)
$100*U_{33}$ / Å^2	0.185(639)	-1.381(739)	-0.651(751)	-0.971(955)	-0.217(685)	-0.053(1.079)	-1.554(786)	0.404(975)	-0.389(1.01)	-2.074(946)
$100*U_{eq}$ / Å^2	0.45	0.13	0.38	0.15	0.63	0.49	0.04	0.73	0.7	-0.14
Nb {1/2, 0, z}	0.506923(32232)	0.488933(3835)	0.494867(594)	0.524566(638)	0.508396(24251)	0.515296(12789)	0.525399(5090)	0.512933(16684)	0.514786(13091)	0.527960(5066)
$100*U_{11}$ / Å^2	-0.188(85)	-0.040(87)	0.012(87)	-0.043(93)	-0.066(92)	-0.032(88)	0.189(94)	-0.038(67)	0.015(94)	-0.497(148)
$100*U_{22}$ / Å^2	-0.028(136)	-0.127(137)	-0.16(135)	-0.042(131)	0.105(142)	-0.020(134)	-0.067(133)	0.311(110)	0.109(149)	0.038(219)
$100*U_{33}$ / Å^2	0.654(2.105)	0.075(274)	0.509(248)	1.888(534)	0.935(1.546)	1.499(975)	2.101(429)	1.129(1.102)	1.607(946)	2.763(679)
$100*U_{eq}$ / Å^2	0.15	-0.03	0.12	0.60	0.32	0.48	0.74	0.47	0.58	0.77
O1 {0, 0, z}	0.527960(27101)	0.525227(3418)	0.532319(4288)	0.551388(4048)	0.540185(19271)	0.545292(9686)	0.550939(29950)	0.542329(13232)	0.544158(9583)	0.552882(2791)
$100*U_{11}$ / Å^2	-0.255(116)	-0.074(122)	-0.103(125)	-0.265(121)	-0.220(119)	0.049(116)	-0.252(121)	-0.140(85)	-0.114(121)	-0.751(159)
$100*U_{22}$ / Å^2	0.171(163)	0.283(170)	0.679(176)	0.458(181)	0.314(176)	0.299(175)	0.693(190)	0.594(139)	0.833(206)	0.952(310)
$100*U_{33}$ / Å^2	0.335(748)	-0.515(774)	-0.936(608)	0.089(214)	0.093(342)	0.124(269)	0.301(235)	0.378(308)	-0.117(246)	0.740(389)
$100*U_{eq}$ / Å^2	0.08	-0.1	-0.12	0.09	0.06	0.16	0.25	0.28	0.2	0.31
O2 {1/2, y, z}	0.247196(1782), 0.287792(27797)	0.245766(1393), 0.267044(6230)	0.245532(1124), 0.272813(8292)	0.246753(710), 0.299889(4232)	0.247079(1453), 0.287010(21125)	0.246615(866), 0.294739(9988)	0.246951(725), 0.298438(3208)	0.246687(1082), 0.290813(13626)	0.247591(874), 0.292533(10395)	0.247594(910), 0.302243(2953)
$100*U_{11}$ / Å^2	0.424(77)	0.412(79)	0.543(8)	0.596(81)	0.569(8)	0.597(79)	0.779(83)	0.688(58)	0.811(83)	0.580(128)
$100*U_{22}$ / Å^2	-0.029(117)	0.219(131)	0.031(128)	0.291(125)	0.148(128)	0.308(125)	0.479(131)	0.445(100)	0.294(140)	-0.035(205)
$100*U_{33}$ / Å^2	0.060(1.014)	1.737(584)	1.448(641)	-0.208(162)	0.452(850)	0.168(337)	-0.233(145)	0.154(430)	0.560(391)	0.520(203)
$100*U_{23}$ / Å^2	0.355(236)	0.458(166)	0.318(140)	0.476(101)	0.422(181)	0.286(120)	0.412(100)	0.460(135)	0.268(117)	0.436(145)
$100*U_{eq}$ / Å^2	0.15	0.79	0.67	0.23	0.39	0.36	0.34	0.43	0.55	0.35

Table D.3: (Cont). Atom parameters for the tetragonal phase of $KNbO_3$ under conventional heating determined by Rietveld refinement of neutron diffraction data.

Tetragonal phase	Temperature / K				
Atom parameters	523	543	563	583	603
K { 0, 0, 0}					
$100*U_{11}=100*U_{22}$ / Å^2		0.861(102)	0.929(69)	1.203(100)	1.124(69)
$100*U_{33}$ / Å^2		-2.029(797)	0.882(1.119)	-0.346(1.168)	0.629(1.173)
$100*U_{eq}$ / Å^2	1.45	-0.1	0.91	0.69	0.96
Nb { 1/2, 1/2, *z* }	0.547105(5791)	0.544584(6608)	0.514408(44920)	0.533933(12277)	0.517830(33609)
$100*U_{iso}$ / Å^2	0.679(317)				
$100*U_{11}=100*U_{22}$ / Å^2		0.381(62)	0.427(42)	0.535(62)	0.423(42)
$100*U_{33}$ / Å^2		2.141(286)	0.874(1.663)	1.582(581)	1.020(1.222)
$100*U_{eq}$ / Å^2	0.68	0.97	0.58	0.88	0.62
O1 { 1/2, 1/2, *z* }	0.074185(2461)	0.073221(3041)	0.052198(35794)	0.066955(7811)	0.055607(25318)
$100*U_{iso}$ / Å^2	0.534(369)				
$100*U_{11}=100*U_{22}$ / Å^2		0.803(93)	0.897(59)	0.868(87)	0.932(58)
$100*U_{33}$ / Å^2		0.033(146)	0.154(417)	0.115(159)	0.047(138)
$100*U_{eq}$ / Å^2	0.53	0.55	0.65	0.62	0.64
O2 { 1/2, 0, *z* }	0.055607(2738)	0.569541(3383)	0.548610(37968)	0.564227(8226)	0.549331(28511)
$100*U_{iso}$ / Å^2	0.425(222)				
$100*U_{11} = 100*U_{22}$ / Å^2		0.677(90)	0.681(61)	0.622(84)	0.762(6)
$100*U_{33}$ / Å^2		0.279(129)	0.633(809)	0.3768(128)	0.809(649)
$100*U_{eq}$ / Å^2	0.43	0.36	0.53	0.39	0.57

Table D.3: (Cont). Fitting parameters for $KNbO_3$ under conventional heating determined by Rietveld refinement of neutron diffraction data.

Goodness	Temperature / K													
of fit	343	363	383	403	423	443	463	483	503	523	543	563	583	603
χ^2	20.06	23.7	24.04	24.3	23.69	22.78	24.08	11.92	23.78	22.27	26.78	12.28	23.76	11.65
wRp	0.0529	0.0591	0.0584	0.0608	0.0601	0.0600	0.0616	0.0616	0.0650	0.0582	0.0717	0.0647	0.0655	0.0651
Rp	0.0459	0.0499	0.0498	0.0518	0.0527	0.0521	0.0511	0.0528	0.0545	0.0505	0.0593	0.0577	0.0583	0.0589

Table D.4: Cell parameters for orthorhombic and tetragonal phases in $KNbO_3$ under microwave heating determined by Rietveld refinement of neutron diffraction data.

	Orthorhombic phase				Tetragonal phase		
Temperature / K	a / Å	b / Å	c / Å	V / Å^3	a / Å	c / Å	V / Å^3
343	3.970884(90)	5.689189(134)	5.712901(136)	129.061(8)			
393	3.976400(85)	5.689590(128)	5.710931(131)	129.205(7)			
431	3.977134(88)	5.689437(132)	5.710852(135)	129.223(8)			
461	3.980266(94)	5.690529(147)	5.709926(150)	129.329(8)			
493	3.980450(134)	5.688366(301)	5.707071(255)	129.221(9)	3.990518(93)	4.056707(108)	64.600(4)
516					3.991244(70)	4.057873(78)	64.642(3)

Table D.4: (Cont). Atom parameters for the orthorhombic and tetragonal phases of $KNbO_3$ under microwave heating determined by Rietveld refinement of neutron diffraction data.

Orthorhombic	Temperature / K				
phase	393	431	461	493	516
K {0, 0, 0}					
$100*U_{11}$ / Å^2	3.186(0.218)	2.092(0.198)	3.097(0.241)		
$100*U_{22}$ / Å^2	0.59(0.309)	0.845(0.309)	-1.045(0.351)		
$100*U_{33}$ / Å^2	0.298(0.459)	-1.591(0.547)	2.788(0.662)		
$100*U_{iso}$ / Å^2				1.695(0.483)	
Nb {1/2, 0, z}	0.49722(506)	0.47575(179)	0.48846(375)	0.46506(419)	
$100*U_{11}$ / Å^2	-0.405(0.096)	-0.409(0.093)	-0.949(0.1)		
$100*U_{22}$ / Å^2	1.336(0.181)	0.817(0.174)	1.975(0.22)		
$100*U_{33}$ / Å^2	0.954(0.333)	0.214(0.348)	0.314(0.262)		
$100*U_{iso}$ / Å^2				-0.054(0.213)	
O1 {0, 0, z}	0.53052(506)	0.52073(272)	0.52561(424)	0.52202(414)	
$100*U_{11}$	0.362(0.141)	0.724(0.14)	0.1(0.146)		
$100*U_{22}$	-0.126(0.201)	-0.654(0.186)	-1.322(0.236)		
$100*U_{33}$	1.696(0.343)	-0.496(0.791)	2.945(0.402)		
$100*U_{iso}$				-0.675(0.246)	
O2 {1/2, y, z}	0.24126(132), 0.28144(462)	0.24065(126), 0.25684(279)	0.24036(132), 0.27901(359)	0.24600(110), 0.27637(401)	
$100*U_{11}$ / Å^2	0.574(0.09)	0.459(0.089)	0.402(0.096)		
$100*U_{22}$ / Å^2	0.329(0.163)	0.758(0.173)	0.635(0.201)		
$100*U_{33}$ / Å^2	-0.775(0.227)	1.69(0.361)	-0.876(0.204)		
$100*U_{23}$ / Å^2	1.672(0.174)	1.206(0.165)	2.047(0.214)		
$100*U_{iso}$/ Å^2				0.901(0.221)	

Tetragonal phase					
K {0, 0, 0}					
$100*U_{11}=100*U_{22}$ / Å^2				0.85(0.209)	1.443(0.115)
$100*U_{33}$ / Å^2				-1.037(2.2481)	2.642(2.354)
Nb {1/2, 1/2, z}				0.46586(649)	0.47889(3279)
$100*U_{11}=100*U_{22}$ / Å^2				-0.28(0.114)	0.201(0.065)
$100*U_{33}$ / Å^2				0.248(1.081)	0.648(1.145)
O1 {1/2, 1/2, z}				-0.01327(3452)	0.02241(3079)
$100*U_{11}=100*U_{22}$ / Å^2				0.91(0.158)	1.118(0.097)
$100*U_{33}$ / Å^2				3.218(0.812)	0.645(0.913)
O2 {1/2, 0, z}				0.51165(1071)	0.52394(2940)
$100*U_{11}$ / Å^2				0.24(0.15)	0.759(0.092)
$100*U_{22}$ / Å^2				1.147(0.162)	0.079(0.098)
$100*U_{33}$ / Å^2				-0.509(0.477)	0.238(0.614)

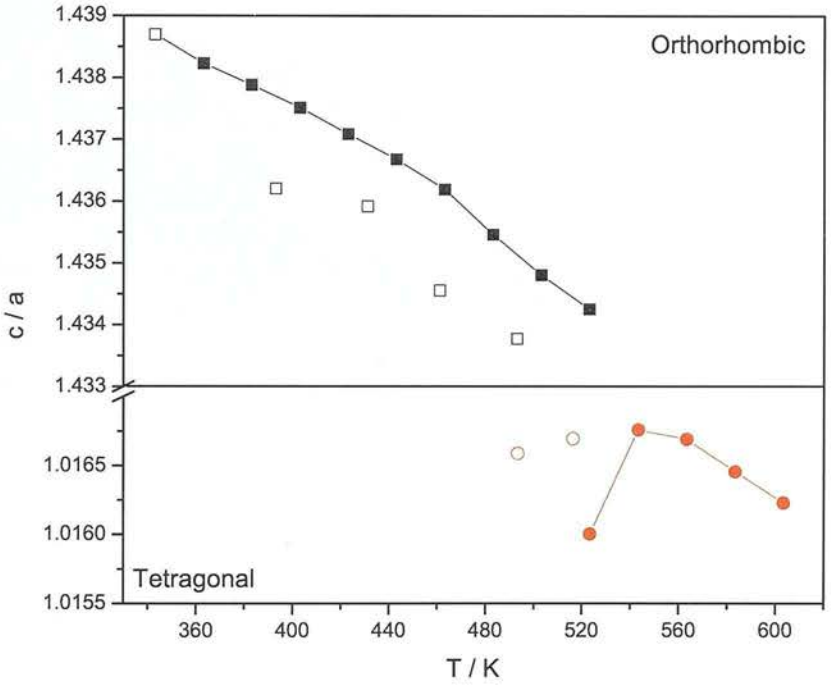

Figure D.3: c/a ratio as a function of temperature for $KNbO_3$ for neutron diffraction data on conventional and microwave heating. Symbols represent the microwave (□, ○) and, the conventionally (■, ●) heated sample.

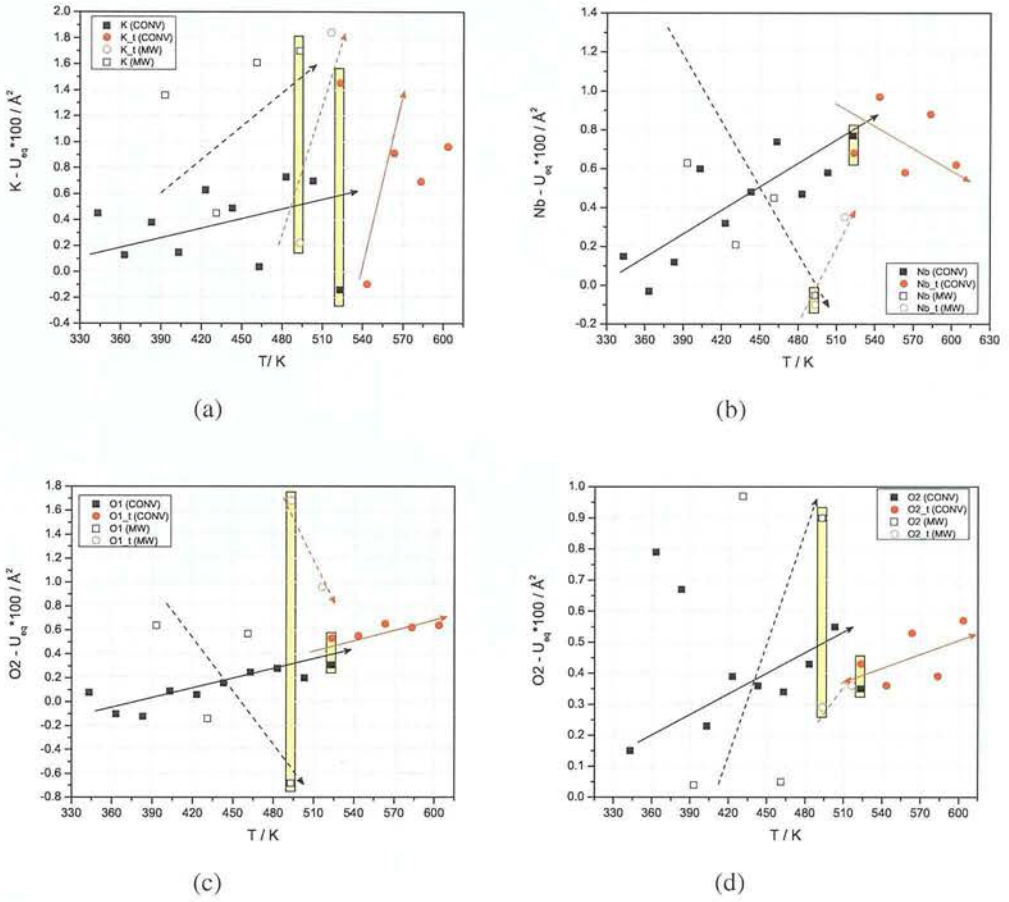

Figure D.4: Atomic displacement parameters for $KNbO_3$ determined by Rietveld refinement for neutron diffraction data with conventional and microwave heating. U_{eq} for: (a) K, (b) Nb, (c) O1 and (d) O2. The arrows are only a guide for the eye. The solid arrows represents the data tendency observed for conventionally heated samples while the dotted arrows represent data tendency for microwave heated samples. Highlighted areas mark the point where the phase transition was observed for both heating methods used. From legend (insets) MW refers to the microwave irradiated samples, CONV to the conventionally heated samples and 't' refers to the tetragonal phase.

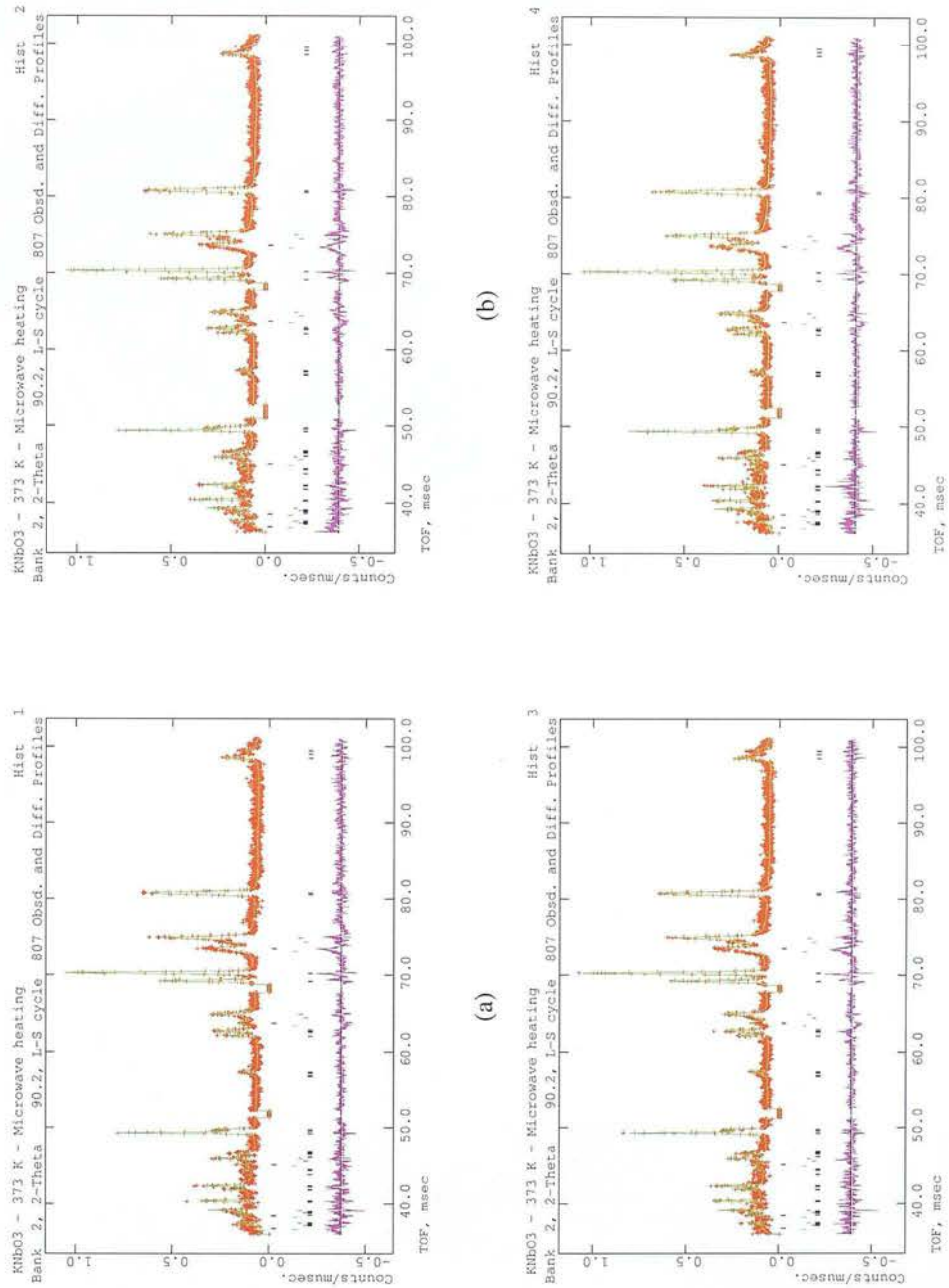

Figure D.5: Rietveld refinement graphs for $KNbO_3$ for neutron diffraction data during microwave heating at 343 K. (a) Hist. 1, (b) Hist. 2, (c) Hist. 3 and, (d) Hist. 4. The small red + represent the observed pattern, the green continuous line represents the calculated pattern and the difference between the calculated and the observed pattern is shown in the bottom graph (in magenta). The tick marks indicate the different phases used in the refinement - the four upper sets for the brass of the microwave waveguide, and the bottom set for the orthorhombic phase.

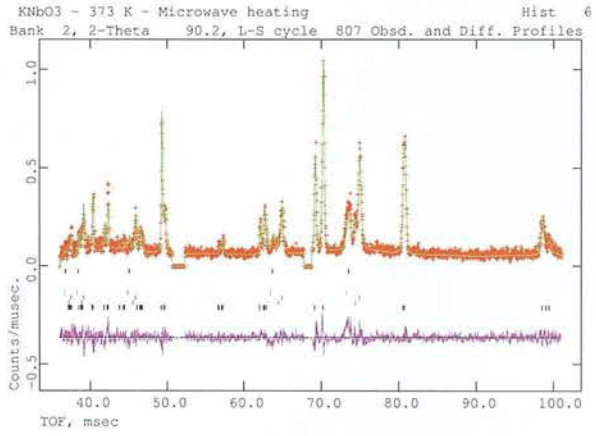

(e)

Figure D.5: (Cont). Rietveld refinement graphs for $KNbO_3$ for neutron diffraction data during microwave heating at 343 K. (e) Histogram 6. The small red + represent the observed pattern, the green continuous line represents the calculated pattern and the difference between the calculated and the observed pattern is shown in the bottom graph (in magenta). The tick marks indicate the different phases used in the refinement - the four upper sets for the brass of the microwave waveguide, and the bottom set for the orthorhombic phase.

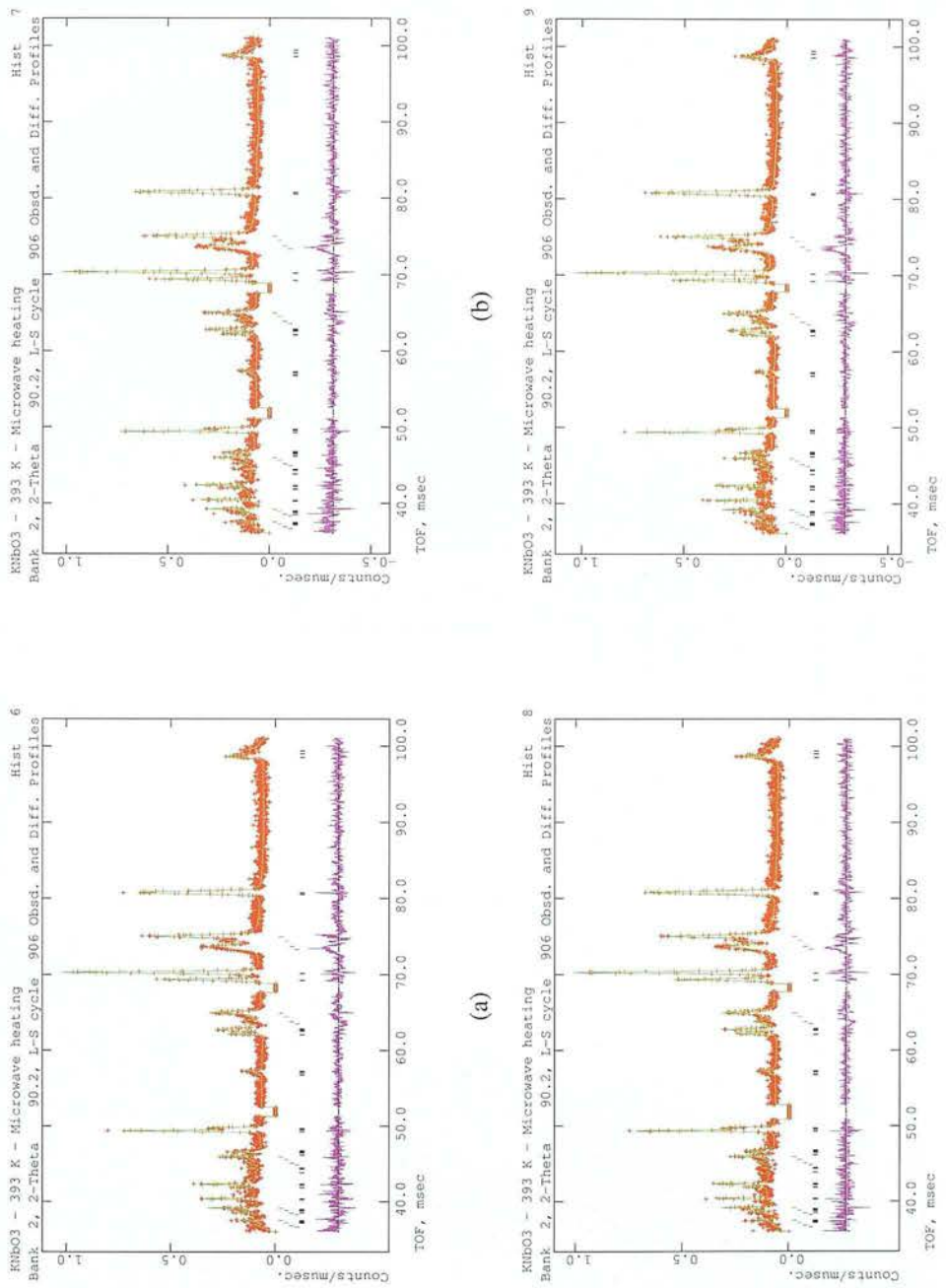

Figure D.6: Rietveld refinement graphs for $KNbO_3$ for neutron diffraction data during microwave heating at 393 K. (a) Hist. 6, (b) Hist. 7, (c) Hist. 8 and, (d) Hist. 9. The small red + represent the observed pattern, the green continuous line represents the calculated pattern and the difference between the calculated and the observed pattern is shown in the bottom graph (in magenta). The tick marks indicate the different phases used in the refinement - the four upper sets for the brass of the microwave waveguide, and the bottom set for the orthorhombic phase.

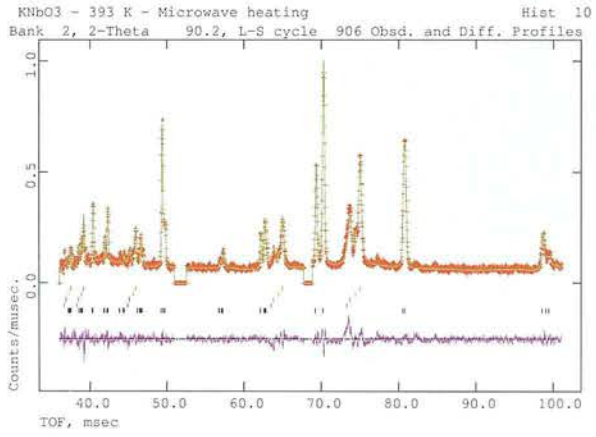

(e)

Figure D.6: (Cont). Rietveld refinement graphs for $KNbO_3$ for neutron diffraction data during microwave heating at 393 K. (e) Histogram 10. The small red + represent the observed pattern, the green continuous line represents the calculated pattern and the difference between the calculated and the observed pattern is shown in the bottom graph (in magenta). The tick marks indicate the different phases used in the refinement - the four upper sets for the brass of the microwave waveguide, and the bottom set for the orthorhombic phase.

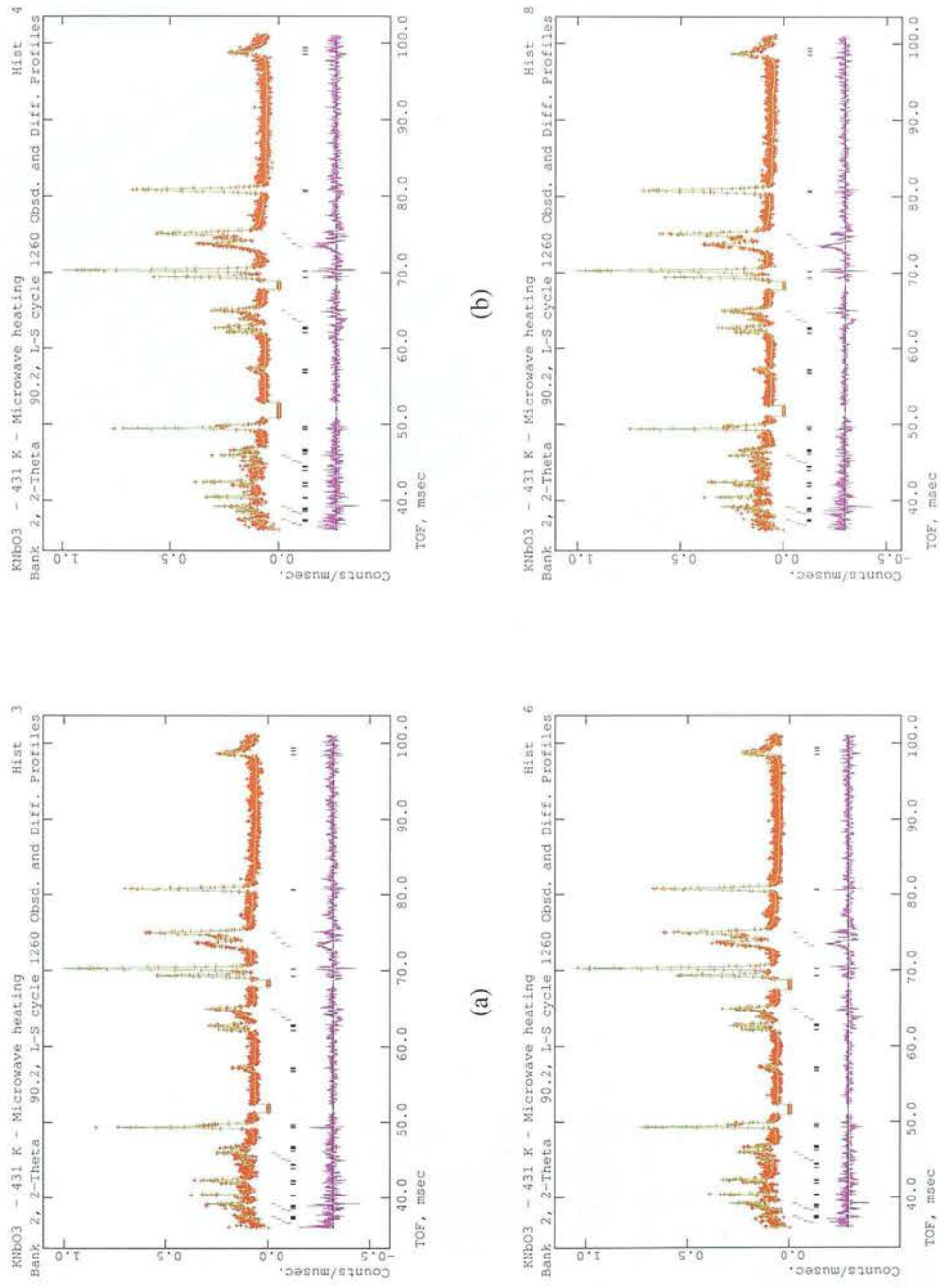

Figure D.7: Rietveld refinement graphs for $KNbO_3$ for neutron diffraction data during microwave heating at 431 K. (a) Hist. 3, (b) Hist. 4, (c) Hist. 6 and, (d) Hist. 8. The small red + represent the observed pattern, the green continuous line represents the calculated pattern and the difference between the calculated and the observed pattern is shown in the bottom graph (in magenta). The tick marks indicate the different phases used in the refinement - the four upper sets for the brass of the microwave waveguide, and the bottom set for the orthorhombic phase.

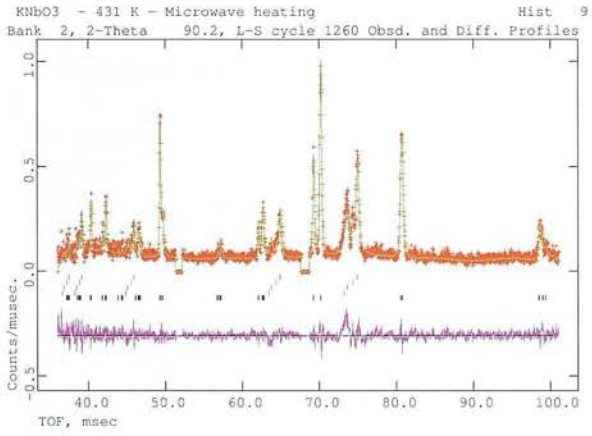

(e)

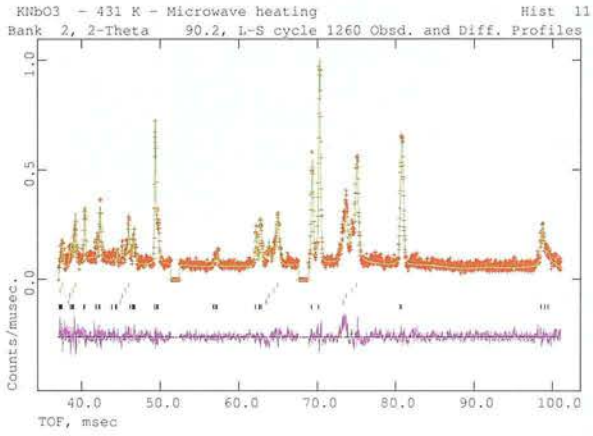

(f)

Figure D.7: (Cont). Rietveld refinement graphs for $KNbO_3$ for neutron diffraction data during microwave heating at 431 K. (e) Hist. 9 and, (f) Hist. 11. The small red + represent the observed pattern, the green continuous line represents the calculated pattern and the difference between the calculated and the observed pattern is shown in the bottom graph (in magenta). The tick marks indicate the different phases used in the refinement - the four upper sets for the brass of the microwave waveguide, and the bottom set for the orthorhombic phase.

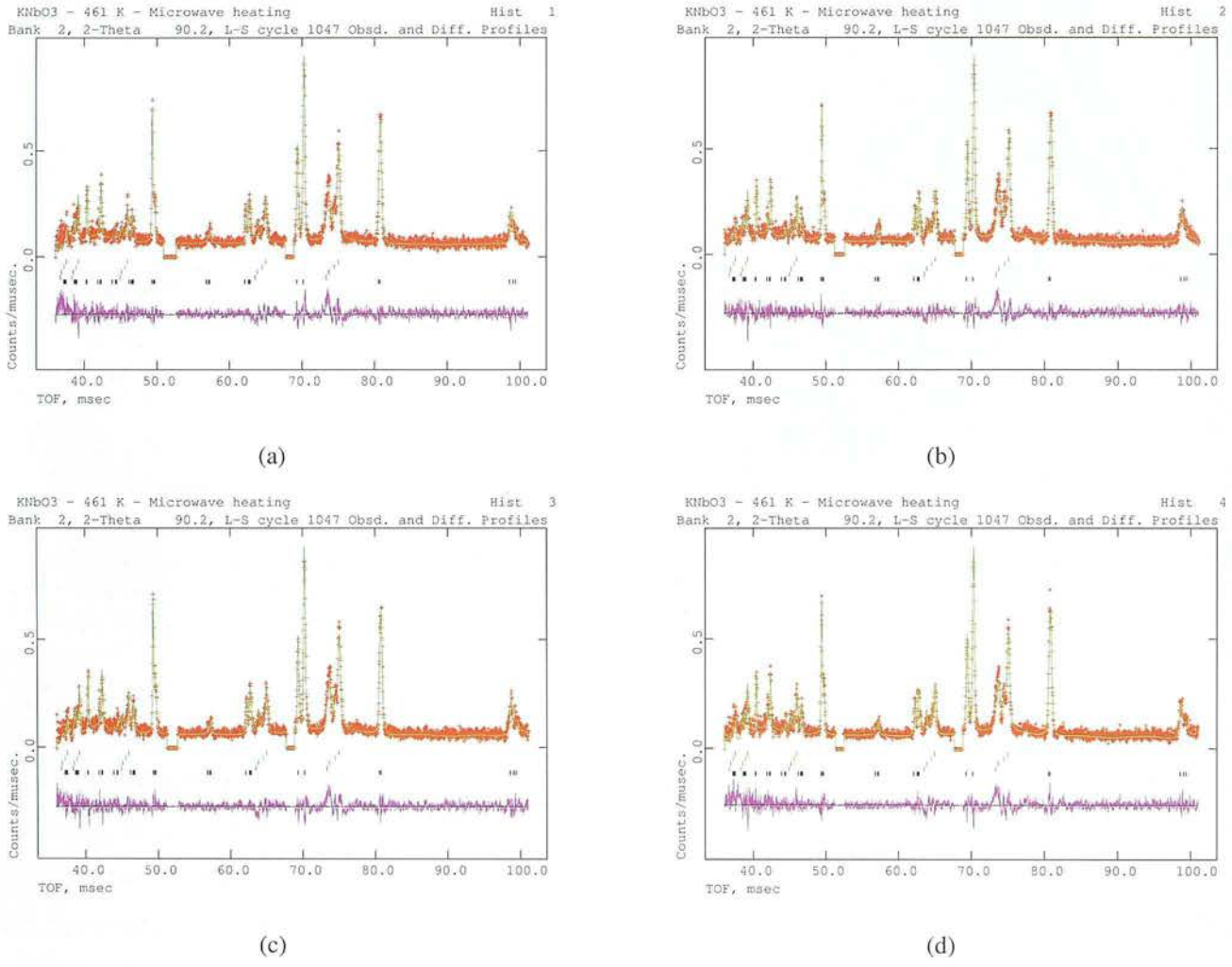

Figure D.8: Rietveld refinement graphs for $KNbO_3$ for neutron diffraction data during microwave heating at 461 K. (a) Hist. 1, (b) Hist. 2, (c) Hist. 3 and, (d) Hist. 4. The small red + represent the observed pattern, the green continuous line represents the calculated pattern and the difference between the calculated and the observed pattern is shown in the bottom graph (in magenta). The tick marks indicate the different phases used in the refinement - the four upper sets for the brass of the microwave waveguide, and the bottom set for the orthorhombic phase.

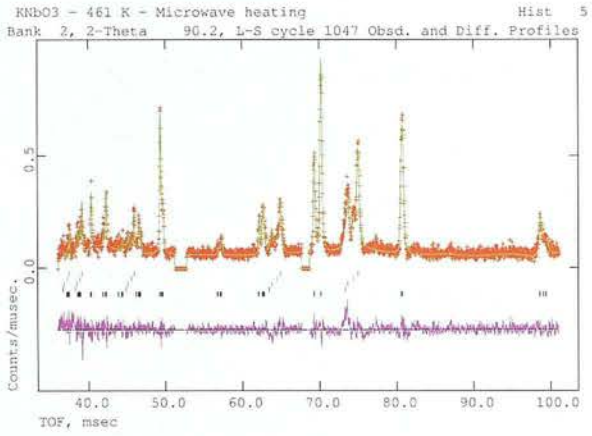

(e)

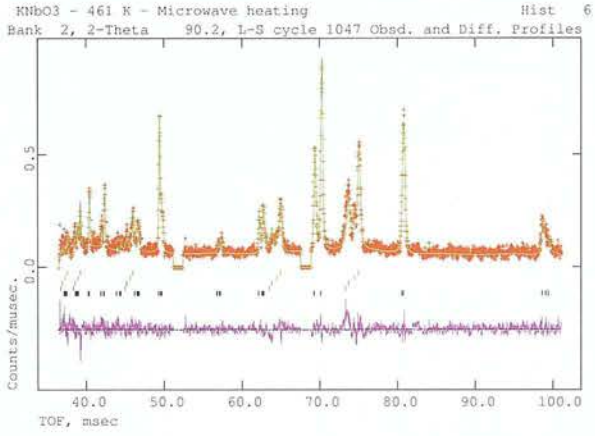

(f)

Figure D.8: (Cont). Rietveld refinement graphs for $KNbO_3$ for neutron diffraction data during microwave heating at 461 K. (e) Hist. 5 and, (f) Hist. 6. The small red + represent the observed pattern, the green continuous line represents the calculated pattern and the difference between the calculated and the observed pattern is shown in the bottom graph (in magenta). The tick marks indicate the different phases used in the refinement - the four upper sets for the brass of the microwave waveguide, and the bottom set for the orthorhombic phase.

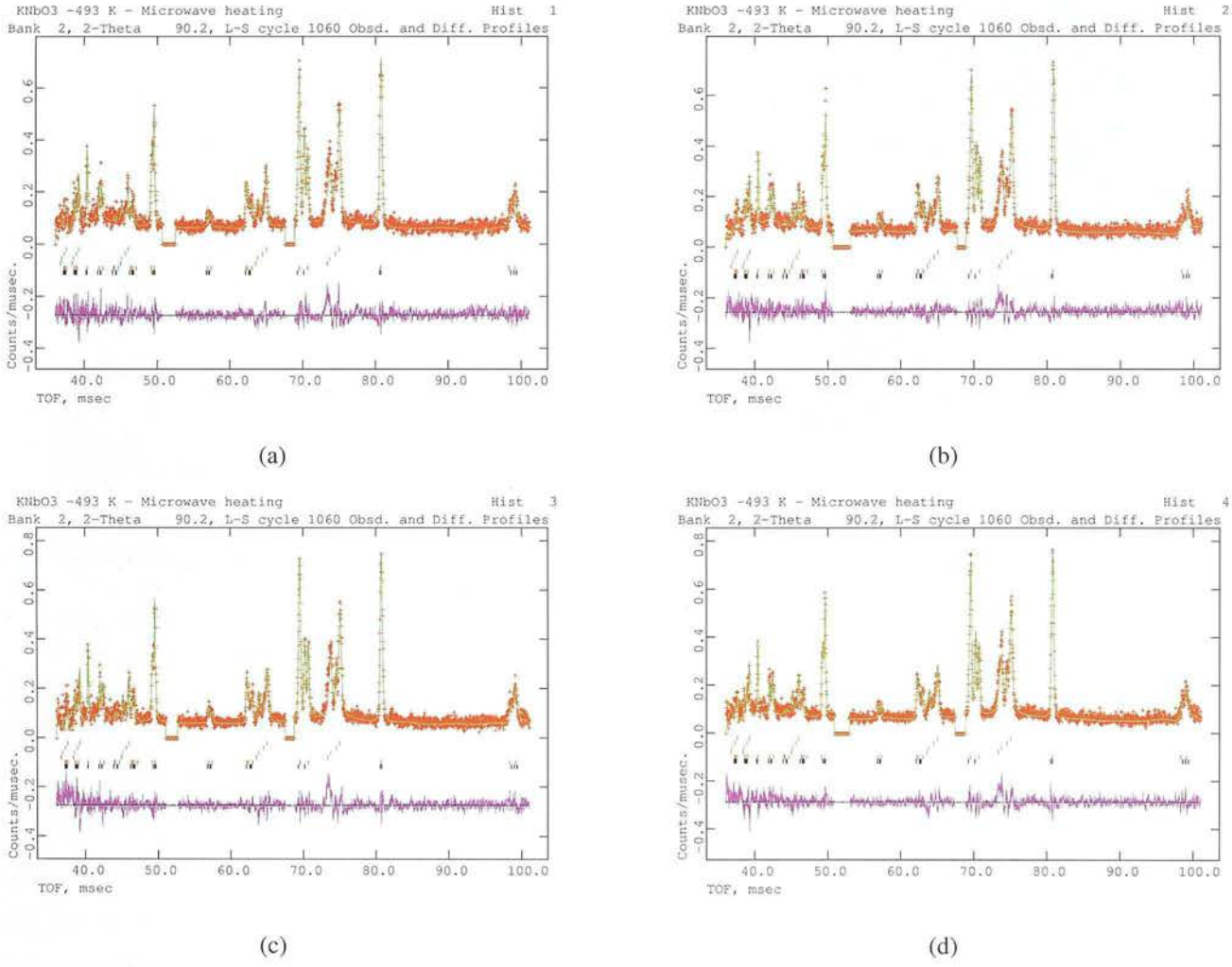

Figure D.9: Rietveld refinement graphs for $KNbO_3$ for neutron diffraction data during microwave heating at 493 K. (a) Hist. 1, (b) Hist. 2, (c) Hist. 3 and, (d) Hist. 4. The small red + represent the observed pattern, the green continuous line represents the calculated pattern and the difference between the calculated and the observed pattern is shown in the bottom graph (in magenta). The tick marks indicate the different phases used in the refinement - the four upper sets for the brass of the microwave waveguide, and the two bottom sets for the orthorhombic and tetragonal phase respectively.

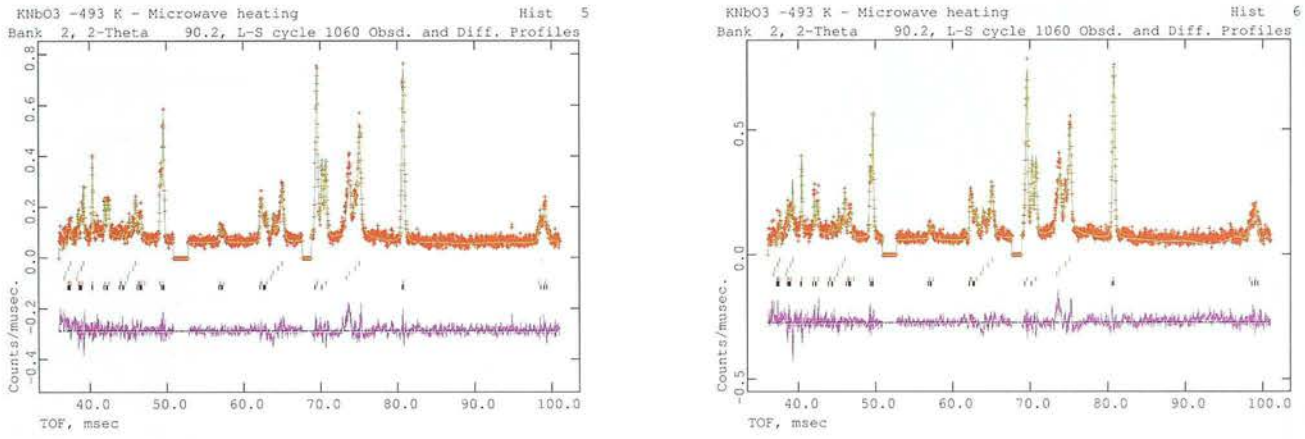

(e) (f)

Figure D.9: (Cont). Rietveld refinement graphs for $KNbO_3$ for neutron diffraction data during microwave heating at 493 K. (e) Hist. 5 and, (f) Hist. 6. The small red + represent the observed pattern, the green continuous line represents the calculated pattern and the difference between the calculated and the observed pattern is shown in the bottom graph (in magenta). The tick marks indicate the different phases used in the refinement - the four upper sets for the brass of the microwave waveguide, and the two bottom sets for the orthorhombic and tetragonal phase respectively.

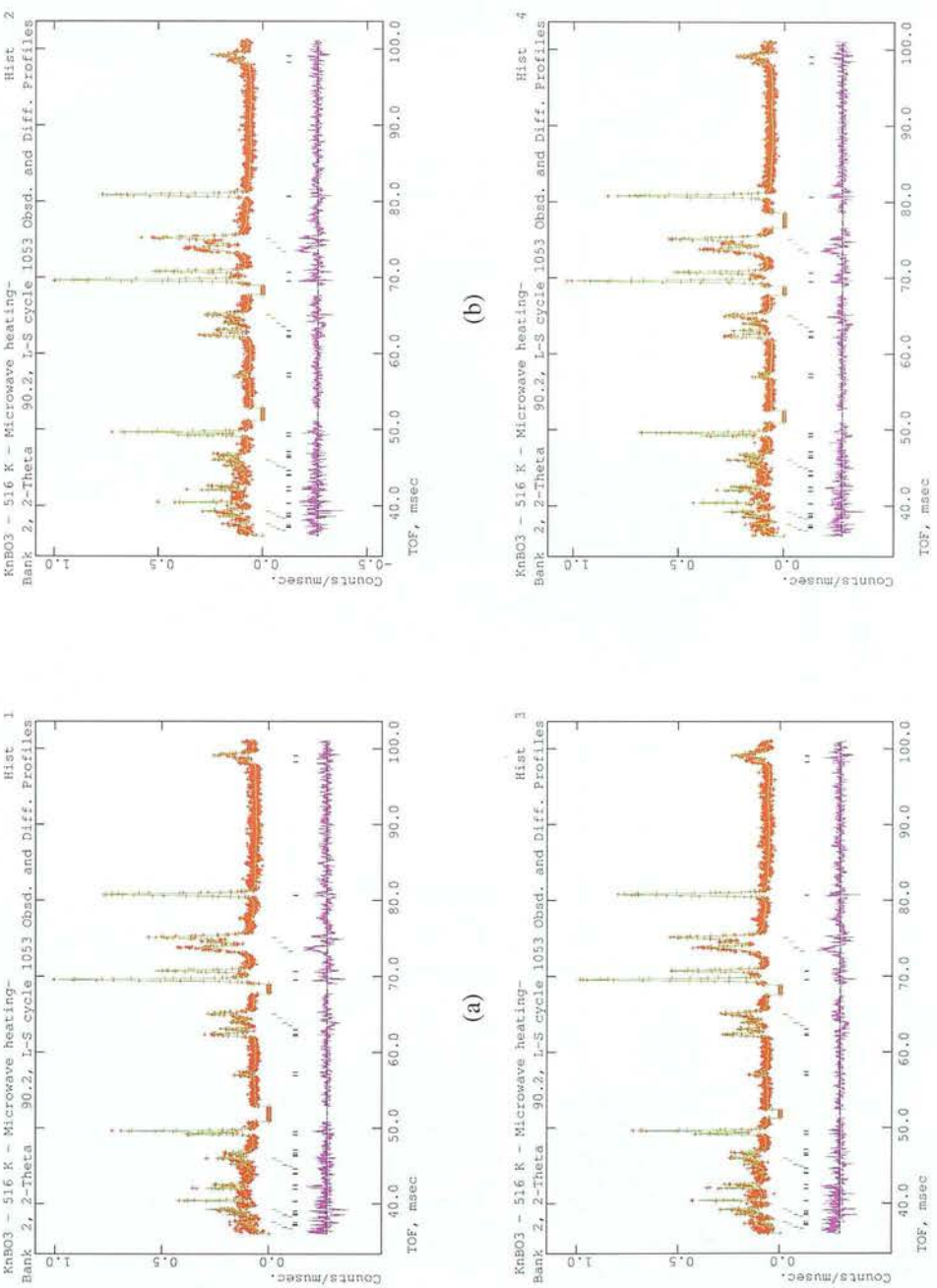

Figure D.10: Rietveld refinement graphs for $KNbO_3$ for neutron diffraction data during microwave heating at 516 K. (a) Hist. 1, (b) Hist. 2, (c) Hist. 3 and, (d) Hist. 4. The small red + represent the observed pattern, the green continuous line represents the calculated pattern and the difference between the calculated and the observed pattern is shown in the bottom graph (in magenta). The tick marks indicate the different phases used in the refinement - the four upper sets for the brass of the microwave waveguide, and the two bottom sets for the orthorhombic and tetragonal phase respectively.

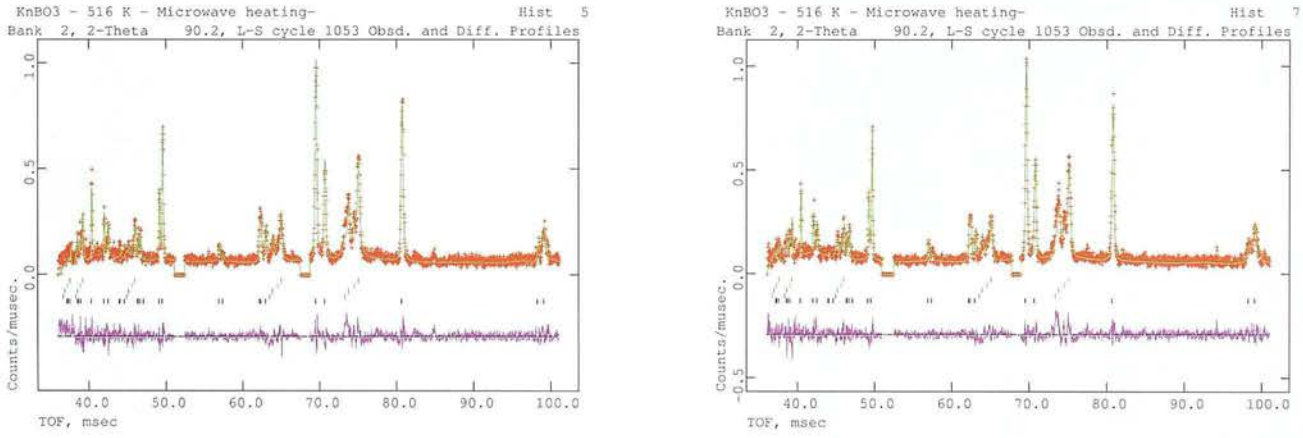

(e) (f)

Figure D.10: (Cont). Rietveld refinement graphs for $KNbO_3$ for neutron diffraction data during microwave heating at 516 K. (e) Hist. 5 and, (f) Hist. 7. The small red + represent the observed pattern, the green continuous line represents the calculated pattern and the difference between the calculated and the observed pattern is shown in the bottom graph (in magenta). The tick marks indicate the different phases used in the refinement - the four upper sets for the brass of the microwave waveguide, and the two bottom sets for the orthorhombic and tetragonal phase respectively.

Appendix E

Rietveld refinement results for Nickel and MoS_2 supported catalysts

E.1 Neutron diffraction data for the Ni(10%)/Al_2O_3 catalyst

Table E.1: Rietveld refinement results obtained for nickel particles on a Ni(10%)/Al_2O_3 catalysts during conventional heating.

	Temperature / K					
Nickel	291	323	373	423	473	516
a / Å	3.522503(117)	3.523702(89)	3.526297(88)	3.528776(92)	3.531266(91)	3.533983(91)
V / $Å^3$	43.707(4)	43.752(3)	43.849(3)	43.941(3)	44.034(3)	44.136(3)
100*Uiso	0.378(46)	0.214(37)	0.286(36)	0.347(38)	0.361(37)	0.737(38)
γ_1	15.71(4.402)	26.08(3.475)	23.15(3.391)	35.60(3.575)	41.39(3.506)	20.70(3.540)
γ_2	71.13(2.444)	65.34(1.942)	66.97(1.902)	59.73(1.987)	55.62(1.950)	67.65(1.962)
χ^2	5.038	6.218	6.216	6.537	6.216	6.352
wRp	0.0687	0.0534	0.0574	0.0564	0.0542	0.0546
Rp	0.0651	0.0498	0.0526	0.0513	0.0503	0.0519

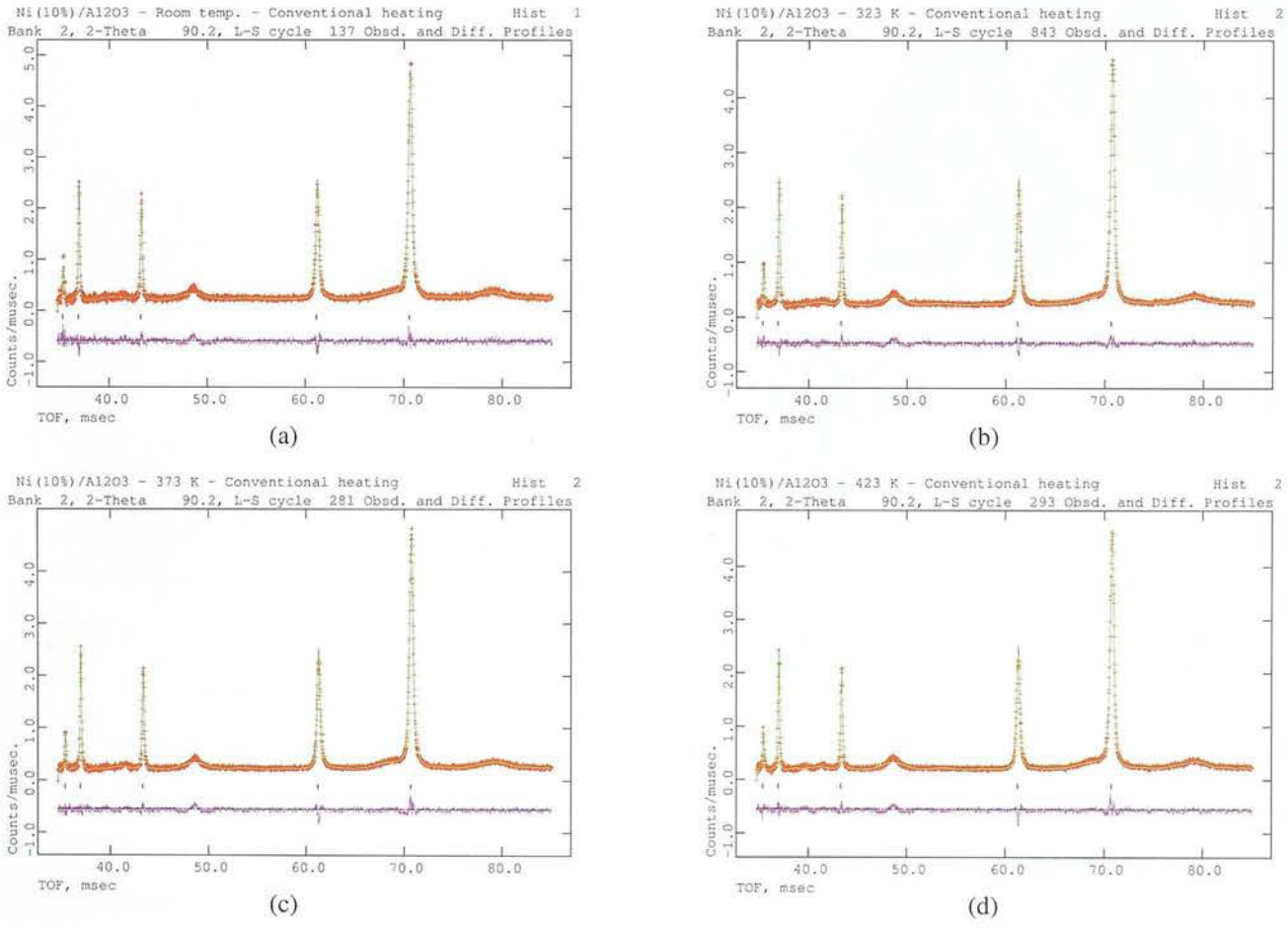

Figure E.1: Rietveld refinement graphs for nickel particles for neutron diffraction data during conventional heating. (a) 293 K, (b) 323 K, (c) 373 K and, (d) 423 K. The small red + represent the observed pattern, the green continuous line represents the calculated pattern and the difference between the calculated and the observed pattern is shown in the bottom graph (in magenta). The tick marks show the reflections for the nickel phase.

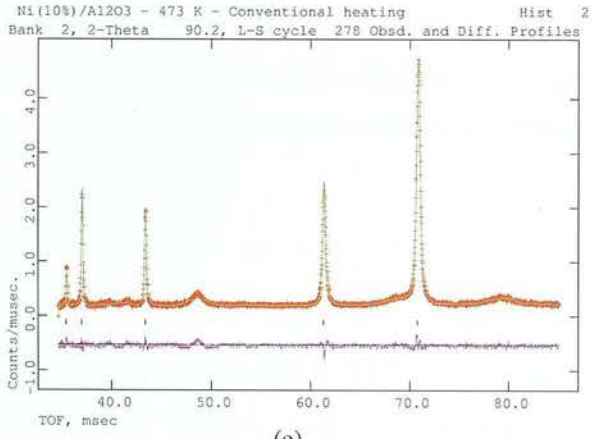

(e)

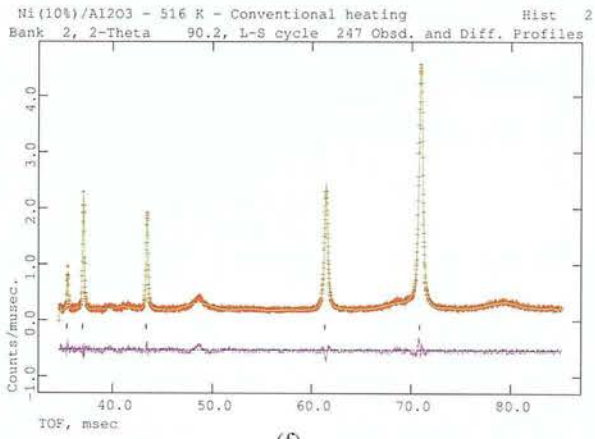

(f)

Figure E.1: (Cont). Rietveld refinement graphs for nickel particles for neutron diffraction data during conventional heating. (e) 473 K and (f) 516 K. The small red + represent the observed pattern, the green continuos line represents the calculated pattern and the difference between the calculated and the observed pattern is shown in the bottom graph (in magenta). The tick marks show the relections for the nickel phase.

Table E.2: Rietveld refinement results obtained for nickel particles on a Ni(10%)/Al_2O_3 catalysts during microwave heating. * Values used for the sample at room temperature are those of the conventionally heated sample (for details refer to section 6.4.2, Chapter 6.

	Temperature / K					
Nickel	291*	323	373	423	473	516
a / Å	3.522503(117)	3.523126(61)	3.526389(63)	3.529889(66)	3.533639(94)	3.534729(86)
V / Å^3	43.707(4)	43.730(2)	43.852(2)	43.983(2)	44.123(4)	44.164(3)
100*Uiso		0.353(25)	0.527(29)	0.525(30)	0.607(42)	0.648(39)
χ^2	5.530	5.618	5.900	6.140	6.160	6.319
wRp (Powder totals)	0.1472	0.1327	0.1521	0.3455	0.1618	0.1732
Rp (Powder totals)	0.1123	0.1142	0.1190	0.1211	0.1245	0.1289

Table E.2: (Cont). Rietveld refinement results, profile parameter γ_1, obtained for nickel particles on a Ni(10%)/Al_2O_3 catalysts during microwave heating. * Values used for the sample at room temperature are those of the conventionally heated sample (for details refer to section 6.4.2, Chapter 6.

	Temperature / K					
Nickel	291*	323	373	423	473	516
γ_1	107.3(7.637)	55.02(7.544)	40.17(7.681)	76.18(8.405)	86.4(9.255)	93.51(4.605)
	73.89(7.143)	87.43(8.022)	62.65(8.132)	78.6(8.042)	76.14(8.605)	0(7.997)
	68.56(7.052)	47.6(7.335)	67.94(8.195)	47.09(8.085)	60.52(8.622)	46.02(8.625)
		50.83(7.584)	19.72(7.28)	48.59(7.999)	89.8(9.154)	30.17(8.547)
		60.14(7.786)	23.09(7.493)	52.83(8.202)	50.07(8.396)	55.91(8.679)
		51.3(7.427)	58.27(7.807)	61.43(8.23)	56.99(8.631)	68.28(9.038)
		39.91(7.215)	40.46(7.335)	54.68(8.123)	93.64(9.382)	93.84(9.575)
		62.81(7.677)	45.01(7.513)	82.93(8.219)		79.78(9.227)
		47.14(7.171)	19.98(7.399)	78.99(8.499)		75.2(9.518)
		22.76(6.926)	44.51(7.624)	46.69(7.899)		45.83(8.862)
		67.51(7.292)	70.9(7.971)	97.13(8.603)		
		80.36(7.869)	46.28(6.376)	66.24(8.42)		
		38.82(7.239)	41.92(7.842)	11.65(8.085)		

Table E.2: (Cont). Rietveld refinement results, profile parameter γ_2, obtained for nickel particles on a Ni(10%)/Al_2O_3 catalysts during microwave heating. * Values used for the sample at room temperature are those of the conventionally heated sample (for details refer to section 6.4.2, Chapter 6.

	Temperature / K					
Nickel	291*	323	373	423	473	516
γ_2	24.24(4.105)	55.62(4.136)	64.29(4.238)	41.53(4.521)	43.35(5.014)	93.51(4.605)
	37.43(3.887)	35.91(4.338)	50.29(4.412)	38.08(4.334)	42.54(4.661)	61.01(4.724)
	44.41(3.855)	57.81(4.037)	46.44(4.435)	61.64(4.432)	56.88(4.727)	69.28(4.721)
		55.47(4.165)	73.03(4.036)	55.78(4.3589	38.4(4.927)	54.5(4.735)
		49.78(4.239)	73.68(4.168)	54.39(4.477)	60.93(4.615)	48.35(4.9)
		50.96(4.062)	49.21(4.247)	52.91(4.498)	56.13(4.734)	36.48(5.13)
		57.46(3.976)	61.14(4.047)	57.42(4.447)	37.72(5.053)	41.18(4.976)
		50.89(4.195)	55.12(4.104)	34.56(4.427)		46.58(5.131)
		54.85(3.938)	73.2(4.097)	44.96(4.6)		59.15(4.851)
		67.42(3.864)	59.32(4.192)	56.32(4.324)		
		44.12(3.985)	41.12(4.32)	32.22(4.63)		
		40.58(4.283)	55.99(3.587)	46.94(4.574)		
		61.06(3.982)	61.24(4.301)	73.44(4.531)		

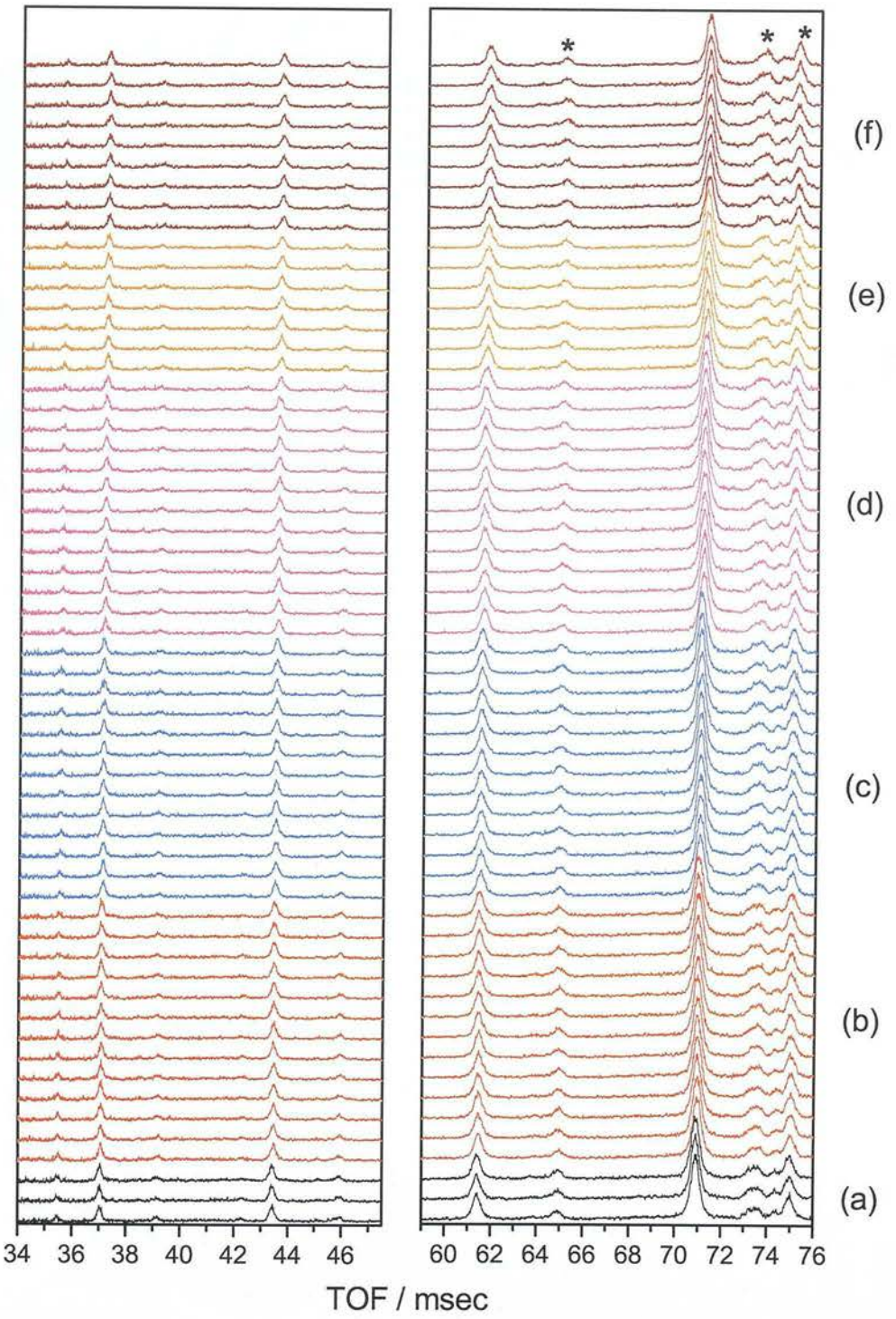

Figure E.2: Complete set of patterns for neutron diffraction data of nickel particles on a Ni(10%)/Al_2O_3 catalyst during microwave irradiation. (a) 291 K, (b) 323 K, (c) 373 K, (d) 423 K (e) 473 K and, (f) 516 K. Scans were taken approximately every 6 minutes. Asterisks (*) indicate reflections from the microwave applicator.

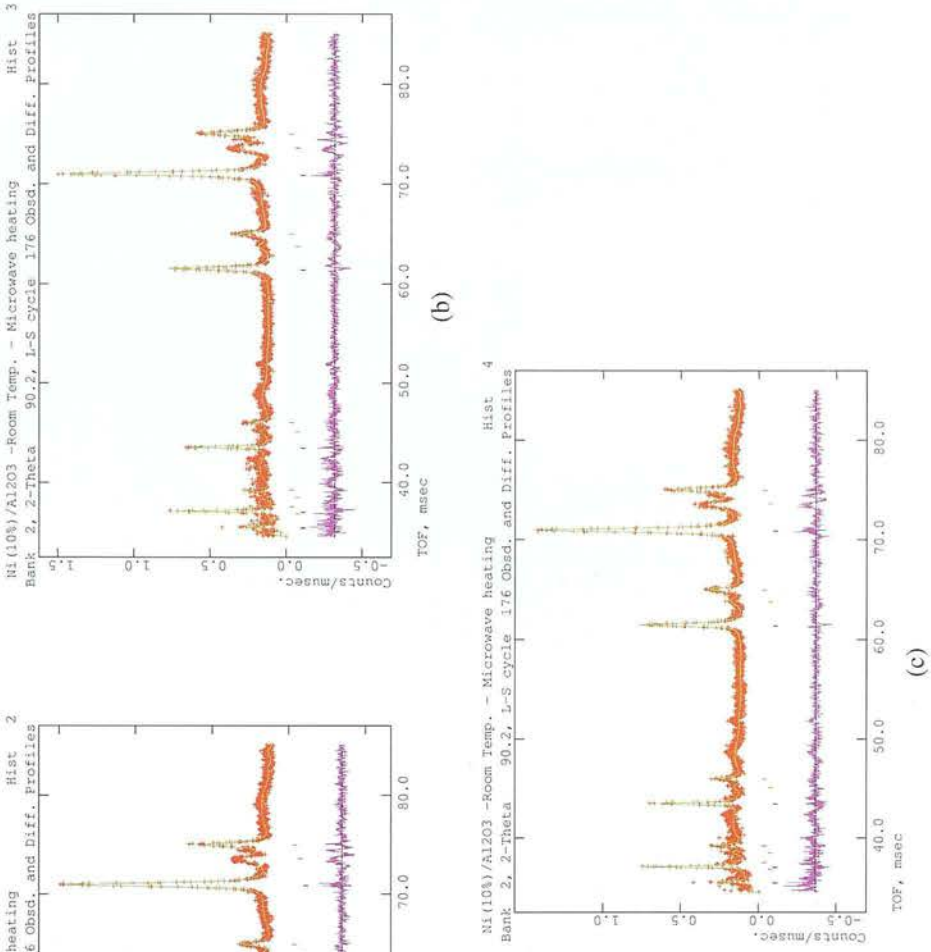

Figure E.3: Rietveld refinement graphs for nickel particles for neutron diffraction data during microwave radiation at 293 K. (a) Hist. 2, (b) Hist. 3, (c) Hist. 4. The small red + represent the observed pattern, the green continuous line represents the calculated pattern and the difference between the calculated and the observed pattern is shown in the bottom graph (in magenta). The tick marks show the reflections included in the refinement - top ticks (blue and red) for brass contributions from the waveguide and the top ticks (black) for the nickel phase.

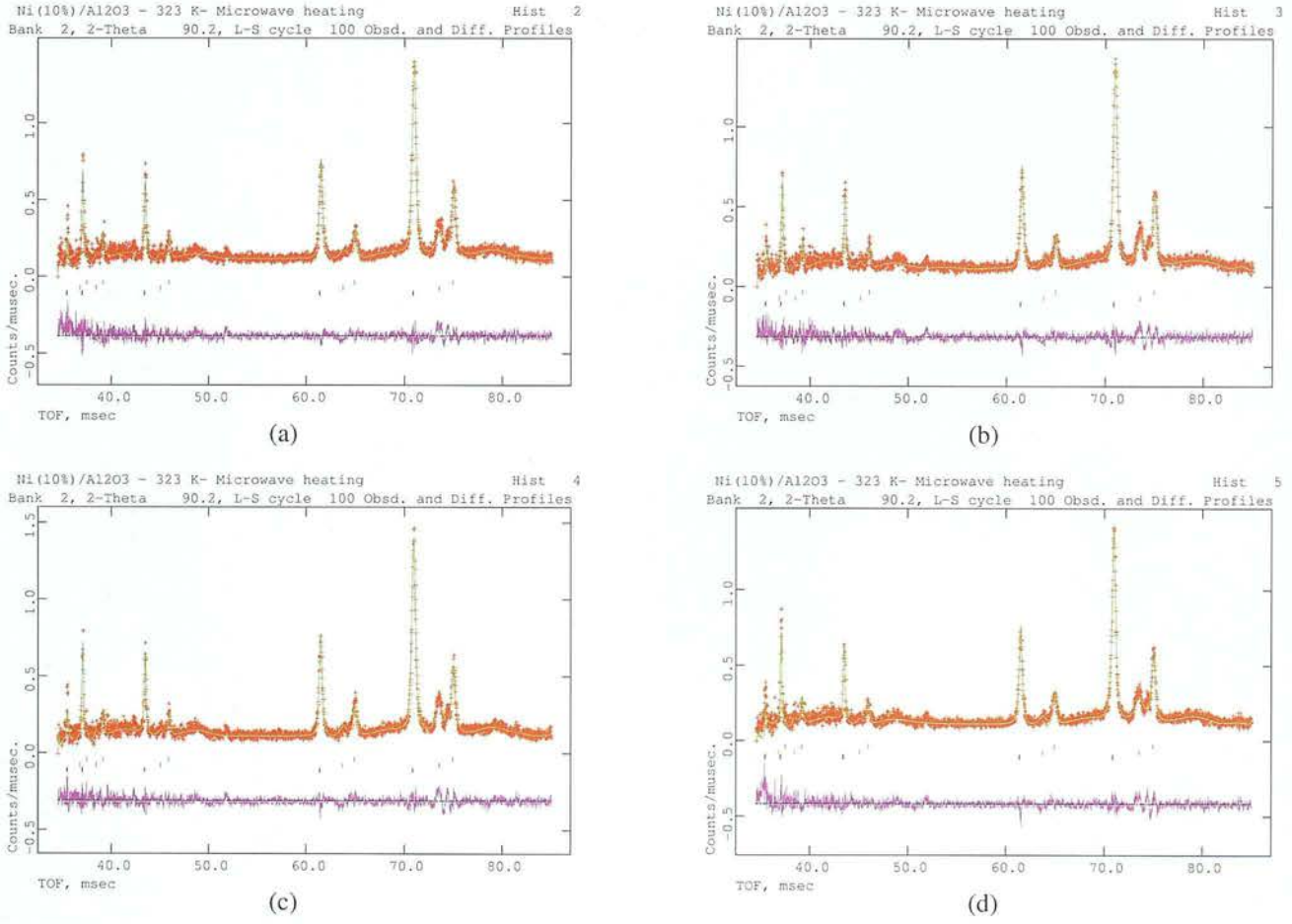

Figure E.4: Rietveld refinement graphs for nickel particles for neutron diffraction data during microwave radiation at 323 K. (a) Hist. 2, (b) Hist. 3, (c) Hist. 4 and, (d) Hist. 5. The small red + represent the observed pattern, the green continuous line represents the calculated pattern and the difference between the calculated and the observed pattern is shown in the bottom graph (in magenta). The tick marks show the reflections included in the refinement - top ticks (blue and red) for brass contributions from the waveguide and the top ticks (black) for the nickel phase.

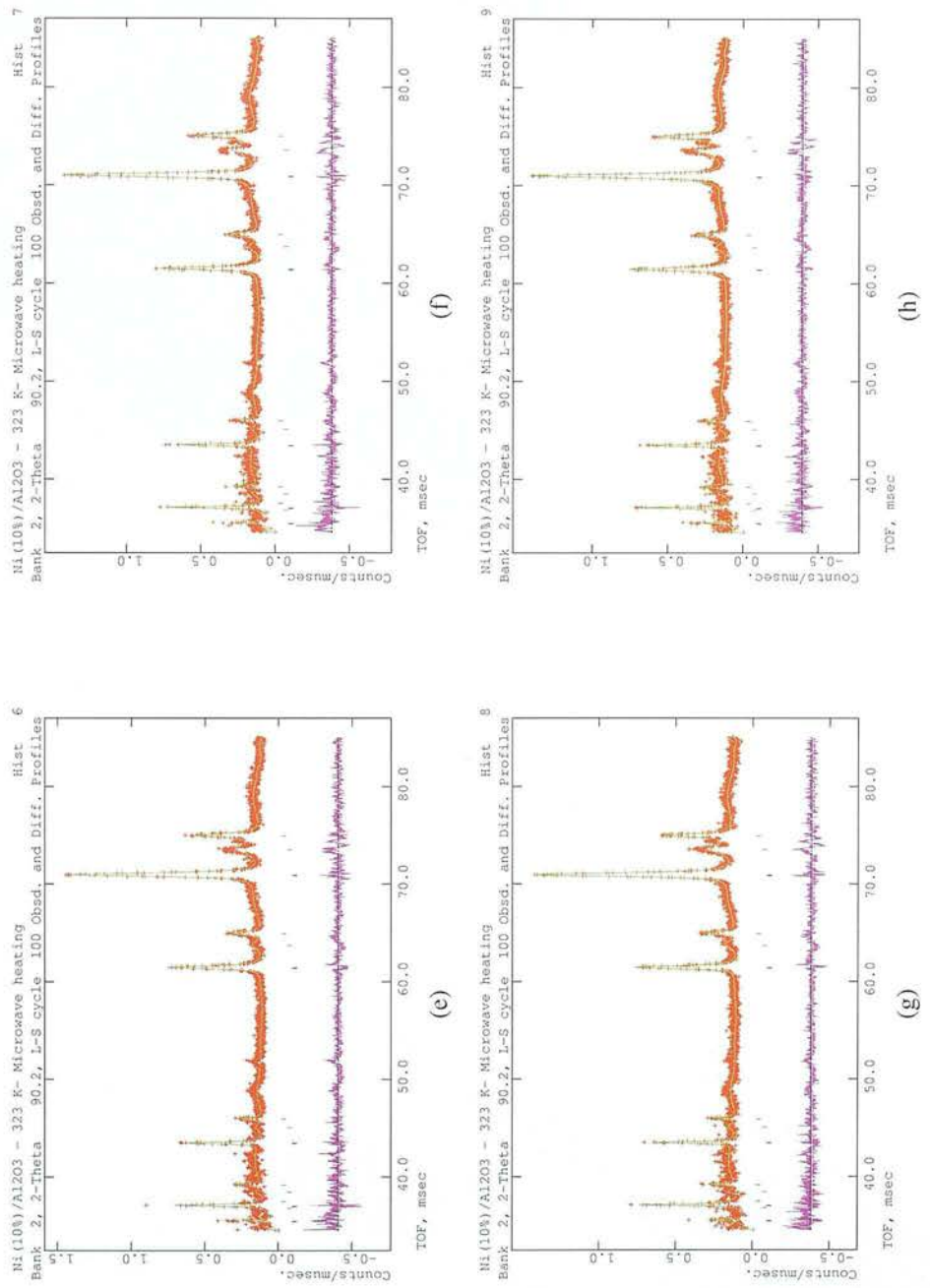

Figure E.4: (Cont). Rietveld refinement graphs for nickel particles for neutron diffraction data during microwave radiation at 323 K. (e) Hist. 6, (f) Hist. 7, (g) Hist. 8 and, (h) Hist. 9. The small red + represent the observed pattern, the green continuos line represents the calculated pattern and the difference between the calculated and the observed pattern is shown in the bottom graph (in magenta). The tick marks show the relections included in the refinement - top ticks (blue and red) for brass contributions from the waveguide and the top ticks (black) for the nickel phase.

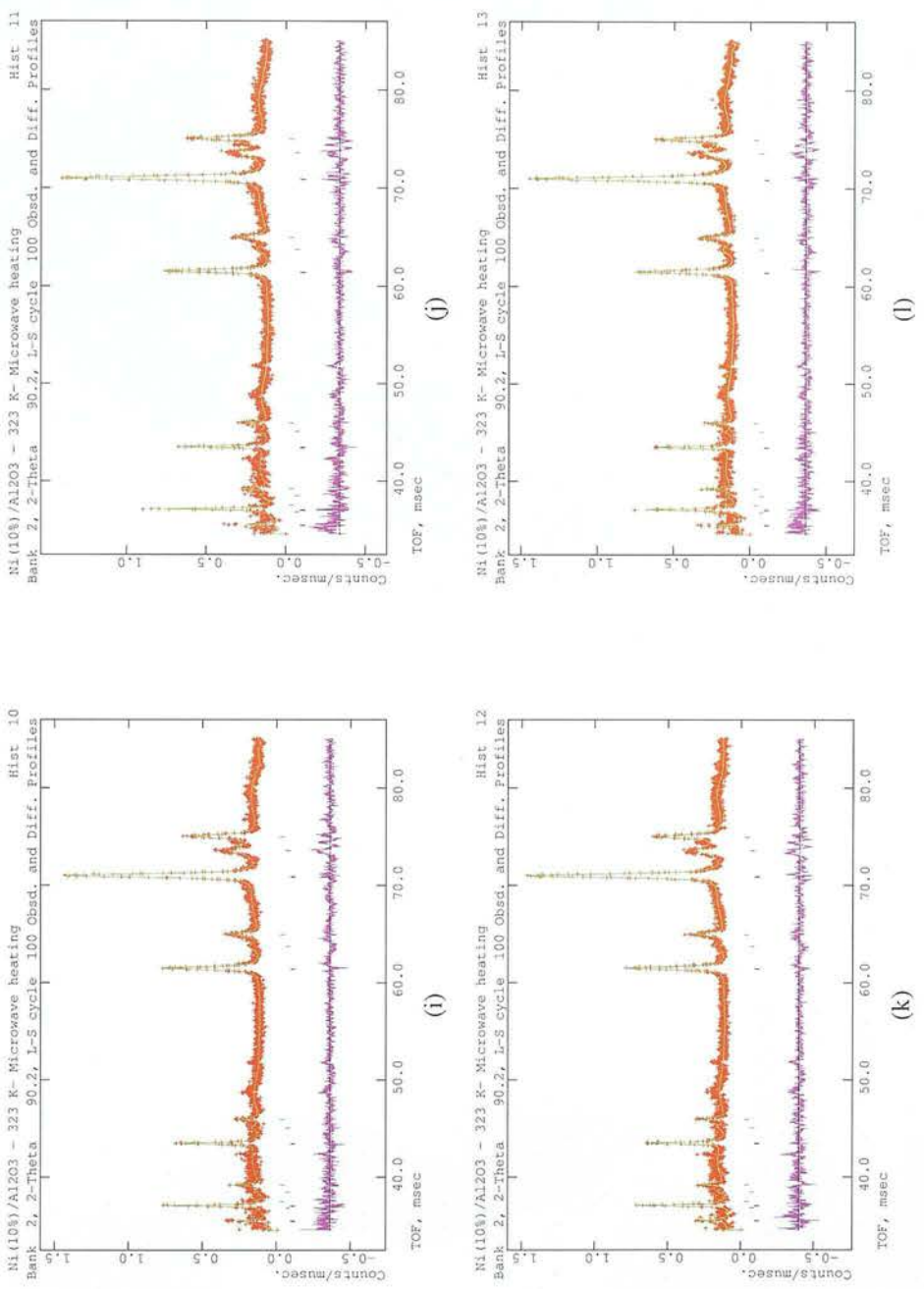

Figure E.4: (Cont). Rietveld refinement graphs for nickel particles for neutron diffraction data during microwave radiation at 323 K. (i) Hist. 10, (j) Hist. 11, (k) Hist. 12 and, (l) Hist. 13. The small red + represent the observed pattern, the green continuos line represents the calculated pattern and the difference between the calculated and the observed pattern is shown in the bottom graph (in magenta). The tick marks show the relections included in the refinement - top ticks (blue and red) for brass contributions from the waveguide and the top ticks (black) for the nickel phase.

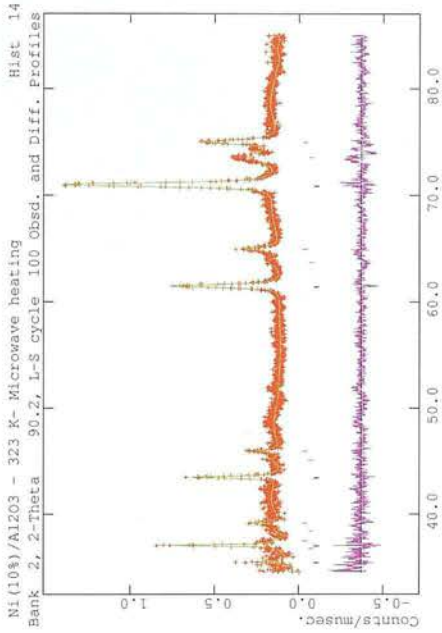

Figure E.4: (Cont). Rietveld refinement graphs for nickel particles for neutron diffraction data during microwave radiation at 323 K. (m) Hist. 14. The small red + represent the observed pattern, the green continuos line represents the calculated pattern and the difference between the calculated and the observed pattern is shown in the bottom graph (in magenta). The tick marks show the relections included in the refinement - top ticks (blue and red) for brass contributions from the waveguide and the top ticks (black) for the nickel phase.

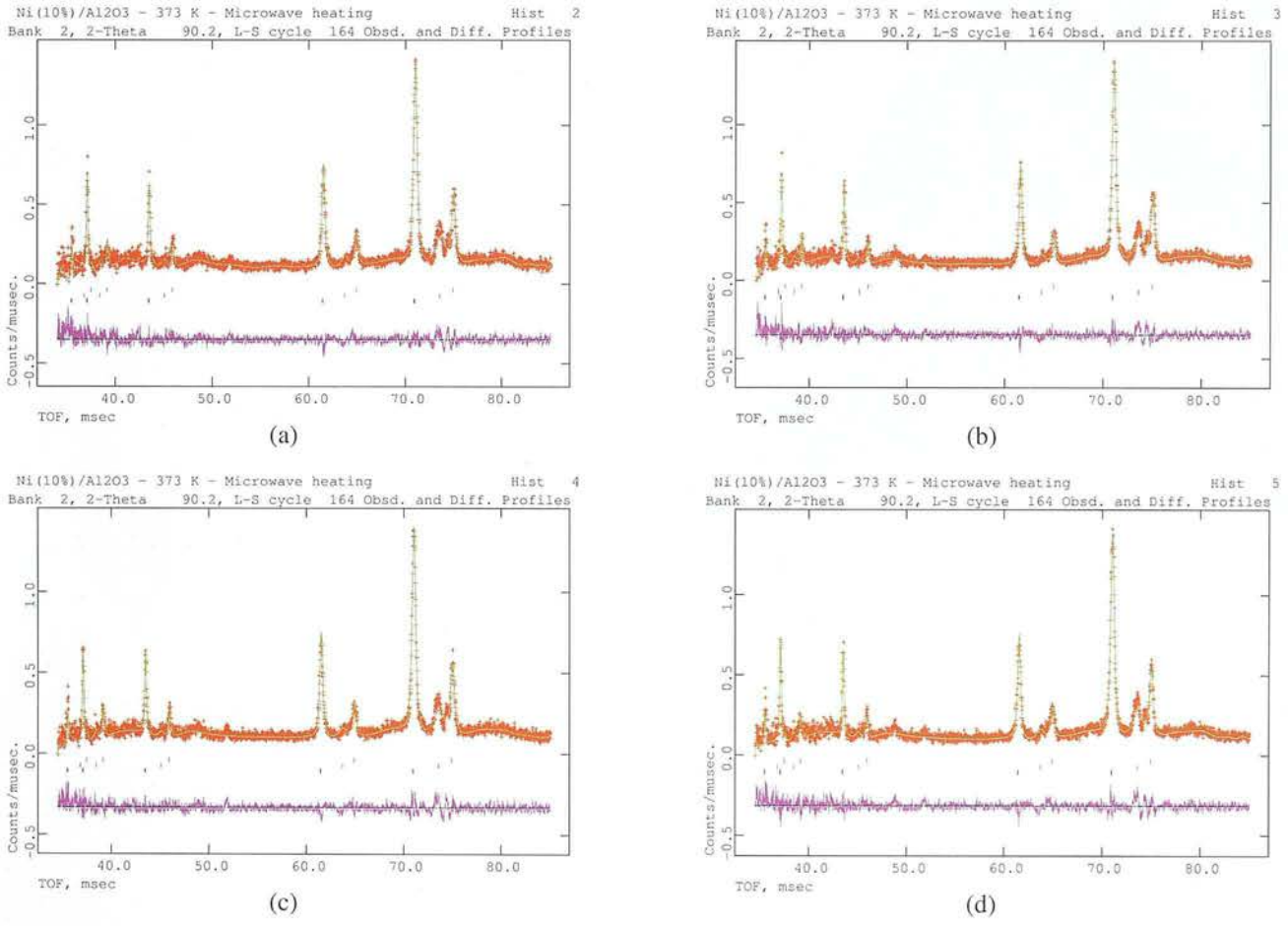

Figure E.5: Rietveld refinement graphs for nickel particles for neutron diffraction data during microwave radiation at 373 K. (a) Hist. 2, (b) Hist. 3, (c) Hist. 4 and, (d) Hist. 5. The small red + represent the observed pattern, the green continuous line represents the calculated pattern and the difference between the calculated and the observed pattern is shown in the bottom graph (in magenta). The tick marks show the reflections included in the refinement - top ticks (blue and red) for brass contributions from the waveguide and the top ticks (black) for the nickel phase.

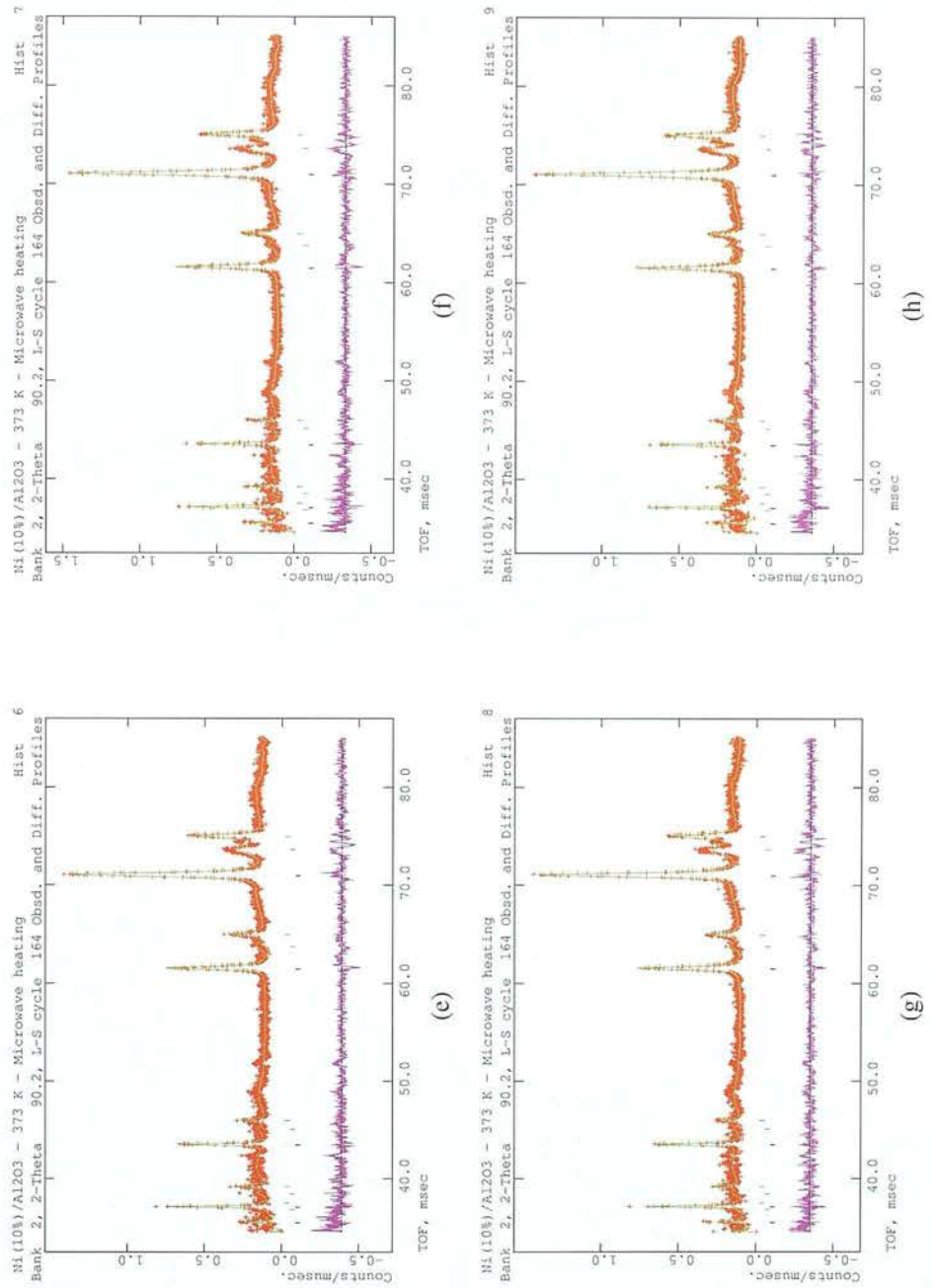

Figure E.5: (Cont). Rietveld refinement graphs for nickel particles for neutron diffraction data during microwave radiation at 373 K. (e) Hist. 6, (f) Hist. 7, (g) Hist. 8 and (h) Hist. 9. The small red + represent the observed pattern, the green continuos line represents the calculated pattern and the difference between the calculated and the observed pattern is shown in the bottom graph (in magenta). The tick marks show the relections included in the refinement - top ticks (blue and red) for brass contributions from the waveguide and the top ticks (black) for the nickel phase.

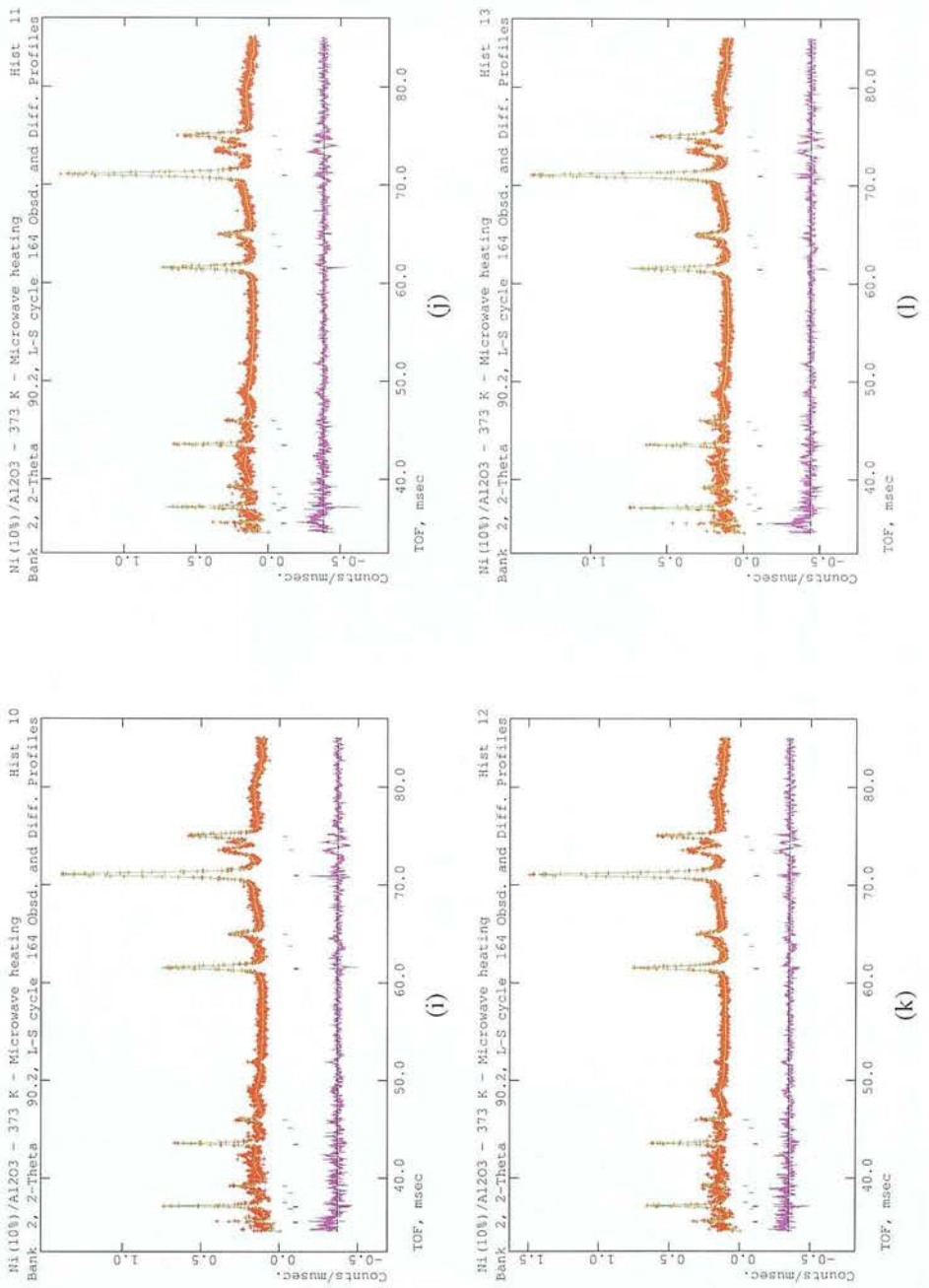

Figure E.5: (Cont). Rietveld refinement graphs for nickel particles for neutron diffraction data during microwave radiation at 373 K. (i) Hist. 10, (j) Hist. 11, (k) Hist. 12 and (l) Hist. 13. The small red + represent the observed pattern, the green continuos line represents the calculated pattern and the difference between the calculated and the observed pattern is shown in the bottom graph (in magenta). The tick marks show the relections included in the refinement - top ticks (blue and red) for brass contributions from the waveguide and the top ticks (black) for the nickel phase.

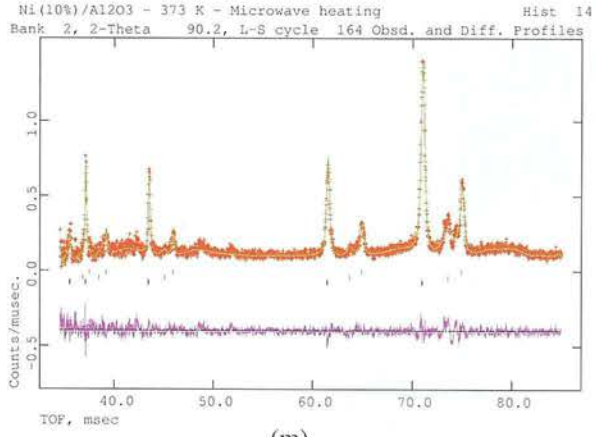

(m)

Figure E.5: (Cont). Rietveld refinement graphs for nickel particles for neutron diffraction data during microwave radiation at 373 K. (m) Hist. 14. The small red + represent the observed pattern, the green continuos line represents the calculated pattern and the difference between the calculated and the observed pattern is shown in the bottom graph (in magenta). The tick marks show the relections included in the refinement - top ticks (blue and red) for brass contributions from the waveguide and the top ticks (black) for the nickel phase.

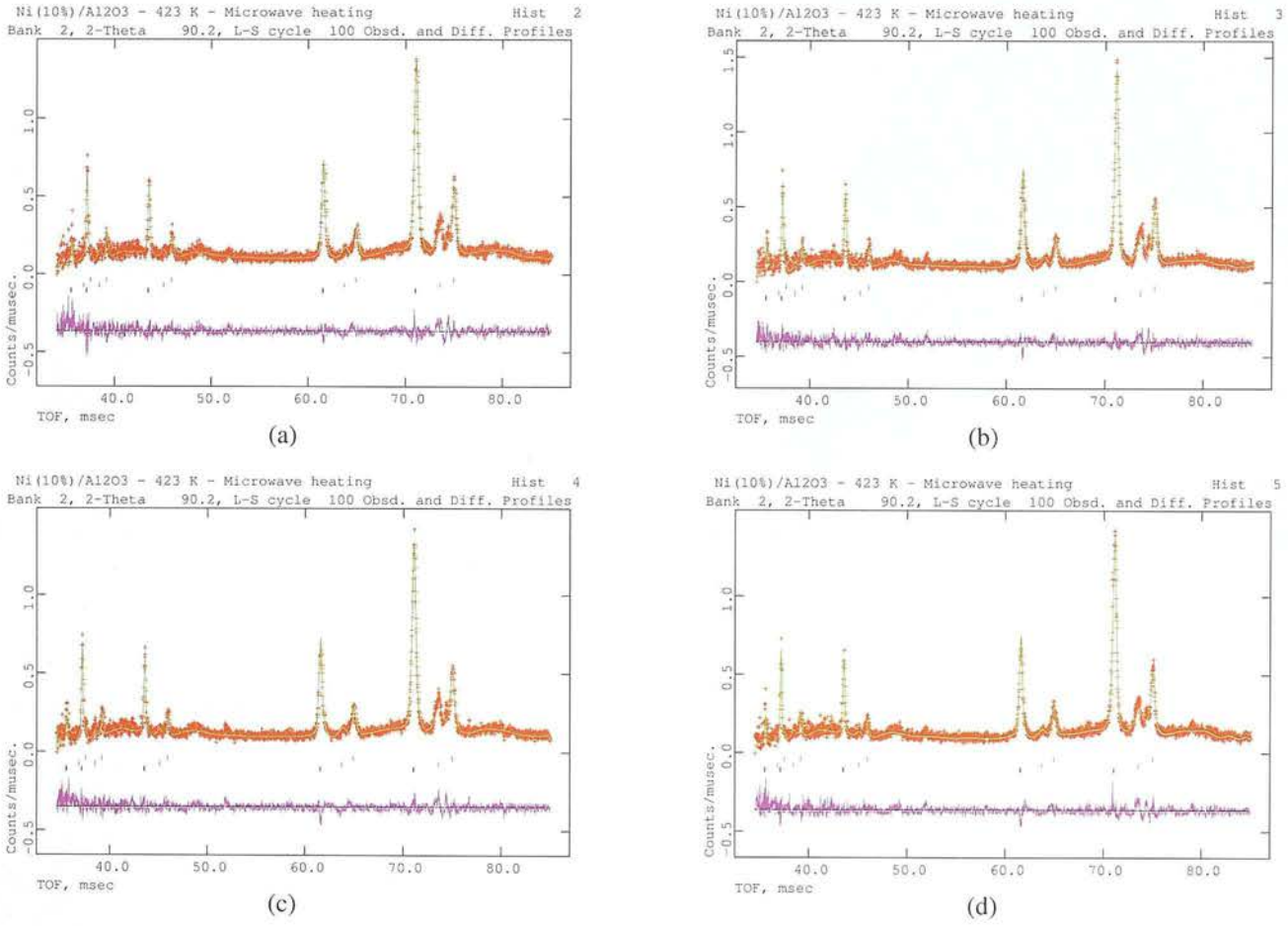

Figure E.6: Rietveld refinement graphs for nickel particles for neutron diffraction data during microwave radiation at 423 K. (a) Hist. 2, (b) Hist. 3, (c) Hist. 4, and (d) Hist. 5. The small red + represent the observed pattern, the green continuous line represents the calculated pattern and the difference between the calculated and the observed pattern is shown in the bottom graph (in magenta). The tick marks show the reflections included in the refinement - top ticks (blue and red) for brass contributions from the waveguide and the top ticks (black) for the nickel phase.

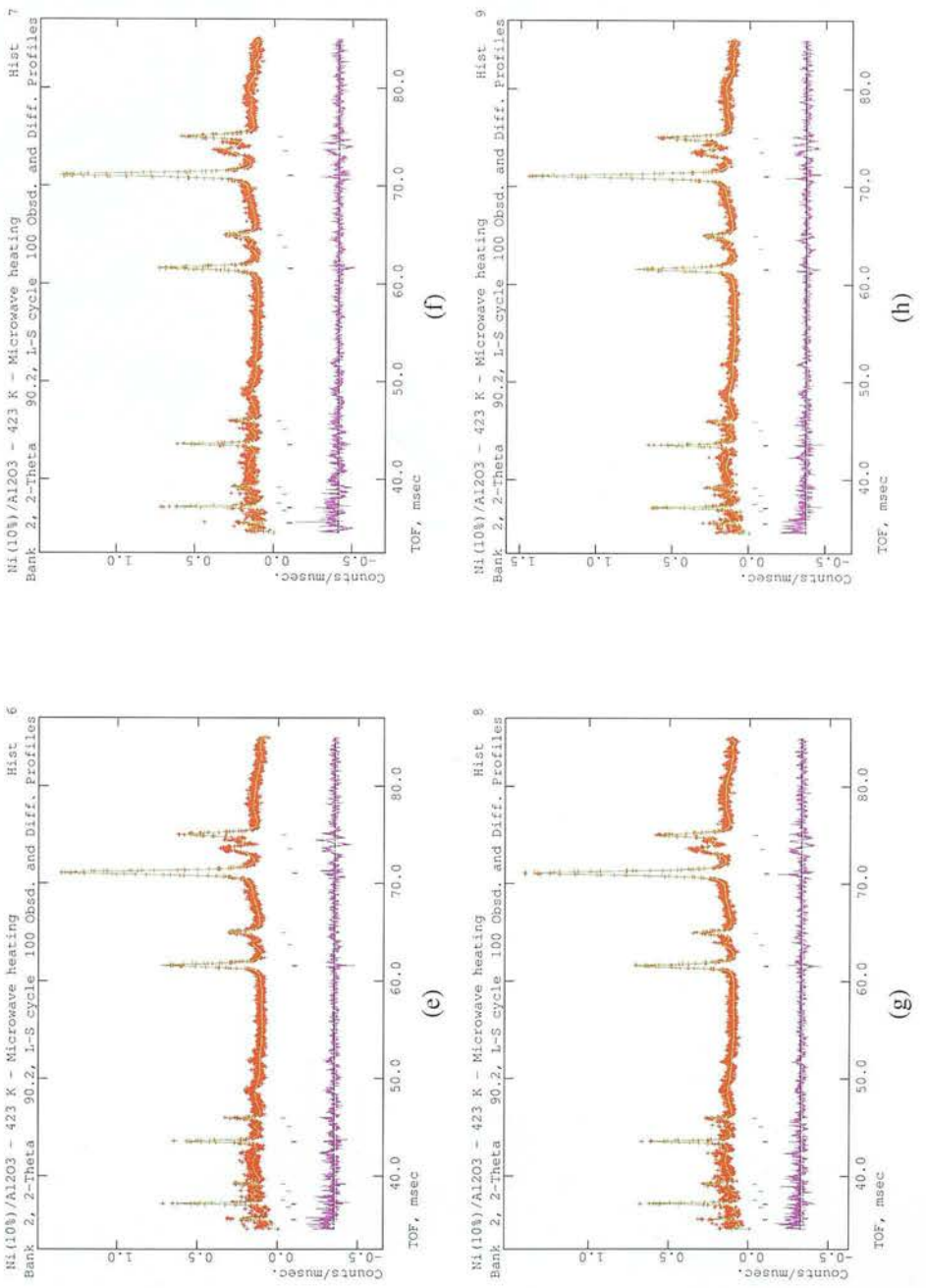

Figure E.6: (Cont). Rietveld refinement graphs for nickel particles for neutron diffraction data during microwave radiation at 423 K. (e) Hist. 6, (f) Hist. 7, (g) Hist. 8 and (h) Hist. 9. The small red + represent the observed pattern, the green continuous line represents the calculated pattern and the difference between the calculated and the observed pattern is shown in the bottom graph (in magenta). The tick marks show the reflections included in the refinement - top ticks (blue and red) for brass contributions from the waveguide and the top ticks (black) for the nickel phase.

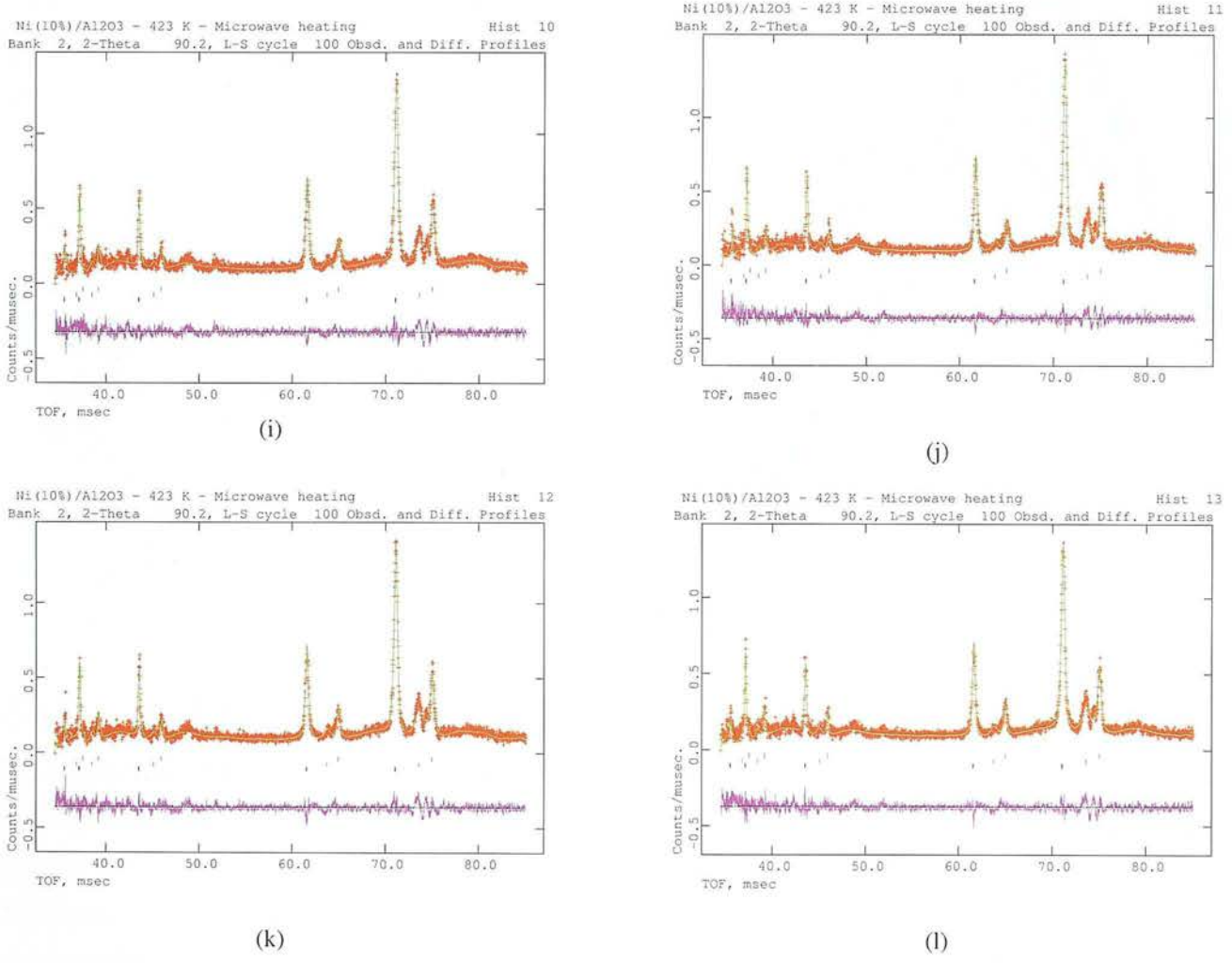

Figure E.6: (Cont). Rietveld refinement graphs for nickel particles for neutron diffraction data during microwave radiation at 423 K. (i) Hist. 10, (j) Hist. 11, (k) Hist. 12 and (l) Hist. 13. The small red + represent the observed pattern, the green continuous line represents the calculated pattern and the difference between the calculated and the observed pattern is shown in the bottom graph (in magenta). The tick marks show the reflections included in the refinement - top ticks (blue and red) for brass contributions from the waveguide and the top ticks (black) for the nickel phase.

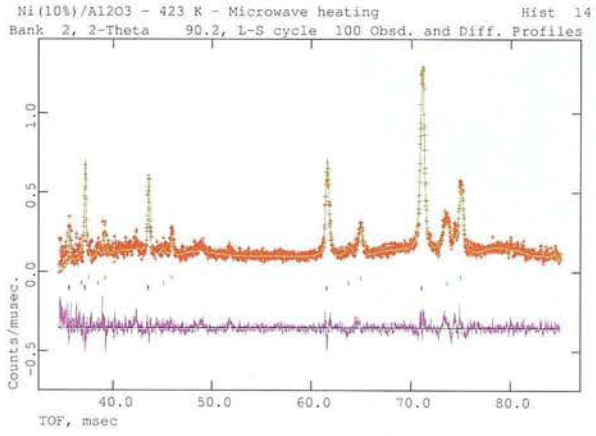

(m)

Figure E.6: (Cont). Rietveld refinement graphs for nickel particles for neutron diffraction data during microwave radiation at 423 K. (m) Hist. 14. The small red + represent the observed pattern, the green continuous line represents the calculated pattern and the difference between the calculated and the observed pattern is shown in the bottom graph (in magenta). The tick marks show the reflections included in the refinement - top ticks (blue and red) for brass contributions from the waveguide and the top ticks (black) for the nickel phase.

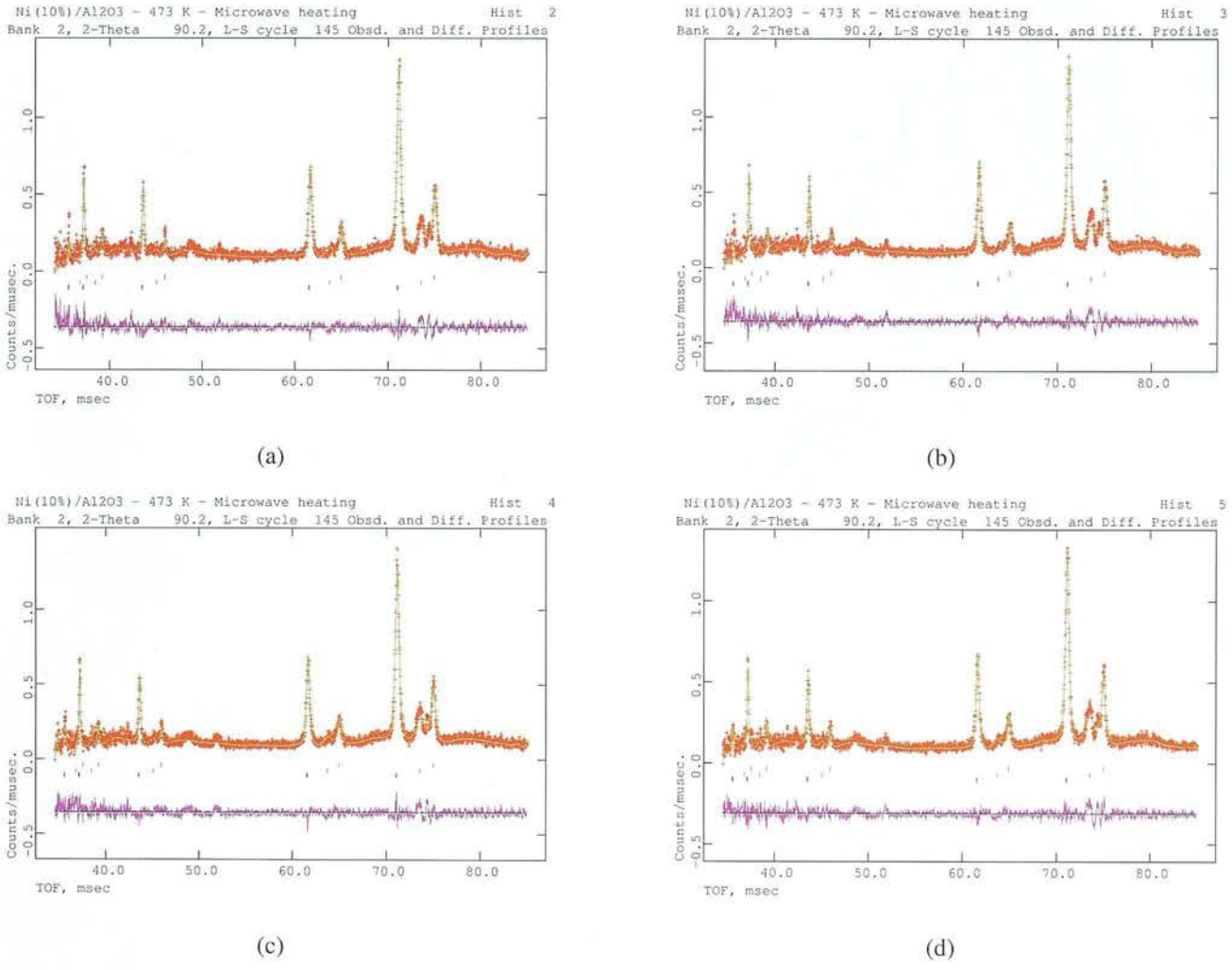

Figure E.7: Rietveld refinement graphs for nickel particles for neutron diffraction data during microwave radiation at 473 K. (a) Hist. 2, (b) Hist. 3, (c) Hist. 4 and (d) Hist. 5. The small red + represent the observed pattern, the green continuous line represents the calculated pattern and the difference between the calculated and the observed pattern is shown in the bottom graph (in magenta). The tick marks show the reflections included in the refinement - top ticks (blue and red) for brass contributions from the waveguide and the top ticks (black) for the nickel phase.

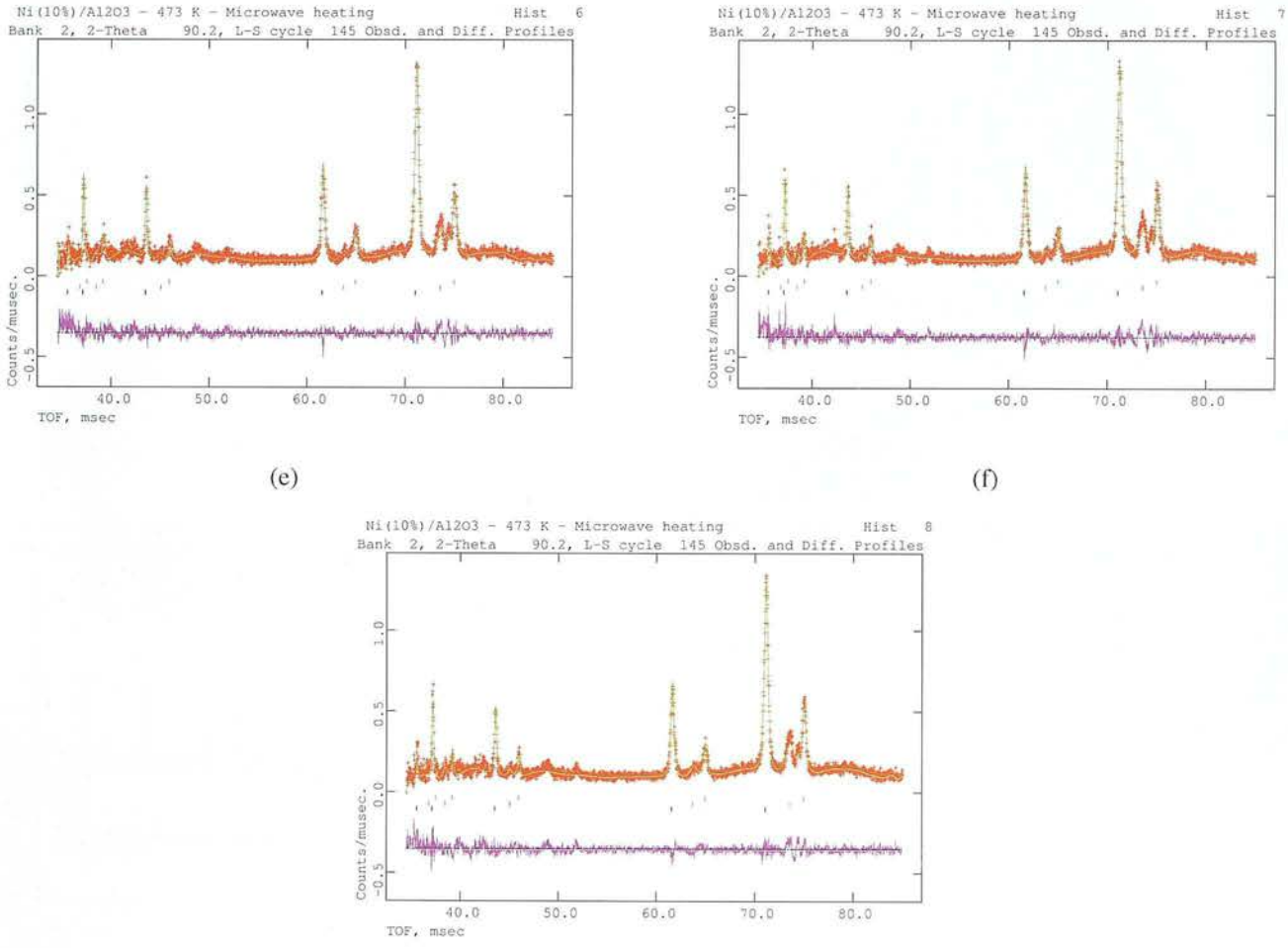

Figure E.7: (Cont). Rietveld refinement graphs for nickel particles for neutron diffraction data during microwave radiation at 473 K. (e) Hist.6, (f) Hist. 7, and (g) Hist. 8. The small red + represent the observed pattern, the green continuous line represents the calculated pattern and the difference between the calculated and the observed pattern is shown in the bottom graph (in magenta). The tick marks show the reflections included in the refinement - top ticks (blue and red) for brass contributions from the waveguide and the top ticks (black) for the nickel phase.

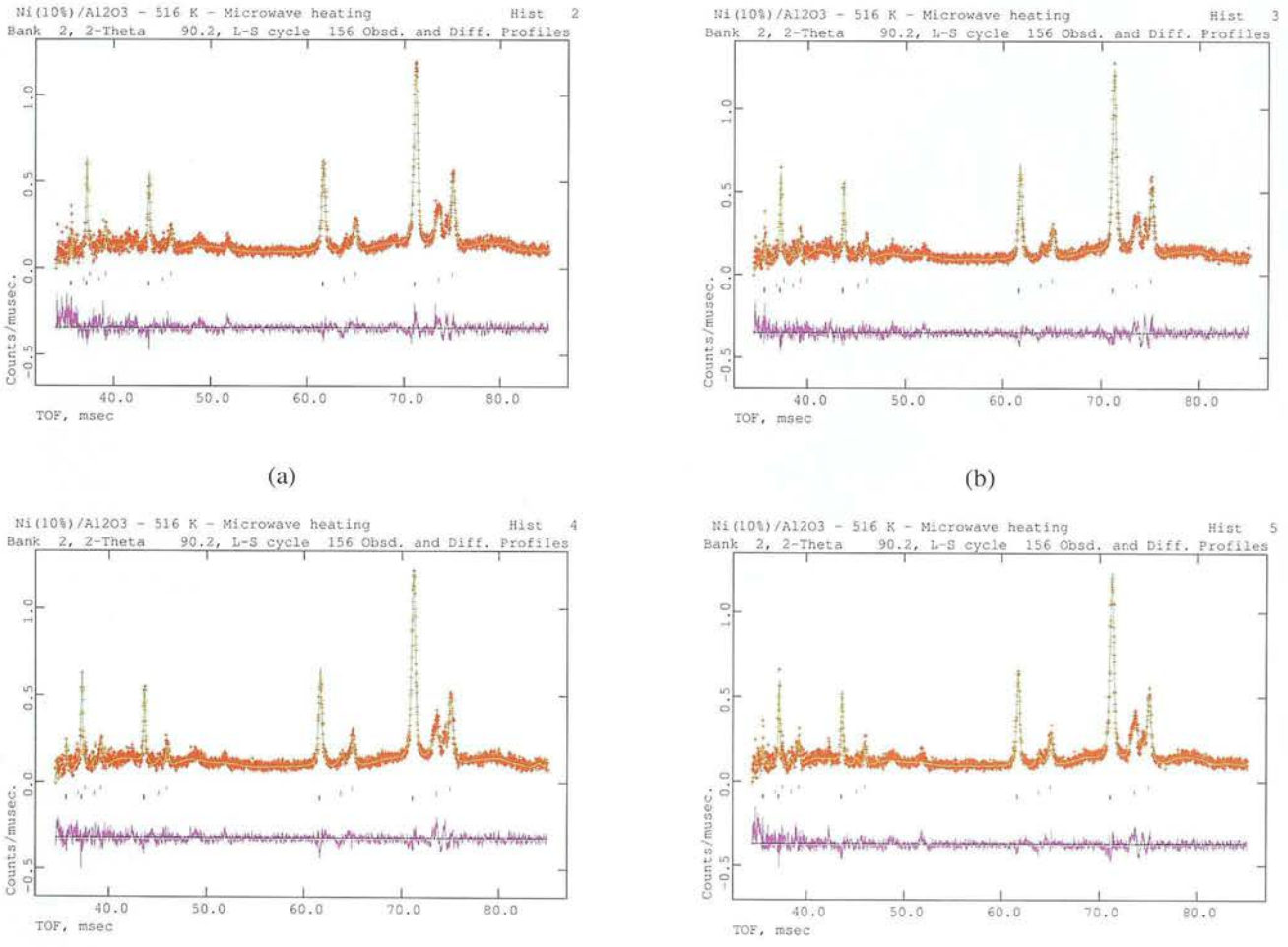

Figure E.8: Rietveld refinement graphs for nickel particles for neutron diffraction data during microwave radiation at 516 K. (a) Hist. 2, (b) Hist. 3, (c) Hist. 4, and (d) Hist. 5. The small red + represent the observed pattern, the green continuous line represents the calculated pattern and the difference between the calculated and the observed pattern is shown in the bottom graph (in magenta). The tick marks show the reflections included in the refinement - top ticks (blue and red) for brass contributions from the waveguide and the top ticks (black) for the nickel phase.

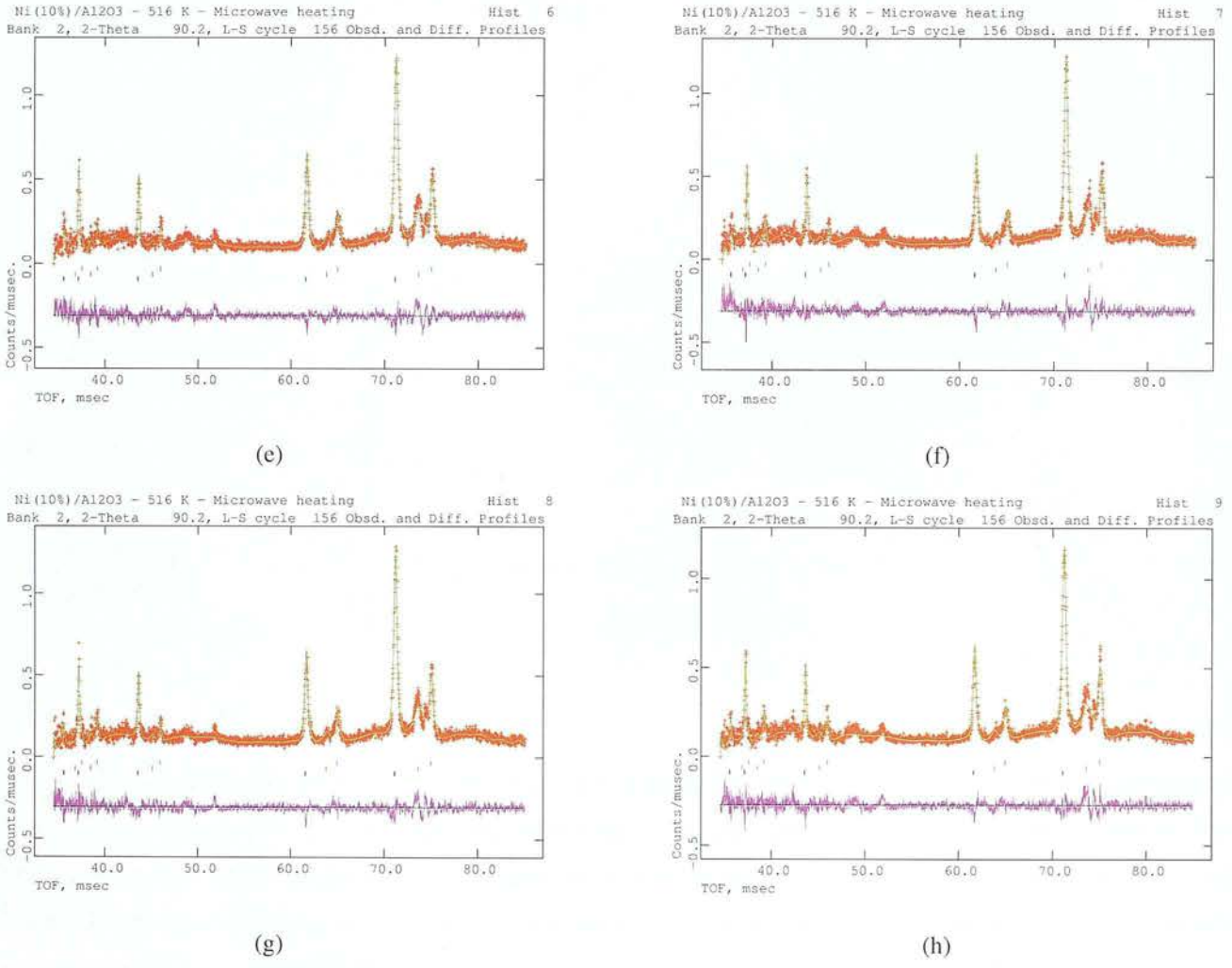

Figure E.8: (Cont). Rietveld refinement graphs for nickel particles for neutron diffraction data during microwave radiation at 516 K. (e) Hist. 6, (f) Hist.7, (g) Hist. 8, and (h) Hist. 9. The small red + represent the observed pattern, the green continuous line represents the calculated pattern and the difference between the calculated and the observed pattern is shown in the bottom graph (in magenta). The tick marks show the reflections included in the refinement - top ticks (blue and red) for brass contributions from the waveguide and the top ticks (black) for the nickel phase.

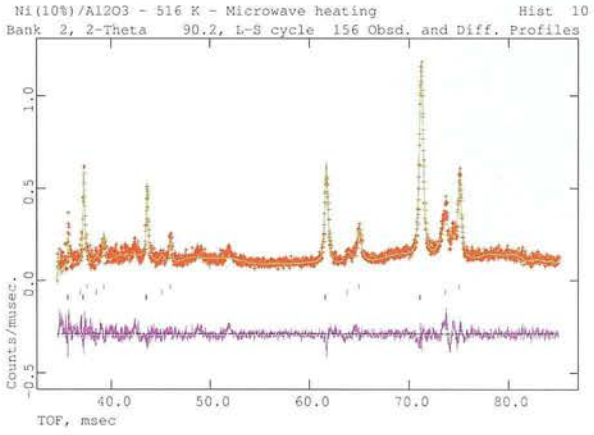

(i)

Figure E.8: (Cont). Rietveld refinement graphs for nickel particles for neutron diffraction data during microwave radiation at 516 K. (i) Hist. 10. The small red + represent the observed pattern, the green continuous line represents the calculated pattern and the difference between the calculated and the observed pattern is shown in the bottom graph (in magenta). The tick marks show the reflections included in the refinement - top ticks (blue and red) for brass contributions from the waveguide and the top ticks (black) for the nickel phase.

E.2 Neutron diffraction data for the MoS_2(30%)/α-Al_2O_3(70%) catalyst

Table E.3: Cell parameters for MoS_2 and α-Al_2O_3 particles under conventional heating determined by Rietveld refinement of neutron diffraction data.

	Temperature / K				
MoS_2	291	473	673	873	1073
a / Å	3.157611(107)	3.161377(110)	3.165422(110)	3.170355(117)	3.175174(180)
c / Å	12.283665(683)	12.307070(714)	12.333823(731)	12.358918(793)	12.389227(812)
V / $Å^3$	106.066(7)	106.522(7)	107.027(7)	107.579(7)	108.171(7)
fraction	34.028(0.152921)	35.538(0.172764)	34.490(0.164407)	31.956(0.169838)	31.222(0.171345)
α-Al_2O_3					
a / Å	4.754929(98)	4.760084(95)	4.766811(87)	4.774691(90)	4.782277(91)
c / Å	12.980574(279)	12.996263(274)	13.016985(254)	13.040908(260)	13.064955(261)
V / $Å^3$	254.163(13)	255.022(13)	256.152(12)	257.471(12)	258.821(12)
fraction	65.972(0.104145)	67.462(0.0981973)	67.510(0.0912369)	68.044(0.0922098)	68.778(0.0919496)
Goodness of fit					
χ^2	27.82	23.47	17.71	15.70	15.55
wRp	0.1154	0.0722	0.0769	0.0763	0.0756
Rp	0.0921	0.0608	0.0668	0.0675	0.0684

Table E.3: (Cont). Atom parameters for MoS_2 and α-Al_2O_3 particles under conventional heating determined by Rietveld refinement of neutron diffraction data.

	Temperature / K				
MoS_2	291	473	673	873	1073
z_{S2-}	0.120850(252)	0.121146(278)	0.121255(274)	0.122215(289)	0.122597(297)
γ_1	32.36(6.173)	7.950(6.888)	56.72(6.697)	93.06(7.437)	112.6(7.631)
γ_2	60.01(3.163)	67.77(3.470)	48.02(3.326)	33.75(3.624)	43.7(0.9327)
α-Al_2O_3					
z_{Al+3}	0.353212(98)	0.352912(99)	0.353266(93)	0.353082(97)	0.373576(96)
$100*U_{11}$	-0.215(61)	-0.33(62)	-0.109(56)	0.038(58)	0.28(59)
$100*U_{22}$	-0.215(61)	-0.33(62)	-0.109(56)	0.038(58)	0.28(59)
$100*U_{33}$	1.365(104)	1.21(103)	1.336(1.336)	1.768(103)	1.832(104)
$100*U_{12}$	-0.108(30)	-0.165(31)	-0.054(28)	0.01(29)	0.14(3)
x_{O-2}	0.693893(139)	0.693369(148)	0.693854(153)	0.693666(140)	0.693114(144)
$100*U_{11}$	0.838(47)	0.82(51)	0.86(44)	1.115(46)	1.302(46)
$100*U_{22}$	-0.107(58)	-0.36(6)	0.042(54)	0.159(56)	0.475(58)
$100*U_{33}$	0.512(42)	0.32(4)	0.532(38)	0.836(39)	1.038(4)
$100*U_{12}$	-0.054(29)	-0.18(3)	0.021(27)	0.08(28)	0.237(29)
$100*U_{13}$	0.139(21)	0.195(22)	0.204(21)	0.23(22)	0.232(22)
$100*U_{23}$	0.278(42)	0.389(45)	0.409(41)	0.46(43)	0.464(44)
γ_1	4.438(1.740)	0000(1.811)	0.000(1.644)	3.005(1.692)	2.371(1.713)
γ_2	42.05(0.9668)	48.08(0.9903)	45.74(0.9060)	43.92(0.9263)	28.89(3.676)

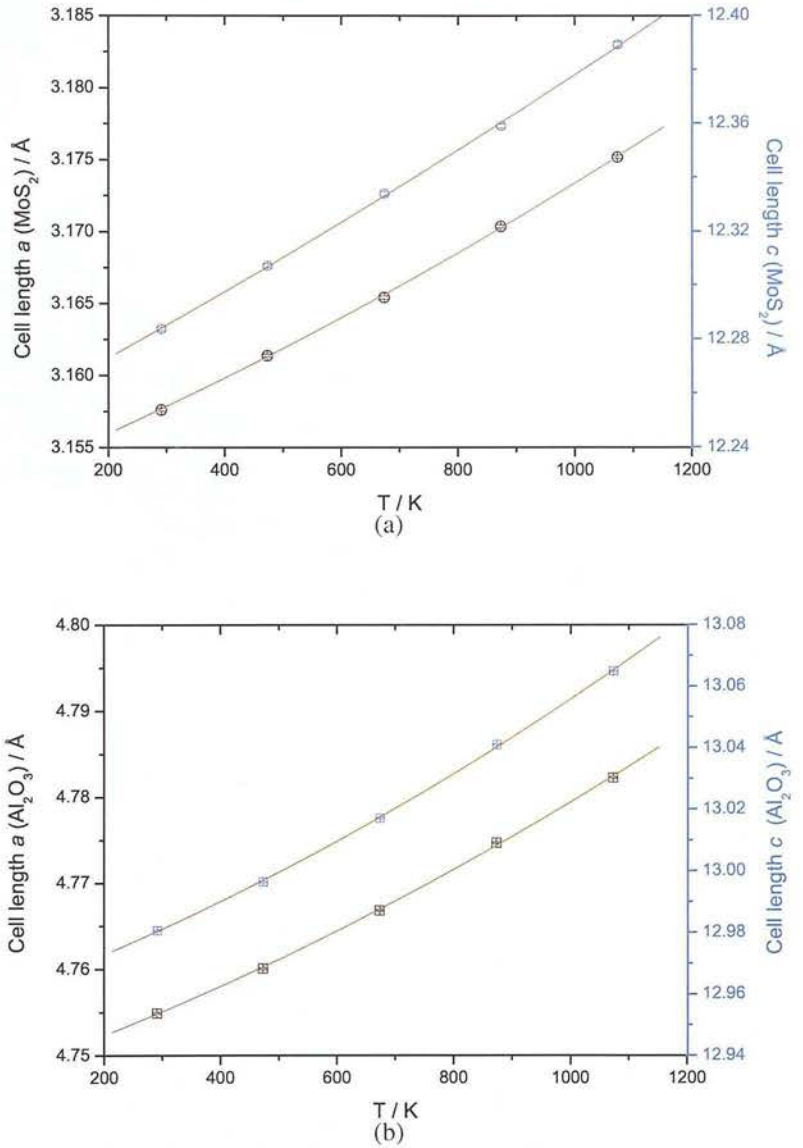

Figure E.9: Thermal expansion in cell parameters a (○, □) and c (○, □) for (a) MoS_2 and (b) α-Al_2O_3 particles obtained from neutron diffraction data during conventional heating.

Table E.4: Results of fitting lattice parameters or volume following equation 6.5 in Chapter 6 for the thermal expansion (from 291 to 1073 K) of MoS_2 and α-Al_2O_3 in conventional heating.

	Parameters					
Phase	x_0	Error$*10^4$	$x_1 * 10^5$	Error $*10^6$	$x_2 * 10^9$	Error$*10^9$
a_{MoS_2-CONV}	3.15239	4.92478	1.6837	1.61253	4.12992	1.16610
c_{MoS_2-CONV}	12.24935	36.4	11.4855	11.9154	13.9874	8.61657
V_{MoS_2-CONV}	105.42112	250.9	211	821.418	421.531	59.40070
$a_{Al_2O_3-CONV}$	4.74729	9.8181	2.32553	3.21476	8.84851	2.32475
$c_{Al_2O_3-CONV}$	12.95794	23.5	6.79869	7.70825	29.9097	5.5742
$V_{Al_2O_3-CONV}$	252.96161	1122.1	356	367.402	1788.37	265.686

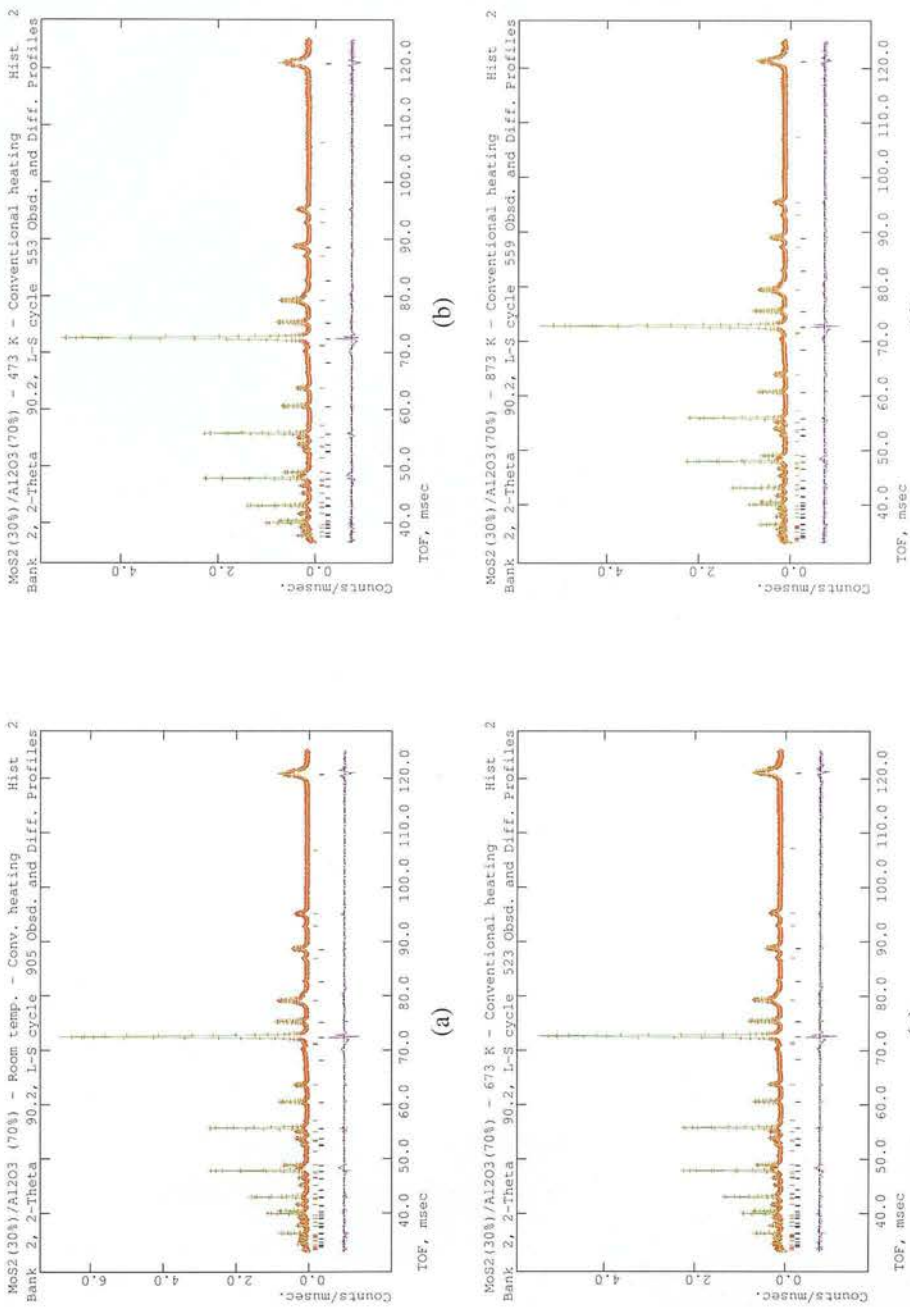

Figure E.10: Rietveld refinement graphs for MoS_2 and α-Al_2O_3 particles for neutron diffraction data during conventional heating. (a) 293 K, (b) 473 K, (c) 673 K and, (d) 873 K. The small red + represent the observed pattern, the green continuous line represents the calculated pattern and the difference between the calculated and the observed pattern is shown in the bottom graph (in magenta). The tick marks show the reflections for MoS_2 (top) and α-Al_2O_3 (bottom) phase.

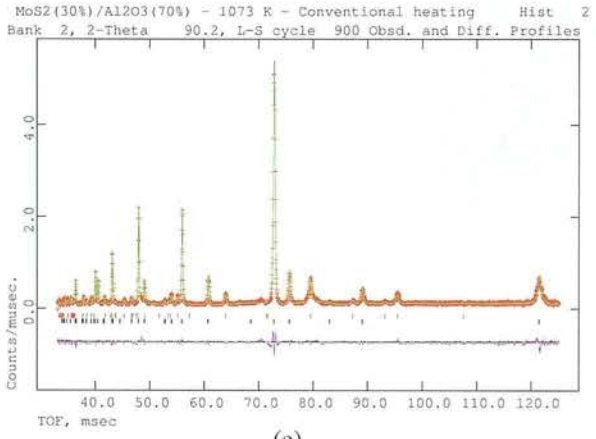

(e)

Figure E.10: (Cont). Rietveld refinement graphs for MoS_2 and α-Al_2O_3 particles for neutron diffraction data during conventional heating. (e) 1073 K. The small red + represent the observed pattern, the green continuous line represents the calculated pattern and the difference between the calculated and the observed pattern is shown in the bottom graph (in magenta). The tick marks show the reflections for MoS_2 (top) and α-Al_2O_3 (bottom) phase.

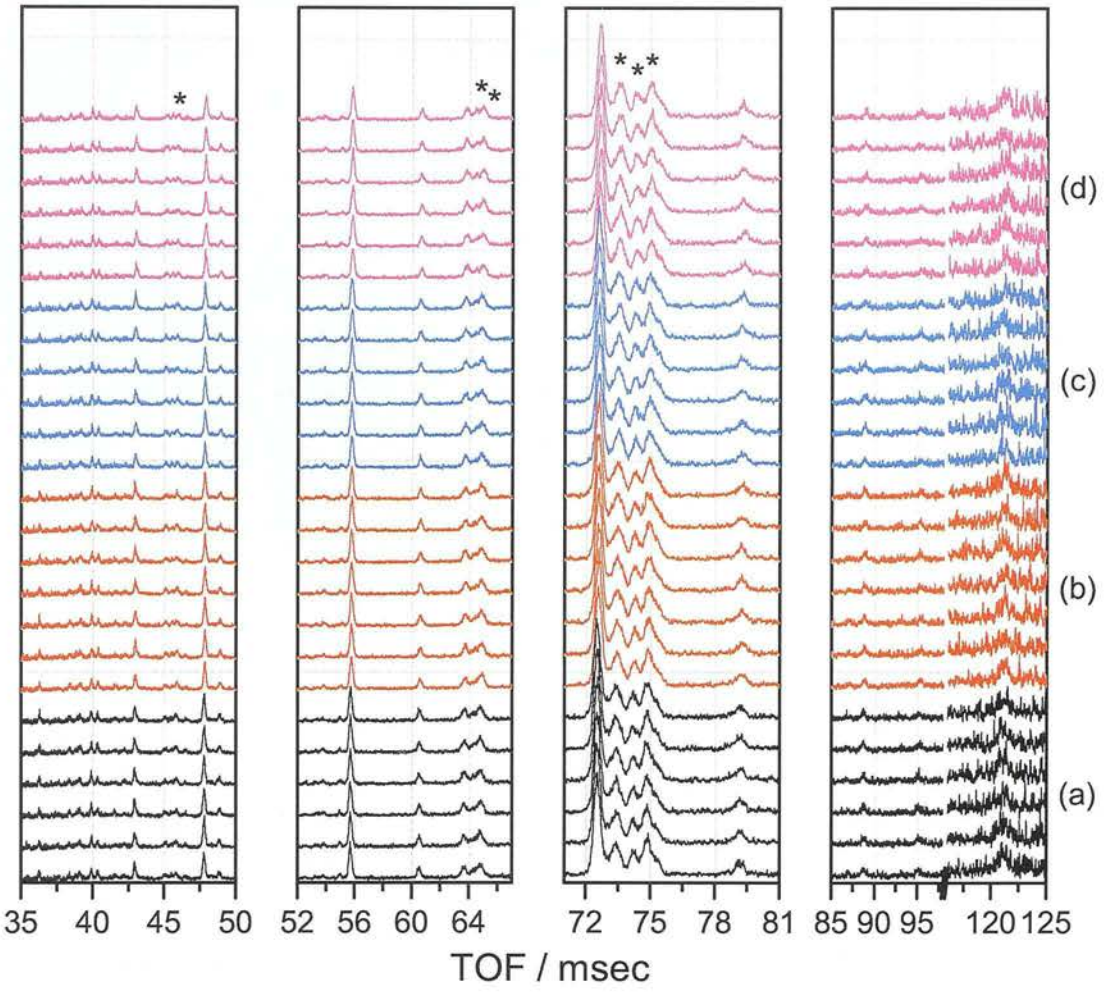

Figure E.11: Complete set of patterns for MoS_2(30%)/α-Al_2O_3(70%) catalyst from neutron diffraction during microwave irradiation. (a) 291 K, (b) 353 K, (c) 413 K and, (d) 473 K. Scans were taken approximately every 6 minutes. Asterisks (*) indicate reflections from the microwave applicator.

Table E.5: Cell parameters for MoS_2 and α-Al_2O_3 particles under microwave heating determined by Rietveld refinement of neutron diffraction data. * Cell parameters used for the sample at 291 K are those of the conventionally heated sample (for details refer to section 6.4.2, Chapter 6.

	Temperature / K			
MoS_2	291*	353	413	473
a / Å	3.157611(107)	3.159594(201)	3.160728(240)	3.161390(236)
c / Å	12.283665(68)	12.304543(167)	12.307673(199)	12.335317(199)
V / Å^3	106.066(7)	106.38(12)	106.483(14)	106.767(14)
Al_2O_3				
a / Å	4.754939(98)	4.758132(126)	4.759308(135)	4.762027(132)
c / Å	12.980574(279)	12.986522(394)	12.990847(424)	12.997292(423)
V / Å^3	254.163(13)	254.622(17)	254.833(18)	255.251(18)
Goodness of fit				
χ^2	7.633	6.992	6.902	7.017
wRp	0.2358	0.1902	0.1974	0.2074
Rp	0.1980	0.1806	0.1910	0.1883
Histogram no.	Fraction ratio (Al_2O_3/MoS_2)			
3	3.4196	2.4528	2.1987	2.4944
4	3.4397	2.8021	2.1630	2.4503
5	3.5980	2.6231	2.5070	2.2155
6	3.0891	2.6107	2.5308	2.4923
7	3.1174	3.0821	2.4620	2.5112
8	3.6624	2.7932	2.4894	2.5058
9		2.6575		

Table E.5: (Cont). Atom and profile parameters (the later for each histogram used) for MoS_2 and α-Al_2O_3 particles under microwave heating determined by Rietveld refinement of neutron diffraction data. * Atom parameters were not refined in the case of the sample at 291 K (for details refer to section 6.4.2, Chapter 6.

	Temperature / K			
MoS_2	291*	353	413	473
z_{S2-}		0.106615(834)	0.103898(927)	0.107999(884)
γ_1	106.4(9.803)	124.6(9.681)	164.3(11.88)	146.6(12.26)
	90.43(8.980)	112.9(10.76)	171.4(12.13)	135.4(10.63)
	97.95(9.874)	125.8(10.98)	159.8(12.80)	137.6(10.07)
	131.5(10.66)	107.5(9.470)	129.7(10.42)	120.1(9.711)
	141.5(11.93)	80.31(8.806)	129.8(10.57)	156.3(13.52)
	104.5(10.70)	111.7(10.60)	131.4(10.36)	145.4(11.71)
		116.7(11.06)		
α-Al_2O_3				
z_{Al+3}		0.351190(151)	0.351465(159)	0.351492(164)
$100*U_{11}$		0.067(92)	0.035(97)	0.313(100)
$100*U_{22}$		0.067(92)	0.035(97)	0.313(100)
$100*U_{33}$		-1.391(154)	-1.443(163)	-1.230(165)
$100*U_{12}$		0.033(46)	0.018(49)	0.157(50)
x_{O-2}		0.694030(220)	0.693657(248)	0.692178(274)
$100*U_{11}$		-0.887(65)	-0.513(74)	-0.270(77)
$100*U_{22}$		-1.141(85)	-1.232(89)	-1.105(90)
$100*U_{33}$		0.664(66)	0.570(69)	0.879(73)
$100*U_{12}$		-0.571(42)	-0.616(45)	-0.552(45)
$100*U_{13}$		0.314(36)	0.422(40)	0.775(43)
$100*U_{23}$		0.627(73)	0.843(80)	1.550(85)
γ_1	89.52(1.477)	83.12(1.316)	83.20(1.394)	86.53(1.456)
	84.03(1.472)	83.86(1.453)	84.89(1.413)	86.71(1.448)
	86.41(1.443)	85.85(1.453)	82.02(1.396)	80.55(1.415)
	90.59(1.428)	84.69(1.425)	87.99(1.448)	83.91(1.420)
	87.22(1.466)	87.77(1.452)	85.93(1.447)	82.69(1.429)
	87.89(1.499)	85.15(1.447)	85.57(1.421)	85.65(1.411)
		82.41(1.440)		

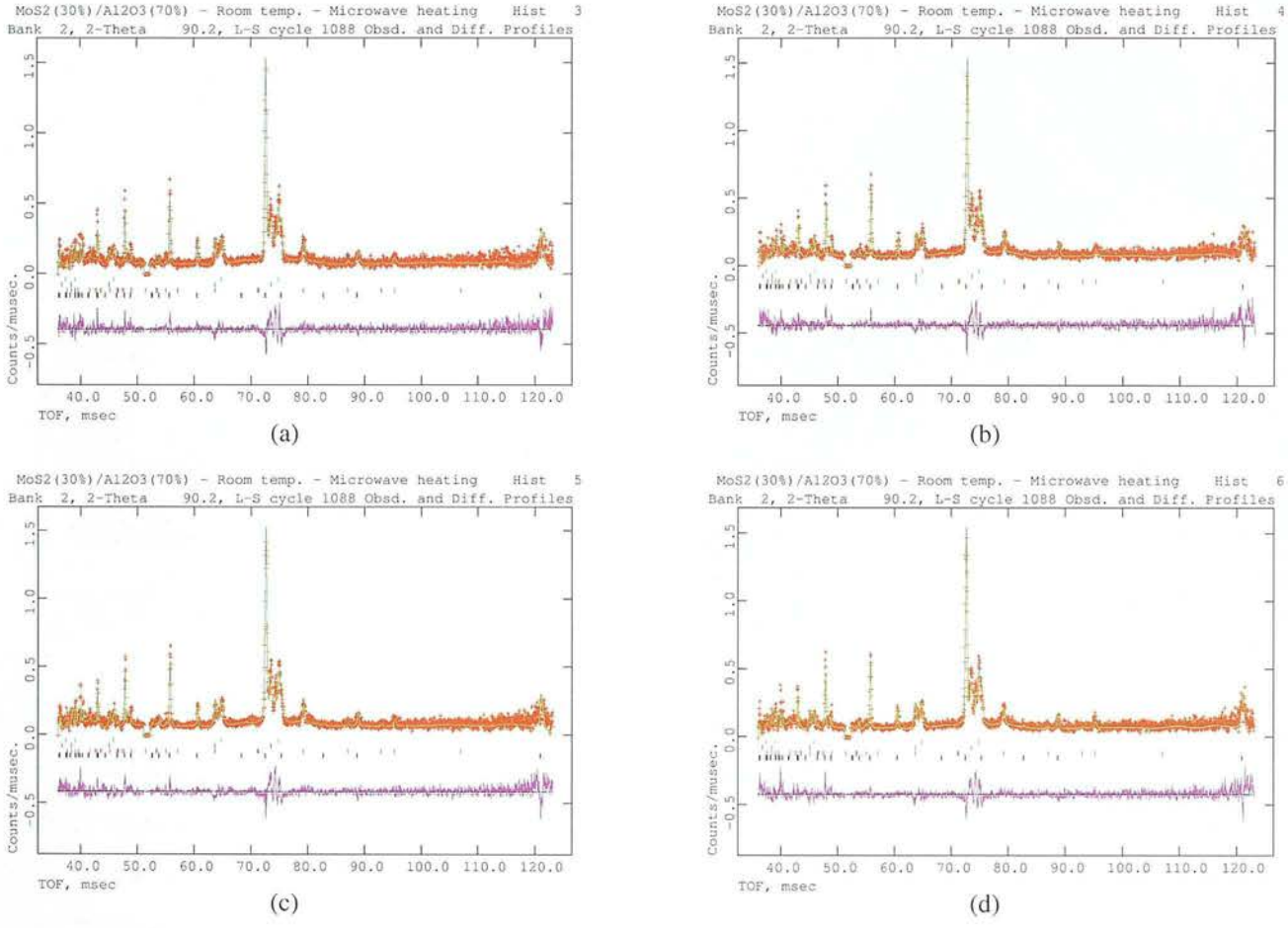

Figure E.12: Rietveld refinement graphs for MoS_2 and α-Al_2O_3 particles for neutron diffraction data during microwave radiation at 291 K. (a) Hist. 3, (b) Hist. 4, (c) Hist. 5, and (d) Hist. 6. The small red + represent the observed pattern, the green continuous line represents the calculated pattern and the difference between the calculated and the observed pattern is shown in the bottom graph (in magenta). The tick marks show the reflections included in the refinement - top ticks (green and blue) for brass contributions from the waveguide and the top ticks (red and black) for the MoS_2 and α-Al_2O_3 phase respectively.

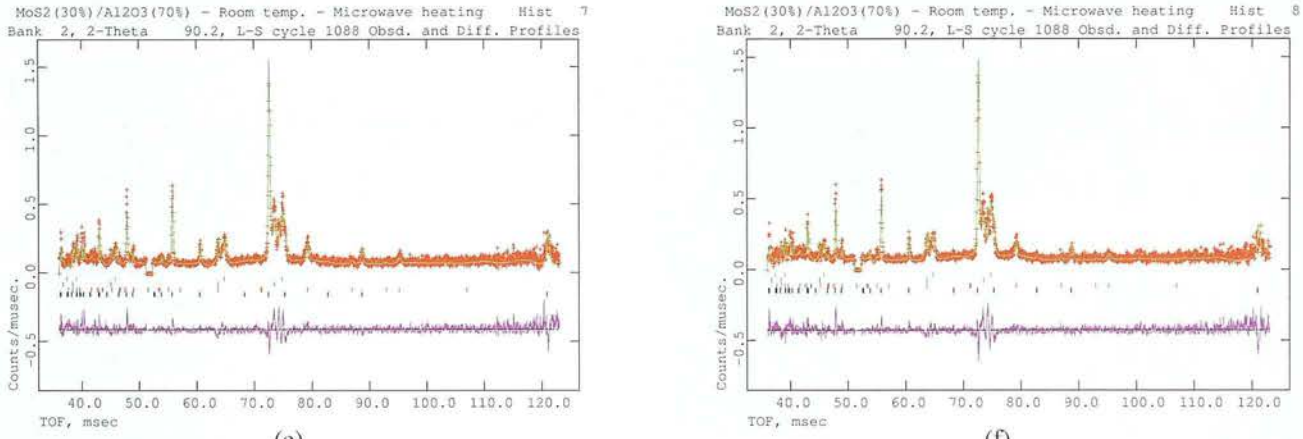

Figure E.12: (Cont). Rietveld refinement graphs for MoS_2 and α-Al_2O_3 particles for neutron diffraction data during microwave radiation at 291 K. (e) Hist. 7, (f) Hist. 8. The small red + represent the observed pattern, the green continuous line represents the calculated pattern and the difference between the calculated and the observed pattern is shown in the bottom graph (in magenta). The tick marks show the reflections included in the refinement - top ticks (green and blue) for brass contributions from the waveguide and the top ticks (red and black) for the MoS_2 and α-Al_2O_3 phase respectively.

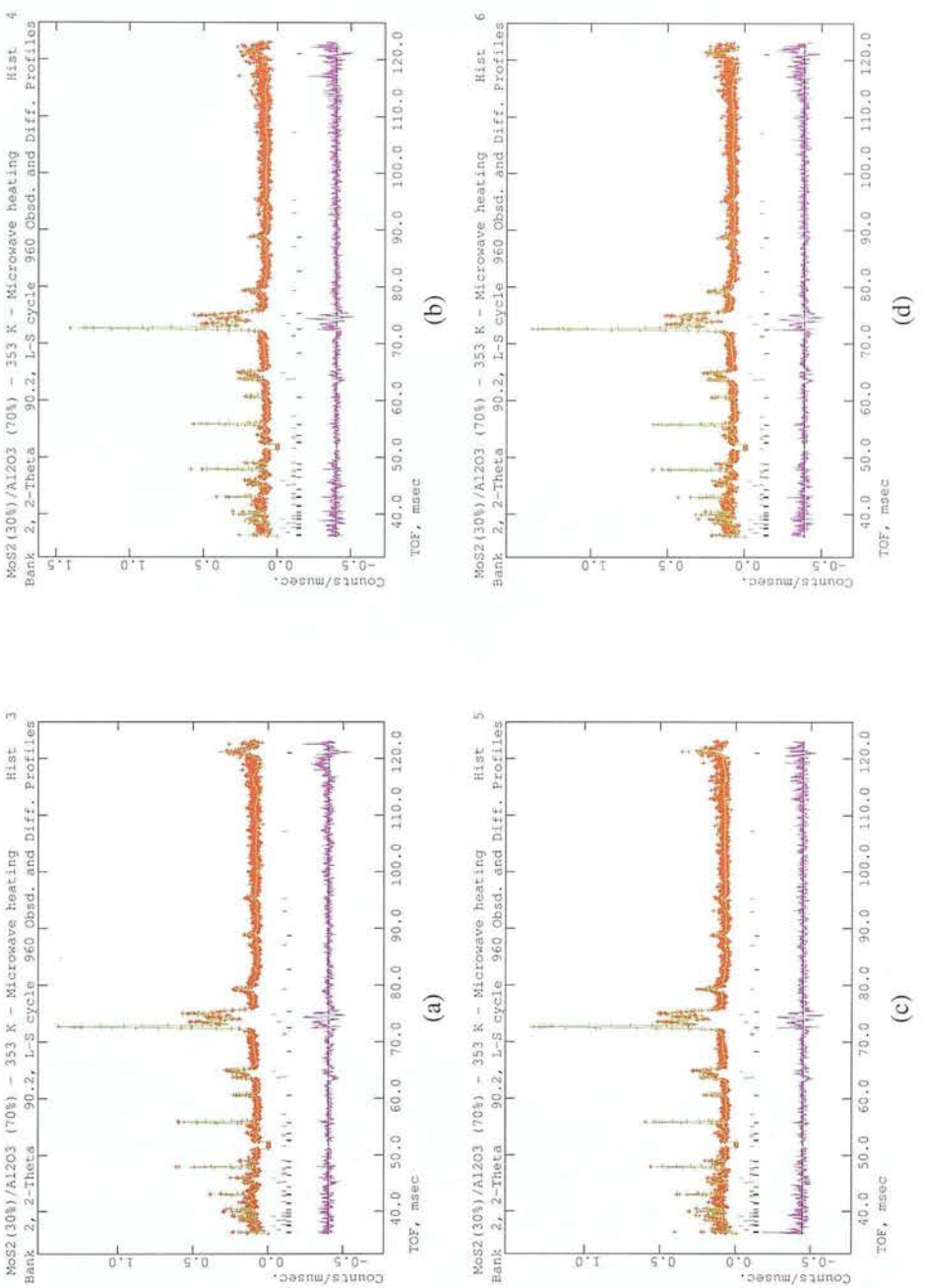

Figure E.13: Rietveld refinement graphs for MoS_2 and α-Al_2O_3 particles for neutron diffraction data during microwave radiation at 353 K. (a) Hist. 3, (b) Hist. 4, (c) Hist. 5, and (d) Hist. 6. The small red + represent the observed pattern, the green continuous line represents the calculated pattern and the difference between the calculated and the observed pattern is shown in the bottom graph (in magenta). The tick marks show the reflections included in the refinement - top ticks (green and blue) for brass contributions from the waveguide and the top ticks (red and black) for the MoS_2 and α-Al_2O_3 phase respectively.

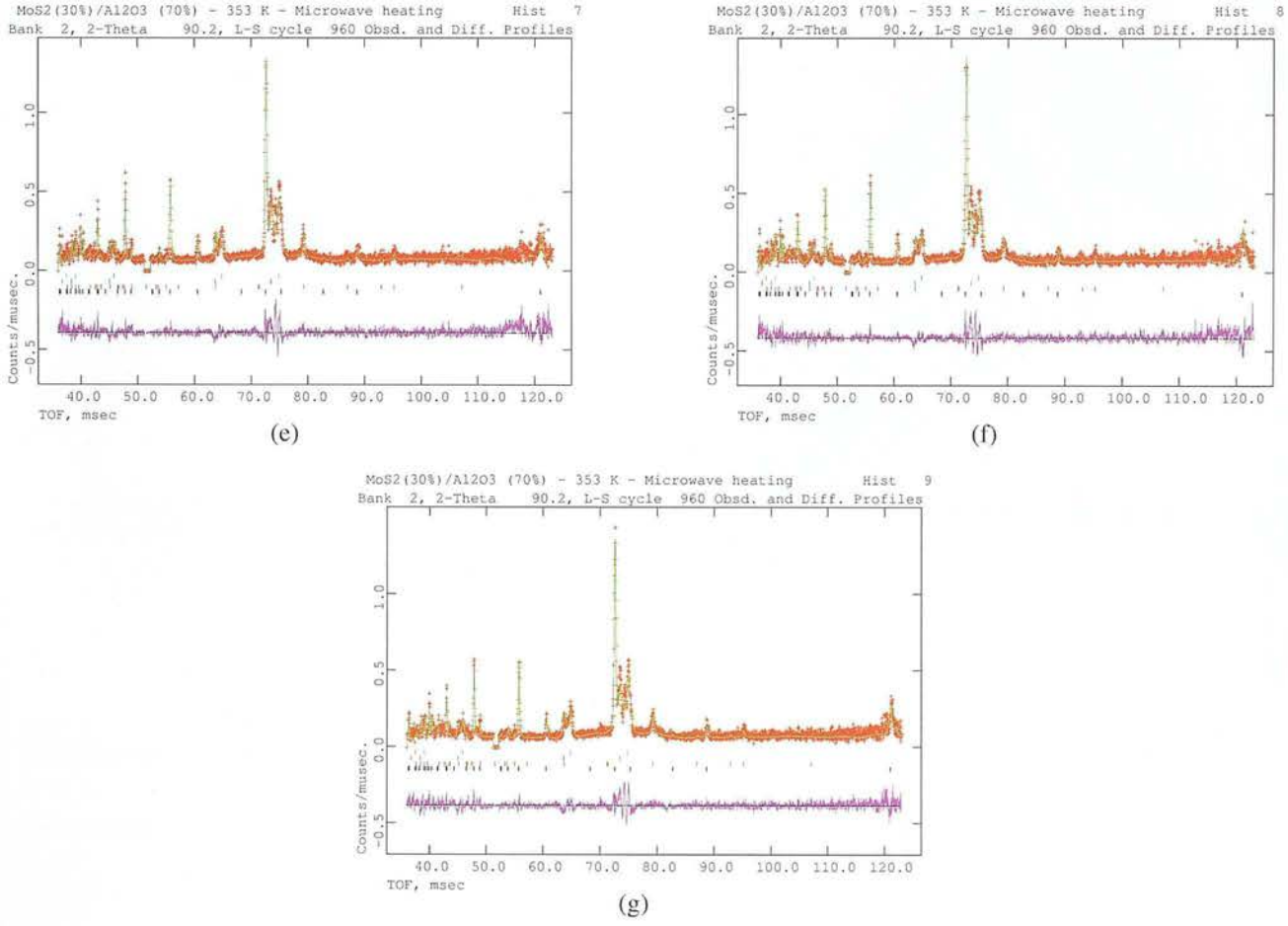

Figure E.13: (Cont). Rietveld refinement graphs for MoS_2 and α-Al_2O_3 particles for neutron diffraction data during microwave radiation at 353 K. (e) Hist. 7, (f) Hist. 8, and (g) Hist. 9. The small red + represent the observed pattern, the green continuous line represents the calculated pattern and the difference between the calculated and the observed pattern is shown in the bottom graph (in magenta). The tick marks show the reflections included in the refinement - top ticks (green and blue) for brass contributions from the waveguide and the top ticks (red and black) for the MoS_2 and α-Al_2O_3 phase respectively.

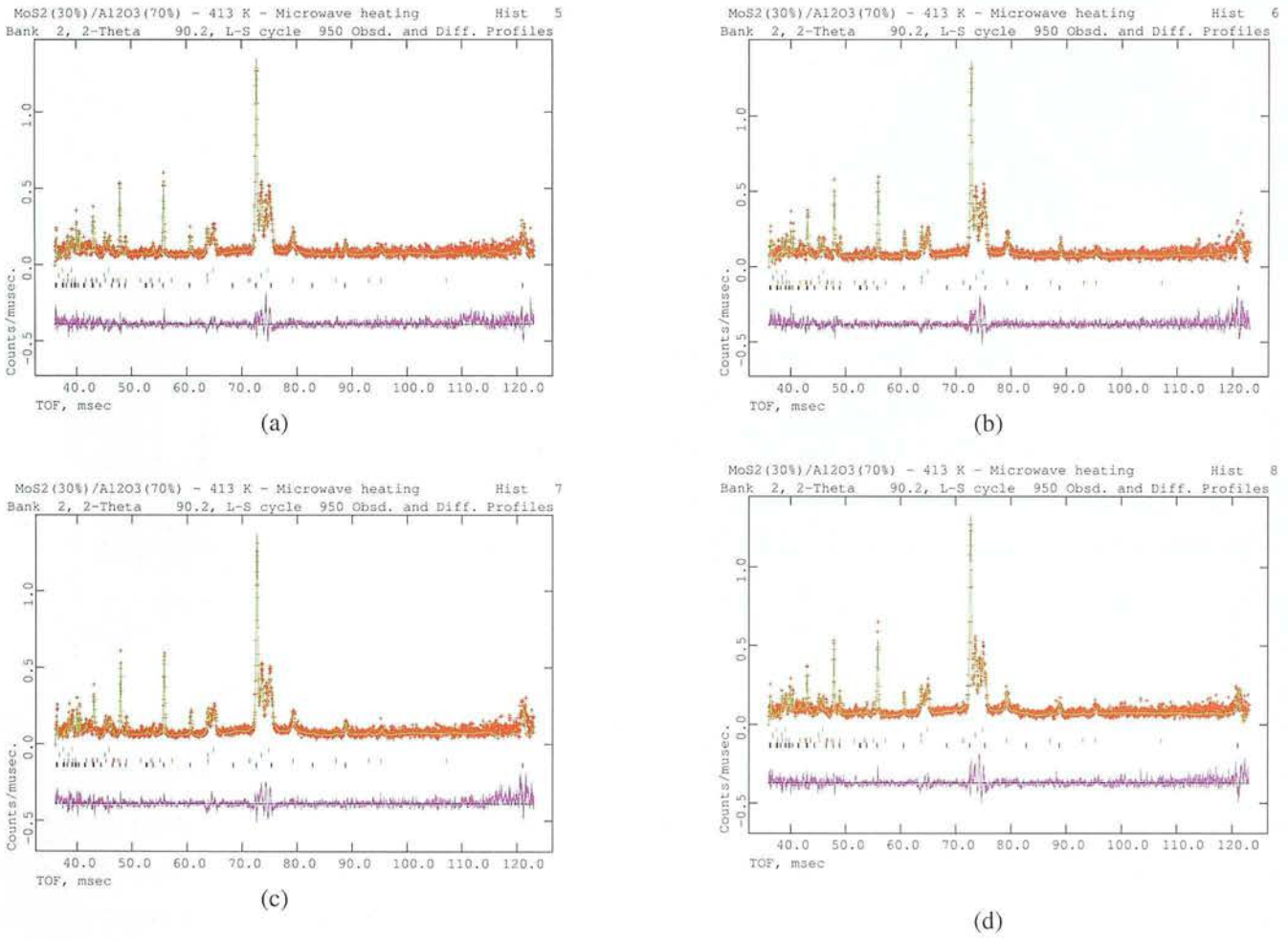

Figure E.14: Rietveld refinement graphs for MoS_2 and α-Al_2O_3 particles for neutron diffraction data during microwave radiation at 413 K. (a) Hist. 5, (b) Hist. 6, (c) Hist. 7, and (d) Hist. 8. The small red + represent the observed pattern, the green continuous line represents the calculated pattern and the difference between the calculated and the observed pattern is shown in the bottom graph (in magenta). The tick marks show the reflections included in the refinement - top ticks (green and blue) for brass contributions from the waveguide and the top ticks (red and black) for the MoS_2 and α-Al_2O_3 phase respectively.

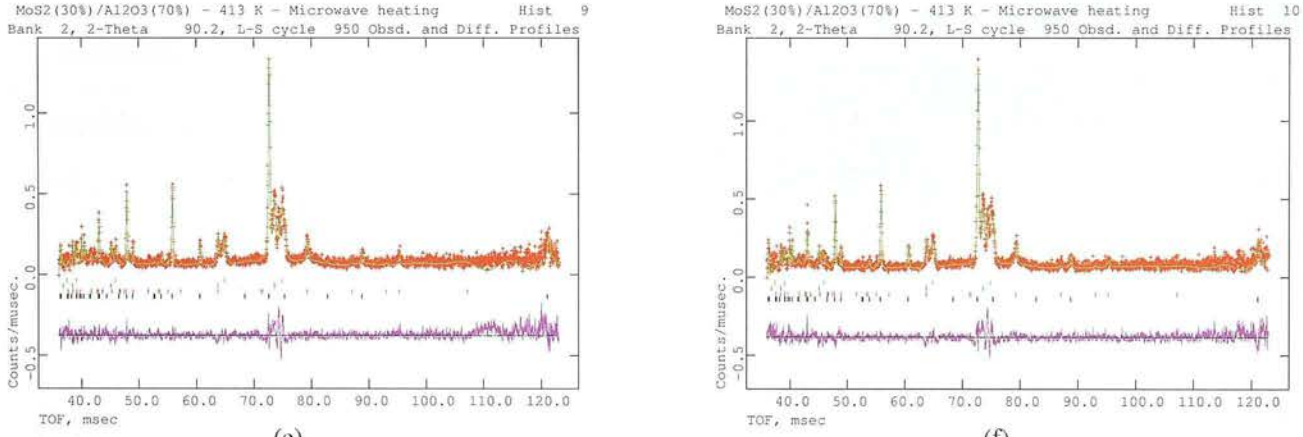

Figure E.14: (Cont). Rietveld refinement graphs for MoS_2 and α-Al_2O_3 particles for neutron diffraction data during microwave radiation at 413 K. (e) Hist. 9, and (f) Hist. 10. The small red + represent the observed pattern, the green continuous line represents the calculated pattern and the difference between the calculated and the observed pattern is shown in the bottom graph (in magenta). The tick marks show the reflections included in the refinement - top ticks (green and blue) for brass contributions from the waveguide and the top ticks (red and black) for the MoS_2 and α-Al_2O_3 phase respectively.

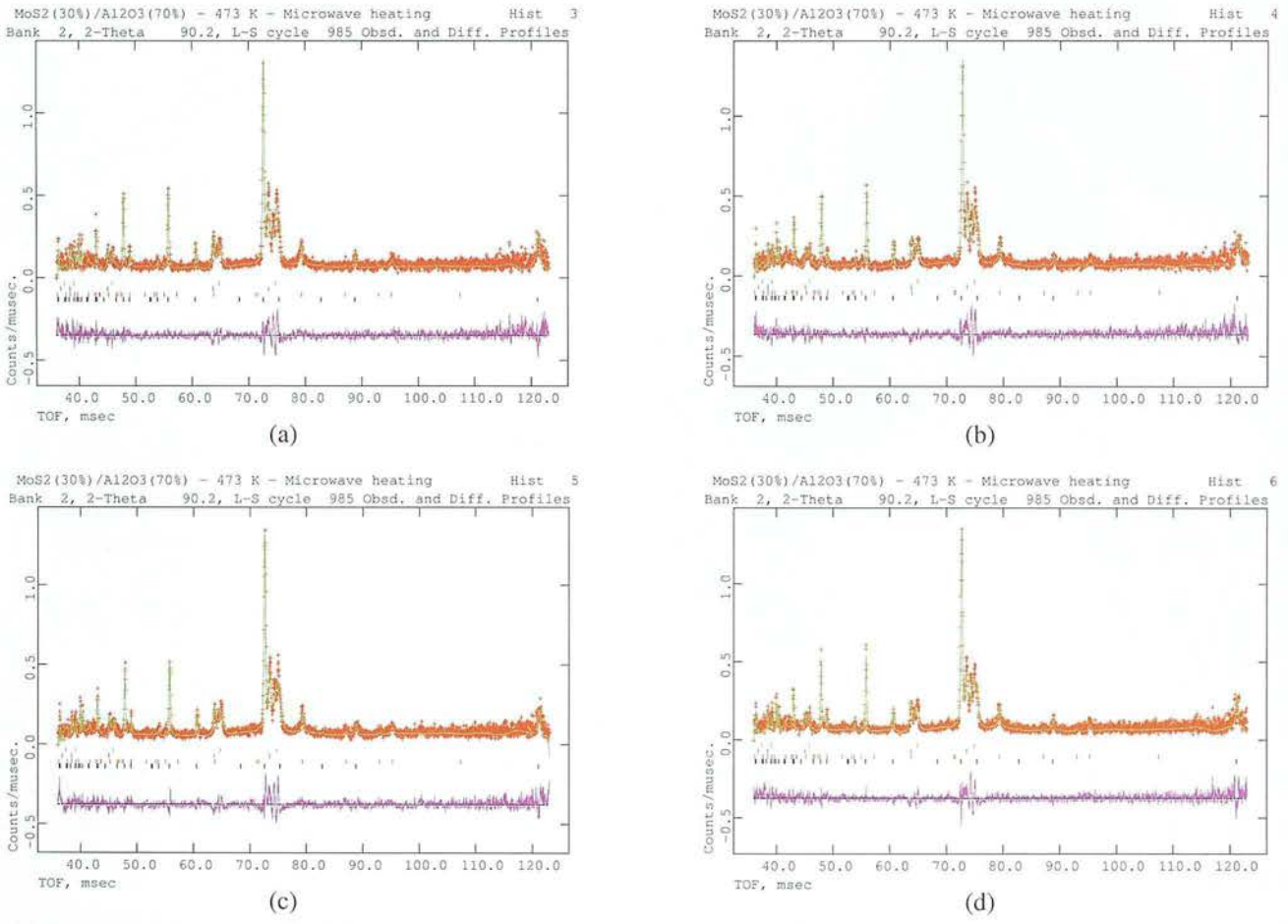

Figure E.15: Rietveld refinement graphs for MoS_2 and α-Al_2O_3 particles for neutron diffraction data during microwave radiation at 473 K. (a) Hist. 3, (b) Hist. 4, (c) Hist. 5, and (d) Hist. 6. The small red + represent the observed pattern, the green continuous line represents the calculated pattern and the difference between the calculated and the observed pattern is shown in the bottom graph (in magenta). The tick marks show the reflections included in the refinement - top ticks (green and blue) for brass contributions from the waveguide and the top ticks (red and black) for the MoS_2 and α-Al_2O_3 phase respectively.

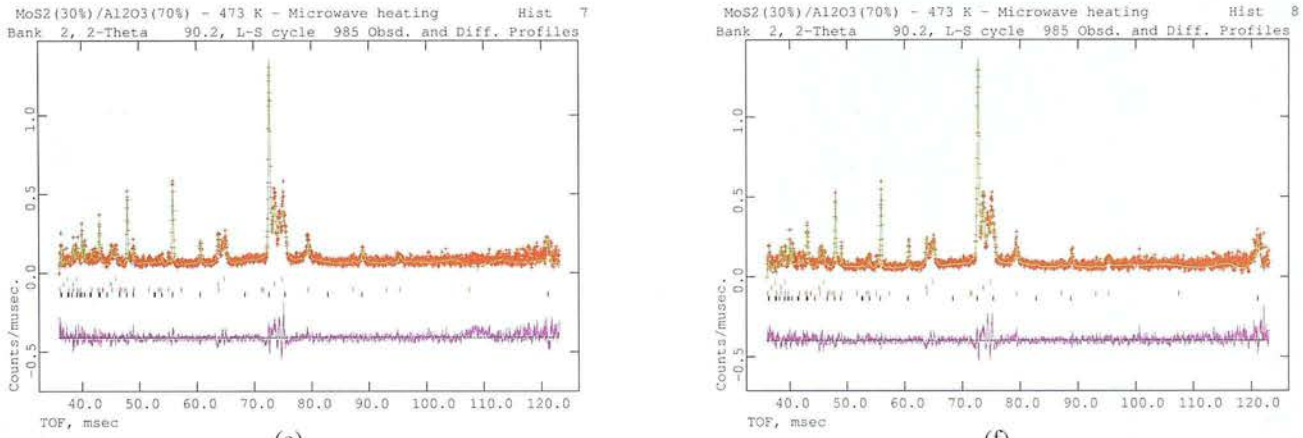

Figure E.15: (Cont). Rietveld refinement graphs for MoS_2 and α-Al_2O_3 particles for neutron diffraction data during microwave radiation at 473 K. (e) Hist. 7, and (f) Hist. 8. The small red + represent the observed pattern, the green continuous line represents the calculated pattern and the difference between the calculated and the observed pattern is shown in the bottom graph (in magenta). The tick marks show the reflections included in the refinement - top ticks (green and blue) for brass contributions from the waveguide and the top ticks (red and black) for the MoS_2 and α-Al_2O_3 phase respectively.

Appendix F

Rietveld refinement results for AgI

F.1 Rietveld refinement results for X-ray diffraction data

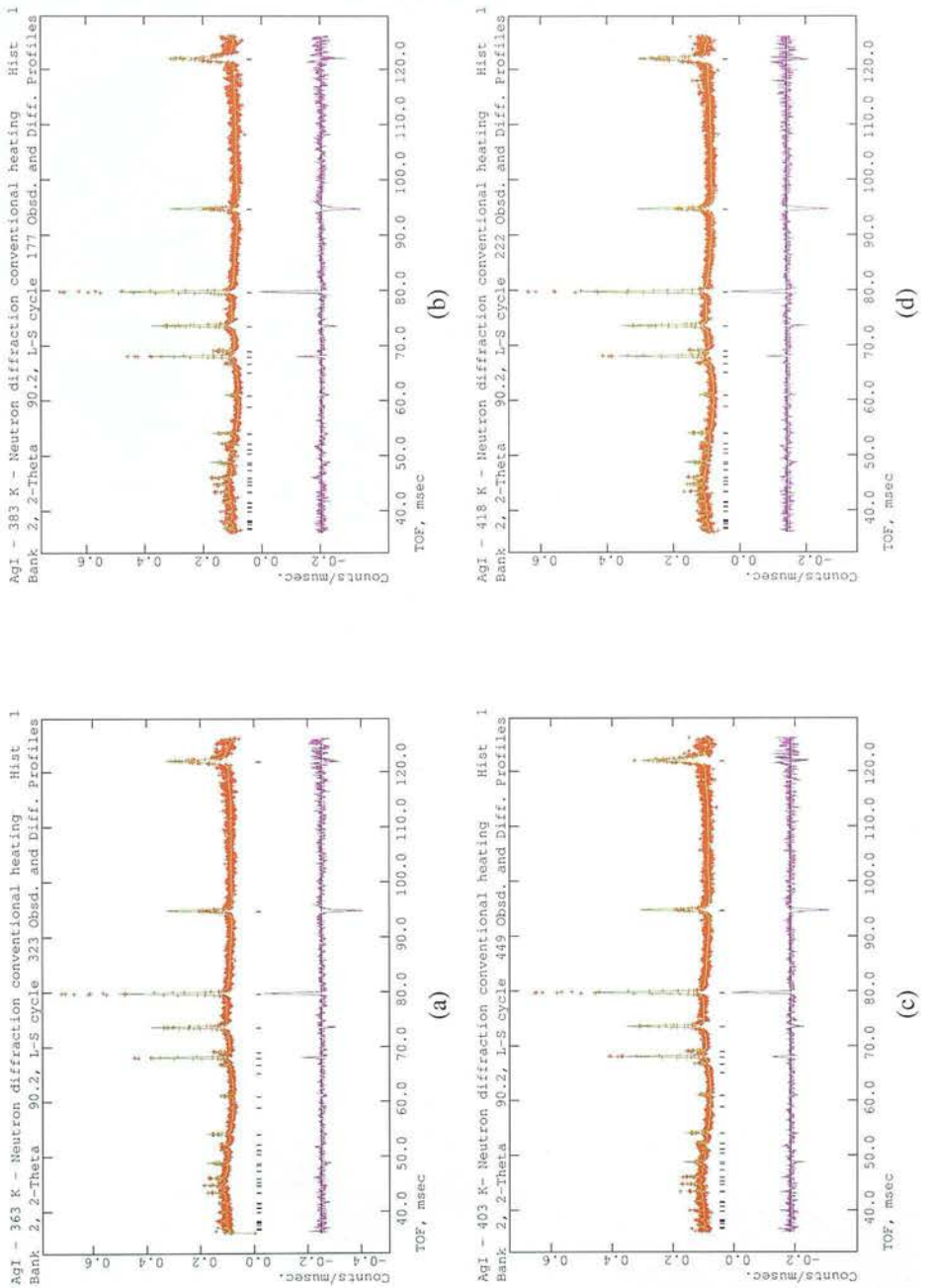

Figure F.1: Rietveld refinement graphs for AgI on neutron diffraction data during conventional heating. (a) 363 K, (b) 383 K, (c) 403 K and, (d) 418 K. The small red + represent the observed pattern, the green continuous line represents the calculated pattern and the difference between the calculated and the observed pattern is shown in the bottom graph (in magenta). The tick marks show the reflections for the hexagonal phase.

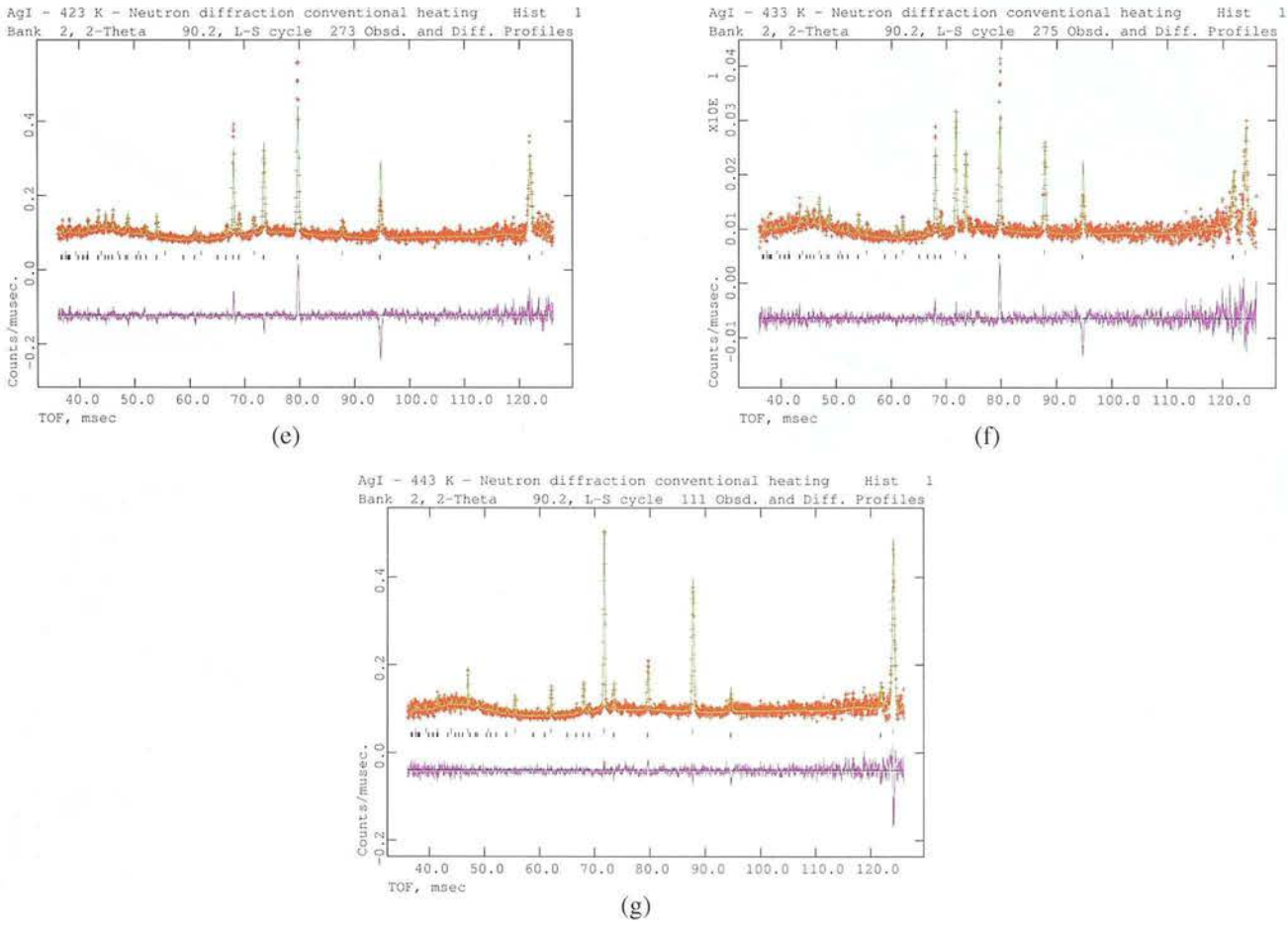

Figure F.1: (Cont). Rietveld refinement graphs for AgI on neutron diffraction data during conventional heating. (e) 423 K, (f) 433 K and, (g) 443 K. The small red + represent the observed pattern, the green continuous line represents the calculated pattern and the difference between the calculated and the observed pattern is shown in the bottom graph (in magenta). The tick marks show the reflections for the cubic and hexagonal phases respectively.

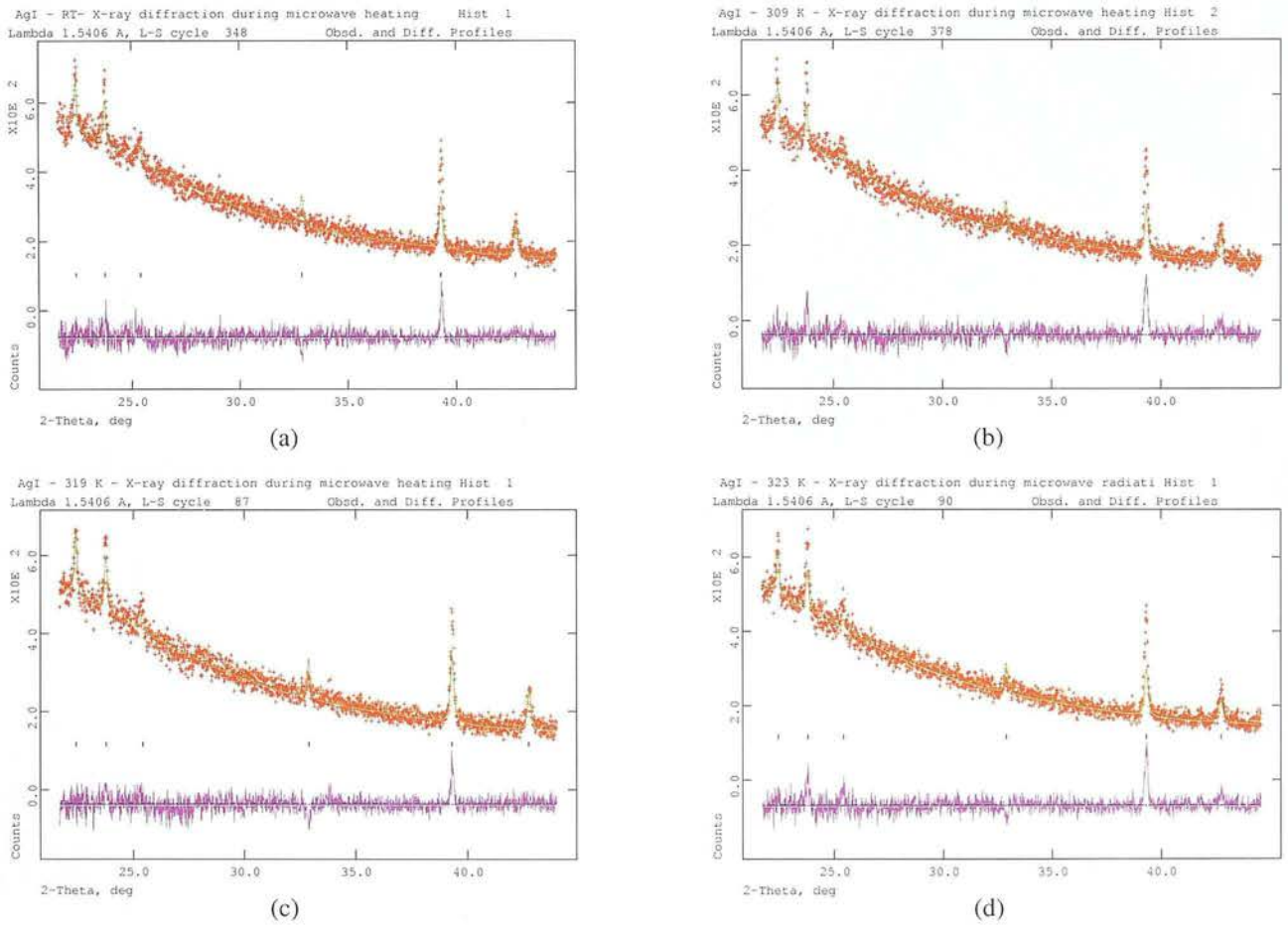

Figure F.2: Rietveld refinement graphs for AgI on X-ray diffraction data during microwave heating. First heating stage. (a) 297, (b) 309 K, (c) 319 K and, (d) 323 K. The small red + represent the observed pattern, the green continuous line represents the calculated pattern and the difference between the calculated and the observed pattern is shown in the bottom graph (in magenta). The tick marks show the reflections for the hexagonal phase.

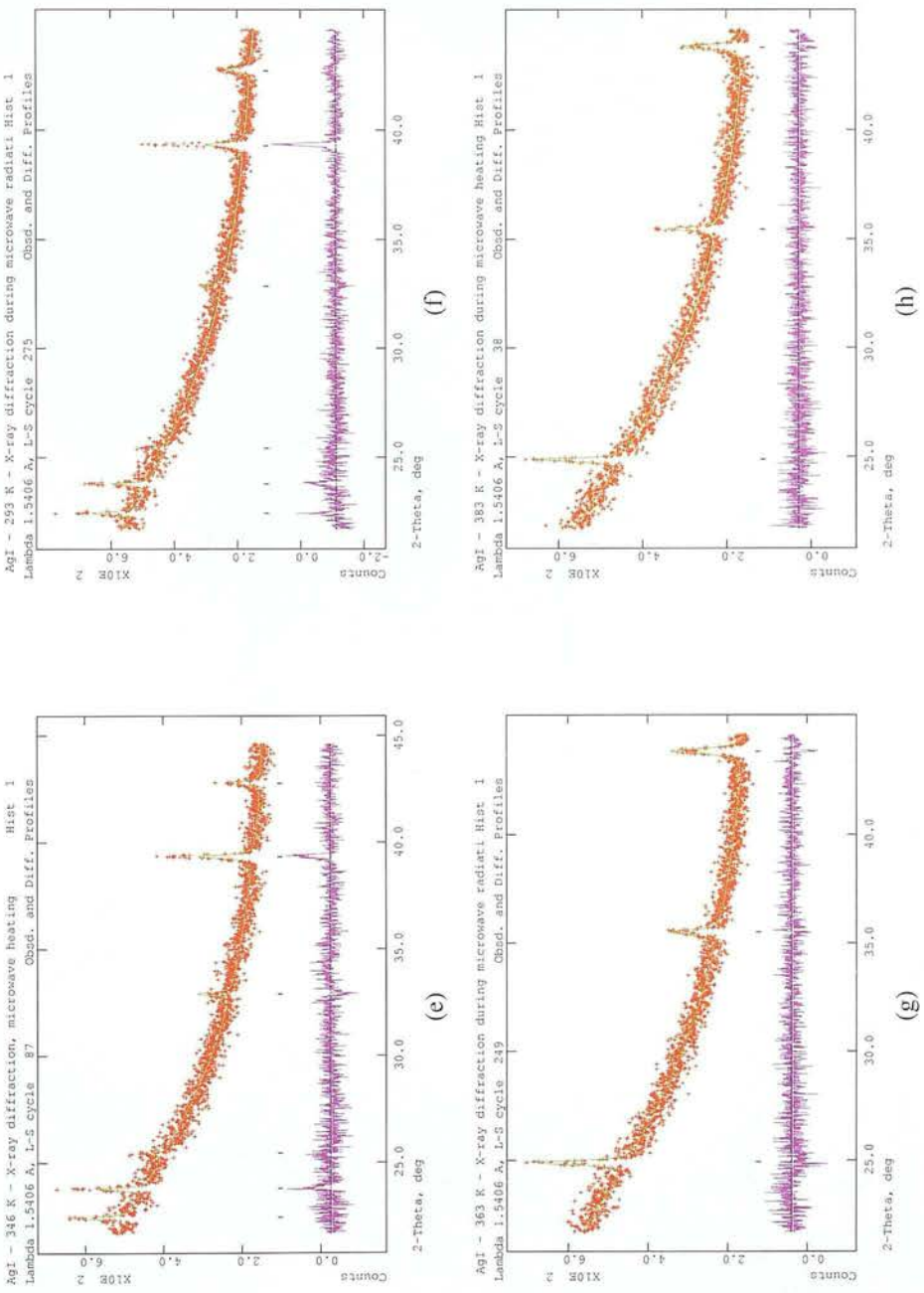

Figure F.2: (Cont). Rietveld refinement graphs for AgI on X-ray diffraction data during microwave heating. First heating stage: (e) 346 K, and second heating stage: (f) 293 K, (g) 363 K and, (h) 383 K. The small red + represent the observed pattern, the green continuous line represents the calculated pattern and the difference between the calculated and the observed pattern is shown in the bottom graph (in magenta). The tick marks show the reflections for the hexagonal and cubic phases respectively.

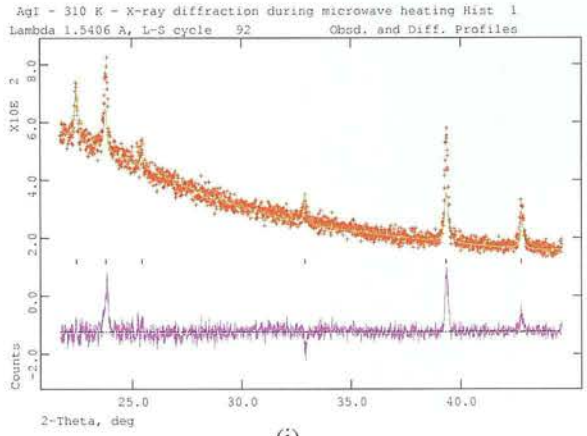

(i)

Figure F.2: (Cont). Rietveld refinement graphs for AgI on X-ray diffraction data during microwave heating. Second heating stage. (i) 310 K. The small red + represent the observed pattern, the green continuous line represents the calculated pattern and the difference between the calculated and the observed pattern is shown in the bottom graph (in magenta). The tick marks show the reflections for the cubic phase.

F.2 Gaussian fitting of α- and β-AgI reflections of X-ray and neutron diffraction data

The best fit was obtained for a Gaussian curve which is described as a bell-shape curve like the normal probability distribution function (section 7.3.5, Chapter 7).

$$y = y_0 + \frac{A}{w\sqrt{\pi/2}} \exp \frac{-2(x - x_0)^2}{w^2} \tag{F.1}$$

where

y_0 is the baseline offset,

A is the total area under the curve from the baseline,

x_0 is the centre of the peak,

w is 2σ, approximately 0.849 the width of the peak at half height.

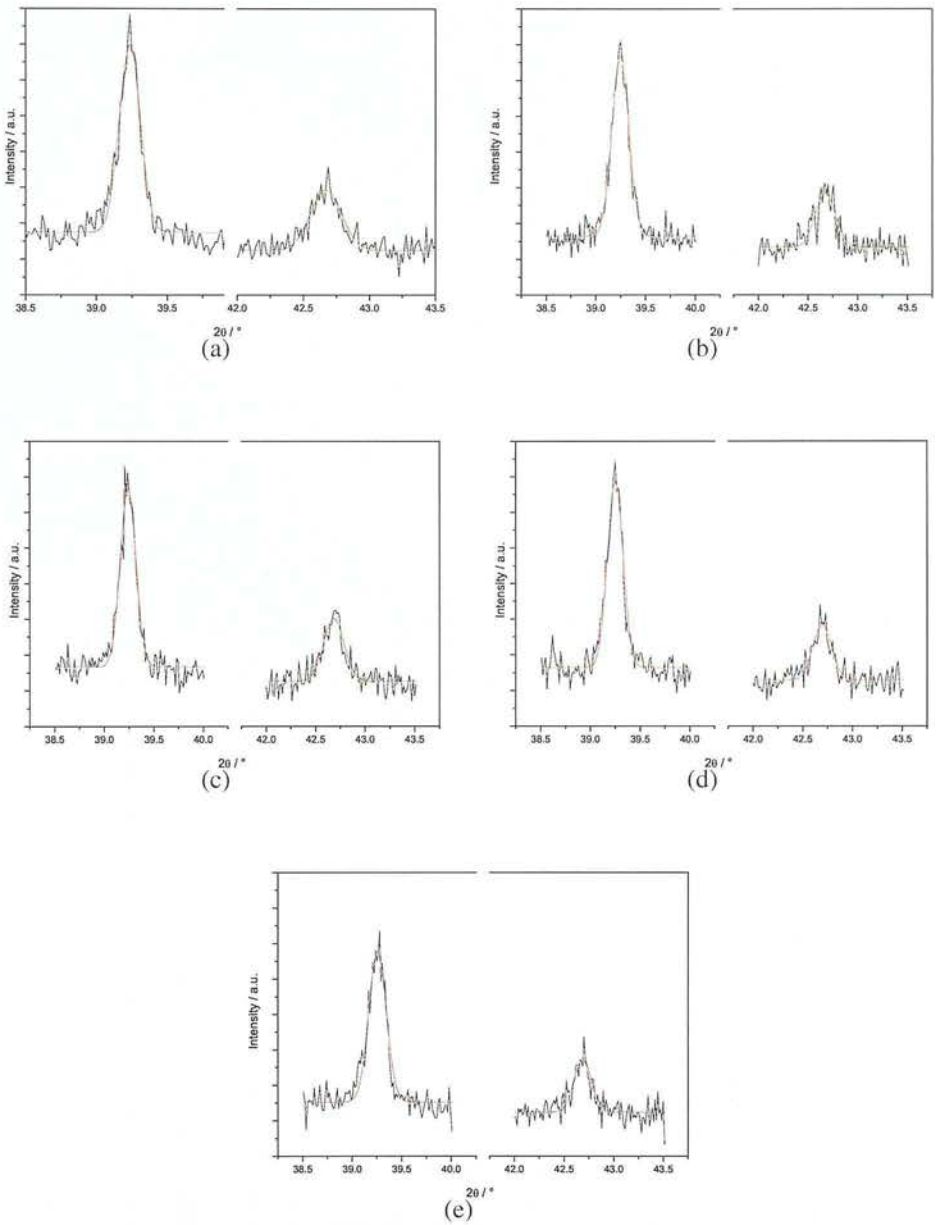

Figure F.3: Gaussian fit graphs for β-AgI on the (110) and (103) reflections -left and right hand side on each graph respectively- for X-ray diffraction data during microwave heating. 1st heating stage. (a) 297 K, (b) 309 K, (c) 319 K, (d) 323 K and, (e) 346 K. All graphs shown are at the same scale. Red continuous line represents the best Gaussian fit obtained.

Table F.1: Gaussian fit parameters obtained for X-ray diffraction data of (110) and (103) β-AgI reflections on heating up with microwave radiation. 1st heating stage.

	β-AgI: (110) reflection						
Temperature / K	y_0	x_0	w	A	χ^2	R^2	Height
297	185.8915(1.38644)	39.23367(193)	0.14798(400)	49.03032(1.23217)	225.64201	0.9476	264.36
309	180.77848(1.48481)	39.24286(186)	0.17025(398)	54.3313(1.22856)	169.93616	0.96934	254.62
319	182.13047(1.70075)	39.23977(211)	0.15653(447)	43.31642(1.34935)	230.63162	0.95515	251.38
323	181.07233(1.76775)	39.24558(209)	0.15642(444)	51.5631(1.40199)	249.22963	0.95568	263.02
346	175.88071(1.79862)	39.25150(273)	0.17623(584)	46.95793(1.51411)	245.62008	0.93993	212.61
	β-AgI: (103) reflection						
297	161.09438(1.31827)	42.66714(667)	0.23495(1429)	25.05424(1.48128)	176.51386	0.77519	85.084
309	165.58635(1.72863)	42.66999(761)	0.20386(1655)	19.53758(1.57222)	213.89936	0.71927	76.468
319	161.5872(1.62150)	42.67925(616)	0.20710(1343)	23.07003(1.48644)	186.56174	0.80048	88.883
323	163.48115(1.5087)	42.69006(636)	0.18777(1371)	18.4194(1.31693)	170.01469	0.76115	78.268
346	161.57191(1.56201)	42.68137(690)	0.17716(1479)	16.32837(1.3244)	187.245	0.70997	73.537

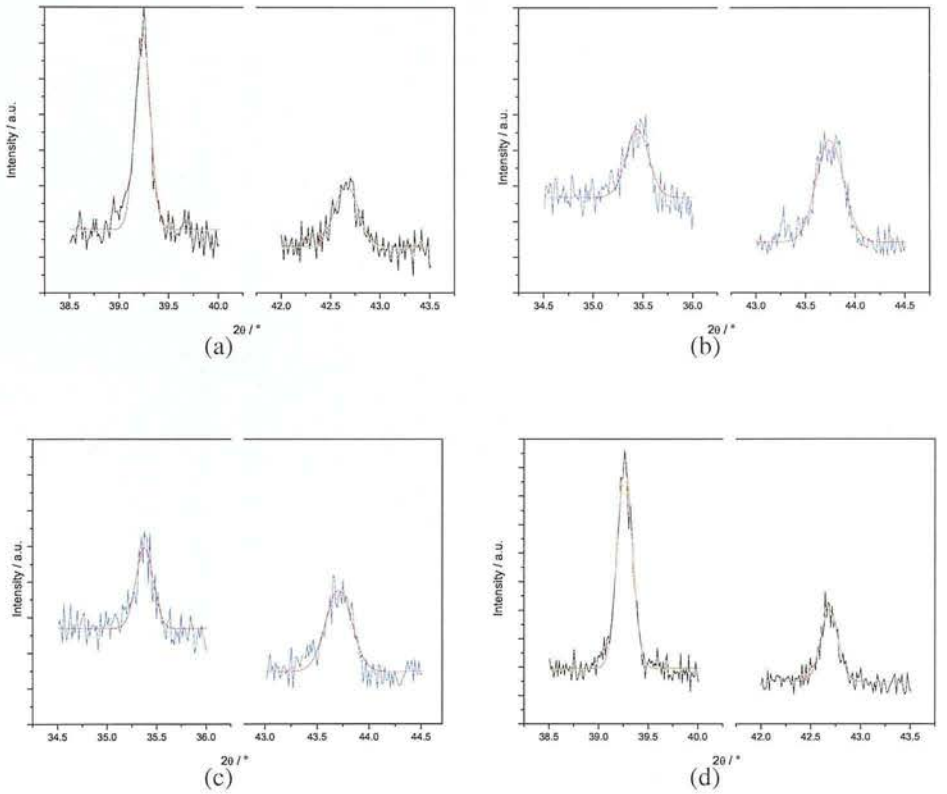

Figure F.4: Gaussian fit graphs on the (110) and (103) reflections for β-AgI and, the (200) and (211) reflections of α-AgI -left and right hand side on each graph respectively- for X-ray diffraction data on heating up with microwave radiation. 2nd heating stage. (a) 293 K, (b) 363 K, (c) 380 K and, (d) 310 K. All graphs shown are at the same scale. Red continuous line represents the best Gaussian fit obtained for each peak while β and α phases are represented by the black and blue continuous lines respectively.

Table F.2: Gaussian fit parameters obtained for X-ray diffraction data of β- and α-AgI on heating up with microwave radiation. Second heating stage. Diffraction peaks at 293 and 310 K are those of low temperature β-AgI for the sample before heating and after heating respectively. † and ‡ shows the reflections for β- and α-AgI respectively.

	β-AgI†: (110) and α-AgI‡:(200)						
Temperature / K	y_0	x_0	w	A	χ^2	R^2	Height
293†	187.91515(1.99692)	39.23791(225)	0.1531(477)	52.57084(1.56688)	320.59533	0.94705	273.97
363‡	233.77426(2.20007)	35.4384(782)	0.22546(1727)	27.08519(2.09486)	321.419	0.74248	95.850
380‡	234.02344(2.05549)	35.3739(581)	0.17573(1246)	25.07205(1.72791)	321.19278	0.77392	113.84
310†	197.66817(1.86641)	39.25994(165)	0.15565(350)	68.55065(1.47659)	278.34366	0.97169	351.4
	β-AgI†: (103) and α-AgI‡:(211)						
293†	164.43385(1.8287)	42.65644(746)	0.24182(1664)	25.77908(1.81149)	214.83358	0.77914	85.058
363‡	170.68273(2.04277)	43.74081(498)	0.27596(1141)	49.41612(2.15191)	236.3554	0.90746	142.88
380‡	173.40416(1.96893)	43.70268(597)	0.25392(1346)	36.33497(1.98956)	236.10196	0.8569	114.88
310†	174.09097(1.55305)	42.68305(399)	0.17532(854)	27.7049(1.30994)	185.96238	0.8779	126.08

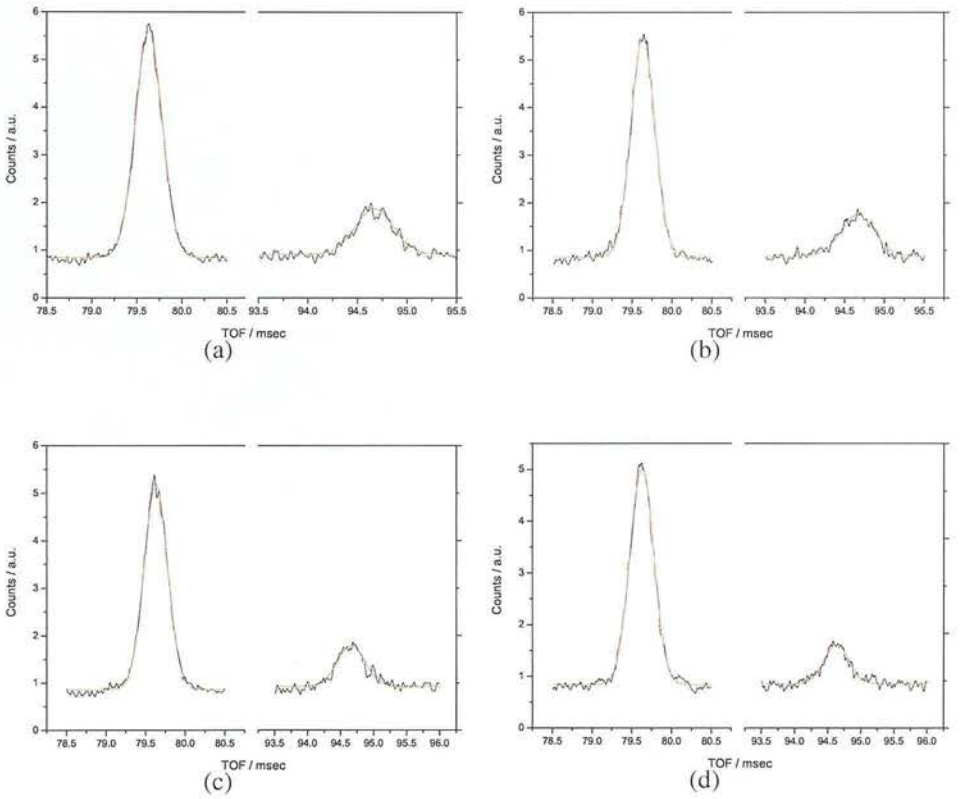

Figure F.5: Gaussian fit graphs for (110) and (102) β-AgI reflections (left and right hand side on each graph respectively) for neutron diffraction during conventional heating. (a) 363, (b) 383 K, (c) 403 K and, (d) 418 K. Red continuous line represents the best Gaussian fit obtained for the β phase which is represented by the black continuous line. All graphs are at the same scale.

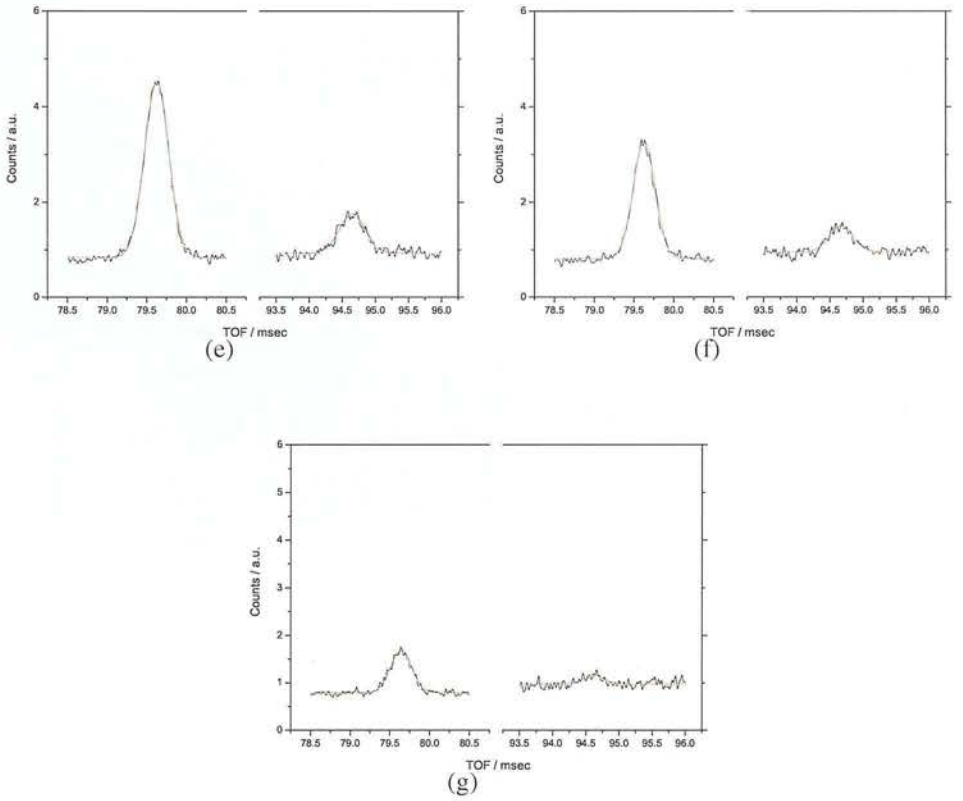

Figure F.5: (Cont). Gaussian fit graphs for (110) and (102) β-AgI reflections (left and right hand side on each graph respectively) for neutron diffraction during conventional heating. (e) 423 K, (f) 433 K, and (g) 443 K. All graphs are at the same scale. Red continuous line represents the best Gaussian fit obtained for the β phase which is represented by the black continuous line. All graphs are at the same scale.

Table F.3: Gaussian fit parameters obtained for neutron diffraction data of (110) and (102) β-AgI reflections on heating up with conventional heating.

	β-AgI (110) reflection						
Temperature / K	y_0	x_0	w	A	χ^2	R^2	Height
363	0.83628(562)	79.62868(53)	0.29636(117)	1.77255(706)	0.00483	0.99784	4.7722
383	0.84718(615)	79.62916(60)	0.29910(132)	1.73833(776)	0.00575	0.99730	4.6371
403	0.84292(589)	79.62479(62)	0.29840(136)	1.61688(744)	0.00529	0.99714	4.3233
418	0.83073(575)	79.62031(62)	0.29779(136)	1.56751(724)	0.00504	0.99711	4.1999
423	0.82293(440)	79.6213(54)	0.30324(119)	1.40571(559)	0.00291	0.99787	3.6987
433	0.80083(443)	79.62097(80)	0.27464(176)	0.84251(536)	0.00315	0.99441	2.4477
443	0.78079(323)	79.63532(161)	0.26711(351)	0.29602(385)	0.00170	0.97688	0.88426
	β-AgI (102) reflection						
363	0.90317(610)	94.66555(361)	0.38315(800)	0.45956(974)	0.00583	0.94045	0.95700
383	0.86446(751)	94.65564(396)	0.42942(949)	0.46787(1137)	0.00516	0.94613	0.86933
403	0.90866(637)	94.65457(419)	0.42112(946)	0.45872(1065)	0.00591	0.93147	0.86912
418	0.93020(570)	94.62588(386)	0.37090(852)	0.38608(895)	0.00520	0.92889	0.83055
423	0.91414(572)	94.64334(393)	0.39187(874)	0.40589(923)	0.00503	0.93255	0.82643
433	0.94004(862)	94.66174(524)	0.35683(115)	0.24647(796)	0.00489	0.93993	0.55111
443	0.96512(509)	94.60147(1373)	0.28784(294)	0.07089(703)	0.00474	0.40227	0.19651

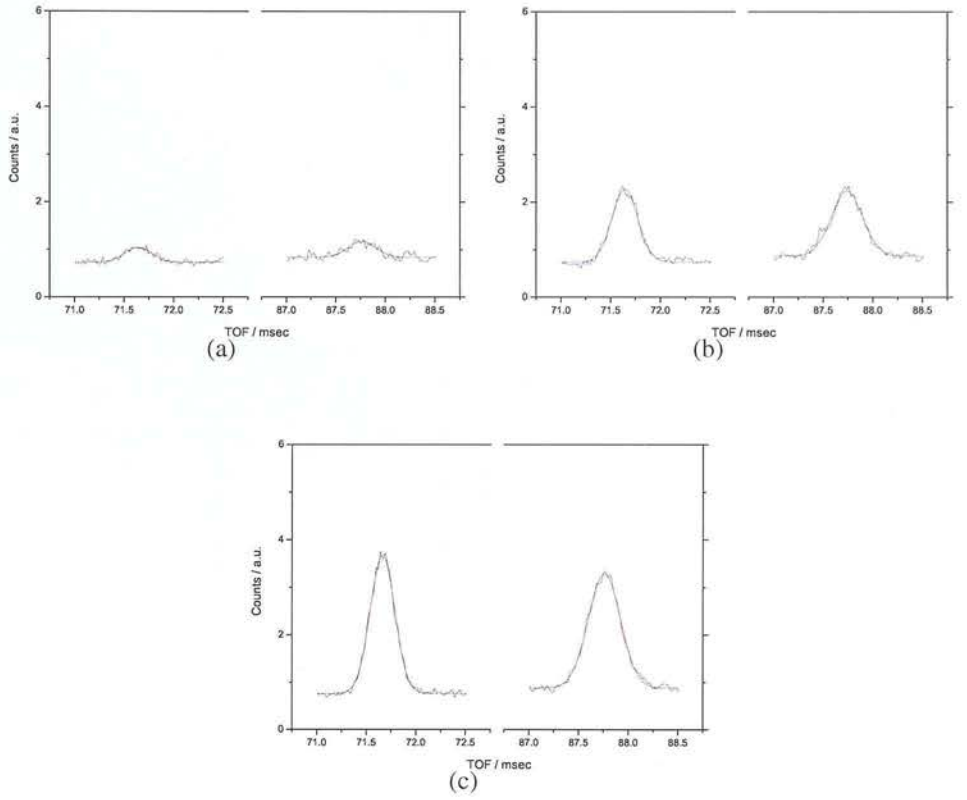

Figure F.6: Gaussian fit graphs for (211) and (200) α-AgI reflections measured by neutron diffraction during conventional heating. (e) 423 K, (f) 433 K, and (g) 443 K. All graphs are at the same scale. Red continuous line represents the best Gaussian fit obtained for the α phase which is represented by the blue continuous line. All graphs are at the same scale.

Table F.4: Gaussian fit parameters obtained for neutron diffraction data of (211) and (200) α-AgI reflections on heating up with conventional heating.

	α-AgI (211) reflection						
Temperature / K	y_0	x_0	w	A	χ^2	R^2	Height
423	0.72054(353)	71.64412(395)	0.26899(902)	0.10413(366)	0.00137	0.88487	0.30889
433	0.73213(523)	71.63774(117)	0.25880(266)	0.49873(532)	0.00311	0.98796	1.5376
443	0.75344(507)	71.65884(60)	0.24612(134)	0.90039(503)	0.00305	0.99660	2.9190
	α-AgI (200) reflection						
423	0.82435(624)	87.75883(645	0.27852(1482)	0.11749(660)	0.00342	0.7889	0.3365
433	0.85549(788)	87.73419(198	0.31790(474)	0.54587(890)	0.0047	0.97954	1.3701
443	0.87647(678)	87.75343(97)	0.32308(233)	0.97324(772)	0.00341	0.99513	2.4035

Bibliography

1. http://www.mic-d.com/curriculum/lightandcolor/images/electromagneticfigure1.jpg. [Online; accessed February-2006].

2. Pozar, D. *Microwave Engineering*. John Wiley & Sons, Inc., 2nd edition, (1998).

3. Elander, N., Jones, J. R., Lu, S.-Y., and Stone-Elander, S. *Chemical Society Reviews* **29**(4), 239–249 (2000).

4. Maxwell, J. C. *Treatise on Electricity and Magnetism*. Courier Dover Publications, (1954).

5. http://micro.magnet.fsu.edu/primer/java/electromagnetic/. [Online; accessed February-2006].

6. Metaxas, A. C. and Meredith, R. J. *Industrial Microwave Heating*. IEE, (1983).

7. Meredith, R. J. *Engineer's Book of Industrial Microwave Heating*. IEE, (1998).

8. Gabriel, C., Gabriel, S., Grant, E. D., Halstead, B. S. J., and Mingos, D. M. P. *Chemical Society Reviews* **27**(3), 213–223 (1998).

9. Mingos, D. and Baghurst, D. *Chemical Society Reviews* **20**(1), 1–47 (1991).

10. Mingos, D. and Whittaker, A. G. In *Chemistry Under Extreme Conditions or Non-clasical Conditions,* van Eldik, R. and Hubbard, G., editors, 479–515. Wiley (1997).

11. Berlan, J. *Radiation Physics and Chemistry* **45**(4), 581–589 (1995).

12. Lidström, P., Tierney, J., Wathey, B., and Westman, J. *Tetrahedron* **57**, 9225–9283 (2001).

13. Caddick, S. *Tetrahedron* **51**(38), 10403–10432 (1995).

14. Rao, K. J., Vaidhyanathan, B., Ganguli, M., and Ramakrishnan, P. A. *Chemistry of Materials* **11**(4), 882–895 (1999).

15. Whittaker, A. G. and Mingos, D. *Journal of the Chemical Society. Dalton Transactions* , 2751–2752 (1992).

16. Whittaker, A. G. and Mingos, D. *Journal of the Chemical Society. Dalton Transactions* (16), 2541–2543 (1993).

17. Mingos, D. and Whittaker, A. G. *Journal of the Chemical Society. Dalton Transactions* , 2073–2079 (1995).

18. Baghurst, D. and Mingos, D. *Journal of Chemistry Society. Chemical Communications* **12**, 829–830 (1988).

19. Kaatze, U. *Radiation Physics and Chemistry* **45**(4), 539–548 (1995).

20. Szabo, D. V. and Vollath, D. *Advanced Materials* **11**(15), 1313 (1999).

21. Brooks, D. J., Brydson, R., and Douthwaite, R. E. *Advanced Materials* **17**, 2474 (2005).

22. Binner, J. G. P., Prince, D. M., and Vaidhyanathan, B. In *4th World Congress on Microwave and Radio Frequency Applications*, 435–442, (2004).

23. Günter, M. M., Korte, C., Brunauer, G., Boysen, H., Lerch, M., and Suard, E. *Zeitschrift fur Anorganische und Allgemeine Chemie* **631**, 1227–1284 (2005).

24. Rybakov, K. I. and Semenov, V. E. *Physical Reviews B* **49**(1), 64–68 (1994).

25. Bykov, Y. V., Rybakov, K. I., and Semenov, V. E. *Journal of Physics D: Applied Physics* **34**(13), R55 (2001).

26. Booske, J. H., Cooper, R. F., and Dobson, I. *Journal of Materials Research* **7**(2), 495–501 (1992).

27. Rybakov, K. I., Semenov, V. E., Freeman, S. A., Booske, J. H., and Cooper, R. F. *Physical Reviews B* **55**(6), 3559–3567 (1997).

28. Whittaker, A. G. *Chemistry of Materials* **17**(13), 3426–3432 (2005).

29. Stuerga, D. and Gaillard, P. *Tetrahedron* **52**(15), 5505–5510 (1996).

30. Jacob, J., Chia, L., and Boey, F. *Journal of Materials Science* **30**, 5321–5327 (1995).

31. Emsley, J. *New Scientist* **12**, 56–60 (1988).

32. Galema, S. A. *Chemical Society Reviews* **26**(3), 233–238 (1997).

33. Mingos, D. *Chemistry and Industry* , 596–599 (1994).

34. Whittaker, A. G. and Mingos, D. M. P. *Journal of Microwave Power and Electromagentic Energy* **29**(4), 195–219 (1994).

35. Fini, A. and Breccia, A. *Pure and Applied Chemistry* **71**(4), 573–579 (1999).

36. Kubrakova, I. V. *Russian Chemical Reviews* **71**(4), 283–294 (2002).

37. Cresswell, S. L. and Haswell, S. J. *Journal of Chemical Education* **78**(7), 900–904 (2001).

38. van de Roer, T. G. *Microwave Electronic Devices*. Chapman & Hall, Eindhoven, The Netherlands, (1994).

39. http://hyperphysics.phy-astr.gsu.edu/hbase/waves/magnetron.html. [Online; accessed February-2006].

40. Bond, G., Moyes, A. R. B., Pollington, A. S. D., and Whan, A. D. A. *Measurement Science and Technology* **2**(6), 571–572 (1991).

41. http://www.omega.com/techref/iredtempmeasur.html. [Online; accessed February-2006].

42. http://www.omega.com/techref/fiberoptics.html. [Online; accessed February-2006].

43. Pert, E., Carmel, Y., Birnboim, A., Olorunyolemi, T., Gershon, D., Calame, J., Lloyd, I. K., and Wilson, C. *Journal of the American Ceramic Society* **84**(9), 1981–1986 (2001).

44. West, A. R. *Solid State Chemistry and its Applications*. John Wiley & Sons, (1984).

45. Chung, D., De Haven, P., Arnold, H., and Ghosh, D. *X-ray diffraction at elevated temperature. A method for in situ process analysis*. VCH Publisers, (1993).

46. Klug, H. P. and Alexander, L. E. *X-ray Diffraction Procedures for Crystalline and Amorphous Materials*. John Wiley & Sons, 2nd edition, (1974).

47. Trueblood, K. N., Bisirgi, H.-B., Burzlaff, H., Dunitz, J. D., Gramaccioli, C. M., Shultz, H. H., Shmueli, U., and Abrahams, S. C. *Acta Crystallographica A* **52**, 770–781 (1996).

48. Patterson, A. L. *Physical Reviews* **56**(10), 978–982 Nov (1939).

49. Scherrer, P. *Gottinger Nachrichten* , 96–100 (1918).

50. http://www.isis.rl.ac.uk/crystallography/hrpd/. [Online; accessed 17-February-2006].

51. Rietveld, H. *Journal of Applied Crystallography* **2**, 65–71 (1969).

52. Larson, A. C. and Von Dreele, R. B. *General Structure Analysis System (GSAS)*, (1986).

53. Toby, B. H. *Journal of Applied Crystallography* **34**, 210–213 (2001).

54. Norby, P. *Journal of American Chemical Society* **119**(22), 5215–5221 (1997).

55. Norby, P., Christensen, A. N., and Hanson, J. C. *Studies in Surface Science and Catalysis (Zeolites and related microporous materials: State of the art. Studies in surface science and catalysis)* **84**, 179–186 (1994).

56. Norby, P. and Hanson, J. C. *Catalysis Today* **39**(4), 301–309 (1998).

57. Christensen, A. N., Jensen, T. R., Norby, P., and Hanson, J. C. *Chemistry of Materials* **10**(6), 1688–1693 (1998).

58. Munn, J., Barces, P., Hauserman, D., Axon, S. A., and Klinowski, J. *Phase Transitions* **39**, 129–134 (1992).

59. Evans, J. S. O., Francis, R., O'Hare, D., Price, S. J., Clark, S. M., Flaherty, J., Gordon, J., Nield, A., and Tang, C. C. *Review of Scientific Instruments* **66**(3), 2442–2445 (1995).

60. Davies, A. T., Sankar, G., Catlow, C. R. A., and Clark, S. M. *Journal of Physical Chemistry B* **101**(48), 10115–10120 (1997).

61. Muncaster, G., Davies, A. T., Sankar, G., Catlow, C. R. A., Thomas, J. M., Colston, S. L., Barnes, P., Walton, R. I., and O'Hare, D. *Physical Chemistry Chemical Physics* **2**(15), 3523–3527 (2000).

62. Walton, R. I., Norquist, A. J., O'Hare, D., Neeraj, S., Natarajan, S., and Rao, C. N. R. *Chemical Communications* (19), 1990–1991 (2001).

63. Walton, R. I. and O'Hare, D. *Chemical Communications* (23), 2283–2291 (2000).

64. Parise, J. B., Cahill, C. L., and Lee, Y. J. *Canadian Mineralogist* **38**, 777–800 (2000).

65. Evans, J. S. O. and Evans, I. R. *Chemical Society Reviews* **33**(8), 539 – 547 (2004).

66. Robb, G., Djandazov, R., Whittaker, G., and Harrison, A. *Proceedings of the International Conference in Microwave Chemistry* , 295–298 (2000).

67. Harrison, A., Robb, G., and Whittaker, G. (Unpublished).

68. Whittaker, A. G., Harrison, A., Oakley, G. S., Youngson, I. D., Heenan, R. K., and King, S. M. *Review of Scientific Instruments* **72**(1), 173–176 (2001).

69. Harrison, A., Ibberson, R., Robb, G., Whittaker, G., Wilson, C., and Youngson, D. *Faraday Discussions* **122**, 122–124 (2002).

70. `http://www.boedeker.com/teflon_p.htm`. [Online; accessed 02-May-2006].

71. `http://www.precision-ceramics.co.uk/macor.htm`. [Online; accessed 26-April-2006].

72. `http://www.precision-ceramics.co.uk/shapal.htm`. [Online; accessed 26-April-2006].

73. http://www.hamptonresearch.com/products/Product.aspx?sid=110. [Online; accessed 02-May-2006].

74. Weller, M. T. *Inorganic Materials chemistry*. Oxford University Press, (1994).

75. Rabo, J. A. and Schoonover, M. W. *Applied Catalysis A. General* **222**(1-2), 261–275 (2001).

76. Davis, M. E. and Lobo, R. F. *Chemistry of Materials* **4**(4), 756–763 (1992).

77. Francis, R. J. and O'Hare, D. *Journal of the Chemical Society. Dalton Transactions* , 3133–3148 (1998).

78. Byrappa, K. and Yoshimura, M. *Handbook of Hydrothermal Technology. A Thecnology for Crystal Growth and Materials Processing*. Noyes Publications, (2001).

79. Feng, S. and Xu, R. *Accounts of Chemical Research* **34**(3), 239–247 (2001).

80. Barrer, R. *Hydrothermal Chemistry of Zeolites*. Academic Press Inc. LTD, (1982).

81. Robson, H. *Journal of Microporous and Mesoporous Materials* **22**(4-6), 265–670 (2001).

82. Dyer, A. *An introduction to zeolite molecular sieve*. John Wiley & Sons, (1988).

83. Townsend, R. P. and Harjula, R. In *Post Synthesis Modification I,* Karge, H. G. and Weitkamp, J., editors, volume 3 of *Molecular Sieves. Science and Technology*, 2–39. Springer (2002).

84. Chu, P. and Dwyer, G. In *Intrazeolite Chemistry,* Stucky, G. and Dwyer, G., editors, volume 218 of *American Chemical Society Symposium Series*, 59–78. American Chemical Society (1983).

85. Karge, H. G. and Beyer, H. K. In *Post synthesis Modification I,* Karge, H. G. and Weitkamp, J., editors, volume 3 of *Molecular Sieves. Science and Technology*, 47–201. Springer (2002).

86. Breck, D. W. *Zeolite Molecular Sieves. Structure, Chemistry and Use*. Wiley-Interscience Publication, (1974).

87. Whittington, B. and Milestone, N. *Zeolites* **12**(7), 815–818 (1992).

88. Komarneni, S. and Menon, V. C. *Materials Letters* **27**(6), 313–315 (1996).

89. Zhu, J., Wang, Y., Chun, Y., Xing, Z., and Xu, Q. *Materials Letters* **35**(3-4), 177–182 (1998).

90. Braun, I., Schulz-Ekloff, G., Bockstette, M., and Wohrle, D. *Zeolites* **19**(2-3), 128–132 (1997).

91. Corporation, M. O., (1990). Eur. Pat. Appl. 0 358 827.

92. Cundy, C. S. *Collection Czech Chemical Communications* **63**(11), 1699–1723 (1998).

93. Arafat, A., Jansen, J., Ebaid, A., and van Beckkum, H. *Zeolites* **13**(3), 162–165 (1993).

94. Kokotailo, G. T., Lawton, S. L., and Olson, D. H. *Nature* **272**, 437–438 (1978).

95. Rao, C. N. and Gapalakrishnan, J. *New Directions in Solid State Chemistry*. Cambridge University Press, 2nd edition, (1997).

96. Olson, D. H., Kokotailo, G., Lawton, S. L., and Meier, W. M. *Journal of Physical Chemistry* **85**, 2238–2243 (1981).

97. Nicolaides, C. P. *Applied Catalysis A. General* **185**(2), 211–217 (1999).

98. Goretsky, A. V., Beck, L. W., Zones, S. I., and Davis, M. E. *Microporous and Mesoporous Materials* **28**(3), 387–393 (1999).

99. Rollmann, L. D., Schlenker, J. L., Kennedy, C. L., Kennedy, G. J., and Doren, D. J. *Journal of Physical Chemistry B* **104**(4), 721–726 (2000).

100. Woolery, G., Kuehl, G., Timken, H., Chester, A., and Vartuli, J. *Zeolites* **19**(4), 288–269 (1997).

101. Lowe, B., Nee, J., and Casci, J. *Zeolites* **14**(8), 610–619 (1994).

102. Xiao, F. S., Zhang, W., Jia, M., Yu, Y., Fang, C., Tu, G., Zheng, S., Qiu, S., and Xu, R. *Catalysis Today* **50**(1), 117–123 (1999).

103. Le Van Mao, R., Le, T. S., Fairbairn, M., Muntasar, A., Xiao, S., and Denes, G. *Applied Catalysis A: General* **185**(1), 41–52 (1999).

104. Jentys, A., Lugstein, A., and Vinek, H. *Zeolites* **18**(5-6), 391–397 (1997).

105. Chen, L., Chen, H. Y., Lin, J., and Tan, K. L. *Inorganic Chemistry* **37**(20), 5294 –5298 (1998).

106. Kosslick, H., Zubowa, H.-L., Lohse, U., Landmesser, H., Fricke, R., and Caro, J. *Ceramic Transitions (Microwaves: Theory and Applications in Materials Processing IV)* **80**, 523–537 (1997).

107. Xiao, F.-S., Xu, W., Qiu, S., and Xu, R. *Journal of Materials Science Letters* **14**, 598–599 (1995).

108. Xiao, F., Xu, W., Qiu, S., and Xu, R. *Journal of Materials Chemistry* **4**(5), 735–739 (1994).

109. Jacobs, P. A. In *Studies in Surface Science and Catalysis. Synthesis of High-silica Aluminosilicate Zeolites,* Jacobs, P. A., editor, volume 33, 47–111. (1987).

110. Carlin, R. *Magnetochemistry*. Springer, (1986).

111. Zhao, J. P., Cundy, C., and Dwyer, J. *Studies in Surface Science and Catalysis. Progress in zeolite and microporous materials* **105**, 181–187 (1997).

112. Zhao, J. P., Cundy, C., Plaisted, R. J., and Dwyer, J. In *12th International Zeolite Conference. Materials Research Society*, 1591–1594, (1999).

113. Robb, G. R. *The Microwave Effect: Non-thermal Effects of Microwave Radiation in Solid State Chemistry*. PhD thesis, University of Edinburgh, (2005).

114. Newnham, R. E. and Cross, L. E. *Materials Research Society Bulletin* **30**, 845–848 (2005).

115. Lines, M. E. and M., G. A. *Principles and Applications of Ferroelectrics and Related Materials*. Oxford Science Publications, (1979).

116. Megaw, H. D. *Acta Crystallographica B* **24**, 149–153 (1968).

117. Comes, R., Lambert, M., and Guinier, A. *Acta Crystallographica A* **26**, 244–254 (1970).

118. Cohen, R. E. *Nature* **358**, 136–138 (1992).

119. Hewat, A. W. *Journal of Physics C: Solid State Physics* **6**(16), 2559–2572 (1973).

120. Hewat, A. W. *Journal of Physics C: Solid State Physics* **6**(6), 1074–1084 (1973).

121. Katz, L. and Megaw, H. D. *Acta Crystallographica* **22**, 639–648 (1967).

122. `http://www.cds.dl.ac.uk/`. [Online; accessed 26-March-2006].

123. Cochran, W. *The Structures and Properties of Solids, Vol. 3: The Dynamics of Atoms in Crystals*. Crane, Russak, (1973).

124. El-Mahalawy, S. H. and Evans, B. L. *Journal of Applied Crystallography* **9**, 403–406 (1976).

125. `http://irc.swan.ac.uk/ThExpansion.htm`. [Online; accessed 26-March-2006].

126. Zhang, X., Lee, C. S. M., Mingos, D. M. P., and Hayward, D. O. *Applied Catalysis A: General* **249**(1), 151–164 (2003).

127. Seyfried, L., Garin, F., Maire, G., Thiebaut, J.-M., and Roussy, G. *Journal of Catalysis* **148**, 281–287 (1994).

128. Zhang, X. L., Hayward, D. O., and Mingos, D. M. P. *Industrial & Engineering Chemistry Research* **40**(13), 2810–2817 (2001).

129. Zhang, X., Hayward, D. O., and Mingos, D. M. P. *Catalysis Letters* **88**(12), 33–38 (2003).

130. Hajek, M. *Collection of Czechoslovak Chemical Communications* **62**(2), 347–354 (1997).

131. Zhang, X., Hayward, D. O., Lee, C., and Mingos, D. M. P. *Applied Catalysis B: Environmental* **33**(2), 137–148 (2001).

132. Perry, W. L., Cooke, D. W., Katz, J. D., and Datye, A. K. *Catalysis Letters* **47**(1), 1–4 (1997).

133. Bosman, H., Tang, W., Lau, Y. Y., and Gilgenbach, R. M. *Applied Physics Letters* **85**(15), 3319–3321 (2004).

134. Binner, J. P. G., Prince, D. M., Reading, M., and Vaidhyanathan, B. *Thermochimica Acta* **443**, 147–151 (2006).

135. Burley, G. *The Journal of Chemical Physics* **38**(12), 2807–2812 (1963).

136. Piltz, R. O. and Barnea, Z. *Journal of Applied Crystallography* **20**, 3–7 (1987).

137. Yoshiasa, A., Koto, K., Kanamaru, F., Emura, S., and Horiuchi, H. *Acta Crystallographica* **B43**, 434–440 (1987).